



**HAL**  
open science

# Effect of Fluids and Frequencies on Properties Elastics of sandstones and carbonates.

Lucas Pimienta

► **To cite this version:**

Lucas Pimienta. Effect of Fluids and Frequencies on Properties Elastics of sandstones and carbonates.. Other [q-bio.OT]. Ecole normale supérieure - ENS PARIS, 2015. English. NNT : 2015ENSU0002 . tel-02295557

**HAL Id: tel-02295557**

**<https://theses.hal.science/tel-02295557>**

Submitted on 24 Sep 2019

**HAL** is a multi-disciplinary open access archive for the deposit and dissemination of scientific research documents, whether they are published or not. The documents may come from teaching and research institutions in France or abroad, or from public or private research centers.

L'archive ouverte pluridisciplinaire **HAL**, est destinée au dépôt et à la diffusion de documents scientifiques de niveau recherche, publiés ou non, émanant des établissements d'enseignement et de recherche français ou étrangers, des laboratoires publics ou privés.



## THÈSE de DOCTORAT

Préparée à l' Ecole Normale Supérieure  
CNRS - Laboratoire de Géologie - UMR 8538

---

Présentée par  
**Lucas Pimienta**

pour obtenir le grade de  
**DOCTEUR en SCIENCES**  
de **L'ÉCOLE NORMALE SUPÉRIEURE**

Spécialité  
Sciences de la Terre et de l'environnement

(École Doctorale des Sciences de la Terre ED 560)

---

### **Effet des Fluides et des Fréquences sur les propriétés élastiques des grès et carbonates.**

---

Soutenance le 12 Février 2015

Membres du jury :

|                     |                    |
|---------------------|--------------------|
| Pr. Joerg Renner    | Rapporteur         |
| Pr. Jean Sulem      | Rapporteur         |
| Dr. Elisabeth Bemer | Examineur          |
| Pr. Christian David | Examineur          |
| Dr. Joel Sarout     | Examineur          |
| Dr. Claudio Madonna | Examineur          |
| Pr. Yves Guéguen    | Directeur de thèse |
| Dr. Jérôme Fortin   | Directeur de thèse |



*A mon père,*

*Most people say that it is the intellect which makes a great scientist. They  
are wrong : it is character.*

*Albert Einstein*



---

## Avant-Propos

Je tiens tout d'abord à remercier mes deux directeurs de thèse Pr. Yves Guéguen et Dr. Jérôme Fortin pour m'avoir suivi au cours de ces 3 années, pour leur aide scientifique et, surtout, pour leur patience face à un jeune doctorant légèrement dispersif. Je remercie Dr. Elisabeth Bemer et Pr. Christian David pour leurs commentaires constructifs lors de mes commités de thèse, ainsi qu'à ma soutenance. Merci à Pr. Joerg Renner et Pr. Jean Sulem pour leurs rapports constructifs sur mon manuscrit, et à Dr. Claudio Madonna pour ses remarques constructives. Merci enfin Dr. Joel Sarout, d'avoir fait le déplacement depuis Perth pour voir l'évolution de ma recherche depuis mon stage de master, pour nos discussions scientifiques au cours de toutes ces années et d'avoir accepté d'être membre de mon jury.

Je tiens également à remercier Dr. Alexandre Schubnel pour son aide précieuse lors des quelques moments de crise pendant mes calibrations. Merci à tout le personnel ITA et IATOS du laboratoire qui m'a accompagné durant cette thèse : Damien Deldique, Khaled Oubellouch, Nasser Bacha, Pierpaolo Dubernet, Catherine Archat, Delphine Coudert. En particulier, merci à Yves Pinquier pour son aide technique et ses avis, et à Isabelle Lavaleix, Micheline Rialet et Angélique Manchon pour leur grande aide et leur patience. Merci aussi à tout le personnel CNRS et enseignants du laboratoire pour leur aide ponctuelle au cours de ces 3 années. En particulier, merci à Matthias Delescluse et Luce Fleitout pour leur aide théorique, et à Patrick Meunier pour nos discussions scientifiques.

Un grand merci aux doctorants qui ont pris en charge les commandes de café pour le laboratoire, Aurélien Boiselet, Emilie Klein et Damian Walver, sans qui mon taux de travail aurait considérablement chuté. Merci à tous les doctorants et post-doctorants qui ont su être là dans les bons et mauvais jours. Merci en particulier à ceux qui m'ont aussi permis d'étayer ces journées plus difficiles que sont les samedi, dimanche et jours fériés : Pauline Maury, Max Bolot, Noé Lahaye ... les "climato"; et François Passelègue, Aurélien Nicolas, Audrey Bonnelye ... les "géologues". Un grand merci à François, co-bureau et amis, dont la compagnie lors des soirs et week-ends de travail au labo m'a été très précieuse. Merci donc pour cette vie commune de trois ans, peuplée de discussions et émulations scientifiques. Merci aussi à Suzanne d'avoir accepté de rejoindre notre bureau, pour nos discussions constructives, pour ta simplicité et, surtout, de m'avoir permis d'enrichir ma culture générale. Je remercie aussi mes amis de longue date, mes frères et ma mère pour leur patience, leur soutien et leur compréhension. Merci enfin à Pauline, pour ton aide, ton soutien et ta patience au cours de ces dernières années.



---

## Résumé Étendu

La sismique et la sismologie sont des moyens puissants pour comprendre la croûte terrestre. Ces deux méthodes reposent néanmoins sur la compréhension d'ondes sismiques traversant des milieux sédimentaires saturés en fluides. Ce travail, surtout expérimental, a pour but de comprendre les effets statique et dynamique du fluide sur la réponse élastique de roches clastiques saturées. Dans le cadre de l'interaction fluide-roche, deux questions spécifiques sont étudiées : (i) l'interaction fluide-roche physico-chimique, le "shear weakening", affectant la réponse élastique de la roche ; et (ii) l'interaction mécanique, le "frequency effect", induisant une dépendance des propriétés élastiques à la fréquence de mesure. Deux types de roche étudiés : les grès et les roches calcitiques. Les échantillons de roche à l'étude sont choisis pour leurs propriétés isotropes et leur forte concentration en un minéral dominant, i.e. le quartz pour les grès et la calcite pour les carbonates.

Utilisant un large éventail de grès et carbonates, le "shear weakening" est étudié soit pour des très faibles saturations, soit pour des saturations totales. L'effet des très faibles saturations est étudié en faisant varier l'humidité relative. Le paramètre clef est l'adsorption. Aucun affaiblissement est mesuré dans les carbonates, au contraire un large affaiblissement est observé dans certains grès. Pour cette interaction fluide-roche, non seulement le module de cisaillement est affecté, mais le module d'incompressibilité l'est aussi. L'affaiblissement élastique est global. L'effet ne semble pas provenir d'une différence intrinsèque entre les minéraux de quartz et de calcite. Grâce à un modèle micro-mécanique, cette différence semble provenir du caractère granulaire et du degré de cimentation de la roche. Cela permet d'expliquer pourquoi l'affaiblissement est important dans les grès peu cimentés et faible dans les carbonates fortement cimentés. Lors de saturation totale, aucun affaiblissement n'est observé dans les carbonates. Au contraire, un large affaiblissement est mesuré sur les compressibilités d'un échantillon de grès de Berea. L'affaiblissement est de l'ordre de 40 Cela implique que l'interaction (physico-chimique) fluide-roche est due à l'adsorption et implique un affaiblissement élastique global dans les roches (gréseuses et probablement carbonatées) granulaires peu cimentées.

L'effet de fréquence est étudié dans les grès de Fontainebleau et de Berea. Deux méthodes sont étudiées, toutes deux basées sur le principe de "stress-strain" (i.e. contrainte-déformation) : l'oscillation "isotrope" (de la pression de confinement) et "déviatorique" (de la contrainte déviatorique). Cette étude a été permise par l'existence d'une cellule tri-axiale mise en place par l'équipe de physique des roches de l'Ecole Normale Supérieure. Au cours de ce travail, de nombreux tests ont été nécessaires pour calibrer les deux modes d'oscillations. Dans ce but, avant de s'intéresser aux roches, plusieurs standards (e.g. aluminium, verre, gypse, plexiglass) ont été mesurés. Ensuite, des échantillons de grès de Fontainebleau et de Berea, saturés par des fluides de différentes viscosités, ont été mesurés avec ces deux modes d'oscillation. Pour le premier mode d'oscillation, dit "isotrope", ce travail a

permis de (i) mettre en évidence trois régimes élastiques distincts; et (ii) mesurer à la fois la conséquence (i.e. dispersion et atténuation du module d'incompressibilité) et la cause (i.e. écoulement fluide global) de la transition en fréquence entre état drainé et état non-drainé. Pour le second mode d'oscillation, dit "déviatorique", cela a permis de mesurer le module de Young et le coefficient de Poisson pour une gamme de fréquence apparente de  $f \in [10^{-3}; 10^5]$  Hz. Pour un échantillon de grès de Fontainebleau, cette large gamme de fréquence a permis l'observation des deux transitions entre les trois régimes élastiques. Les mesures sont cohérentes avec les théories existantes. Un modèle 1D, prenant en compte les conditions de bord du système, est développé. Ce modèle donne des résultats cohérents, et explique l'effet du volume mort sur les propriétés mesurées dans le cas d'une oscillation isotrope. Pour le mode "déviatorique", une implémentation du modèle est nécessaire. En particulier, les conditions de bord latérales doivent être prises en compte en construisant un modèle 2D.



## Extended Abstract

Seismics or Seismology are powerful tools to investigate Earth's crust. However, both rely on seismic waves that travelled through fluid-saturated sedimentary layers. This work, mainly experimental, aims at understanding the static and dynamic effects of the saturating fluid on the elastic response of clastic rocks. In this framework, two specific studies are emphasized : (i) the rock-fluid physico-chemical interaction, often addressed as the "shear weakening" effect, thought to affect the rock overall elastic response ; and (ii) the rock-fluid mechanical interaction, addressed as "frequency effect", thought to induce a dependence of elastic properties to the measuring frequency. Two main rock types are investigated : Sandstone and Limestone. All rock samples are chosen to be isotropic and composed of a dominant mineral content, i.e. quartz for sandstone and calcite for limestone.

Using a large set of limestone and sandstone samples, the "shear weakening" phenomenon is investigated at very low and full saturation. The effect of very low saturations is investigated from varying the air relative humidity. The parameter of interest is moisture adsorption. No elastic weakening is measured in the limestone samples, yet a large one is observed in some sandstone samples. It is shown that, for this rock-fluid interaction, not only the shear modulus of the rock sample is affected but also the bulk modulus, leading to a global "elastic weakening". No difference is expected between quartz and calcite minerals' intrinsic properties for this effect. Using a micro-mechanic model, this fundamental difference is shown to directly relate to both the granular characteristic and the degree of cement of the rock. This explains why large effects are observed in the granular sandstone samples, yet very low ones are observed in the well-cemented limestone samples. At full saturation, no weakening is observed on the limestone samples, yet a large weakening is observed on the bulk compressibilities of the Berea sandstone sample. This weakening amounts to about 40%. This suggests that the rock-fluid physico-chemical interaction is ruled by adsorption and leads to a global elastic weakening (only) in loosely-cemented (sandstone and probably limestone) granular rocks.

The frequency effect is investigated in well-known Fontainebleau and Berea sandstone samples. Two methods are used, both based on the stress-strain principle : the "isotropic" (i.e. confining pressure oscillations) and "deviatoric" (i.e. axial load oscillations) oscillations. This study was allowed by the existing experimental set-up developed by the rock physics group at the Ecole Normale Supérieure. During this work, extensive tests were needed to calibrate both oscillation modes. For this purpose, before measuring porous rock samples, various standard materials (e.g. aluminium, glass, gypsum, plexiglass) were measured. Then, Fontainebleau and Berea sandstone samples, saturated by fluids of differing viscosities, were measured for these two oscillations modes. In case of the first, isotropic, oscillation mode, this work allowed (i) to evidence three elastic regimes, and measure a transition between two elastic regime ; and (ii) for measuring both the consequence (i.e. bulk modulus

dispersion and attenuation) and the cause (i.e. global fluid-flow) of the drained/undrained transition. In case of the second, axial, oscillation mode, it allowed for measuring both Young modulus and Poisson ratio for a range in apparent frequency of  $f \in [10^{-3}; 10^5]$  Hz. For one particular Fontainebleau sandstone, this range in frequency allowed for the observation of both drained/undrained and relaxed/unrelaxed transitions. All measurements compare favourably with the existing theory. A 1D model is finally developed to consider the experimental boundary conditions. The model gives consistent results and proves to properly account for the effect of dead volume for the isotropic oscillation mode. In the case of the axial oscillation mode, further modelling of the experiment is to be developed. The lateral boundary conditions need to be accounted for by developing a 2D model.



---

## Table des matières

---

|           |  |           |
|-----------|--|-----------|
| <b>I</b>  | <b>Introduction générale</b>   | <b>1</b>  |
| <b>1</b>  | <b>General framework</b>   | <b>3</b>  |
| 1.1       | Elasticity of rocks : Effect of composition and microstructure . . . . .   | 4         |
| 1.1.1     | Elasticity fields in homogeneous materials . . . . .   | 4         |
| 1.1.2     | Case of sedimentary rocks . . . . .  | 4         |
| 1.1.3     | Physical representation of clastic rocks . . . . .   | 6         |
| 1.2       | Elasticity of rocks : Thermodynamic relations between rock's bulk moduli . .   | 7         |
| 1.2.1     | Notion of a rock's compressibility/bulk modulus . . . . .  | 7         |
| 1.2.2     | Experimental validation . . . . .  | 9         |
| 1.3       | Elasticity of rocks : Effect of fluids & frequencies . . . . .   | 10        |
| 1.3.1     | Dispersion & Attenuation . . . . .   | 10        |
| 1.3.2     | Dispersion & Attenuation mechanisms in rocks . . . . .   | 11        |
| 1.3.3     | Chemical effect of the fluid : Fluid-rock interaction . . . . .  | 14        |
| 1.3.4     | Coupling of fluid's mechanical and chemical effects . . . . .  | 16        |
| 1.4       | Framework for the study . . . . .  | 17        |
| 1.4.1     | Limestone samples chosen . . . . .   | 17        |
| 1.4.2     | Sandstone samples . . . . .  | 21        |
| 1.4.3     | Overview . . . . .   | 22        |
| <b>II</b> | <b>Effet de l'adsorption sur les propriétés élastiques des grès et carbonates</b>  | <b>23</b> |
| <b>1</b>  | <b>Introduction &amp; Fondements physiques</b>   | <b>27</b> |
| <b>2</b>  | <b>Investigation of elastic weakening in limestone and sandstone samples from<br/>moisture adsorption (<i>GJI, 2014</i>)</b> | <b>33</b> |

|   |  |           |
|---|--|-----------|
| 2.1   | Introduction . . . . .   | 34        |
| 2.2   | Experimental approach and samples studied . . . . .                                | 35        |
| 2.2.1   | Samples studied . . . . .  | 35        |
| 2.2.2   | Experimental set-up . . . . .  | 37        |
| 2.3   | Experimental results . . . . .   | 39        |
| 2.3.1   | Elastic properties ( $V_p$ - $V_s$ ) at low RH . . . . .                           | 39        |
| 2.3.2   | Evolution of properties with RH . . . . .  | 40        |
| 2.4   | Interpretation of elastic weakening using Effective Medium Theories . . . . .      | 41        |
| 2.4.1   | Model from Murphy et al. (1984) applied to velocity data . . . . .                 | 43        |
| 2.4.2   | Low-porosity sandstone samples : Modified model . . . . .                          | 46        |
| 2.5   | Discussion . . . . .   | 49        |
| 2.5.1   | Relation between bonding radius and porosity . . . . .                             | 49        |
| 2.5.2   | Relation between saturation and elastic weakening . . . . .                        | 51        |
| 2.5.3   | Waves amplitudes variations and attenuation . . . . .                              | 53        |
| 2.5.4   | Surface energy variations from adsorption . . . . .                                | 54        |
| 2.6   | Conclusions . . . . .  | 54        |
| <b>3</b>  | <b>Discussion &amp; Conclusion</b> . . . . .                                       | <b>57</b> |
| 3.1   | Further discussions on the adsorption study . . . . .                              | 57        |
| 3.1.1   | Another output from the modified model . . . . .                                   | 57        |
| 3.1.2   | Relation between amplitudes losses and attenuation . . . . .                       | 57        |
| 3.1.3   | Relation between weakening, attenuation and amount of adsorption . . . . .         | 59        |
| 3.1.4   | Elastic weakening in carbonates or in sandstones? . . . . .                        | 60        |
| 3.2   | Measurements at full saturation under drained conditions . . . . .                 | 60        |
| 3.2.1   | Case of the limestone samples . . . . .  | 61        |
| 3.2.2   | Case of the Berea sample . . . . .   | 62        |
| 3.3   | General conclusion . . . . .   | 64        |
| <b>III Oscillations de la pression de confinement :</b> |  |           |
| <b>Calibrations &amp; Mesures</b> . . . . .             |  | <b>67</b> |
| <b>1</b>  | <b>Introduction &amp; Principes de mesure</b> . . . . .                            | <b>71</b> |
| <b>2</b>  | <b>Bulk modulus dispersion and attenuation (<i>Geophysics, 2015</i>)</b> . . . . . | <b>77</b> |
| 2.1   | Introduction . . . . .   | 78        |
| 2.2   | Samples, experimental apparatus & procedure . . . . .                              | 79        |
| 2.2.1   | Samples studied . . . . .  | 79        |
| 2.2.2   | Experimental apparatus & procedure . . . . .                                       | 80        |
| 2.2.3   | Processing method for the low frequency set-up . . . . .                           | 84        |
| 2.3   | Calibration Results . . . . .  | 87        |

|   |  |            |
|---|--|------------|
| 2.3.1   | Limitations of the apparatus . . . . .                                       | 87         |
| 2.3.2   | Confining pressure effect for the reference samples . . . . .                | 88         |
| 2.3.3   | Frequency effect for the reference samples . . . . .                         | 89         |
| 2.4   | Results on Fontainebleau sandstone . . . . .                                 | 89         |
| 2.4.1   | Pressure dependence of the samples' elastic properties . . . . .             | 90         |
| 2.4.2   | Frequency dependence in the LF range at 1 MPa . . . . .                      | 92         |
| 2.4.3   | Frequency dependence in the LF range at four effective pressures . . . . .   | 93         |
| 2.5   | Interpretation . . . . .   | 95         |
| 2.5.1   | Rock physics framework . . . . .   | 95         |
| 2.5.2   | Interpretation of the frequency effects at 1 MPa . . . . .                   | 97         |
| 2.5.3   | Variation of attenuation with frequency . . . . .                            | 99         |
| 2.6   | Conclusion . . . . .   | 102        |
| <b>3</b>  | <b>Additional Calibrations &amp; Results</b>                                 | <b>105</b> |
| 3.1   | Measured Ultrasonic properties . . . . .                                     | 105        |
| 3.1.1   | Ultrasonic properties of the standard samples . . . . .                      | 105        |
| 3.1.2   | Ultrasonic wave velocities for the Fontainebleau samples . . . . .           | 106        |
| 3.1.3   | Porosity variation from confining pressure . . . . .                         | 108        |
| 3.1.4   | Inferred ultrasonic moduli for the Fontainebleau samples . . . . .           | 108        |
| 3.2   | Strain amplitude effects . . . . .   | 109        |
| 3.2.1   | Amplitudes of strains reached . . . . .                                      | 109        |
| 3.2.2   | Effect of the strain amplitude on the rock's elastic response . . . . .      | 111        |
| 3.3   | Evidence of a macroscopic fluid flow out of the sample . . . . .             | 112        |
| 3.4   | Measurements on a Berea sample . . . . .                                     | 113        |
| <b>4</b>  | <b>Conclusion &amp; Perspectives</b>   | <b>115</b> |
| 4.1   | Conclusion . . . . .   | 115        |
| 4.2   | Perspectives . . . . .   | 115        |
| <br><b>IV Oscillation de la contrainte déviatorique :</b> |  |            |
| <b>Calibrations &amp; Mesures</b>                         |  | <b>119</b> |
| <b>1</b>  | <b>Introduction &amp; Principes de mesure</b>                                | <b>123</b> |
| <b>2</b>  | <b>Effect of fluids and frequencies on Young modulus (<i>Geophysics</i>)</b> | <b>131</b> |
| 2.1   | Introduction . . . . .   | 132        |
| 2.2   | Experimental apparatus and Samples studied . . . . .                         | 133        |
| 2.2.1   | Samples studied . . . . .  | 133        |
| 2.2.2   | Experimental apparatus & procedure . . . . .                                 | 134        |
| 2.2.3   | Processing method . . . . .  | 136        |

|          |  |            |
|----------|--|------------|
| 2.3      | Calibration Results : Measurements under dry conditions . . . . .                    | 139        |
| 2.3.1    | Confining pressure effect for the reference samples . . . . .                        | 140        |
| 2.3.2    | Frequency effect for the plexiglass sample . . . . .                                 | 141        |
| 2.3.3    | Effect of the static axial load on dry rock samples . . . . .                        | 144        |
| 2.4      | Effect of fluids on sandstone samples' Young modulus . . . . .                       | 145        |
| 2.4.1    | Pressure dependence of the samples' Young modulus . . . . .                          | 145        |
| 2.4.2    | Frequency dependence of Young modulus for Fo7 sample . . . . .                       | 146        |
| 2.4.3    | Frequency dependence of hydraulic properties . . . . .                               | 147        |
| 2.5      | Interpretation & Discussion . . . . .  | 148        |
| 2.5.1    | Viscosity effect and Apparent frequency . . . . .                                    | 148        |
| 2.5.2    | Fluid flow at different scales in Fo7 . . . . .                                      | 150        |
| 2.5.3    | Young modulus and bulk modulus variations . . . . .                                  | 152        |
| 2.6      | Conclusion . . . . .   | 155        |
| <b>3</b> | <b>Effect of fluids and frequencies on Poisson ratio (GRL, submitted)</b>            | <b>157</b> |
| 3.1      | Introduction . . . . .   | 158        |
| 3.2      | Samples & Experimental procedure . . . . .   | 158        |
| 3.2.1    | Samples . . . . .  | 158        |
| 3.2.2    | Experimental apparatus & procedure . . . . .   | 159        |
| 3.3      | Results : Effect of pressure and frequency on Poisson ratio . . . . .                | 160        |
| 3.3.1    | Poisson ratio of standard samples . . . . .  | 160        |
| 3.3.2    | Dependence to fluids and pressure . . . . .  | 162        |
| 3.3.3    | Dependence to fluids and frequencies . . . . .                                       | 162        |
| 3.4      | Interpretation : Fluid flow and effective medium theories . . . . .                  | 164        |
| 3.4.1    | Fluid-flow theories and frequency dependence of elastic properties . . . . .         | 164        |
| 3.4.2    | Effective medium theories and values of $\nu$ in the three elastic regimes . . . . . | 166        |
| 3.4.3    | Experimental limits in the drained regime . . . . .                                  | 167        |
| 3.4.4    | Inferred $V_p/V_s$ ratio . . . . .   | 167        |
| 3.5      | Conclusion . . . . .   | 168        |
| <b>4</b> | <b>Discussions &amp; Perspectives</b>  | <b>169</b> |
| 4.1      | Effect of fluids on Poisson ratio of sandstone samples . . . . .                     | 169        |
| 4.2      | Effect of the boundary conditions . . . . .  | 171        |
| 4.2.1    | Bulk and shear moduli for Fo7 . . . . .  | 171        |
| 4.2.2    | Strain gauge position and local pore pressure . . . . .                              | 172        |
| 4.3      | Conclusions . . . . .  | 175        |

|  |            |
|--|------------|
| <b>V Transition Drainé/Non-Drainé en fréquence :</b>   |            |
| <b>Modélisation de l'expérience</b>  | <b>177</b> |
| <b>1 Introduction : Understanding the experiment</b>   | <b>181</b> |
| <b>2 General 1D model : Isotropic solicitation</b>   | <b>183</b> |
| 2.1 Theoretical boundary conditions . . . . .  | 183        |
| 2.1.1 Model derivation . . . . .   | 183        |
| 2.1.2 Drained and Undrained boundary conditions . . . . .  | 184        |
| 2.1.3 Comparison with the measurements on Fo7 . . . . .  | 190        |
| 2.2 Role of the dead volume : Experimental boundary condition . . . . .                                  | 191        |
| 2.2.1 Role of the dead volumes . . . . .   | 191        |
| 2.2.2 Quasi-static conditions . . . . .  | 192        |
| 2.2.3 Model predictions . . . . .  | 194        |
| 2.3 Direct comparison with the measurements . . . . .  | 196        |
| 2.3.1 Case of Fo7 sandstone . . . . .  | 197        |
| 2.3.2 Case of the Berea sample . . . . .   | 199        |
| <b>3 Conclusion &amp; Perspectives</b>   | <b>201</b> |
| 3.1 Conclusions . . . . .  | 201        |
| 3.2 General 1D model : Deviatoric solicitation . . . . .   | 202        |
| 3.2.1 Model derivation . . . . .   | 202        |
| 3.2.2 Effect of the dead volume . . . . .  | 203        |
| 3.2.3 Insight from the measurements : Skempton coefficient versus Conso-<br>lidation parameter . . . . . | 203        |
| 3.3 Perspectives : 2D poroelastic model . . . . .  | 204        |
| <b>VI Conclusion &amp; Perspectives</b>  | <b>209</b> |
| <b>1 Summary &amp; Perspectives</b>  | <b>211</b> |
| 1.1 Summary of the results . . . . .   | 211        |
| 1.1.1 Effect of frequency on the elastic properties of rocks . . . . .                                   | 211        |
| 1.1.2 Existence of a shear weakening in carbonates? . . . . .  | 212        |
| 1.2 Perspectives . . . . .   | 213        |
| 1.2.1 Frequency effects in carbonate rock samples . . . . .  | 213        |
| 1.2.2 Investigation of the fundamental relations the elastic moduli . . . . .                            | 213        |
| <b>Bibliography</b>  | <b>225</b> |
| <b>Annexes</b>   | <b>227</b> |

---

|          |  |            |
|----------|--|------------|
| <b>A</b> | <b>Experimental investigation of elastic and poroelastic properties of sandstone and limestone samples</b> | <b>229</b> |
| A.1      | Principle, Samples & Experimental set-up . . . . .   | 230        |
| A.1.1    | Principle . . . . .  | 230        |
| A.1.2    | Samples . . . . .  | 231        |
| A.1.3    | Experimental set-up . . . . .  | 232        |
| A.2      | Experimental protocol & properties measured . . . . .  | 235        |
| A.2.1    | Unjacketed measurement . . . . .   | 235        |
| A.2.2    | Undrained measurement . . . . .  | 237        |
| A.2.3    | Drained measurement : Confining pressure oscillations . . . . .  | 238        |
| A.2.4    | Drained measurement : Pore pressure oscillations . . . . .   | 239        |
| A.3      | Preliminary results . . . . .  | 240        |
| A.3.1    | Effect of the fluid volume on the pore compressibilities . . . . .   | 240        |
| A.3.2    | Skeleton bulk modulus . . . . .  | 241        |
| A.3.3    | Bulk compressibility of the Berea sandstone . . . . .  | 242        |
| A.3.4    | Bulk compressibility of limestone samples . . . . .  | 243        |
| A.3.5    | Effect of the dead volume under undrained conditions . . . . .   | 244        |
| A.4      | Conclusion . . . . .   | 246        |

**PARTIE I**

**Introduction générale**

|          |  |          |
|----------|--|----------|
| <b>1</b> | <b>General framework</b>   | <b>3</b> |
| 1.1      | Elasticity of rocks : Effect of composition and microstructure . . . . .     | 4        |
| 1.2      | Elasticity of rocks : Thermodynamic relations between rock's bulk moduli . . | 7        |
| 1.3      | Elasticity of rocks : Effect of fluids & frequencies . . . . .               | 10       |
| 1.4      | Framework for the study . . . . .  | 17       |



---

## General framework

---

Seismic and Seismology aim at identifying the rocks from the seismic waves that travelled through it. Yet, it directly implies for the rock's intrinsic properties to be known and theoretically understood. This, in turn, is one of the aims of theoretical/experimental rock physics. The particular case of sedimentary rocks is of interest. Indeed, all geological reservoirs (i.e. gas, oil or water) are found in sedimentary rocks. Even for Seismology that has interests in the Earth's mantle, the seismic waves recorded at the surface inevitably pass through the sedimentary layers. Their knowledge is thus needed to understand the waves signals.

Because sedimentary layers are porous and micro-cracked media often saturated by fluids of differing natures, one needs to understand how fluid affects their intrinsic properties. The work presented in this PhD, mainly experimental, aims at understanding some aspects ruling elasticity in sedimentary rocks. Out of the many fields concerned by these effects, we are here interested in the water-rock interactions on the static and dynamic properties of these media. Although intrinsically related, two specific points can be emphasized. The first one is the understanding of the static effect of water on the integrity of the rock. In the most dramatic cases, such effect may involve mineral dissolution that is for example the cause for large subsidence or even collapse of a reservoir or of a land (e.g. karst). The second one is related to the dynamic properties of the sedimentary media, and thus to the correspondence between seismic/seismology and rock physics : the frequency effect. Indeed, while the waves radiated by earthquakes lead typically to recorded waveforms below  $f = 1$  Hz and seismic field studies never exceed the frequency of  $f = 1$  kHz, the laboratory measurements are at  $f = 1$  MHz. It is thus of importance to investigate the correspondence of measurements that have a frequency that ranges up to about six orders of magnitude.

## 1.1 Elasticity of rocks : Effect of composition and microstructure

### 1.1.1 Elasticity fields in homogeneous materials

**Elasticity in homogeneous materials :** Materials can be characterized by their intrinsic strain response to an applied stress. A material is elastic if the deformation is instantaneous and reversible. For linearly elastic homogeneous materials, a linear relation exists between the applied stress and the resulting strain that is known as the stiffness (or compliance) tensor. The complexity of the stiffness (or compliance) tensor characterizing a material relates to its symmetries, or isotropic properties. In case of highly anisotropic materials, several constants of the tensor remain independent. On the contrary, in the particular case of an isotropic material, only two constants remain independent. Although the two constants chosen may differ, they are all intrinsically related by linear equations.

**Large deformations :** A distinction has to be made here based on the amplitude of deformation. Elasticity is concerned with small strains, and is the relevant domains in case of small reversible deformations. Depending on the applied stress and the material's stiffness, strains can be large enough so that deformations are not elastic anymore. At this point, other domains should be considered.

**Typical measuring methods :** In order to understand experimentally a given effect, the measuring method plays a crucial role. In the laboratory, two standard measurements of elasticity in rocks are :

- Measuring the velocity of propagation of elastic waves in the sample. The typical characteristics of these waves are a strain amplitude below  $10^{-7}$  and a frequency of about 1 MHz.
- Measuring the static moduli of the sample by applying a stress and measuring the sample's strain. While experiments can never reach the static sollicitation conditions, this quasi-static method can consistently be assumed to allow for measurements at a frequency below  $10^{-3}$  Hz. If made with slow enough pressure ramp. Owing to the accuracy of the measuring set-up, strain magnitudes can be as large as  $10^{-4} - 10^{-3}$ .

When comparing static and dynamic measurements, the difference in frequency is an important parameter. However, as pointed out by several authors, the effect of the strain amplitude are particularly important in many rocks.

### 1.1.2 Case of sedimentary rocks

Sedimentary rocks are usually grouped in three main rock types : sandstones, carbonates and shales. While the first two rock types may be isotropic materials, the third one

is intrinsically anisotropic and is not investigated here. Although more simple than shales, sandstone and carbonate rocks can also be seen as complex materials.

Rocks are aggregates of elastic minerals. As a direct consequence, a rock is expected to be elastic at ambient pressure and temperature. The properties are controlled by the mineral composition and the microstructure. Mineral composition is variable between rocks. It is however the microstructure that can produce the stronger variations on the rock's physical properties. This is because this term accounts for all possible "defects" of the rock bulk. It accounts for the degree of cementing of a rock, for the amount of inter- or intra-granular microcracks, and for the porosity morphology. Because microstructure rules both mechanical and hydraulic properties of a rock, its knowledge is of importance.

**Sandstones :** are sedimentary rocks whose dominant mineral is quartz. Because quartz is a strong mineral that transforms only in a high pressure and temperature environment, sandstones' microstructures are relatively simple and repetitive. This rock type is often found to be a granular aggregate, more or less cemented. Owing to their repetitive microstructures, sandstones have been largely investigated over the past decades. As compared to carbonates, their properties are better understood and predicted.

**Carbonate rocks :** represent up to 50-60% of sub-surface sedimentary rocks, and are efficient natural oil and gas reservoirs. Well-known carbonate oil reservoirs are for example Middle East micritic calcites (e.g., Volery et al., 2009), North America's dolomitic reservoirs, North Sea's chalks, or even Brazil's pre-salt carbonates. Yet, better understanding of carbonates is strongly needed. The reason is that, on the contrary to sandstones, carbonates are highly heterogeneous (Sun, 1995); and there is a large variety in depositional environments and burial history (Murray and Pray, 1965; Wardlaw, 1976).

The depositional environment is expected to dictate both the intrinsic properties of the pore fluid and the major constituent of this rock that can be fossils, oolites, peloids or crystals (Dürrast and Siegesmund, 1999). Burial history encompasses here diagenetic history (e.g. cementation, dissolution, and recrystallization) and tectonic history (e.g. fracturing). Tectonic processes may result in fractures and also crystallographic preferred orientation of rock-forming minerals, thus affecting the anisotropy (e.g., Ratschbacher et al., 1994).

Diagenetic history will be directly related to intrinsic nature of both pore fluid and major constituent (Moore, 2001). Diagenesis is particularly important in carbonate rocks due to the very reactive nature of calcite or dolomite at ambient conditions (Langmuir, 1971; Sigg et al., 2000). These processes may alter mineralogy and pore structure, by either dissolving or cementing at the grain contact, and lead to very different/variable microfabrics (e.g., Archie, 1952; Choquette and Pray, 1970; Lucia, 1983).

This large variety of pore types results in varying elastic properties measured for a given porosity (e.g., Anselmetti and Eberli, 1993; Eberli et al., 2003). While porosity is only inter-

granular in sandstones, intra-granular micropores are observed in carbonates (e.g., Eberli et al., 2003; Casteleyn et al., 2010, 2011), thus disrupting the usual porosity to velocity correlations. Owing to this microstructure variability, several concepts such as the critical-porosity (Nur et al., 1998), relevant for sandstone reservoirs, rarely apply to carbonates (e.g., Røgen et al., 2004). Several studies (e.g., Wang, 1997; Assefa et al., 2003; Baechle et al., 2008; Verwer et al., 2008; Fournier and Borgomano, 2009) thus aimed at understanding the controlling role of pore types and geometry on elastic properties of carbonate rocks, and emphasized the need for more work on this aspect.

The "Carbonate" term encompasses in fact two main rock types that are the dolostones, mainly constituted from dolomites, and limestones, dominantly constituted of calcite. Only the limestones, and thus the calcite, are investigated below.

**Sandstone versus limestone :** To sum it up, two main differences can be noted between the two rock types. As noted above, microstructure differs. While it is relatively repetitive in sandstones, a wide range in microstructures may be found for limestones. Second, the mineral content and its intrinsic properties differs. Quartz,  $SiO_2$ , is known as a "covalent" mineral, with a strong bond linking the silicium to the oxygen. Calcite,  $CaCO_3$ , is a "ionic" crystal as the weak bond between the calcium  $Ca^{2+}$  and the carbonate  $CO_3^{2-}$  holds only from ionic forces, and may be easily broken.

### 1.1.3 Physical representation of clastic rocks

To understand and model in a simple way the variability of the elastic properties in these materials, Effective Medium Theories were developed. EMT encompasses two dominant classes that fundamentally differ in their approach to build the effective rock.

In Hertz-Mindlin theory, the building block is the understanding of the elasticity at the contact between two grains. Then, the rock is defined as an aggregate of grains, and thus of grain contacts. In such approach, the porosity of the aggregate is introduced through the knowledge of nearest neighbours (i.e. coordinance number) for a given grain. More details can be found for example in the PhD manuscripts from E. Klein (2002) or J. Fortin (2005).

In the theories following Eshelby's inclusion problem, the approach is reversed. The building block considered is an homogeneous background in which defects of a given geometry are introduced. More details can be found for example in the PhD manuscripts of A. Schubnel (2003), J. Fortin (2005), J. Sarout (2006), M. Adelinet (2010) and E. David (2013).

While this study does not aim at explaining the fundamentals underlying these theories, these two distinct approaches are still introduced as they may allow to understand one fundamental difference between sandstones and carbonates. Because quartz grains do not easily dissolve at ambient P-T conditions, sandstones can consistently be considered as granular media that are more or less cemented. For the particular case of the loosely ce-

mented samples, Hertz-Mindlin theory applies particularly well. Because calcite may easily dissolve and re-precipitate, even at ambient P-T conditions, limestone can on the reverse rarely be considered as a granular and uncemented medium. A better representation of this second rock type is thus of an homogeneous background in which pores/inclusions are introduced, which is modelled using Eshelby approach.

## 1.2 Elasticity of rocks : Thermodynamic relations between rock's bulk moduli

Before introducing the effects of the fluids and frequencies on the elastic properties, one may investigate the relations between the rock's intrinsic bulk moduli. In the following, we consider small reversible strains under isothermal conditions. It can be assumed that the considered deformations remain in the field of linear elasticity.

### 1.2.1 Notion of a rock's compressibility/bulk modulus

#### Definition

Bulk modulus  $K$ , or compressibility  $C = K^{-1}$ , is the material's constant that quantifies its volume  $V$  change when a confining pressure  $P_c$  is applied to it :

$$K^{-1} = C = -\frac{1}{V} \left( \frac{\delta V}{\delta P_c} \right). \quad (1.1)$$

For a standard non-porous material, only one bulk modulus  $C = K^{-1}$  needs to be defined. A sedimentary rock is a porous medium that can be schematically considered as composed of both a solid matrix and a pore space filled by fluid (e.g. air or water). Noting  $V_f$  and  $V_s$  the fluid's and solid's volumes, bulk moduli ( $K_f$  and  $K_s$  respectively) are directly obtained for these two homogeneous materials such that :

$$K_f^{-1} = C_f = -\frac{1}{V_f} \left( \frac{\delta V_f}{\delta p_f} \right), \quad \& \quad K_s^{-1} = C_s = -\frac{1}{V_s} \left( \frac{\delta V_s}{\delta P_c} \right). \quad (1.2)$$

#### Compressibility coefficients from Zimmerman et al. (1986)

Because the rock is porous, a third volume needs to be considered. The rock's "bulk" volume  $V_b$  is the addition of the solid matrix's ( $V_s$ ) and pore space's ( $V_p$ ) volumes. The ratio of pore volume  $V_p$  over bulk volume  $V_b$  defines an intrinsic property of the rock : its porosity  $\phi$ . Considering the two independent volumes  $V_b$  and  $V_p$ , two pressures are defined :

- The confining pressure  $P_c$  applied to the rock bulk volume  $V_b$ .
- The pore pressure  $p_f$  applied to the pore space  $V_p$ .

It is useful to introduce a third pressure, the differential pressure, defined as  $P_d = P_c - p_f$ . It is the pressure applied to the solid matrix  $V_s$ .

Because two independent pressures and volumes are defined, four bulk moduli (or compressibility) may be defined. These compressibility coefficients were defined by Zimmerman et al. (1986), using straightforward subscripts to indicate the volume change and its cause (Zimmerman, 2000).

The bulk compressibility coefficients  $C_{bc}$  and  $C_{bp}$  are associated with  $V_b$  variations caused by either a confining pressure ( $P_c$ ) or pore pressure ( $p_f$ ) variation respectively, which leads to :

$$C_{bc} = -\frac{1}{V_b} \left( \frac{\partial V_b}{\partial P_c} \right)_{p_f}, \quad \& \quad C_{bp} = \frac{1}{V_b} \left( \frac{\partial V_b}{\partial p_f} \right)_{P_c}. \quad (1.3)$$

Note that the defined  $C_{bc}$  strictly corresponds to the well-known drained bulk modulus such that  $C_{bc} = K_d^{-1}$ .

The pore compressibility coefficients  $C_{pc}$  and  $C_{pp}$  are associated with  $V_p$  variations caused by either a confining pressure ( $P_c$ ) or pore pressure ( $p_f$ ) variation respectively, which leads to :

$$C_{pc} = -\frac{1}{V_p} \left( \frac{\partial V_p}{\partial P_c} \right)_{p_f}, \quad \& \quad C_{pp} = \frac{1}{V_p} \left( \frac{\partial V_p}{\partial p_f} \right)_{P_c}. \quad (1.4)$$

The compressibility  $C_{pc}$  is sometimes noted  $C_{pc} = K_\phi^{-1}$ .

Finally,  $K_s$  can also be obtained for the porous rock. For a constant  $P_d$ , both pore and confining pressures apply the same load on the solid matrix so that :

$$K_s^{-1} = C_s = -\frac{1}{V_b} \left( \frac{\partial V_b}{\partial P_c} \right)_{P_d} = -\frac{1}{V_p} \left( \frac{\partial V_p}{\partial P_c} \right)_{P_d}. \quad (1.5)$$

Note that we neglect for simplicity the possible effect of a micro-inhomogeneity (e.g., Brown and Korrington, 1975; Müller and Sahay, 2014).

### Relations between compressibility coefficients

From thermodynamics considerations (and Maxwell relations), direct relations can be obtained between these compressibility coefficients. Defining the isothermal free energy and enthalpy variations, one obtains :

$$C_{bp} = \phi C_{pc}, \quad \text{or} \quad C_{bp} = \phi K_\phi^{-1}. \quad (1.6)$$

Assuming the rock statistically homogeneous, defining the bulk volume variation  $dV_b$  leads to :

$$C_{bp} = \phi C_{pc} = C_{bc} - C_s, \quad \text{or} \quad \phi K_\phi^{-1} = K_d^{-1} - K_s^{-1}. \quad (1.7)$$

In the same way, defining the pore volume variation  $dV_p$  leads to :

$$C_{pp} = C_{pc} - C_s, \quad \text{or} \quad C_{pp} = K_\phi^{-1} - K_s^{-1}. \quad (1.8)$$

Note that there are four drained compressibilities (Eqs. 1.3 & 1.4) plus  $C_s$  (Eq. 1.5), which makes five compressibilities. There are three equations relating them (Eqs. 1.6, 1.7 & 1.8) so that only two independent compressibilities are obtained. Three bulk moduli are used : the drained modulus  $K_d$ , the pore modulus  $K_\phi$  and the matrix (or skeleton) modulus  $K_s$ . Two of them only are independent.

### 1.2.2 Experimental validation

In order to validate the assumption of purely elastic measurements, a possible approach could be to compare the different compressibility coefficients measured using the above equations. An experimental protocol was designed to measure these coefficients experimentally using low amplitude and low frequency pressure oscillations (see Appendix A). A 19% porosity Berea sandstone is used for the study. The frequency of the oscillations was chosen so that the measurements can consistently be considered quasi-static. Because the amplitude of strain (i.e. peak-to-peak amplitude) remains lower than about  $10^{-5}$ , the measurements are assumed to remain in the field of linear elasticity.

Because the experiment aims at testing the above relations for a given rock sample, the notation of Zimmerman et al. (1986) is preferred. From the experimental method,  $C_{pc}$  and  $C_{pp}$  show a dependence to the fluid total volume, i.e. sample and dead volume. For simplicity, only  $C_s$ ,  $C_{bc}$  and  $C_{bp}$  are thus reported here. The measured compressibility values measured for a fluid-saturated Berea sandstone sample are reported (Table 1.1). For the

**Table 1.1 :** Measured compressibilities for a fluid-saturated Berea sandstone sample at an effective pressure of  $P_{eff} = 1$  MPa.

| $C_s$ (Pa <sup>-1</sup> ) | $C_{bc}$ (Pa <sup>-1</sup> ) | $C_{bp}$ (Pa <sup>-1</sup> ) |
|---------------------------|------------------------------|------------------------------|
| $2.82 \cdot 10^{-11}$     | $1.87 \cdot 10^{-10}$        | $1.56 \cdot 10^{-10}$        |

skeleton bulk modulus, we obtain  $K_s = 35.5$  GPa. Consistently, the value is near the bulk modulus of the dominant mineral (i.e. quartz) of about 37 GPa. The lower value could be explained by (i) the measuring accuracy, (ii) the content in other minerals such as clay minerals, or (iii) the weak granular nature of the rock.

From the measurements, we find  $C_{bc} - C_{bp} = 3.1 \cdot 10^{-11}$  Pa<sup>-1</sup>. This is close to the value obtained for the skeleton bulk compressibility of  $C_s = 2.82 \cdot 10^{-11}$  Pa<sup>-1</sup>. Thus, the measurements fit relatively well with equation (1.6). The measuring method thus proves to give consistent results for the three compressibilities  $C_{bc}$ ,  $C_{bp}$  and  $C_s$ .

## 1.3 Elasticity of rocks : Effect of fluids & frequencies

### 1.3.1 Dispersion & Attenuation

**Viscoelasticity in homogeneous materials :** Because there always exists a condition (e.g. pressure, temperature, presence of fluid) for which a material is not purely elastic even at low strain, one may observe a loss in the elastic energy when an elastic wave travels through it. The amount of energy loss defines the material's viscoelastic properties. Large descriptions for viscoelasticity in homogeneous materials may be found for example in Nowick and Berry (1972) and in Toksöz and Johnston (1981).

**Characterisation of the viscoelasticity :** The loss in energy is characterised by an attenuation coefficient ( $\alpha$ ) that quantifies the exponential decay of the wave's amplitude ( $A$ ) when travelling through the medium :

$$A(x) = A_0 e^{-\alpha x}. \quad (1.9)$$

Where  $x$  is the distance travelled through, and  $A_0$  is the initial wave amplitude. An easy way to quantify this attenuation is through the quality factor ( $Q^{-1}$ ), defined as the ratio of dissipated ( $\Delta W$ ) over stored (or elastic  $W$ ) energy :

$$Q^{-1} = \frac{\Delta W}{2 \pi W}. \quad (1.10)$$

From viscoelasticity, one can define a complex modulus  $M = M_R + i M_I$ , so that the energy loss rewrites (e.g., Winkler and Nur, 1979; Hofmann, 2006) :

$$Q^{-1} = \frac{M_I}{M_R} = \tan(\Delta\phi). \quad (1.11)$$

Where  $\Delta\phi$  is the phase shift between applied stress and induced strain. This last representation is of main importance as it allows a direct measurement of the  $Q^{-1}$  of a given material using quasi-static stress oscillations. Then, it can be shown that :

$$Q^{-1} = \frac{\alpha V}{\pi f}. \quad (1.12)$$

Where  $V$  and  $f$  are the wave velocity and frequency.

**Attenuation versus quality factor :** Attenuation  $\alpha$  and quality factor  $Q^{-1}$  by definition relate in case of body waves travelling through a medium. By analogy, it is however considered (e.g., Winkler and Nur, 1979) that the  $Q^{-1}$  directly relates to attenuations for the well-known bulk  $K$ , shear  $G$  and Young  $E$  moduli. The underlying reason for such assumption is that these moduli relate the induced strain to the applied stress.

**Causes for attenuation :** The energy loss is expected to have different causes such as induced heat or fluid flow. The cause depends on the material studied and the conditions (i.e. pressure and temperature) of study. Quantifying the amount of energy loss is thus an important mean to better characterize the material investigated. Yet, it implies for the mechanism to be thoroughly understood.

### 1.3.2 Dispersion & Attenuation mechanisms in rocks

From measurements at room pressure and temperature conditions, no frequency effects are usually measured on dry rocks. Only when fluid is present in the porous network are the elastic properties dependent to the measuring frequency. It implies that the viscoelastic-like phenomena occur in rocks due to the presence of fluid.

#### 1.3.2.1 Mechanical effect of the fluid : Existence of elastic regimes

**Representative Elementary Volume (REV) :** Let us consider a given porous rock/material. This material can be described at three different scales : the micro-, mini- and macro-scales. In the present study, the macro-scale corresponds to the scale of the sample. The micro-scale, in turn, is the scale of the grains and pores, or other microscopic discontinuity, inside the sample. Although heterogeneous at the micro-scale the rocks are often homogeneous at the macro-scale, and at a scale below it : the mini-scale. This third intermediate scale is the one of interest and considers volume large enough that contains a large number of pores and grains. It is usually addressed as the Representative Elementary Volume (REV).

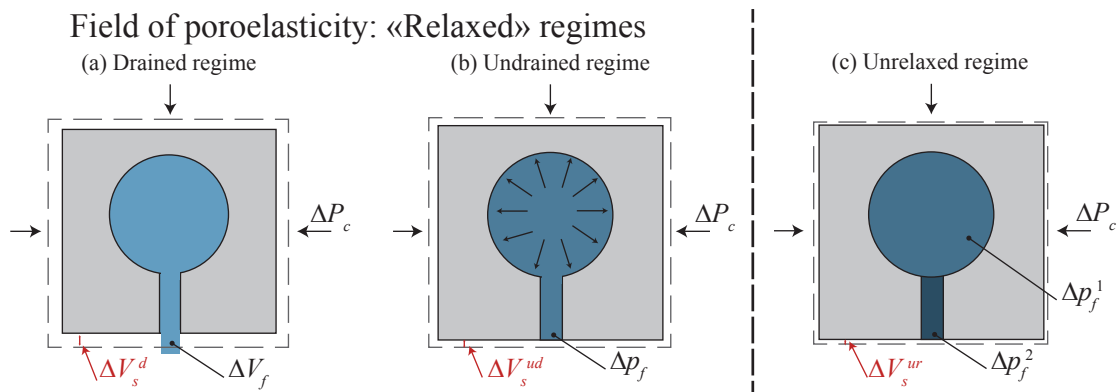


**Figure 1.1 :** Schematics of the poroelastic response of a porous material under either drained or undrained conditions to a pressure solicitation.

**Poroelasticity :** Poroelasticity (also called Biot theory) is concerned with small strains and provides the key results to handle small reversible deformations in materials. Poroelasticity investigates the elasticity of porous materials saturated by fluids, which is typically

the case of sedimentary rocks. Although it can be traced back to the work of Terzaghi in soil mechanics, it was the work of Biot (1941, 1955, 1962) that gave the basic theoretical framework. An appropriate and efficient presentation in Geosciences was published later by Rice and Cleary (1976). More extended developments are to be found in Detournay and Cheng (1993) and Wang (2000).

Because it provides the expression of porous rocks' elastic moduli in terms of fluid content and fluid compressibility, poroelasticity is a powerful tool. It allows to compare informations gained on the pores behaviours, and in particular to characterize the different bulk moduli. Poroelasticity accounts for two distinct regimes, both isobaric. The drained regime is that when fluid is allowed to flow in and out of a REV. In the undrained regime, fluid is not allowed to flow out of the REV. An example of differentiation between both regimes is illustrated in case of a confining pressure solicitation (Fig. 1.1).

In the drained regime (Fig. 1.1a), properties can be reached by understanding the fluid flow and matrix deformation responses to a given pressure solicitation. In the undrained regime (Fig. 1.1b), fluid exerts a mechanical response to the applied pressure. It can intuitively be found that, for a same applied pressure, the volumetric strain will result larger under drained conditions than in undrained ones. As a consequence, the compressibility of the rock is lower and its bulk modulus is stiffer in undrained conditions. This simple consideration is the framework of Biot-Gassmann equations, i.e.  $K_{ud} > K_d$ . Note that, Biot-Gassmann theory relies on a strong assumption on the rock's shear modulus : the fluid does not contribute to the rock's response to a shear solicitation, i.e.  $G_{ud} = G_d$ . This point will be discussed later.

**Unrelaxed regime :** One may finally imagine a last case scenario where the fluid has no time to flow locally from one inclusion to the next one (Fig. 1.1c) so that a third regime is built. In this final case, the fluid is not isobaric at the scale of the REV anymore. The regime is called "unrelaxed". It can intuitively be found that (i) the build-up pore fluid pressure inside the different inclusions intrinsically depends on the inclusion's geometry ; and (ii) the build-up pressure in the compressible defects is much higher than in the undrained regime, leading to an even smaller volumetric deformation. The resulting compressibility of the medium decreases, leading to the relations :  $K_{ur} > K_{ud}$  and  $G_{ur} > G_{ud}$ . Note that, at this stage, fluid is expected to contribute to the rock's response to a shear solicitation, leading to the increase in the shear modulus.

### 1.3.2.2 Link between regimes and frequency

As discussed by different authors in the case of clastic rocks, frequency effect originate from fluid flow, or pressure re-equilibration, induced by the travelling acoustic wave (e.g., Sarout, 2012). This phenomenon is thought to originate mainly from the existence in the rock of families of inclusions with different compliances, and is dictated by the ability of

the fluid to flow between the different families.

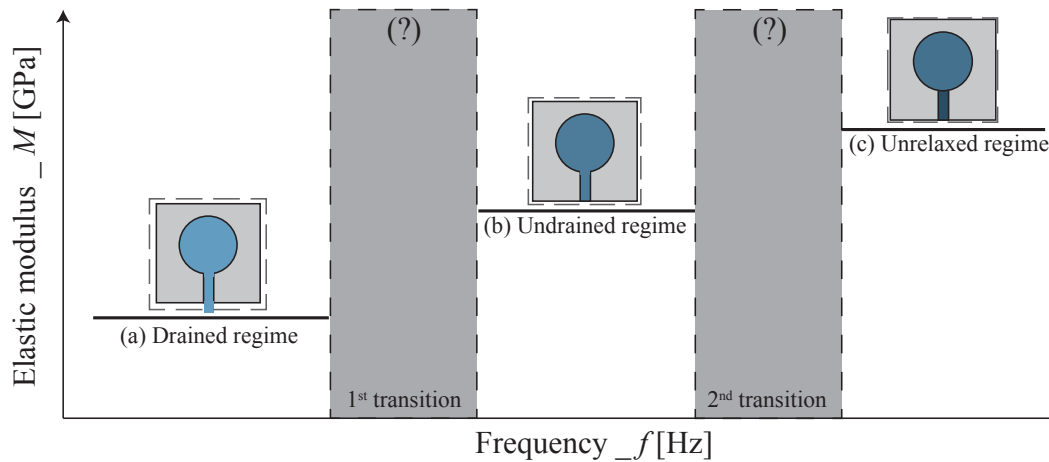


**Figure 1.2 :** Schematics of the frequency dependence of the sample's elastic modulus. The three regimes are highlighted, and the transitions are noted as grey zones.

**Low Frequency framework :** Poroelasticity accounts for two distinct regimes, both isobaric at the REV scale. The transition between the two regimes can be chosen experimentally by changing the boundary conditions, i.e. allowing or not fluid out of sample, but can also be ruled by the measuring frequency. As shown by Cleary (1978), another parameter may also determine the transition between the regimes : the hydraulic conductivity ( $\kappa/\eta$ ), which indicates the interplay between the rock's intrinsic permeability and the fluid's viscosity. Because the undrained modulus is expected to be larger than the drained one, a frequency-dependent dispersion/attenuation phenomenon is thus expected to occur.

**High Frequency framework :** Many scientists have emphasized however that Biot assumptions may not be applicable to all situations. In particular, such situations may not be achieved if the wave frequency is high enough to prevent isobaric relaxation through fluid flow inside the REV. A squirt flow (local flow) effect may introduce frequency-dependent dispersion in elastic moduli (e.g., Müller et al., 2010), and a third, unrelaxed, regime may be reached. Most of the theoretical work on this aspect has been compiled in two volumes of the Geophysics reprint series edited by Wang and Nur (1992, 2000).

Note however that, on the contrary to the first, poroelastic, transition, this squirt-flow effect intrinsically relates to the geometry of pores present at the REV scale. Only if these inclusions bear differing compressibilities, can a pressure-induced fluid-flow occur from one inclusion to the other.

**Transitions between regimes :** While it is theoretically expected to observe three regimes in the seismic frequency range, the evolution of the elastic properties in between

these regimes is poorly known (Fig. 1.2). Although several models intended at predicting these transitions, no direct measurements allowed to confirm these models. In case of a viscoelastic-like response, a strong variation of the quality factor should also be observed. Yet, for example, nothing indicates that this "attenuation" peak should be symmetric as the standard viscoelastic models indicate it.

One aim of the study is to give insights on these frequency-dependent transitions on the dispersion and quality factors of the different elastic properties investigated.

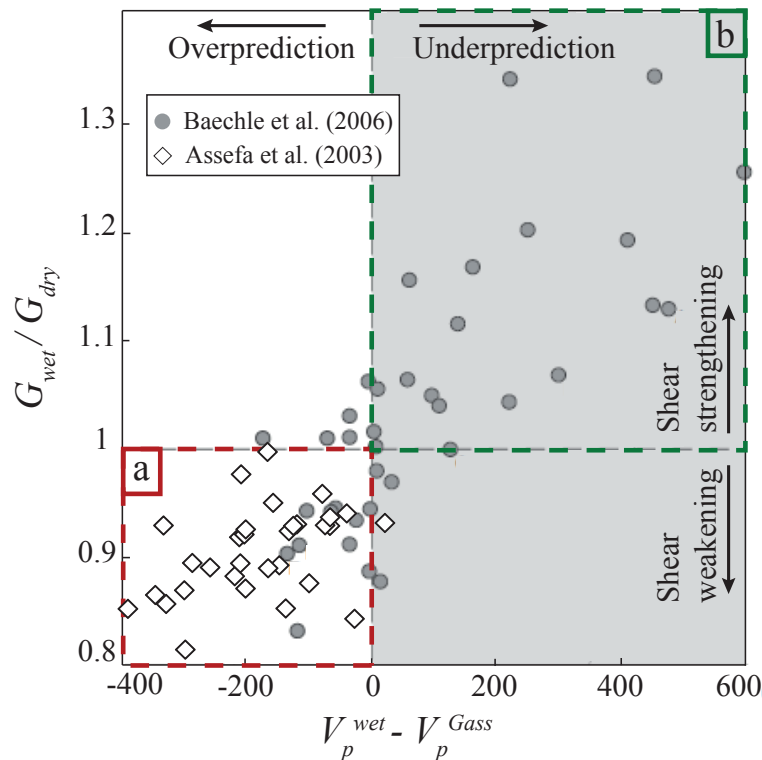


**Figure 1.3** : Comparison between measured and Biot-Gassmann's water saturated P-waves and S-waves (in terms of shear moduli) velocities. The figure is modified from Baechle et al. (2009) to introduce data from Assefa et al. (2003), also measured at room T-P conditions, and highlight the zones of interest for water (a) weakening and (b) strengthening.

### 1.3.3 Chemical effect of the fluid : Fluid-rock interaction

Adding up to the intrinsic difficulties in characterising the elastic properties of the microstructurally complex carbonates, another complexity arises when saturating the rock by water. Fluid is generally expected to only affect elastic properties through its density and bulk compressibility, and the mechanical effect of fluid is the one expected to occur. Biot-Gassmann equation was in particular proved to apply well in case of the sandstone samples.

However, deviations from the usual understanding are observed in carbonate rocks

(e.g., Vega et al., 2007). The shear modulus of the rock sample appears to decrease when under water full saturation (Assefa et al., 2003; Røgen et al., 2005; Baechle et al., 2009). A good way to understand such effect was to compare both P- and S-waves velocities to Biot-Gassmann theory (Baechle et al., 2009), to investigate the full deviation from the theory (Fig. 1.3).

An interesting effect can directly be noted from these results : Out of the four zones drawn from the plot, the carbonates fall in only two defined zones. One corresponds to a "shear weakening" that is accompanied to an overprediction of Biot-Gassmann theory (Fig. 1.3a). The second corresponds to a "shear strengthening" that relates to an underprediction of the theory (Fig. 1.3b). The carbonates of Baechle et al. (2009) either under- or overestimate the theory. However, compiling the data from Assefa et al. (2003) shows that all their samples fall in the zone of a decrease in shear modulus upon water full saturation : the "shear weakening" zone, i.e. a water-rock interaction that softens the rock sample and decreases its shear modulus.

In the particular case of carbonates, this rock-fluid interaction is widely addressed when accounting for deviations from theory. Several studies highlighted rocks' shear modulus changes with fluid saturation in carbonates (Assefa et al., 2003; Adam et al., 2006; Baechle et al., 2008; Verwer et al., 2008; Baechle et al., 2009; Verwer et al., 2010). The softening effect of water was attributed by authors (e.g., Khazanehdari and Sothcott, 2003) to different effects such as viscous coupling or chemical alteration and reactivity (e.g., Vialle and Vannorio, 2011). Yet, the precise cause for such phenomenon, evasively addressed as "shear weakening" or "Rhebinder effect" remains to be fully explained. Another hint on this fluid-rock softening effect has however been given by Baechle et al. (2009) : The observed "shear weakening" is a reversible phenomenon, i.e. the shear modulus increase back to its original value once the rock is dried back. Furthermore, according to Verwer et al. (2010), an important parameter for the magnitude of this rock-fluid effect remains pore structure.

Note further from Baechle et al. (2009) results (Figs. 1.3a & 1.3b) that "shear weakening" (or strengthening) is always accompanied by an overprediction (or underprediction) of Biot-Gassmann theory. Although P-wave velocities are indeed expected to directly depend on the shear modulus, the decrease (or increase) in shear modulus upon water saturation does not explain the total amount of overprediction (or underprediction) from Biot-Gassmann theory. It directly implies a full coupling between the elastic moduli, i.e. the rock's bulk modulus is equally affected. In case of strengthening, frequency effects are involved, which consistently lead to a similar effect on P- and S-wave velocities (and ultrasonic both bulk and shear moduli). In case of weakening (Fig. 1.3a), the fluid-rock interaction is involved, leading to the often addressed "shear weakening" but also to the forgotten "bulk weakening".

### 1.3.4 Coupling of fluid's mechanical and chemical effects

An important bias in understanding the fluid effects was found in the frequency dependence of the elastic properties (e.g., Baechle et al., 2009). Because standard laboratory set-up involves measuring ultrasonic wave velocities across the sample, HF moduli are investigated. As shown earlier, frequency may alter the measurements, leading to an overall strengthening of the measured elastic properties. As introduced earlier, frequency effects are tightly related to the presence of pressure-dependent thin elongated discontinuities (i.e. microcracks). Although frequency effects are expected to be less important in carbonates that bear fewer microcracks, recent works showed that it was not the case (Adam et al., 2009; Baechle et al., 2009; Verwer et al., 2010). This may be the cause for the samples of Baechle et al. (2009) to fall in the "shear strengthening" zone (Fig. 1.3b). To counter such bias, measurements at low frequencies are needed. As an example, Adam et al. (2009) measured a carbonate sample and showed the existence of a frequency-dependent shear modulus (Fig. 1.4).

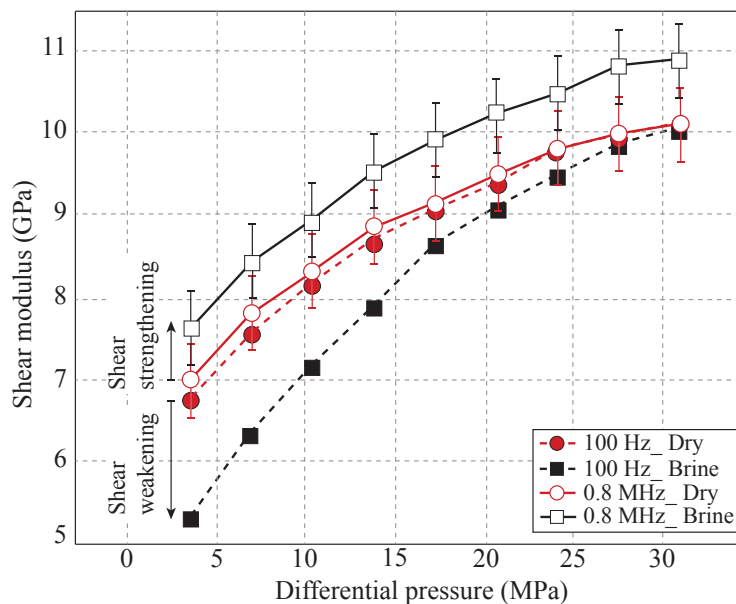


**Figure 1.4** : Measured shear modulus at low (i.e.  $f = 100$  Hz) and ultrasonic (i.e.  $f = 1$  MHz) frequencies on a carbonate sample. The figure is taken and slightly modified from Adam et al. (2009).

As shown, for a given sample that shows a shear strengthening at HF, a shear weakening may also be observed at lower frequencies. Furthermore, the differences with frequency and fluids disappear as effective pressure increases, indicating that the rock-fluid interactions are strong only when the compliant microstructure is open. The results (Fig. 1.4) of Adam et al. (2009) thus add up to the ones (Fig. 1.3) of Baechle et al. (2009), indicating that (i) a shear weakening may also occur for the samples that show strengthening at HF; (ii) existence of compliant microstructure may be a key factor for the weakening to occur;

and (iii) the samples showing weakening at HF may show even more weakening at LF. While Adam et al. (2009) study brings to light added informations, the physical phenomena underlying this rock-fluid interaction effect are still to be understood.

## 1.4 Framework for the study

Two main questions were thus highlighted for this PhD thesis :

1. What is the cause for the "shear weakening" observed in carbonate rocks ? And why is it a phenomenon that is specific to carbonates ?
2. How does frequency affect a rock's elastic moduli ?

A last point would be to question what is the effect of frequency in a rock where rock-fluid (chemical) interaction occurs. However, owing to time constraints, this last point was not addressed in the study. In particular, no frequency dependence of carbonate samples' elastic properties is reported here.

The limestone samples chosen are introduced first. The sandstone samples that correspond to most of the work reported in this manuscript are then introduced afterwards to highlight its relative simplicity. An overview of the samples investigated in during this PhD is detailed in table 1.2.

### 1.4.1 Limestone samples chosen

Many intrinsic parameters of the limestones may play a role, e.g. mineralogy, pore structure, cementing conditions, forming conditions. Most of the samples, except for Tavel and Indiana limestones, originate from Paris basin. The choice for the samples is based on those different criteria, with the aim to simplify the problems investigated.

**Mineralogy :** First, all samples are chosen so that the mineralogy is simple : for all samples, calcite content is above 95 % so that the rocks can consistently be considered as pure calcite. For most of the samples, the content found is 99% calcite. Only in Indiana and Tavel limestones some inclusions of pyrite or magnetite were observed (Fig. 1.5).

Furthermore, the pore structure is globally similar for all samples, i.e. made up of a double porosity. Large pores of about 100  $\mu\text{m}$  size are present between the grains (or grains aggregates), and small pores of about 1  $\mu\text{m}$  size are also present. Interestingly, a second information is obtained. While of differing nature, the rocks always show presence for a fine-grained calcitic matrix (Fig. 1.5) that is referred as micrite.

**Porosity :** The rock samples chosen have a large range in porosity, from 5 % up to 30 %. They all possess a double porosity. On the contrary to sandstones, the double porosity relates to the presence of two distinct families of equant pores. The first family is constituted

**Table 1.2 :** Properties of the tested samples. Porosities ( $\phi$ ) as measured in this work. Approximate permeability ( $\kappa$ ) and pore entry diameter ( $d$ ) are reported from previous studies on the different samples.

| Samples                 | Classification | $\phi$ (%) | $\kappa$ ( $m^2$ ) | $d$ ( $\mu m$ )  |
|-------------------------|----------------|------------|--------------------|------------------|
| Massangis (MaoL)        | Oolite         | 6.1        | $1.10^{-16}$       | 0.1-0.8 and 100  |
| Indiana (IndyL)         | Oolite         | 12.4       | $2.10^{-15}$       | 0.04-1 and 100   |
| Euville (EuvL)          | Oolite         | 15.9       | $4.10^{-15}$       | 0.1 and 1-80     |
| Chauvigny (ChoL)        | Oolite         | 16.3       | –                  | 0.1-2 and 10-50  |
| Tavel (TavL)            | Micrite        | 17.2       | $1.10^{-17}$       | 0.02-0.3 and 100 |
| Anstrude (ByoL)         | Oolite         | 19.5       | $4.10^{-16}$       | 0.3 and 100      |
| Raviere (RavL)          | Oolite         | 19.7       | $2.10^{-16}$       | 0.4 and 100      |
| Lavoux (LavL)           | Oolite         | 22.4       | $1.10^{-14}$       | 0.84 and 20      |
| Fontvieille (FonL)      | Micrite        | 23.6       | –                  | –                |
| Estailades (EstL)       | Micrite        | 28.4       | $2.10^{-13}$       | 0.39 and 19      |
| Chauvigny (ChmL)        | Micrite        | 34.4       | $2.10^{-15}$       | 0.2-3 and 200    |
| Fontainebleau (FoSp2a)  | Granular       | 2.6        | $1.10^{-17}$       | 1-10             |
| Fontainebleau (FoSp2b)  | Granular       | 2.2        | $1.10^{-17}$       | 1-10             |
| Fontainebleau (FoSp4)   | Granular       | 4.7        | $1.10^{-15}$       | 1-10             |
| Fontainebleau (FoSp7a)  | Granular       | 6.8        | $5.10^{-15}$       | 1-10             |
| Fontainebleau (FoSp7b)  | Granular       | 7.2        | $5.10^{-15}$       | 1-10             |
| Fontainebleau (FoSp7c)  | Granular       | 7.4        | $5.10^{-15}$       | 1-10             |
| Fontainebleau (FoSp8)   | Granular       | 8.2        | $1.10^{-14}$       | 10               |
| Fontainebleau (FoSp9a)  | Granular       | 8.7        | $1.10^{-14}$       | 10               |
| Fontainebleau (FoSp9b)  | Granular       | 9.0        | $1.10^{-14}$       | 10               |
| Fontainebleau (FoSp16a) | Granular       | 16.0       | $1.10^{-12}$       | 10-20            |
| Fontainebleau (FoSp16b) | Granular       | 16.7       | $1.10^{-12}$       | 10-20            |
| Fontainebleau (FoSp18a) | Granular       | 18.2       | $5.10^{-12}$       | 10-20            |
| Fontainebleau (FoSp18b) | Granular       | 18.9       | $5.10^{-12}$       | 10-20            |
| Glass                   | Homogeneous    | 0          | 0                  | –                |
| Gypsum                  | Homogeneous    | 0.1        | $> 1.10^{-20}$     | –                |
| Plexiglass              | Homogeneous    | 0          | 0                  | –                |

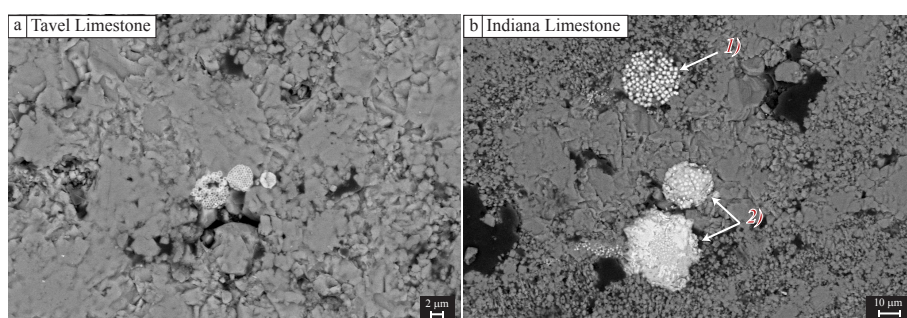


**Figure 1.5 :** SEM images of (a) Tavel and (b) Indiana limestones' thin sections. Few inclusions of magnetite and pyrite are embedded in the calcite matrix for the Tavel and Indiana limestone respectively.

of large pores of about  $100 \mu m$ . The second family is made of micron-sized pores, which locality differ from one rock to the other (Casteleyn et al., 2011).

**Depositional environment :** A distinction is made based on the depositional conditions, i.e. separating globally oolitic-like limestones from the micritic-like ones. As shown from sedimentary studies, several distinctions can be made on the shells building the limestone's matrix such as peloids, oolites, etc. For simplicity, all are considered the same here in order to differentiate them from the micritic-like samples, which building block are micron-size calcite grains. Both rock types differ in the position, and probably the role, of this micro-porosity in the overall properties.

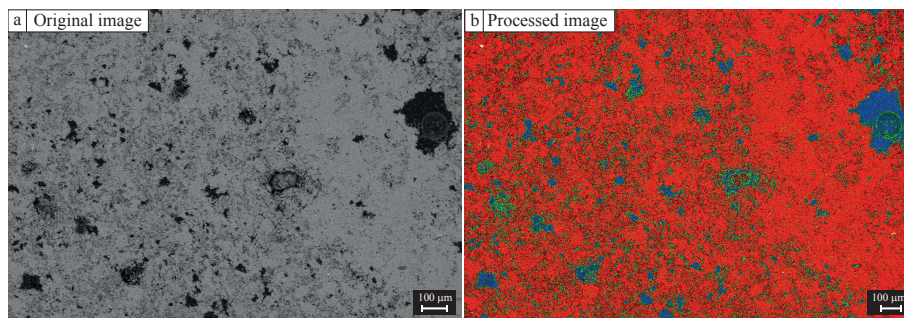


**Figure 1.6 :** SEM images of the micritic Tavel. The original (a) grey levels of the image are replaced by (b) a colour-code accounting for the local densities in the images, ranging from blue for void to red for the denser materials.

An exemple of microstructures is given for oolitic (Fig. 1.7) and micritic (Fig. 1.6) samples. A colouring option, replacing grey levels by colours, is used on the microscope's images in order to highlight in an easier way the differing microstructures of the samples. The threshold is chosen so that low density material (i.e. macro-pores) is in blue, and highest density one (i.e. calcite mineral) is in red. The green colour corresponds to the intermediate case, i.e. n average of a pore and a grain (i.e. micro-pores).

For the micritic samples (Fig. 1.6), sparitic grains are present in the matrix and are surrounded by micron-size grains that are more or less cemented. The cohesion (i.e. cement) between micritic grains gives the overall elastic properties of the sample. Tavel limestone (Fig. 1.6) is a highly cemented limestone, with both macro- and micro-porosities randomly embedded in a cemented micritic background. Reversely, Chauvigny micrite limestone shows the presence of sparitic grains and macro-pores embedded in micritic matrix that is highly micro-porous. The micritic grains appear poorly cemented.

For the oolitic-like samples (Fig. 1.7), presence of shells of various forms (e.g. oolites for the spherical ones) are embedded in a cemented micro-crystalline matrix. The major difference with the micritic samples is the localisation of the micro-porosity. For all oolitic samples, its localisation is within the shells. Such difference may lead to different physical behaviours of both rock types. For some samples (Fig. 1.7), the macro-pores are embedded in the background micritic cement. For other samples, the macro-pores are placed within the oolites. It probably originates from an enhanced dissolution inside the oolites, allowed by the existing micro-porosity. It may again lead to differing physical properties.

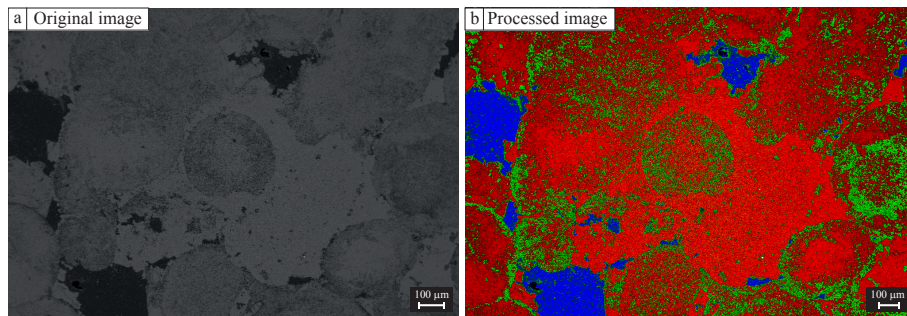


**Figure 1.7 :** SEM images of the oolitic Chauvigny limestone. The original (a) grey levels of the image are replaced by (b) a colour-code accounting for the local densities in the images, ranging from blue for void to red for the denser materials.

**Role of the diagenesis** As stated earlier, during the diagenesis stage, strong dissolution and precipitation processes occur in the limestones. It leads to creation of a strong cement in between the deposited oolites, leading to a cemented micritic matrix. The crystalline phases present in this cemented matrix may also affect the final physical response of the rock. An example is given for the Ravierre limestone investigated using a polarising microscope (Fig. 1.8).

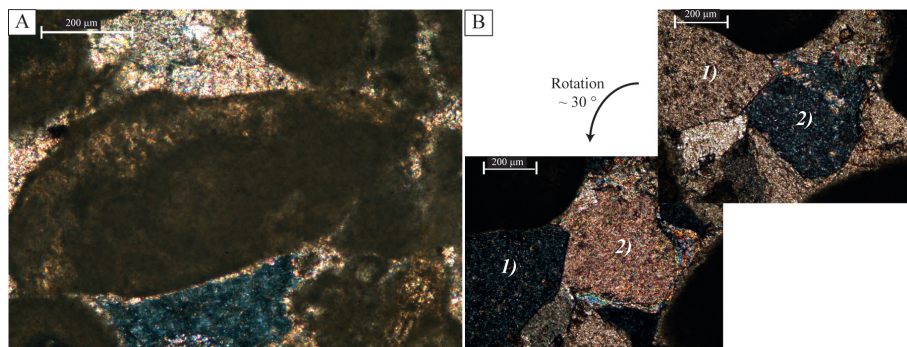


**Figure 1.8 :** (a) Image of a thin section of a Ravierre limestone using a polarising microscope. (b) Example of the rotation of the extinction angle of the cement by rotating the polarising prism.

From such images one can note that (i) the cement is constituted of crystalline material ; (ii) the oolites are constituted of either amorphous material or micro-crystalline materials of differing orientations ; and (iii) all crystalline cements were not formed at the same time, thus leading to the variation in orientations. These variations highlight further the fundamental difference between the oolitic grains, probably more compliant, and the crystalline cement, probably stiffer.

**Consequence :** All samples can be considered as calcite-pure limestones. They all bear both macro- and micro-pores, the position of which differs from sample to sample. Furthermore, all samples can consistently be considered as homogeneous at the sample's scale.

And, from the differing orientations taken by the crystalline cement, it is consistent to consider the rocks as isotropic at the sample's scale.

### 1.4.2 Sandstone samples

The two sandstone chosen are Fontainebleau and Berea sandstones. Both are reference rocks for the rock physics and rock mechanics communities.

Fontainebleau sandstone is well-known for its quartz-pure content and its wide range in porosity, permeability, and elastic properties. The wide range in physical properties of this sandstone originates from its variable degree in cementing (e.g., Bourbie and Zinszner, 1985). An example of microstructures observed for three samples of varying porosities are obtained for this rock using a polarising microscope (Fig. 1.9). The polarising microscope allows for observing the different crystal's preferred orientations. Black zones are not necessarily pores but crystal that are extinct for this orientation. A particularity of this

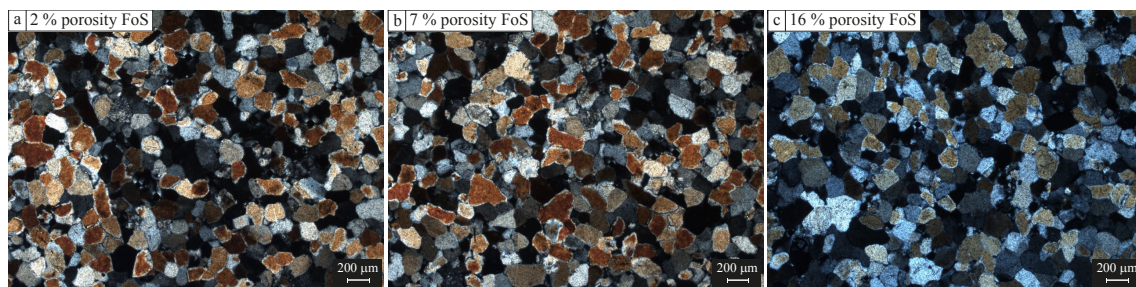


**Figure 1.9 :** Microstructure images of thin sections for three Fontainebleau Sandstone samples (FoS) using a polarising microscope. In (a) a 2% porosity sample is observed, in (b) a 7% porosity is observed and in (c) a 16% porosity sample is observed.

rock is that no observable change in the grains morphology can be noted from varying the porosity of this rock. The quartz grains can consistently be considered as elongated spheroids of repetitive diameter/size of about 200  $\mu\text{m}$ . The difference in cement cannot be observed at this scale, and may occur at the grains' contact. At the REV scale, the rock can consistently be considered homogeneous. Furthermore, the random orientation of the grains make the sample isotropic at the REV scale. All of these properties allow for this rock to be a particularly easy rock to work with.

Although Berea sandstone cannot be considered mono-mineralic because of variable degrees in clay minerals and feldspars, its mean quartz content ranges above about 75%. All the Berea samples previously investigated (Pimienta et al., 2014b), have a porosity is in the range of  $\phi \in [17;22] \%$  and a permeability is in the range of  $\kappa \in [1;10^3] \text{mD}$ . Yet, because of a very uniform degree of cementing for this rock, its physical (e.g. elastic or thermal) properties are very repetitive from one sample to the other. In addition, the rock can consistently be considered as homogeneous and isotropic (although some rocks bear a slight degree of anisotropy) at the REV scale. This rock was in particular investigated for

its poroelastic properties under water full saturation by Hart and Wang (1995). It is thus of particular interest for the study in **chapter II.3** of this manuscript.

### 1.4.3 Overview

This manuscript was written in an article-like format, which overview is as follows :

- In **part II**, the whole set of limestone and sandstone samples is used to investigate a good candidate for the "shear weakening" phenomenon : Adsorption. Before the main study, adsorption and its effects in rocks are briefly introduced (**Chap. II.1**). Then, the study of the effect of adsorption on the rocks' elastic properties is detailed in **chapter II.2** (article published in *Geophysical Journal International*). Additional discussions and new results on the drained bulk moduli under full saturation by different fluids are finally introduced in **chapter II.3**.
- In **part III**, the frequency dependence of Fontainebleau sandstone samples' bulk modulus and hydraulic properties are experimentally investigated. Some complexities of the experimental set-up are first introduced and discussed (**Chap. III.1**). Then, measurements and physical understanding on samples' bulk modulus' and hydraulic properties' frequency dependence are introduced in **chapter III.2** (article in press in *Geophysics*). These measurements rely on added, secondary, measurements that are introduced and discussed in **chapter III.3**. Finally, a general conclusion and some perspectives follow (**Chap. III.4**).
- In **part IV**, the frequency dependence of both Young modulus and Poisson ratio are experimentally investigated in Fontainebleau and Berea sandstone samples. After a short introduction, detailing the particular complexities of this method (**Chap. IV.1**), two main chapters follow. They respectively report the Young modulus (**chapter IV.2**, article submitted to *Geophysics*) and Poisson ratio (**Chap. IV.3**, article submitted to *Geophysical Research Letters*) measured on Fontainebleau sandstone samples. Then, a discussion of the measurements on both properties is detailed in **chapter IV.4**, leading to a general conclusion.
- The reported frequency dependence of both elastic and hydraulic properties introduced the need for a better understanding of the measurements. This is the aim of **part V** that develops a simple model to explain the experiment. In **chapter V.2**, the general 1D model is developed by solving the typical equations of poroelasticity for the theoretically "drained" and the "experimentally undrained" boundary conditions. Some discussions and perspectives are detailed in **chapter V.3**.
- The last **part VI** summarises the main results, and gives some general perspectives.

## PARTIE II

# Effet de l'adsorption sur les propriétés élastiques des grès et carbonates

|          |  |           |
|----------|--|-----------|
| <b>1</b> | <b>Introduction &amp; Fondements physiques</b>   | <b>27</b> |
| <b>2</b> | <b>Investigation of elastic weakening in limestone and sandstone samples from moisture adsorption (<i>GJI, 2014</i>)</b> | <b>33</b> |
| 2.1      | Introduction . . . . .   | 34        |
| 2.2      | Experimental approach and samples studied . . . . .  | 35        |
| 2.3      | Experimental results . . . . .   | 39        |
| 2.4      | Interpretation of elastic weakening using Effective Medium Theories . . . . .  | 41        |
| 2.5      | Discussion . . . . .   | 49        |
| 2.6      | Conclusions . . . . .  | 54        |
| <b>3</b> | <b>Discussion &amp; Conclusion</b>   | <b>57</b> |
| 3.1      | Further discussions on the adsorption study . . . . .  | 57        |
| 3.2      | Measurements at full saturation under drained conditions . . . . .   | 60        |
| 3.3      | General conclusion . . . . .   | 64        |



## Summary

**Résumé :** Cette partie étudie une cause possible du "shear weakening" dans des roches carbonatées : l'adsorption. Une étude comparative est menée sur des échantillons de grès et de carbonate. L'effet de l'adsorption est étudié en faisant varier l'humidité de l'air autour de l'échantillon. La saturation en eau et les vitesses d'ondes P et S sont mesurées.

Alors que les propriétés élastiques des carbonates ne sont pas affectées par l'adsorption, un fort affaiblissement est observé dans les grès. Cet affaiblissement affecte de façon égale les ondes P et S. On est dans un cas d'affaiblissement élastique global. L'affaiblissement élastique n'est pas directement relié au degré de saturation (i.e. quantité adsorbée). Un paramètre majeur semble être le degré de cimentation d'un échantillon. Les mesures sont expliquées par un modèle micro-mécanique prenant en compte l'effet de l'adsorption et le degré de cimentation.

Finallement, une étude des coefficients de compressibilité à saturation totale permet les mêmes observations. Aucun affaiblissement élastique n'est mesuré dans les carbonates, et un fort affaiblissement est observé dans un grès de Berea lors d'une saturation à l'eau. La magnitude de l'affaiblissement est de l'ordre des valeurs obtenues par l'étude à l'humidité relative. Cela pourrait impliquer que l'affaiblissement élastique provient bien du phénomène d'adsorption, et que toutes les observations faites précédemment s'appliquent lors d'une saturation totale à l'eau.

**Abstract :** This part investigates a possible cause for the rock-fluid interaction to induce the so-called "shear weakening" in carbonate samples : Adsorption. A comparative study is introduced between sandstone and limestone samples. The effect of adsorption is studied from varying the air's relative humidity in a closed volume where the sample is placed. For each sample and relative humidity, the water saturation and P- and S-wave velocities are measured.

While the carbonates' elastic properties are not affected by adsorption, a large weakening is observed for the sandstone samples. This weakening is observed similarly on P- and S-wave velocities, implying that the samples' bulk elasticity is also affected by adsorption, i.e. an "elastic weakening" is observed. Saturation (i.e. amount of adsorption) and weakening do not fully correlate. A major parameter is the degree of cement of a sample. The measurements are understood in terms of a micro-mechanical model that accounts for both adsorption and degree of cement.

The same results are obtained from measuring the drained bulk moduli/compressibilities for different saturating fluids. No apparent weakening is observed in the limestone samples. Reversely, a large weakening is observed in a Berea sample that is in the range of values found from the moisture adsorption study. Elastic weakening may indeed originate from adsorption, and the above results remain at full saturation.



---

## Introduction & Fondements physiques

---

Cette partie est motivée par les travaux de Baechle et al. (2009) : Un affaiblissement des propriétés élastiques a été observé dans des carbonates lors de la saturation totale en eau. Cet effet est réversible, i.e. ce n'est pas un effet de dissolution de la roche car les propriétés reviennent à leur état initial après séchage. Cela implique que le meilleur candidat à cet affaiblissement est un phénomène d'adsorption.

L'effet d'affaiblissement par adsorption semble être un effet de faible amplitude, et doit être étudié par un système précis. L'outil de mesure choisi est donc un outil de mesure standard en physique des roches : la mesure des vitesses d'ondes au travers de l'échantillon. Pour étudier précisément ce phénomène, il est nécessaire de l'isoler d'autres causes de variations de propriétés élastiques lors d'une saturation totale à l'eau, tel que l'effet de fréquence. Or, la mesure des vitesses d'ondes dans un échantillon se fait aux fréquences ultrasoniques. L'approche utilisée ici est donc de s'éloigner des effets de dispersion dus à une saturation totale. L'étude de l'adsorption avec des très faibles saturations est donc choisie ici. Après une introduction brève sur la physique du phénomène d'adsorption, l'étude faite est introduite en chapitre 2.

### Phénomène d'adsorption

Dans le but d'une étude des effets d'interactions fluide-roche se produisant dans la surface porale, les concepts et procédés d'étude des surface sont présentés ici. Deux points importants sont introduits : (i) l'adsorption et (ii) l'énergie de surface. En particulier, il est possible de distinguer trois effets reliés à ces deux principes :

- L'adsorption sur une surface et/ou entre deux surfaces : les principes physiques à l'origine de (et reliés à) cet effet y sont introduits et détaillés.

- L'énergie de surface : la relation entre énergie de surface et adsorption y est introduite suivant différentes hypothèses/définitions physiques.
- L'effet de l'énergie de surface sur l'élasticité du matériau : le rôle de la micro-structure et de l'importance de la zone d'adsorption y est introduite.

Ces trois effets sont étudiés dans la suite dans le but de déterminer la physique sous-jacente des affaiblissements élastiques observés.

### Adsorption sur une surface : Surface spécifique & Mono-couches

**Principe :** Tout comme sa porosité, la surface spécifique d'un échantillon de roche est une information importante. Dans les théories/études des surfaces, différentes méthodes telles que le BET permettent de connaître avec précision la quantité de fluide adsorbé sur la surface interne de l'échantillon à une température donnée (e.g., Adamson, 1976). Ces isothermes d'adsorption permettent d'estimer (i) la quantité de surfaces libres d'un échantillon (i.e. Surface Spécifique); et/ou (ii) la quantité de mono-couches présentes sur ces surfaces pour une pression saturante donnée.

En fonction de la taille des inclusions étudiées, différentes molécules sont utilisées dont notamment la molécule  $H_2O$ . Ces études montrent que, tout comme sa taille, les propriétés chimiques de la molécule affectent la quantité adsorbée sur l'échantillon. Ainsi, une affinité entre fluide et échantillon est mise en lumière par ces études (e.g., Clark et al., 1980; Parks, 1984). Seule la molécule d'eau est utilisée dans la suite malgré l'intérêt représenté par l'étude d'une adsorption en différents fluides.

La variation en quantité adsorbée d'un échantillon à l'autre pour une Humidité Relative (i.e. RH pour "Relative Humidity") donnée est donc due à la surface spécifique de l'échantillon et à l'affinité de l'échantillon à l'eau. En supposant que l'interaction fluide-roche a un effet sur les propriétés intrinsèques de la roche, ces deux effets semblent donc se combiner. En effet, l'affinité est directement reliée à l'interaction eau-roche, et cet effet devrait augmenter avec la quantité de surfaces où l'adsorption a lieu.

**Théorie dite BET :** Comme introduit par Adamson (1976), l'adsorption se produit par superposition de mono-couches de molécules déposées sur une surface, d'épaisseur de l'ordre de l'Angstrom. Ces couches possèdent des particularités variables en fonction de la distance à la surface minérale. Comme vu plus tard, toutes les mono-couches déposées n'ont donc pas le même effet. Cette compréhension du phénomène d'adsorption, par mono-couches successives, correspond à la théorie BET utilisée lors de la mesure de surface spécifique. Elle peut être simplifiée en une équation de dépendance à la RH du nombre de molécules adsorbées ( $N_{ads}$ ) telle que (e.g., Wang and Santamarina, 2007) :

$$N_{ads} = \frac{c.RH}{(1 - RH) \cdot (1 + (c - 1) \cdot RH)} \quad (1.1)$$

Où  $c$  est un paramètre relié à la chaleur d'adsorption dans une mono-couche. Il est en particulier prédit que la première mono-couche apparaît pour de faibles RH (i.e.  $\sim 12\%$ ), et jusqu'à dix mono-couches sont attendues pour les RH maximales (i.e.  $\sim 90\%$ ).

**Implications :** L'adsorption d'un fluide sur un solide dépend de différentes forces microscopiques/atomistiques entre minéral et fluide conduisant à une force macroscopique dite "d'adhésion". Ces forces/effets ont un rôle prédominant aux interfaces. Les forces comprises ici (e.g., Maghsoudy-Louyeh and Tittmann, 2008) sont les forces (i) Électrostatique (i.e.  $F_{el}$ ); (ii) de Van der Waals (i.e.  $F_{vdW}$ ); et (iii) Capillaires (i.e.  $F_{cap}$ ). L'adsorption d'eau sur une surface implique donc différents phénomènes physiques :

- Les premières mono-couches d'eau sont particulièrement influencées par l'interaction atomistique avec le minéral. Les propriétés physiques telles que la diffusion ou la constante diélectrique de ce fluide en sont très modifiées, au point que cette nouvelle surface est fréquemment considérée comme un solide.
- La friction à l'interface entre deux surfaces hydrophiles chute considérablement, diminuant donc la cohésion d'un assemblage. Néanmoins, des ponts capillaires peuvent se former en parallèle, créant au contraire une force d'attraction consolidant un édifice. Une compétition entre ces deux effets entre en jeu.

Dans le cas d'étude de matériaux poreux, un niveau de complexité supplémentaire intervient. En effet, l'étude des quantités de mono-couches adsorbées et de leur effet sur une surface diffère lorsque deux surfaces sont très proches l'une de l'autre. En particulier, le volume d'eau adsorbée augmente considérablement.

## Adsorption & Énergie de surface

**Énergie de surface : Définition** Dans la théorie de Gibbs (e.g., Adamson, 1976), et des principes fondamentaux de la thermodynamique, il est possible de définir une énergie libre de surface. Cette énergie, notée  $\gamma_s$ , est définie comme le travail à fournir pour créer une nouvelle surface d'équilibre suivant un processus réversible (e.g., Adamson, 1976; Parks, 1984). Elle est introduite par Griffith (1920) dans l'étude de la création d'une fissure dans l'équation bilan d'énergie d'un système donné.

**Énergie de surface : Théorie de Gibbs** Par application directe de la théorie de Gibbs, il est possible de relier directement la variation d'énergie de surface à une variation d'activité chimique tel que :  $d\gamma_s = -\Gamma.d\mu$ .  $\Gamma$  étant le rapport entre le nombre de moles adsorbées  $N$  et la surface d'adsorption  $\xi$  tel que :  $\Gamma = N/\xi$ .

De part le potentiel chimique  $\mu$ , l'énergie de la surface  $\gamma_s$  est donc diminuée par adsorption d'une molécule ou d'un ion sur la surface par interaction physico-chimique (e.g., Parks, 1984). Il est possible de définir deux cas simples en fonction du fluide adsorbé :

- Dans le cas d'un liquide ionique, la variation d'énergie de surface se définit par les activités  $a$  des ions en solution tel que :  $d\gamma_s = -\Gamma.d\mu = -\Gamma.d(\sum_i a_i)$
- Dans le cas d'un gaz (supposé parfait), l'activité se définit comme la pression partielle  $P$  de sorte que :  $d\gamma_s = -\Gamma.d\mu = -\Gamma.RT.d(\ln P)$

En supposant que la vapeur d'eau (ou RH) est un gaz parfait, il est possible de définir la variation d'énergie de surface telle que :

$$\Delta\gamma_s = \gamma_0 - \gamma_i = RT \int_0^{RH_i} \Gamma \frac{dRH}{RH} \quad (1.2)$$

Il est enfin possible d'approximer la quantité surfacique adsorbée ( $\Gamma$ ) en fonction de la variation de masse en eau dans l'échantillon. L'équation finale prend la forme :

$$\Delta\gamma_s = \frac{RT}{\xi.M_{H_2O}} \int_0^{RH_i} \Delta m(RH) \cdot \frac{dRH}{RH} \quad (1.3)$$

Où  $M_{H_2O}$  est la masse molaire de la molécule adsorbée (l'eau ici).

**Énergie de surface : Théorie BET** Néanmoins, une application directe de cette théorie implique la prise en compte de manière non différenciée de plusieurs mono-couches, i.e. une variation linéaire de  $\gamma_s$  avec l'adsorption. Comme énoncé précédemment, ce n'est pas le cas. La théorie proposée par Parks (1984) dans le cas du quartz (Fig.1.1) implique un effet non linéaire du degré d'adsorption sur  $\gamma_s$ . En particulier, moyennant quelques hypothèses, (Murphy et al., 1984; Wang and Santamarina, 2007) ces auteurs ont introduit la notion de mono-couche et définit une variation de saturation comme reliée au nombre de couches déposées sur la surface.

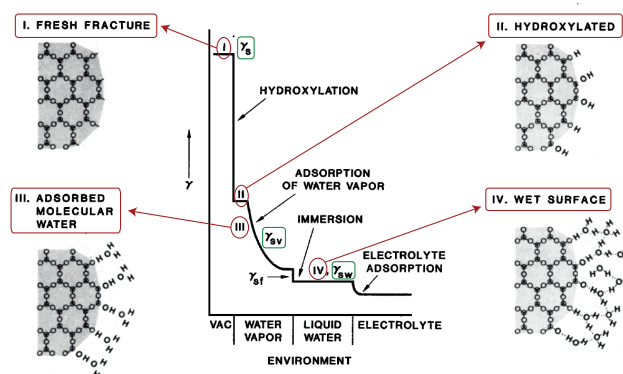


**Figure 1.1 :** Schémas de la variation d'énergie de surface  $\gamma_s$  lors de l'adsorption d'eau sur une surface fraîche de quartz. Figure modifiée de Parks (1984). Quatre domaines d'adsorption sont considérés (en rouge), chacun relié à une valeur d'énergie  $\gamma$ . Trois états de  $\gamma$  sont supposés (vert). L'énergie de surface sous vide,  $\gamma_s$  décroît avec l'adsorption de vapeur d'eau  $\gamma_{sv}$  jusqu'à une valeur minimale dans le cas d'une saturation en eau liquide  $\gamma_{sl}$ .

Comme montré en figure 1.1, les différentes mono-couches n'ont pas le même effet sur

l'énergie de surface. En particulier, les deux premières mono-couches ont un effet prédominant, alors que les couches à plus forte saturation affectent peu  $\gamma_s$ . Ainsi, une faible quantité d'eau adsorbée tend à faire varier de manière importante l'énergie de surface du matériau (Parks, 1984). Il est à noter que la limite supérieure, correspondant à une énergie de surface la plus faible, est le cas de saturation (totale) en eau. Ce dernier point souligne la logique de l'approche utilisée ici : comprendre l'effet de la RH est un préliminaire nécessaire pour comprendre l'adsorption présente dans le cas de saturations totales.



---

### Investigation of elastic weakening in limestone and sandstone samples from moisture adsorption (*GJI*, 2014)

---

L. Pimienta, J. Fortin and Y. Guéguen, Investigation of elastic weakening in limestone and sandstone samples from moisture adsorption, (2014), *Geophysical Journal International*, **199(1)**, 335-347.

---

#### Abstract

Elastic and mechanical weakening from water saturation are widely known to occur in sedimentary rocks, and particularly in carbonate rocks. To improve our understanding of the physics underlying this phenomenon, ultrasonic ( $f \sim 0.5$  MHz) elastic properties are measured on a large suite of clean limestones and sandstones at very low saturations from Relative Humidity (RH) variations at ambient conditions. Measurements clearly highlight an elastic weakening (i.e. decrease in elastic wave velocity) from moisture adsorption. P- and S-wave velocities are similarly affected by adsorption, but in a different way for limestones and sandstone samples. While the elastic properties of limestone samples show almost no RH dependence, a large weakening is observed for samples of Fontainebleau sandstone that increases with the samples' porosity. The main elastic weakening effect is likely to result from adsorption of fluid at grain contacts. It thus affects particularly granular rocks such as sandstones while well-cemented limestones are not affected. The granular model from Murphy et al. (1984), accounting for surface energy effects (Johnson et al., 1971), proves to be appropriate. Applying this model, it is shown that (i) P- and S-wave

velocities have the same dependence on surface energy, which is consistent with the measurements; (ii) Surface energy values obtained from the ultrasonic data using this model correlate with RH, and are consistent with the expected value for quartz crystals at vapour pressure. Yet, porosity, which relates to degree of cementation in the particular case of Fontainebleau sandstone, appears to be an additional parameter. A modified model is thus derived using the cementation model from Digby (1981), accounting for a bonding radius at grain contact. It proves to apply well to the measured data. The fundamental difference between limestones' and sandstones' dependence to RH appears to be related to a microstructural difference. Saturation variations from RH increase depend on specific surface area, which is particularly low in Fontainebleau sandstone and large in microporous limestones. But elastic weakening from RH is more important in sandstones owing to their granular microstructure.

---

## 2.1 Introduction

Sedimentary rocks are porous media that present, under fluid saturation, a large surface area where mineral and fluid are in contact. Depending on the pores' content and shape, rock-fluid interaction may be important enough to directly affect the rock physical properties. This effect has often been evasively referred to as "shear weakening" or "Rebinder effect". While this effect has been observed for sandstones' mechanical strength (e.g., Kirby, 1984; Baud et al., 2000; Klein et al., 2001; Fortin et al., 2007), a few measurements of elastic properties (e.g., Winkler and Murphy III, 1995) also reported it. In recent years, more emphasis was given to the micro-structurally complex carbonates (e.g., Verwer et al., 2008). These rocks have been shown to be very sensitive to the saturating fluid, and elastic properties, such as the shear modulus, appear to decrease upon water saturation (e.g., Assefa et al., 2003; Baechle et al., 2005; Adam et al., 2006; Verwer et al., 2008; Fabricius et al., 2010). Such behaviour is not consistent with established theories that consider the shear modulus as unaffected by fluid (Gassmann, 1951). This elastic weakening phenomenon is reversible and disappears under drying (Baechle et al., 2005), and thus seems related to adsorption. This weakening from adsorption appears to be more important in limestone than in sandstone samples (e.g., Baechle et al., 2005).

In order to understand the elastic weakening linked to adsorption, low saturations (i.e. corresponding to adsorbed volumes) are investigated. Low saturation is attained through varying the partial pressure of the atmosphere surrounding the sample (e.g., Tittmann et al., 1980; Clark et al., 1980). Effects of moisture and adsorption were in particular experimentally investigated to understand the fundamental difference between attenuations of lunar and terrestrial rocks (e.g., Tittmann and Housley, 1973; Tittmann, 1977, 1978), **and** to study the induced elastic weakening (e.g., Clark et al., 1980) and attenuation (e.g., Pandit

and King, 1979; Clark et al., 1980; Murphy III, 1982; Murphy, 1984) at seismic frequencies. Theories have been proposed to explain these observations (e.g., Johnson et al., 1971; Murphy et al., 1984; Tutuncu and Sharma, 1992; Chelidze et al., 1996). In particular, based on the analysis of Johnson et al. (1971), Murphy et al. (1984) and Tutuncu and Sharma (1992) developed models to predict elasticity and/or attenuation variations as a function of moisture adsorption. Yet, velocities (Clark et al., 1980) and attenuations (e.g., Tittmann et al., 1980) were measured at seismic ( $f \sim 1$  kHz) frequencies only and very few clean sandstone and limestone samples were studied.

In the present study, sensitivity of sandstones' and carbonates' elastic properties to adsorption are compared at room T-P. Water saturations and ultrasonic ( $f \sim 0.5$  MHz) wave velocities are measured under controlled Relative Humidity (RH). To understand the underlying physics, the micro-mechanical model of Murphy et al. (1984) is introduced that links effective elasticity to surface energy (Johnson et al., 1971). Finally, cementation is accounted for using the model of Digby (1981) to understand the less porous sandstones.

## 2.2 Experimental approach and samples studied

### 2.2.1 Samples studied

The present study investigates the role of adsorption on elastic properties of clean (i.e. calcite- and quartz-pure respectively) limestones and sandstones of varying porosity. A suite of 11 limestone and 9 sandstone samples, covering a wide range in porosity for both sedimentary rocks, were selected. The samples' main petrophysical features are presented in Table (2.1), that reports measured porosities ( $\phi$ ), along with permeabilities ( $\kappa$ ) and pore entry diameters ( $d$ ) found in the literature. The total pore volume  $V_{pore}$  (leading to  $\phi$ ) is obtained from the dry density of the rock samples and the quartz/calcite crystal densities. As the samples are clean (i.e. quartz- or calcite-pure) rocks, this approach is preferred over any other porosity measuring method.

#### 2.2.1.1 Fontainebleau Sandstone samples

Fontainebleau sandstone is a well-known reference rock. Many experimental investigations have been carried out on this rock (e.g., Song and Renner, 2008; Gomez et al., 2010; Duda and Renner, 2013). It exhibits homogeneous and isotropic properties at the sample scale (e.g., Sulem and Ouffroukh, 2006). Both framework grains and cement are pure quartz, making up a clean sandstone of about 99.9% qtz (e.g., Bourbie and Zinszner, 1985). This aeolian rock is well sorted, with a relatively constant grain radius ( $r$ ) of about  $r \sim 100 \mu\text{m}$ .

Depending on the amount of quartz cementing, its porosity ranges from about  $\phi \sim 2\%$  for highly cemented samples to about  $\phi \sim 25\%$  for less cemented samples (Bourbie and Zinszner, 1985). The variable amount of quartz cement originates from a variation in the

**Table 2.1 :** Properties of the tested samples. Porosities ( $\phi$ ) as measured in this work. Approximate permeability ( $\kappa$ ) and pore entry diameter ( $d$ ) are reported from previous studies on the different samples.

| Samples                 | Classification | $\phi$ (%) | $\kappa$ (m <sup>2</sup> ) | $d$ ( $\mu$ m)   | References                  |
|-------------------------|----------------|------------|----------------------------|------------------|-----------------------------|
| Massangis               | Oolite         | 6.1        | $1.10^{-16}$               | 0.1-0.8 and 100  | Casteleyn et al. (2010)     |
| Indiana                 | Oolite         | 12.4       | $2.10^{-15}$               | 0.04-1 and 100   | Vajdova et al. (2004, 2010) |
| Euville                 | Oolite         | 15.9       | $4.10^{-15}$               | 0.1 and 1-80     | Eslami et al. (2010)        |
| Chauvigny oolite        | Oolite         | 16.3       | –                          | 0.1-2 and 10-50  | Vincent et al. (2011)       |
| Tavel                   | Micrite        | 17.2       | $1.10^{-17}$               | 0.02-0.3 and 100 | Vajdova et al. (2004)       |
| Anstrude                | Oolite         | 19.5       | $4.10^{-16}$               | 0.3 and 100      | Casteleyn et al. (2010)     |
| Raviere                 | Oolite         | 19.7       | $2.10^{-16}$               | 0.4 and 100      | Casteleyn et al. (2010)     |
| Lavoux                  | Oolite         | 22.4       | $1.10^{-14}$               | 0.84 and 20      | Le Guen et al. (2007)       |
| Fontvieille             | Micrite        | 23.6       | –                          | –                | –                           |
| Estailades              | Micrite        | 28.4       | $2.10^{-13}$               | 0.39 and 19      | Le Guen et al. (2007)       |
| Chauvigny micrite       | Micrite        | 34.4       | –                          | 0.2-3 and 200    | This work                   |
| Fontainebleau (FoSp2a)  | Granular       | 2.6        | $1.10^{-17}$               | 1-10             | Bourbie and Zinszner (1985) |
| Fontainebleau (FoSp2b)  | Granular       | 2.2        | $1.10^{-17}$               | 1-10             | Bourbie and Zinszner (1985) |
| Fontainebleau (FoSp4)   | Granular       | 4.7        | $1.10^{-15}$               | 1-10             | Bourbie and Zinszner (1985) |
| Fontainebleau (FoSp7)   | Granular       | 7.2        | $1.10^{-14}$               | 1-10             | Bourbie and Zinszner (1985) |
| Fontainebleau (FoSp9)   | Granular       | 9.0        | $1.10^{-13}$               | 10               | Bourbie and Zinszner (1985) |
| Fontainebleau (FoSp16a) | Granular       | 16.0       | $1.10^{-12}$               | 10-20            | Bourbie and Zinszner (1985) |
| Fontainebleau (FoSp16b) | Granular       | 16.7       | $1.10^{-12}$               | 10-20            | Bourbie and Zinszner (1985) |
| Fontainebleau (FoSp18a) | Granular       | 18.2       | $5.10^{-12}$               | 10-20            | Bourbie and Zinszner (1985) |
| Fontainebleau (FoSp18b) | Granular       | 18.9       | $5.10^{-12}$               | 10-20            | Bourbie and Zinszner (1985) |

silica super-saturated water-table (e.g., Sulem and Ouffroukh, 2006). As a consequence, pore-entry diameters ( $d$ ) decrease with porosity (e.g., Song and Renner, 2008) from  $d \sim 20 \mu\text{m}$  to about  $d \sim 5 \mu\text{m}$ , leading to variations in permeability of about 4 to 5 orders of magnitude (Bourbie and Zinszner, 1985). In this study, Fontainebleau samples with a porosity ranging from about  $\phi \sim 2\%$  up to about  $\phi \sim 20\%$  are investigated.

### 2.2.1.2 Limestones

Apart from Indiana limestone, the limestone samples chosen come from french quarries (e.g., Vincent et al., 2011). They vary in porosity, morphology (e.g. grains and pores size) and sedimentary history (e.g. micritic versus oolitic limestones). All samples are considered as clean limestones, and all of them exhibit a double porosity.

Tavel limestone is a relatively homogeneous micritic limestone (Vajdova et al., 2004) made up of a micro-crystalline matrix relatively well cemented with an average grain diameter of  $\sim 5 \mu\text{m}$ . Its porosity is  $\phi \sim 17\%$ . It is characterized by a bimodal pore-size distribution of few macro-pores (i.e.  $d \sim 100 \mu\text{m}$ ), and mainly sub-micron (i.e.  $d \sim 0.1 \mu\text{m}$ ) pores (Vajdova et al., 2010). Indiana limestone is an oolitic limestone with fossils of about  $\sim 300 \mu\text{m}$  diameter cemented by fine-grained calcite (Vajdova et al., 2004). Estailade and Fontvieille limestones originate from Gard quarries from south-est France. Both are calcite-

pure bioclastic micritic rocks of large porosities (i.e.  $\phi \sim 28.4\%$  and  $\phi \sim 23.6\%$  respectively). Estailade limestone exhibits a bimodal pore size distribution made up of intergranular macro-pores of about  $d \sim 19 \mu\text{m}$  and intra-granular micro-pores of  $d \sim 0.39 \mu\text{m}$  (Youssef et al., 2008).

The other limestones are from the Oolite Blanche carbonate formation of Paris Basin. Euville limestone is an oolitic limestone with a bimodal porosity ( $\phi \sim 22\%$ ) mainly composed of inter- ( $d < 80 \mu\text{m}$ ) and intra- ( $d < 1.5 \mu\text{m}$ ) oolite pores (Eslami et al., 2010). Lavoux and Chauvigny limestones originate from the Dogger formation. Lavoux is an oolitic limestone (Le Guen et al., 2007; Vincent et al., 2011) as for one of the Chauvigny samples (Fortin et al., 2009; Vincent et al., 2011). The other Chauvigny sample is a fine-grained loosely cemented micritic rock. Lavoux sample has a porosity of about  $\phi \sim 22\%$ , and the oolitic and micritic Chauvigny samples have porosities are of about  $\phi \sim 16\%$  and  $\phi \sim 34\%$  respectively. All three samples show micro-porosity in the range of  $d \sim 0.1 - 1 \mu\text{m}$ , and a macro-porosity of about  $d \sim 10 - 100 \mu\text{m}$  (Youssef et al., 2008). Anstrude, Raviere and Massangis limestones are characterised as oolitic limestones, and have a double porosity with very similar pore entry diameters of about  $d \sim 0.1 - 0.6 \mu\text{m}$  for the micro-porosity (Casteleyn et al., 2010). While Anstrude and Raviere samples have similar total porosity of about  $\phi \sim 19\%$ , Massangis limestone has a lower porosity ( $\phi \sim 6\%$ ) that probably originates from differing degrees of cementing during burial.

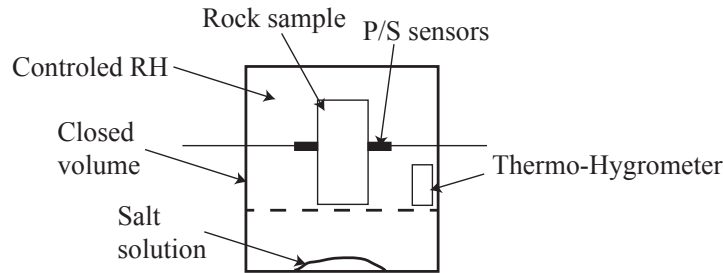
The 20 samples in Table (2.1) are ranked from low porosity to high porosity values. The values of permeability and pore-entry diameter correlate to porosity for the Fontainebleau sandstone samples only.

## 2.2.2 Experimental set-up

In order to measure small quantities of water saturation ( $S_w < 2\%$ ), we impose varying Relative Humidity (RH) in the atmosphere surrounding the rock sample. The present experiment aims at investigating (i) the amount of water adsorbed; and (ii) the effects of adsorption on elastic properties. An experimental protocol is thus devised to study the evolution of rocks' elastic properties with adsorption.

### 2.2.2.1 Relative Humidity control

The atmosphere's RH is defined as the ratio between the water pressure  $P_{H_2O}$  and the pressure of saturating vapour  $P^*$ . Saturating vapour pressure depends on different factors such as temperature, which is continuously monitored during experiment and is about  $T = 20 \pm 2 \text{ }^\circ\text{C}$ . For a given RH, equilibrium between vapour and liquid water leads to adsorption of small amounts of water on the rock pores surfaces. Adsorption equilibrium on a mineral surface from RH is usually reached within a few minutes. Weight measurements showed that final saturation of the rock (i.e. mineral aggregate) is reached in less than one hour



|                        | Salt 1    | Salt 2      | Salt 3     | Atmosphere | Salt 4    | Salt 5    |
|------------------------|-----------|-------------|------------|------------|-----------|-----------|
| Salt name              | Anhydrous | $KCH_3CO_2$ | $K_2CO_3$  |            | NaCl      | $K_2SO_4$ |
| Relative Humidity (RH) | 5 +/- 2 % | 23 +/- 3 %  | 43 +/- 3 % | 60 +/- 5 % | 75 +/- 3% | 95 +/- 3% |

**Figure 2.1 :** Schematic view of the experimental set-up. The prepared sample is placed in the closed volume along with a salt solution that will affect RH. Elastic wave velocities are measured directly on the sample at ambient conditions after RH stabilisation. Five different salts are used to change RH, each corresponding to a different RH value. For a given temperature, each salt (or salt solution) is chosen as leading to a calibrated RH (e.g., Greenspan, 1977).

after RH stabilisation.

The prepared sample is introduced in the hermetically closed glass chamber using a system allowing for direct measurement of elastic wave velocities under controlled atmosphere (Fig. 2.1). In the present study, RH is controlled by the presence of different salts in a closed chamber (e.g., Greenspan, 1977). For a given temperature, each salt (or salt solution) is chosen as leading to a calibrated RH (Fig. 2.1). To measure precisely the RH, a Thermo-Hygrometer "Testo 610", accurate to the 1st decimal, is introduced in the volume. It also allows for a constrained tracking of the RH equilibrium and stabilisation, with an accuracy of  $\sim 0.1\%$ .

In the present study, the sought properties were measured after two hours of RH stabilisation, and after 4 hours in the extreme case of maximum RH (i.e.  $\sim 95\%$ ). RH and elastic wave velocities are measured simultaneously directly in the chamber, and mass is measured directly when opening the chamber.

### 2.2.2.2 P- and S-waves velocities

Cylindrical rock samples of 80 mm length and 40 mm diameter are used in the study. Before experiments, samples are dried in an oven filled with anhydrous salts at  $T \sim 70^\circ C$ , and then weighted to obtain the total pore volume  $V_{pore}$ . Two couples of P- and S- wave piezoelectric transducers of  $f \sim 0.5$  MHz central frequency are directly glued on the sample (Fig. 2.1). P- and S- sensors are opposed as to measure ultrasonic wave propagation across the samples' diameter. In this set-up, the transducers are glued to the samples "once and for all", i.e. they remain on the samples throughout the RH variations, giving constant travel

paths and contact conditions. The sensors' weight is considered to be independent of the RH so that the sample's water saturation can be traced from the weight difference. The piezoelectric sensors are directly related to a standard generator sending a square pulse of  $f \sim 0.5$  MHz central frequency, and a analogical oscilloscope linked to the *Insite ASC Ltd* data acquisition software (e.g., Ougier-Simonin et al., 2011).

Absolute P- and S-wave velocities under dry conditions (i.e. lowest RH of about  $\sim 5\%$ ) are hand-picked. The evolution of the elastic velocities with RH is then obtained by a cross-correlation with this reference state at lowest RH. Measurements of absolute elastic wave velocities may have a low accuracy, owing to (i) the uncertainty in wave arrival ; and (ii) the sensors' position and the sensors-to-sample contact quality that vary from one sample to the other. As a consequence, uncertainty on P- and S-wave velocities' absolute measurement may be as high as about  $\sim 2\%$  and  $\sim 5\%$  respectively. However, P- and S-wave velocities' relative measurements, obtained from waveforms' cross-correlation, allow to discard these sources of uncertainty, leading to an accuracy of about  $\sim 0.1\%$ .

### 2.2.2.3 Water saturation

Mass variation is measured with an accuracy of  $\Delta m \sim 0.01$  mg. Water saturation  $S_w$  is then deduced from pore volume (i.e.  $V_{pore}$ ) and  $\Delta m$  using the relation :

$$S_w = \frac{\Delta m}{\rho_{wat} \cdot V_{pore}}, \quad (2.1)$$

with  $\rho_{wat}$  the water density. The measurement proves to be accurate to about  $\sim 2\%$  for most samples. Only in the case of Fontainebleau sandstones with the lowest porosity, the error in  $S_w$  goes up to about  $\sim 5\%$ .

## 2.3 Experimental results

The first aim is to study the differences between limestones and sandstones. Thus different symbols are used for both rock types in the various figures.

### 2.3.1 Elastic properties ( $V_p$ - $V_s$ ) at low RH

The samples' absolute P- and S-wave velocities measured under dry condition are reported (Fig. 2.2) as a function of their porosity. Overall, P-waves (Fig. 2.2A) and S-waves (Fig. 2.2B) show similar trends. Velocities decrease with increasing porosity. Yet, these trends appear to differ between rock types (i.e. Limestones versus Fontainebleau sandstone samples). While Fontainebleau samples exhibit large velocity variations with porosity, limestones samples show smaller variations.

Clear differences between oolite and micrite limestones dry elastic properties are not

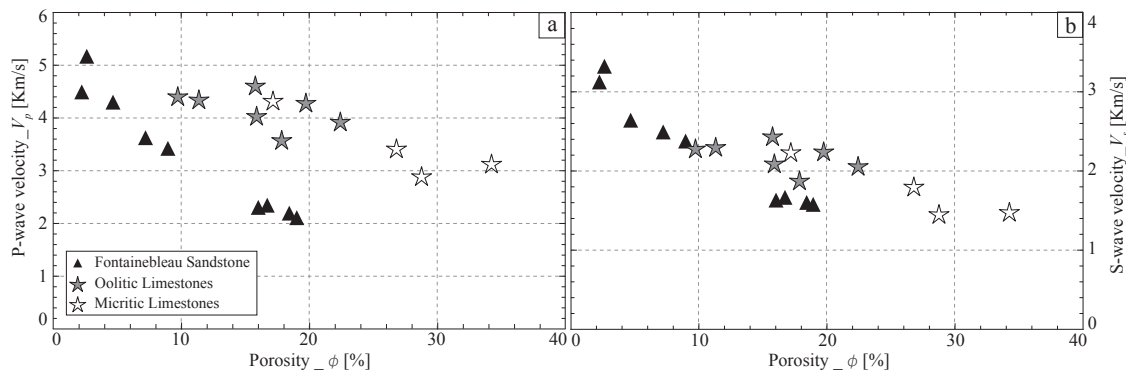


**Figure 2.2 :** Measured dry P- & S-wave velocities at ambient conditions on the Limestones (stars) and Fontainebleau sandstone (triangles) samples. Limestones samples are grouped into oolitic (grey stars) and micritic (white stars).

found. As a consequence, elastic properties of these two limestones families are undifferentiated in the following, and we focus only on the difference between limestones and sandstone samples.

### 2.3.2 Evolution of properties with RH

To fully investigate the effect of adsorption on elasticity, two main properties are measured : (i) Water saturation ; and (ii) Normalised P- and S-wave velocities.

#### 2.3.2.1 Water saturation

The evolution of the sample saturation is measured (Fig. 2.3) as a consequence of an increase in RH. Two important differences appear between rocks type. While limestones exhibit large variations in water saturation with RH, only very small increases are observed for the Fontainebleau samples. Limestones exhibit a large scattering from sample to sample, with values ranging from  $S_w \sim 0.5\%$  up to  $S_w \sim 2.5\%$  at maximum RH. On the reverse, Fontainebleau samples show a small scattering and a water saturation  $S_w$  remaining lower than  $\sim 0.5\%$  at highest RH. Saturation from adsorption thus proves to be larger in limestones than in Fontainebleau samples.

Again no clear difference is observed between oolites and micrites. Also, as the selected Fontainebleau samples have porosities ranging from  $\phi \sim 2\%$  to  $\phi \sim 19\%$ , it is clear that  $S_w$  depends very weakly on porosity in that case.

#### 2.3.2.2 Normalised elastic wave velocities

An example of RH effect on P- and S-waveforms is introduced (Fig. 2.4) for the oolitic Chauvigny limestone and a Fontainebleau sandstone (FoSp16a). These samples have been selected for comparison because of their very similar porosity ( $\phi \sim 16\%$ ). A clear difference between limestone and sandstone samples is observed for both P-(Figs. 2.4A & 2.4B) and

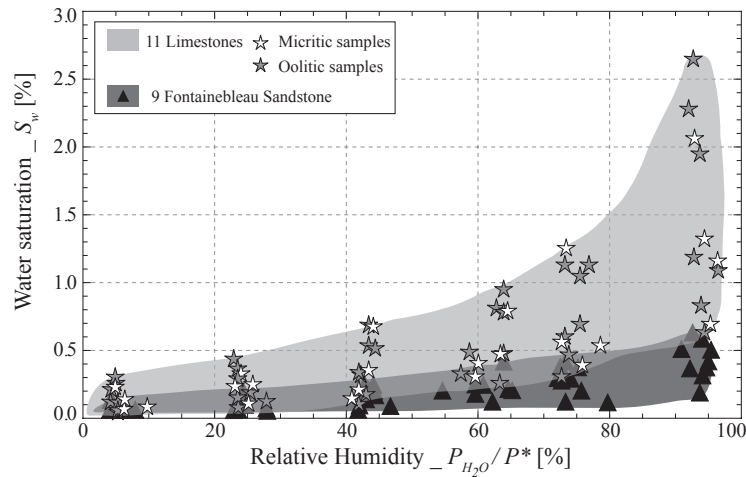


**Figure 2.3** : Measured water saturation variations with Relative Humidity on 11 limestones samples (grey surface and stars) and on 9 Fontainebleau sandstones (triangles).

S-(Figs. 2.4C & 2.4D) waveforms. While waveforms measured on ChLo show no change with RH, large decrease in both arrival times and amplitudes is observed for FoSp16 with increasing RH. P- and S-wave velocities are directly inferred from the arrival times.

Variations of normalized P- and S-wave velocities for all samples are finally reported (Fig. 2.5) as a function of RH. While limestones velocities vary very slightly with RH (up to about  $\sim 0.5\%$  at maximum RH), some sandstone samples exhibit a large decrease (up to about  $\sim 25\%$  at maximum RH) with increasing RH.

Given that the variations for limestones are very small (i.e.  $\leq 0.5\%$ ), it is difficult to evidence any porosity or facies dependence. On the reverse, Fontainebleau sandstone samples show large variations as a function of RH. This dependence to RH correlates well to their porosities. Note that P-wave (i.e. Fig. 2.5A) and S-wave (i.e. Fig. 2.5B) have very similar dependencies on RH, and show the same order of magnitude of decrease at maximum RH.

An anti-correlation appears between saturation (Fig. 2.3) and elastic properties (Fig. 2.5) variations with RH. The limestones exhibit large saturation variations but almost no change in P- and S-waves with RH. On the reverse, the Fontainebleau samples exhibit lower saturation changes but show large P- and S-waves velocity variations.

## 2.4 Interpretation of elastic weakening using Effective Medium Theories

As shown in section 3, elastic velocities in Fontainebleau samples (Fig. 2.5) appear to depend on the moisture content, while such relation is not observed for limestones. Furthermore, weakening in this quartz-pure sandstone increases with porosity. These measurements thus confirm that weakening from moisture does not originate from the presence

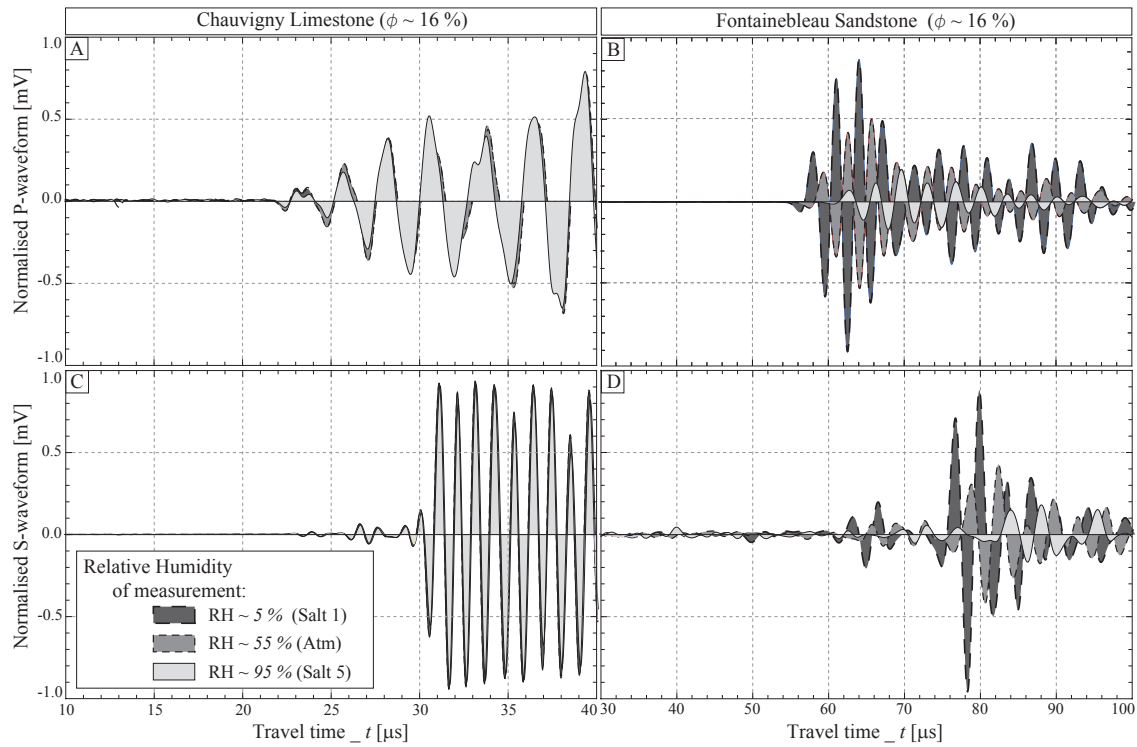


**Figure 2.4 :** Normalized P- & S-waveforms measured at **ambient conditions** on a Chauvigny limestone sample (A & C) and a Fontainebleau sandstone sample (B & D) for three different Relative Humidities.

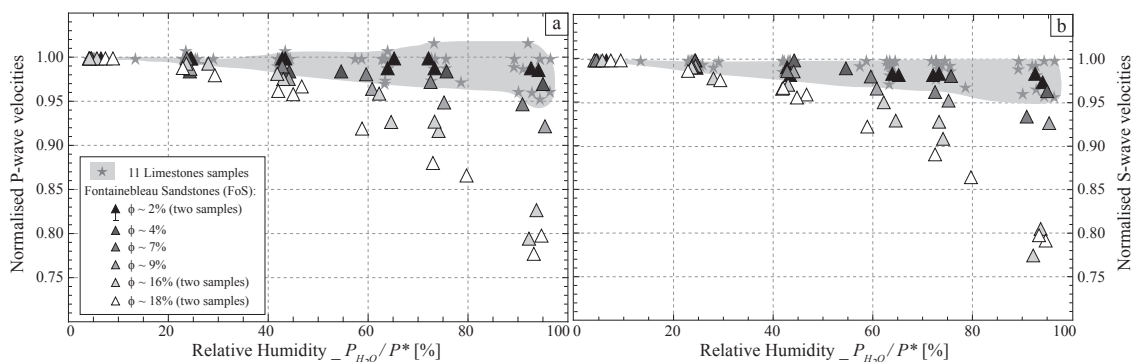


**Figure 2.5 :** Normalized P- & S-wave velocity variations with Relative Humidity measured at ambient conditions on 11 limestones samples (grey surface and stars) and on 9 Fontainebleau sandstone samples (triangles) of increasing porosities (filling in grey levels from black to white).

of clay minerals (Clark et al., 1980), but from the rock micro-structure (Murphy et al., 1984).

Effective medium models are relevant to analyse the reported results. Depending on the rock microstructure, two distinct approaches can be used. The first one consists in describing the pores as inclusions in a matrix. This approach holds particularly well in the case of rocks bearing isolated pores, or in the case of connected pores in a rock with strong grain boundaries. The second approach is more appropriate for a granular medium where stiffnesses at grain contact are the key element (e.g., Digby, 1981). Following Murphy et al. (1984), this second approach is used below to investigate the measurements on the sandstone samples.

In particular, Murphy et al. (1984) developed an effective medium model that allows for adsorption at grain contacts. Adsorption modifies the frame moduli of a granular rock. This is consistent with the observations that RH effect appears mainly in the more porous and probably less cemented Fontainebleau sandstone samples.

### 2.4.1 Model from Murphy et al. (1984) applied to velocity data

The modelling approach from Murphy et al. (1984) relies on (i) the assumption that the rock frame moduli depend on the stiffness at the grain contact (e.g., Digby, 1981), which in turn is a function of the surface energy at the contact between grains (Johnson et al., 1971); and (ii) a thermodynamic approach that relates surface energy to RH.

#### 2.4.1.1 Model derivation

From energy considerations, Johnson et al. (1971) redefined the micro-mechanical model of Mindlin (1949). They showed that the contact radius  $a_1$  at the interface also depends on surface forces (Fig. 2.6A), and thus slightly deviates from Hertz's contact radius  $a_0$ . These surface forces are introduced through the surface energy  $\gamma$  at the interface such that :

$$a_1^3 = \frac{3(1-\nu_m)r}{8G_m} \left( F + 6\gamma\pi r + \sqrt{12\gamma\pi r F + (6\gamma\pi r)^2} \right), \quad (2.2)$$

where  $F$  is the external load applied on the grains of radius  $r$ ,  $G_m$  and  $\nu_m$  are the shear modulus and Poisson ratio of the grain, and  $\gamma = \gamma_0 - \Delta\gamma$  is the surface energy at a given state of adsorption (or RH) as a function of the dry surface energy of the crystal  $\gamma_0$ . In the case of zero surface energy (i.e.  $\gamma = 0$ ), one obtains the usual Hertz expression for contact radius  $a_1 = a_0$ . The  $\gamma$ -dependence predicted by equation (2.2) becomes negligible if  $F \gg 6\pi\gamma r$ . Since  $F \sim Pr^2$ , where  $P$  is the applied pressure, the effect is in theory observed only if  $P \ll P_c = \frac{6\pi\gamma}{r}$ , i.e.  $P_c \sim 10$  MPa.

From this new contact radius  $a_1$ , Johnson et al. (1971) showed that the normal (i.e.  $D_n$ ) and tangential (i.e.  $D_t$ ) stiffnesses from basic contact theory (Mindlin, 1949) were affected

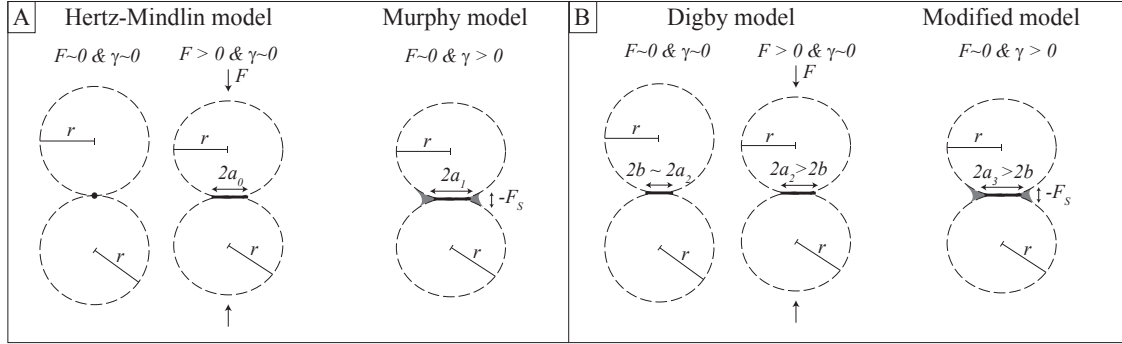


**Figure 2.6 :** Schematic views of grain contact theories for (A) uncemented (i.e. no bonding radius  $b$ ) and (B) cemented (i.e. existing bonding radius  $b$ ) cases. The uncemented Hertz-Mindlin theory (A) is complemented by models from Johnson et al. (1971) and Murphy et al. (1984) for existing surface forces. The cemented theory from Digby (1981) is complemented by the present approach in case of surface forces.

by the surface energy  $\gamma$  at grain contact :

$$\begin{cases} D_n = \frac{2G_m a_1}{1-\nu_m}, \\ D_t = \frac{4G_m a_1}{2-\nu_m}, \end{cases} \quad (2.3)$$

where  $G_m$  and  $\nu_m$  are the shear modulus and Poisson ratio of the mineral grain.

Finally, by combining equations (2.2) and (2.3) (i.e. JKR model) with an homogenisation approach (e.g., Wang and Nur, 1992), Murphy et al. (1984) showed that the effective compressional (i.e.  $M_1$ ) and shear (i.e.  $G_1$ ) moduli of an aggregate (e.g. sandstones) were dependent on surface energy  $\gamma$  :

$$\begin{cases} M_1 = \rho.V_p^2 = \frac{3(1-\phi)\psi}{20.\pi r} (D_n + \frac{2}{3}D_t), \\ G_1 = \rho.V_s^2 = \frac{(1-\phi)\psi}{20.\pi r} (D_n + \frac{3}{2}D_t), \end{cases} \quad (2.4)$$

where  $\psi$  is the average number of contacts per grains (i.e. coordinance), and  $\phi$  is the the sample porosity.

Normalizing  $M_1$  (or  $G_1$ ) to the dry reference state  $M_1(\gamma_0) = M_{1_0}$  (or  $G_1(\gamma_0) = G_{1_0}$ ), one discards parameters such as coordinance number  $\psi$  and the sample porosity  $\phi$ . It is interesting to note that (i) normalisation of either  $M$  or  $G$  leads to the same result ; (ii) the remaining expression corresponds to the ratio of intermediate  $a_1$  over reference  $a_{1_0}$  contact radii ; and (iii) the parameters at hand are constant in all Fontainebleau sandstone samples :

$$\frac{M_1}{M_{1_0}} = \frac{G_1}{G_{1_0}} = \frac{a_1}{a_{1_0}} = f(F, G_m, \nu_m, r, \gamma_0, \gamma). \quad (2.5)$$

The normalised P- and S-wave velocities (i.e.  $RV_p$  and  $RV_s$ ) are directly obtained from the normalised compressional (i.e.  $M_1$ ) and shear (i.e.  $G_1$ ) moduli respectively.

This final result is consistent with the present measurements of normalised  $V_p$  and  $V_s$

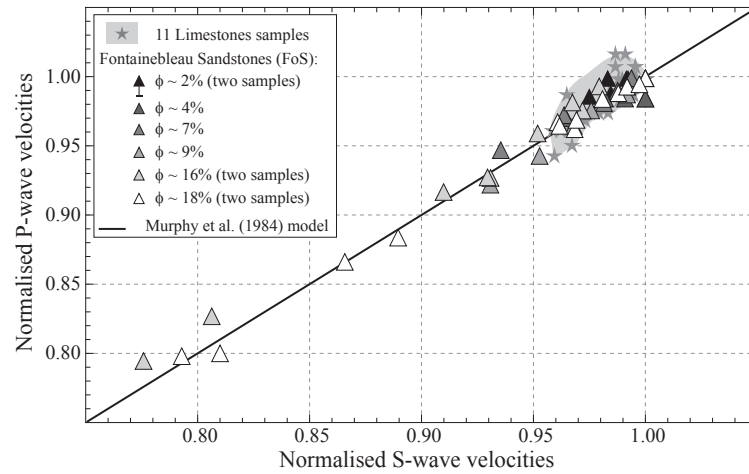


**Figure 2.7** : Relative variation of P-wave velocities as compared to S-waves for varying Relative Humidities and values of surface energy. Measurements (symbols) are compared to the model prediction (black line) from Murphy et al. (1984).

variations with RH that show the exact same trends (Fig. 2.5). Interestingly, compressional and shear modulus appear affected similarly by adsorption. By comparing (Fig. 2.7) the variations of  $RV_p$  relative to  $RV_s$  and equation (2.5), the measurements clearly fall on the linear trend predicted using the model of Murphy et al. (1984).

#### 2.4.1.2 Estimation of the surface energy

In the following, we focus on the data obtained on Fontainebleau samples as they show a large weakening with RH, and, according to equation (2.5), the results should not depend on porosity. Furthermore, all Fontainebleau samples are quartz-pure (i.e.  $G_{quartz} \sim 45$  GPa,  $\nu_{quartz} \sim 0.06$ , and  $\gamma_0 \sim 0.45$  J/m<sup>2</sup>) and have a constant grain radius (of about  $r \sim 100$   $\mu$ m), whichever the porosity.

The model of Murphy et al. (1984) assumes that, for a given rock under fixed room T-P conditions (i.e.  $F \sim 0$ ), elastic weakening solely originates from surface energy  $\gamma$  variations. All the other parameters are constant for the Fontainebleau samples studied. Following this assumption,  $\gamma$  is inverted using a standard Least-Square (i.e.  $LS(\gamma)$ ) minimization between modelled  $EWV_{mod}$  and measured  $EWV_{mes}$  Elastic Wave Velocity such that :

$$LS(\gamma) = (EWV_{mod}(F, G_m, \nu_m, r, \gamma_0, \gamma) - EWV_{mes})^2, \quad (2.6)$$

where  $EWV$  stands for either P- or S-wave velocity, and  $EWV_{mod}$  is obtained from equations (2.2), (2.3), (2.4) and (2.5). Owing to this formulation, the inverted  $\gamma$  values remain lower than the quartz vacuum surface energy  $\gamma_0$ . The surface energy  $\gamma$  considered here corresponds to an homogenisation for all load-bearing grain contacts' surface energy  $\gamma_i$ . The calculated  $\gamma$  can be seen as an average effective surface energy.

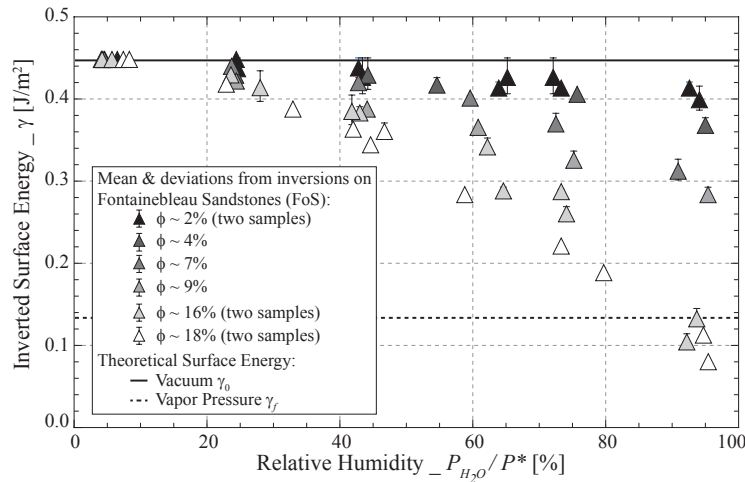


**Figure 2.8 :** Inverted surface energy using LS minimization between measurements and the model of Murphy et al. (1984). Symbols and error bar are respectively mean and standard deviation obtained from surface energies inverted separately from P- and S-wave measurements and models. Surface energies measured by Parks (1984) on a quartz surface under dry and vapour saturating pressure ( $P^*$ ) conditions.

As shown by equation (2.6),  $\gamma$  values are extracted from either P- or S-wave velocity. The dependence to RH of the inverted  $\gamma$  values (Fig. 2.8) can thus be directly inferred from the normalised P- and S-wave velocities (Fig. 2.5). The initial vacuum (i.e.  $\gamma_0$ ) and vapour saturating pressure (i.e.  $\gamma_f$ ) surface energies from the literature (e.g., Murphy et al., 1984) are reported for comparison.

The small error-bars in figure (2.8) emphasize the good fit between P- and S-wave data for all samples, which is consistent with equation (2.5). Comparing the inverted  $\gamma$  to the prediction related to Gibb's theory (Adamson, 1976; Parks, 1984; Murphy et al., 1984; Chelidze et al., 1996), the overall variation appears to be respected and  $\gamma$  decreases with adsorption. Finally, the most important result here is that  $\gamma$  for higher porosity Fontainebleau samples (i.e. FoSp16 & FoSp18) decreases down to about  $\gamma_f \sim 0.12 \text{ J/m}^2$ . This value corresponds to the measured surface energy at vapour pressure (i.e.  $\gamma_f \sim 0.13 \text{ J/m}^2$ ) on a quartz crystal (e.g., Murphy et al., 1984). This implies that the model of Murphy et al. (1984) describes particularly well the phenomenon for the high porosity (i.e.  $\phi \geq 16\%$ ) sandstone samples studied. Yet, for the low porosity samples, changes in  $\gamma$  are smaller. This lower dependence of  $\gamma$  points to the fact that the model is less appropriate for these samples.

### 2.4.2 Low-porosity sandstone samples : Modified model

The above observations suggest that the nature of grain contacts, and their degree of bonding play a role. This is precisely what the model of Digby (1981) takes into account through an additional parameter, namely the bonding radius  $b$ .

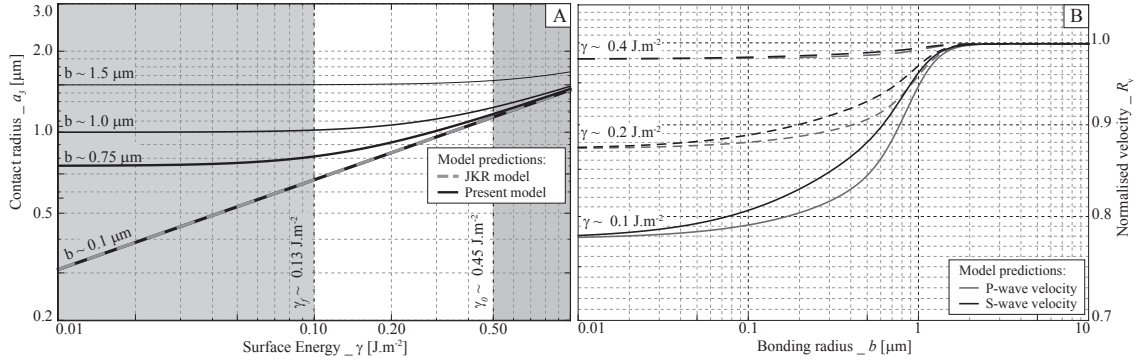


**Figure 2.9 :** Predictions using the modified model : (A) Contact radius  $a_3$  as a function of surface energy  $\gamma$  for different values of bonding radius  $b$  (i.e. black lines); (B) Normalised P-wave (i.e. black curve) and S-wave (i.e. grey curve) velocities as a function of the bounding radius  $b$  for different values of surface energy  $\gamma$ .

#### 2.4.2.1 Model derivation : Bonding at a grain contact

As shown in figure (2.6B), Digby (1981) considered in a mechanistic approach that neighbouring grains are bonded across a circular region of radius  $b$ . The applied external force  $F$  thus not only depends on  $a_0$  and  $r$  as in Hertz's theory, but also on  $b$  such that (Digby, 1981) :

$$F = \frac{4G_m}{3(1-\nu_m)} \frac{\sqrt{a_2^2 - b^2}}{r} (2a_2^2 + b^2). \quad (2.7)$$

Note that (i) for  $b = 0$  one finds back Hertz-Mindlin's relation between  $F$  and  $a_2 = a_0$ ; (ii) in case of no applied force (i.e.  $F = 0$ ),  $a_2 = b$ ; and (iii) under pressure, the contact radius  $a_0$  increases such that  $a_2 \geq b$ .

Let us now modify the purely mechanistic approach of Digby (1981) to introduce the effect of surface forces (Fig. 2.6B). Following the approach (Eq. 2.2) of Johnson et al. (1971), the total forces  $F_{tot}$  at the grain contact may be written in a first approximation as :

$$F_{tot} = F + F_{surf} = \left( F + 6\gamma\pi r + \sqrt{12\gamma\pi r F + (6\gamma\pi r)^2} \right). \quad (2.8)$$

Introducing surface forces and thus replacing  $F$  by  $F_{tot}$  in equation (2.7), one obtains :

$$\sqrt{a_3^2 - b^2} (2a_3^2 + b^2) = \frac{3(1-\nu_m)r}{4G_m} \left( F + 6\gamma\pi r + \sqrt{12\gamma\pi r F + (6\gamma\pi r)^2} \right), \quad (2.9)$$

Note that (i) for  $F = 0$ , one does not find  $a_3 = b$  any more, and the relation  $a_3 \geq b$  remains true for any external load; (ii) the limiting case of  $a_3 = b$  is observed only if none of the forces exist such that  $F_{tot} = 0$  (i.e.  $F = 0$  and  $\gamma = 0$ ); and (iii) equation (2.9) remains valid, and surface forces dominate, for low  $F$  only.

The new grain contact radius  $a_3$  is then obtained by solving the polynomial equation (Eq. 2.9). The predictions of  $a_3 = f(\gamma)$  for differing values of  $b$  are compared to the JKR

model (Eq. 2.2) in figure (2.9A). It appears that (i)  $a_3$  falls in the asymptotic values of  $a_1$  (Eq. 2.2) at elevated surface energies; and (ii) for  $\gamma \in [0.1; 0.5] \text{ J.m}^{-2}$ , the dependence of  $a_3$  on  $\gamma$  decreases with increasing  $b$  and becomes apparently constant for  $b \sim 2 \mu\text{m}$ .

The effective compressional (i.e.  $M_3$ ) and shear (i.e.  $G_3$ ) moduli of a cemented rock are obtained from this modified model as :

$$\begin{cases} M_3 = \frac{a_3}{r} \frac{G_m(1-\phi)\psi}{5.\pi} \left( \frac{3}{1-\nu_m} + \frac{b}{a_3} \frac{4}{2-\nu_m} \right) \\ G_3 = \frac{a_3}{r} \frac{G_m(1-\phi)\psi}{5.\pi} \left( \frac{1}{1-\nu_m} + \frac{b}{a_3} \frac{3}{2-\nu_m} \right) \end{cases} \quad (2.10)$$

By normalizing  $M_3$  (or  $G_3$ ) by the reference state  $M_3(\gamma_0) = M_{3_0}$  (or  $G_3(\gamma_0) = G_{3_0}$ ), one obtains :

$$\begin{cases} \frac{M_3}{M_{3_0}} = \frac{3(2-\nu_m)a_3+4b(1-\nu_m)}{3(2-\nu_m)a_{3_0}+4b(1-\nu_m)} \\ \frac{G_3}{G_{3_0}} = \frac{(2-\nu_m)a_3+3b(1-\nu_m)}{(2-\nu_m)a_{3_0}+3b(1-\nu_m)}, \end{cases} \quad (2.11)$$

thus implying that :

$$\frac{M_3}{M_{3_0}} \neq \frac{G_3}{G_{3_0}} \neq \frac{a_3}{a_{3_0}}. \quad (2.12)$$

The normalised P- and S-wave velocities (i.e.  $RV_p$  and  $RV_s$ ) are directly obtained from the normalised compressional (i.e.  $M_3$ ) and shear (i.e.  $G_3$ ) moduli respectively. Their predicted dependence to the bonding radius  $b$  is introduced (Fig. 2.9B) for three different values of  $\gamma$ . Note that the bonding effect becomes negligible for  $b \ll 0.1 \mu\text{m}$ , and large changes in velocities occur for bonding radius lower than about  $b \sim 2 \mu\text{m}$ . Above this  $b$  value, no change is observed. This rupture point corresponds to the point where bonding forces overcome surface forces. From strength considerations, such critical value is in fact directly inferred from equation (2.9). It corresponds to the value for which the bonding strength is much larger than the surface forces :

$$\frac{8G_m b^3}{3(1-\nu_m)r} \gg 12\gamma_0\pi r, \quad (2.13)$$

For intermediate bonding radius  $b$ , a deviation appears between normalised P- (i.e.  $RV_p$ ) and S-wave (i.e.  $RV_s$ ) velocities (Fig. 2.9B). This deviation decreases at higher bonding values up to  $b \sim 2 \mu\text{m}$  where  $RV_p \sim RV_s \sim 1$ .

#### 2.4.2.2 Estimation of the surface energy

Using the modified model, surface energy is again inverted using a similar least-square minimisation as detailed in equation (2.6). Again, the parameters relate to a quartz-pure rock (i.e.  $G_{\text{quartz}} \sim 45 \text{ GPa}$ ,  $\nu_{\text{quartz}} \sim 0.06$ , and  $\gamma_0 \sim 0.45 \text{ J.m}^{-2}$ ) with a given grain radius (i.e.  $r \sim 100 \mu\text{m}$ ) under atmospheric conditions (i.e.  $F \sim 0 \text{ N}$ ). The modified model (Eq. 2.11) introduces the bonding radius  $b$  as an additional parameter. For the inversion, the

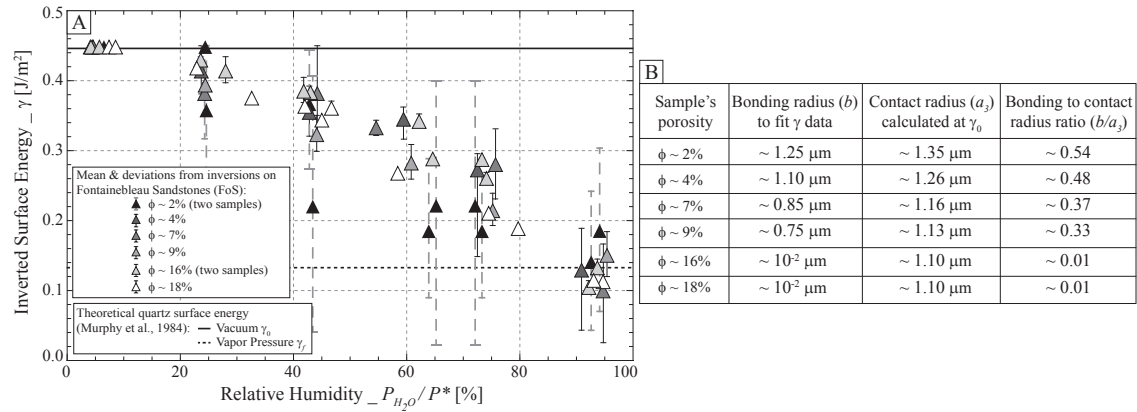


**Figure 2.10** : Data obtained using the modified model : (A) Inverted surface energy using LS minimization between measurements and the modified model. Symbols and error bar are respectively mean and standard deviation obtained from surface energies inverted separately from P- and S-wave measurements and models ; (B) Values of bonding radius allowing for consistent surface energy values at higher RH, and grain contact radius calculated (Eq. 2.9) under dry conditions ( $\gamma_0$ ).

parameter  $b$  is fixed so that  $\gamma \sim 0.13 \text{ J}\cdot\text{m}^{-2}$  is obtained for the highest value of RH.

The resulting surface energies, along with the values of  $b$  (and related ratio  $b/a_3$ ) used, are reported (**Fig. 2.10**) as a function of the samples' porosity. Such procedure leads to inverted surface energy values for all samples falling in the same overall trend (Fig. 2.10A) that was found using the model of Murphy et al. (1984) on the most porous samples (Fig. 2.8).

Note that a scattering appears between P- and S-waves inverted  $\gamma$  values for low porosity samples (Fig. 2.10A). This effect probably results from the small variations measured in low porosity samples. From the reported table (Fig. 2.10B), it appears that one can find realistic values of  $b$ . Yet, values found for all samples with porosities lower than about  $\sim 9\%$  fall in a very narrow range of about  $b \sim 0.5 - 1.5 \mu\text{m}$ .

## 2.5 Discussion

The presented results and interpretations raise several questions on three issues : (i) the relation between bonding radius  $b$  and porosity ; (ii) the relation between elastic weakening and saturation ; and (iii) the effect of RH on attenuation.

### 2.5.1 Relation between bonding radius and porosity

To complement the present dataset on Fontainebleau samples, another dataset from Gomez et al. (2010) is useful. It corresponds to measurements of elastic wave velocities at higher confining pressures (i.e.  $P_c \sim 40 \text{ MPa}$ ). The porosity dependence of the Fontainebleau samples' elastic properties measured at room P conditions and at 40 MPa are compared (Fig. 2.11). As shown by the P- and S-wave velocities zones, the pressure effect increases

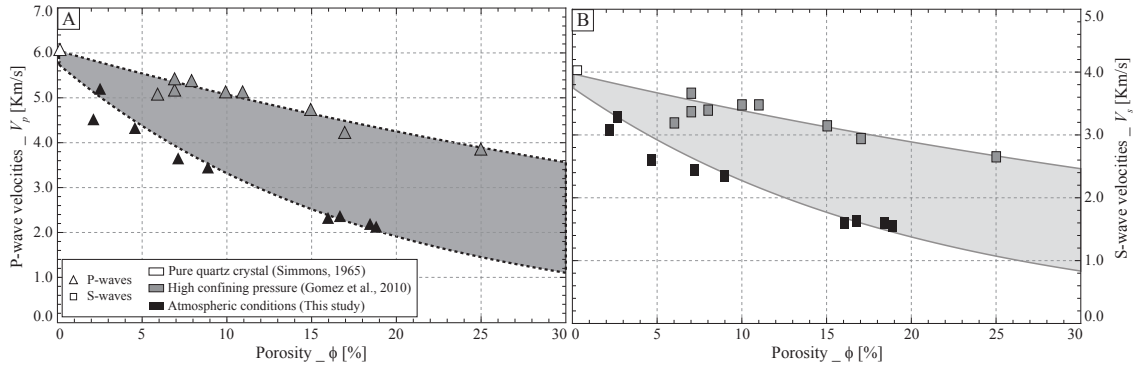


**Figure 2.11** : Dependence of elastic wave velocities to porosity for Fontainebleau sandstones between measurements at lowest Relative Humidity and ambient conditions (black symbols), and dataset from Gomez et al. (2010) measured at elevated (i.e.  $P_c \sim 40$  MPa) confining pressure (grey symbols). The grey areas (i.e. dark-grey for P-waves and light-grey for S-waves) between the best-fit trend-lines represent the effect of pressure on load bearing grain contacts.

with porosity.

The measured P- and S-wave velocities at room P-T are then normalised over high confining measurements from Gomez et al. (2010). The variations of normalised  $RV_p$  and  $RV_s$  with porosity are reported (Fig. 2.12A). It appears that normalised velocities show a clear decrease with increasing porosity, and both  $RV_p$  and  $RV_s$  show very similar dependence to porosity. This decrease can be related to the degree of cement of a given Fontainebleau sample. Such a result could be understood as a variation of the ratio  $b/a_3$  in porous sandstones. In the same manner, one may predict the effect of confining pressure on the effective moduli by determining the change in contact radius  $a_3$  using the model (Eq. 2.10) of Digby (1981). Assuming a value of  $a' \gg b$  at high confining pressure (i.e.  $P_c \sim 40$  MPa), and normalizing the dry elastic moduli at room T-P (i.e.  $M_{3_0}$ ) by the high confining state (i.e.  $M'$ ) one obtains :

$$\begin{cases} \frac{M_{3_0}}{M'} \sim \frac{a_{3_0}}{a'} \left( 1 + \frac{4}{3} \frac{b}{a_{3_0}} \frac{1-\nu_m}{2-\nu_m} \right) \\ \frac{G_{3_0}}{G'} \sim \frac{a_{3_0}}{a'} \left( 1 + 3 \frac{b}{a_{3_0}} \frac{1-\nu_m}{2-\nu_m} \right), \end{cases} \quad (2.14)$$

From the experimental conditions,  $a'$  and  $a_{3_0}$  differ from the applied external load (i.e.  $F_{max}$  and  $F_{atm}$  respectively). Assuming here the surface energy equal to  $\gamma_0 \sim 0.45 \text{ J.m}^{-2}$  for the dataset, both  $a'$  and  $a_{3_0}$  can directly be inferred from equation (2.9) as a sole function of the variable  $b$  such that :

$$\begin{cases} a_{3_0}(b) = a_3 (G_{qtz}, \nu_{qtz}, r, F_{atm}, \gamma_0, b) \\ a'(b) = a_3 (G_{qtz}, \nu_{qtz}, r, F_{max}, \gamma_0, b), \end{cases} \quad (2.15)$$

Noting that  $F \sim Pr^2$ ,  $F_{max}$  and  $F_{atm}$  are expected to differ by about two orders of magnitude. We choose  $F_{max} \sim 1 \text{ N}$  for the **measurements at high confining pressure** (i.e.  $P_c \sim 40$  MPa) and  $F_{atm} \sim 10^{-2} \text{ N}$  for the ones at atmospheric conditions. Finally, the other parameters being fixed, the ratio defined from equation (2.14) are a sole function of the

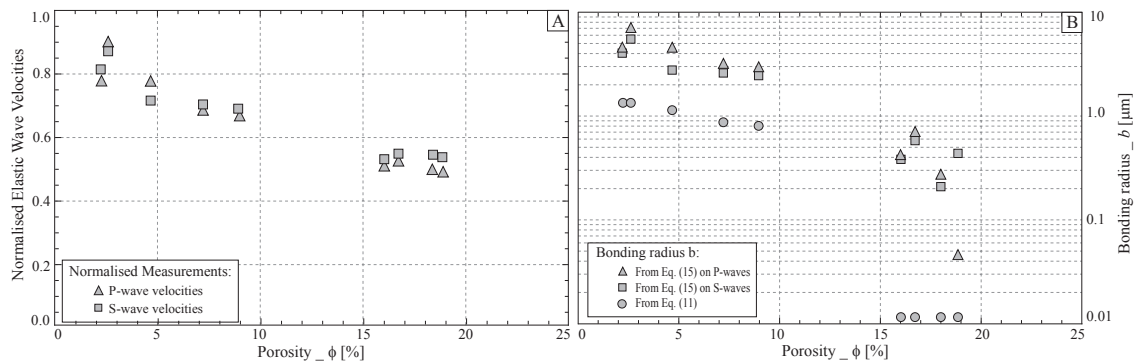


**Figure 2.12 :** (A) P- & S-wave velocities (i.e. grey triangles and squares, respectively) measured at ambient conditions normalised as a function of high confining measurements from Gomez et al. (2010) plotted against porosity. (B) Comparison of the bonding radius  $b$  obtained using either results from the adsorption study (i.e. light-gray dots) or the confining study for P-wave (i.e. light-gray triangles) and S-wave (i.e. light-gray squares) measurements.

bonding radius  $b$ . To invert for  $b$ , as in equation (2.6), a least-square minimization is then applied to the difference between the normalised model (Eq. 2.10) and data (Fig. 2.12A).

The values of bonding radius  $b$  obtained with this method are compared (Fig. 2.12B) to the ones obtained in Section 4 (Fig. 2.10B). It appears from figure (2.12B) that both methods lead to relatively similar values of bonding radius  $b$ . While the values found from equation (2.14) overestimate the ones from equation (2.10), the overall trend seems to be respected and the  $b$  values decrease with increasing porosity. The deviation found could originate from the different hypothesis made, but the modified model introduced in Section 4.2 (Eq. 2.9) seems to qualitatively account for adsorption on cemented granular rocks.

## 2.5.2 Relation between saturation and elastic weakening

While adsorption (and thus  $S_w$ ) remains the limiting factor without which no elastic weakening would be observed, it was shown in section 3 that elastic weakening (Fig. 2.5) and  $S_w$  (Fig. 2.3) from adsorption do not correlate. In particular, the absence of weakening in any of the 11 limestones rises a question. Is the absence of weakening in limestones related to its non-granular microstructure or to an intrinsic difference between calcite and quartz?

Saturation from RH relies on physi-sorption of water molecules on the mineral surfaces, which relates to (i) affinity of a mineral to water (e.g., Maghsoudy-Louyeh and Tittmann, 2008); and (ii) the amount of surface allowing for adsorption (e.g., Goertz and Knight, 1998). Quartz crystals are known to bear a large affinity to water, leading to large quantities (up to several monolayers) of adsorption on the mineral surface (e.g., Goertz and Knight, 1998). Measurements by Maghsoudy-Louyeh and Tittmann (2008) showed that adhesion forces on quartz, mica and calcite minerals (i) are of the same magnitude; and (ii) increase similarly with RH. It may indicate that affinity of both minerals to adsorbed water is of the

same order of magnitude, and implies that the measured differences in saturation between limestones and sandstones do not relate here to a difference in mineral affinity.

The water saturation  $S_w$  is the measure of mass change ( $\Delta m$ ) from adsorption over the pore volume ( $V_{pore}$ ). As mass changes occur solely from adsorption on the pore surface,  $S_w$  can also be written as a function of the number of moles of water ( $\alpha$ ) adsorbed on the internal surface ( $S_{pore}$ ) such that :

$$S_w = \alpha \cdot \frac{S_{pore}}{\rho_{wat} \cdot V_{pore}}. \quad (2.16)$$

The fact that  $S_w$  varies very weakly with porosity in Fontainebleau samples indicates that the specific surface area ( $S_s$ ) weakly depends on porosity, which is consistent with Bourbie and Zinszner (1985). The large differences in  $S_w$  between Fontainebleau sandstone and limestone samples is probably linked to differences in specific surface area. As an example, Dana and Skoczylas (1999) measured a very low specific surface area (i.e.  $S_{s_{FoS}} \sim 0.03 \text{ m}^2 \cdot \text{g}^{-1}$ ) on a Fontainebleau sample of  $\phi \sim 9\%$  porosity. On the opposite, large specific surface areas ranging up to about  $S_{s_{Ls}} \sim 3 \text{ m}^2 \cdot \text{g}^{-1}$  were measured by Vincent et al. (2011) on some microporous limestone samples, and by Clark et al. (1980) on their limestones and sandstones samples. This may explain the large differences in saturation between Fontainebleau sandstone and the rocks measured by Clark et al. (1980).

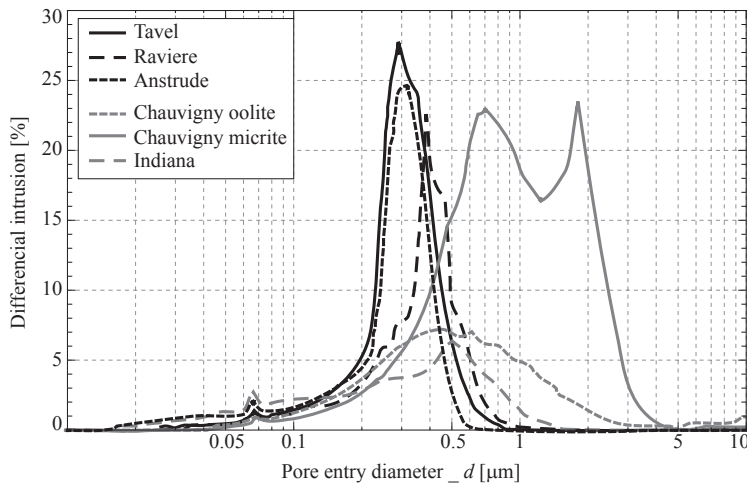


**Figure 2.13 :** Normalised intruded volume as a function of pore entry diameter measured using a typical MICP technique. Example of measurements for six representative limestone samples.

Note that the largest  $S_w$  (at high RH) are obtained for the Anstrude, Raviere, Massangis and Tavel limestones. A standard procedure of mercury injection (i.e. MICP) was used to study these rocks' pore entry diameters (e.g., Casteleyn et al., 2010). On the contrary to other limestones, MICP measurements (Fig. 2.13) on three of these four rocks show a narrow peak for very small pore entry diameters of sub-microns size. MICP measurements

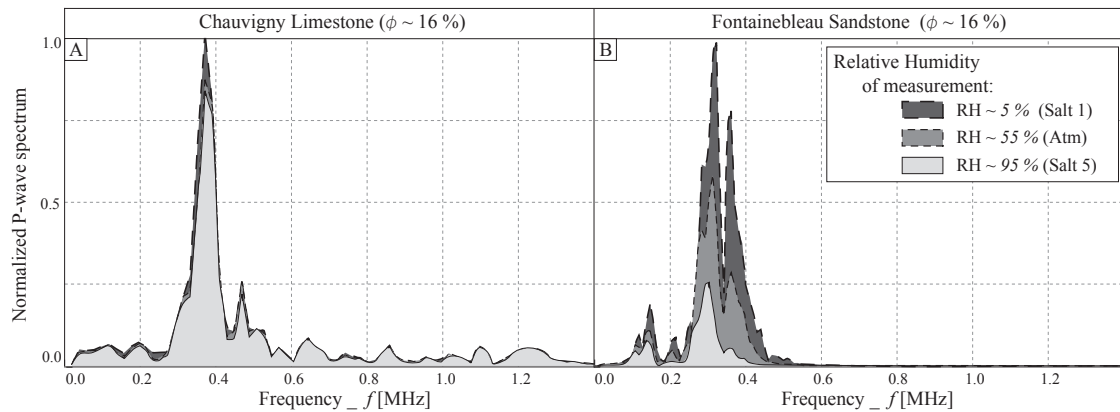


**Figure 2.14** : Normalized P-wave Fourier spectra measured at ambient conditions on a Chauvigny limestone and a Fontainebleau sandstone sample for three different Relative Humidities.

may thus confirm that adsorption relates to pores size, and thus to specific surface area.

### 2.5.3 Waves amplitudes variations and attenuation

As observed from figure 2.4, the waveform's amplitude is also affected by RH. As for elastic waves velocities, P- and S-waves amplitudes show large decrease with increasing RH in the Fontainebleau sample studied (Fig. 2.4B). To characterise this effect, the Fourier spectra of the full waveforms can be directly computed, as shown for the example of P-amplitude spectra (Fig. 2.14) of the two samples chosen (Fig. 2.4). Again, a clear difference is observed between the limestone (Fig. 2.14A) and FoSp16a (Fig. 2.14B) P-amplitudes spectra. While the limestone spectra show no change with RH, large decrease in P-amplitudes is observed for FoSp16a with increasing RH. In particular, the normalised amplitude obtained for FoSp16 between measurements under dry (i.e.  $A_0$ ) and maximum RH conditions (i.e.  $A_i$ ) are as low as about  $A_i/A_0 \sim 0.2$ .

Waves attenuations, in terms of quality factors, could be obtained using the spectrum ratio principle (Toksöz et al., 1976; Bourbie and Zinszner, 1985) from these amplitude variations. Assuming that attenuation relates to amplitude variations would lead to the conclusion that elastic weakening and attenuation correlate in their RH dependence. Such result, of elastic weakening and attenuation variations with RH, was observed by Clark et al. (1980). As assumed by different authors (e.g., Murphy et al., 1986; Chelidze et al., 1996), dispersion and attenuation from moisture are thought to originate from fluid movements at the grain contacts, and could be expected to occur in granular rocks. Yet, reporting such measurement would imply (i) using as a reference the amplitude of a non-attenuating standard such as an aluminium (e.g., Bourbie and Zinszner, 1985); and (ii) compare the amplitudes of the different samples, which obtained with different contact positions and quality. As a consequence, attenuation was not investigated here to concentrate on elastic weakening.

Note that, previously, elastic weakening (Clark et al., 1980) and attenuation (e.g., Tittmann, 1977, 1978; Tittmann et al., 1980; Clark et al., 1980) from adsorption have only been measured at lower frequencies (i.e.  $f \sim 1$  kHz). In the particular case of **measurements by Clark et al. (1980)**, elastic properties are obtained using the Resonant Bar Technique (e.g., Tittmann et al., 1980). This widely used apparatus allows for measurements of shear and extensional elastic moduli and seismic attenuation at intermediate frequencies (i.e.  $f \in [1;20]$  kHz). On the reverse, the present dataset was obtained using a typical ultrasonic apparatus leading to waves frequency of about  $f \sim 0.3$  MHz. The present experiment thus complements existing datasets and shows that, at a given RH, attenuation and elastic weakening also appear at frequencies as high as  $f \sim 0.3$  MHz.

#### 2.5.4 Surface energy variations from adsorption

As shown above, a variation in surface energy ( $\gamma$ ) with increasing RH (Figs. 2.8 & 2.10) is inferred. In particular, the values obtained (at high RH) using the model of Murphy et al. (1984) in the case of the most porous sandstones (Fig. 2.8) fit particularly well the value of  $\gamma_f \sim 0.13 \text{ J.m}^{-2}$  directly measured at vapour saturating pressure on a quartz surface by Parks (1984). Furthermore, using the newly developed model, the same  $\gamma$  value can be reached for all Fontainebleau samples for realistic values of bonding radii  $b$ .

Using BET theory (Adamson, 1976), Murphy et al. (1984) predicted the RH dependence of  $\gamma$ . As schematized by Parks (1984), the prediction is that  $\gamma$  variations are **much** larger at the lowest RH. The first adsorbed monolayer is expected to develop at very low RH values (i.e.  $\sim 10\%$ ), and to strongly affect  $\gamma$ . This strong effect at low RH values is not supported by the estimates for surface energy values inferred from the measurements on Fontainebleau sandstone's samples (Figs. 2.8 and 2.10). While investigating the cause for such deviation may be of interest, it would imply modelling the thermodynamics of adsorption variations at an interface and its effect on surface energy. Such investigation is out of the scope of the present study.

## 2.6 Conclusions

An experimental set-up has been designed to investigate the effect of adsorption on limestones and sandstone samples' elastic properties. From varying Relative Humidity (RH), saturation and elasticity measurements at ultrasonic frequencies (i.e.  $f \sim 0.5$  MHz) on limestones and sandstones have been obtained. The results show that RH affects the sample properties. Both rock types show varying degrees of adsorption with RH, and varying effects on elasticity. Limestones show large adsorption effects, but no elastic weakening is observed. On the reverse, large elastic weakening is observed on Fontainebleau sandstone samples. The weakening effects measured are similar for P- and S-wave velocities.

As elastic weakening affects preferentially the granular sandstones, grain contact theories have been used to interpret the present measurements. Using the model of Murphy et al. (1984), the rock-fluid adsorption effect is explained in terms of surface energy variations (Johnson et al., 1971; Murphy et al., 1984). It appears that this model predicts the same weakening for both P- and S-wave velocities, which is consistent with the data. An effective surface energy is obtained for the Fontainebleau samples. For the highest porosity samples, this surface energy proves to be consistent with quartz mineral surface energy at vapour saturating pressure. **The model of Murphy et al. (1984)** describes well high porosity loosely cemented sandstones.

Yet, the amount of variation in **surface energy** with RH decreases with **decreasing** the sample porosity and a very small variation is found for the lowest porosity sandstones. Fontainebleau sandstone is a typical granular rock in which cementation increases with decreasing porosity. In order to account for this, the approach of Murphy et al. (1984) has been modified using the cemented granular model of Digby (1981). An additional parameter is the bonding radius  $b$ . For the problem's parameters at hand, it was found that surface effects are important only for values of  $b$  lower than about  $b \sim 2 \mu\text{m}$ .

In addition, a comparison between limestones and sandstones shows that the fundamental difference between their respective elastic weakening from adsorption originate from a microstructural difference. Fontainebleau sandstone is a typical grain aggregate where the contact between grains is a key parameter. On the reverse, limestones may be considered as bearing porosity embedded in a very fine cemented matrix.

## Acknowledgements

The authors would like to thank Prof. Christian David from the University of Cergy and Dr. Elizabeth Bemer from IFPEN for providing us with limestones samples. Prof. Christian David and Jean-Christian Coulombier are thanked for their help on MICP measurements on some of the samples.



---

## Discussion & Conclusion

---

### 3.1 Further discussions on the adsorption study

#### 3.1.1 Another output from the modified model

As a direct output from the modified model, the bonding radius  $b$  could be inferred for each rock sample independently of the applied pressure conditions (see Fig. 2.11 in chap. 2). However, the cement ratio  $b/a$  is always preferred as the indication for the rock's cement degree. This ratio can also be directly inferred from the two models (Eqs. 2.10 & 2.14). The resulting dependence to porosity of the  $b/a$  obtained from the different methods (i.e. RH study versus confining pressure study) can thus be consistently compared (Fig. 3.1) using again the results on the Fontainebleau sandstone samples.

For both methods, the cement ratio compares particularly well. Both methods lead to a decrease from about 0.6 for the tight and cemented samples to about 0 for the highly porous Fontainebleau samples. Comparing this figure to Fig. (2.12B) implies that although the inferred contact  $a$  and cement  $b$  radii intrinsically depend on the method used, the  $b/a$  ratio does not. It indicates that the parameter to characterize a given granular sample is indeed  $b/a$ , i.e. an independent cement indicator. In addition, it seems to further highlight the good applicability of the model developed in chapter (2).

#### 3.1.2 Relation between amplitudes losses and attenuation

The pulse transmission method (Birch, 1960) used for elastic wave velocities measurements could also be used to measure the wave amplitude variations from one sample to the other (Wang, 1997). Attenuations are obtained from the spectrum amplitudes  $A_i$  following

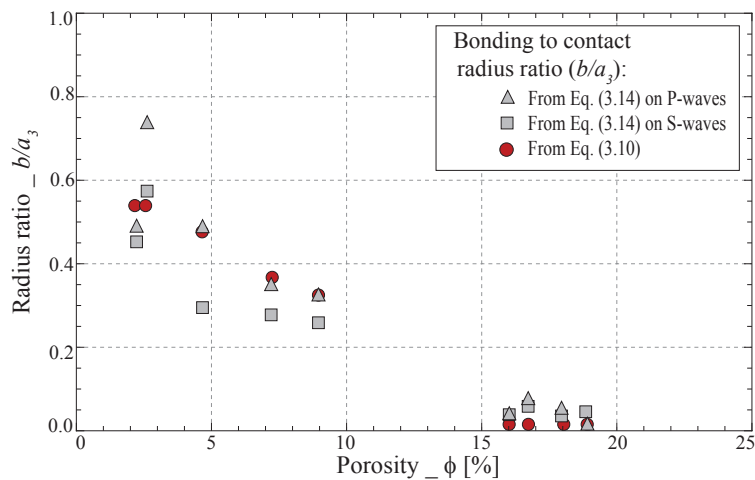


**Figure 3.1** : Dependence to porosity of the inferred ratio  $b/a$  for the Fontainebleau sandstone samples. Comparison between the cement ratio obtained using the RH study (i.e. red dots) and the pressure dependence study (i.e. grey triangles and squares).

the spectrum ratio principle (Toksöz et al., 1976; Bourbie and Zinszner, 1985) :

$$\ln \frac{A_0}{A_i} = -\pi d \left[ \frac{1}{Q_0 V_0} - \frac{1}{Q_i V_i} \right] f, \quad (3.1)$$

where  $d$  is the sample diameter, and  $f$ ,  $V_i$ ,  $A_i$  and  $Q_i$  are respectively the sample wave frequency, and the velocity, amplitude and attenuation at a given RH step  $i$ . The case 0 is the reference state. Note that this reference state is usually chosen to be a standard material such as the aluminium, compared to which the rock samples are usually more attenuating.

In this present approach, only relative measurements (i.e. same experimental condition and RH variation) are considered (owing to and) leading to its very high accuracy. On the contrary, comparing measurements on different samples would involve introducing a bias particularly important : the quality of the sensor-to-sample contact. This bias is expected to lead to inaccuracies larger than the expected variations, which precise assessment is not experimentally possible. Trusting a reference measurement on a standard aluminium sample than to introduce an added strong assumption, i.e. the dry reference state is assumed as non-attenuating so that  $1/Q_0 \sim 0$  and the equation by Toksöz et al. (1976) simplifies to (Bourbie and Zinszner, 1985) :

$$\frac{1}{RQ_i} = \frac{V_i}{\pi d f} \ln \frac{A_0}{A_i} \quad (3.2)$$

Attenuation is obtained from waves spectra maximum amplitudes (Bourbie and Zinszner, 1985) at central frequencies. From the amplitudes, relative attenuations of P-wave (i.e.  $RQ_p^{-1}$ ) and S-wave (i.e.  $RQ_s^{-1}$ ) are computed and plotted against RH (Fig. 3.2). The overall trends show a very small increase in attenuation with RH for limestones samples, and a strong one for sandstones.

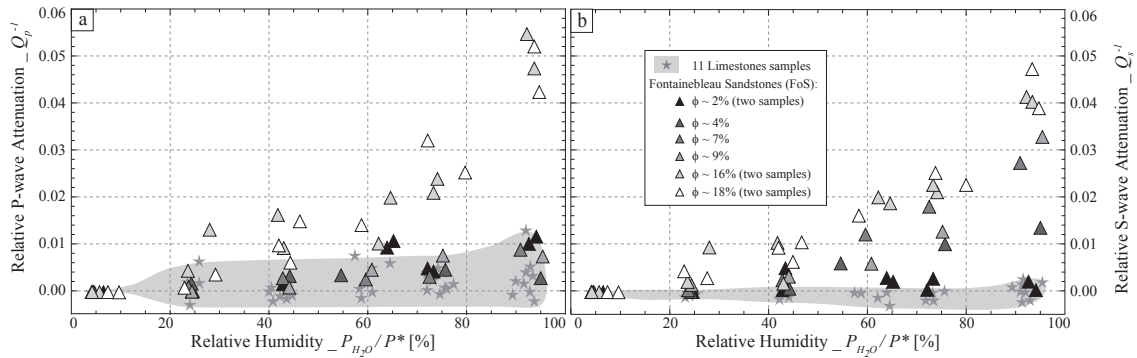


**Figure 3.2 :** P- and S-wave relative attenuation with Relative Humidity measured at **ambient conditions** on 11 limestones samples (i.e. stars & light-grey area) and on 9 Fontainebleau sandstone samples (triangles) of increasing porosities (filling in grey levels from black to white).

Note that the trends of attenuations (i.e.  $RQ_p^{-1}$  &  $RQ_s^{-1}$ ) with RH observed are similar to the ones measured for P- and S-wave velocities : (i) The limestones and less porous Fontainebleau samples (i.e. FoSp2a & FoSp2b) show little to no relative attenuation variations with RH; and (ii) The more porous Fontainebleau samples show increase in both P- and S-wave relative attenuations with RH. Moreover, at maximum RH,  $RQ_p^{-1}$  is larger than  $RQ_s^{-1}$  for the most porous sandstones.

### 3.1.3 Relation between weakening, attenuation and amount of adsorption

Weakening could be expected to increase as adsorption increase as considered by Clark et al. (1980) and (Murphy et al., 1984). These authors however considered that the weakening observed in sandstones originated from the large specific surface area of these samples. This statement can be tested by comparing the elastic weakening (Fig. 3.3a) and variations in relative attenuations (Fig. 3.3b) to the measured saturation. In order to compare the measurements with existing ones of Clark et al. (1980), only the S-wave relative variations in velocity and attenuation are investigated. Note from earlier results that the exact same variations are expected from P-waves variations.

Comparing the measured variations for the Fontainebleau sandstones relative to the carbonate samples, two distinct behaviours are highlighted. Large variations in elastic properties are observed for the Fontainebleau sandstone samples. The exact reverse is observed for the limestone samples. However, the data of Clark et al. (1980) show indeed a correlation between elastic properties variations (and weakening) and water saturation, i.e. specific surface area. A Berea sandstone sample has also been measured with the present set-up. The measurements fit with the ones of Clark et al. (1980). The elastic weakening in the Berea sample shows indeed a positive correlation with saturation. The difference does not originate from the different measuring set-ups but from the samples measured. The use of Fontainebleau samples allowed here to discard one parameter, i.e. specific surface area.

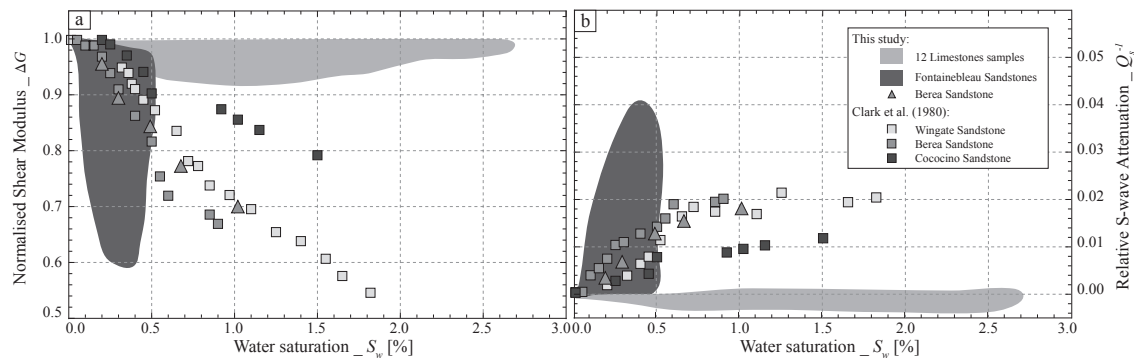


**Figure 3.3 :** Elastic properties and attenuation measured against water saturation for limestones (i.e. stars & light-grey area), Fontainebleau sandstones (i.e. triangles & dark-grey area) and three different sandstones (i.e. squares). Comparison between measured data and measurements from Clark et al. (1980).

The major controlling parameter is the granular characteristic of the rock sample, and its degree of cement.

### 3.1.4 Elastic weakening in carbonates or in sandstones ?

The initial aim was to investigate the elastic weakening in carbonates, which has been shown to occur by previous authors. It is thus of interest to try and use the present results as a mean to understand what is theoretically expected in case of full saturations.

First, in case of elastic weakening, it has been shown that adsorption modifies both P- and S-waves in the same way. One should thus consider this phenomenon as an "elastic weakening" phenomenon more than a "shear weakening" one, i.e. both bulk and shear moduli are modified.

Secondly, elastic weakening showed experimentally a dependence to adsorption only in the case of the loosely cemented sandstone samples. No effect is observed in the carbonate samples of study. Two possibilities arise : whether the shear weakening effect observed by authors does not relate to a physical adsorption or the carbonate samples used were not good candidates. In the second case, the carbonates samples showing those effects are expected to be granular ill-cemented materials.

## 3.2 Measurements at full saturation under drained conditions

This part is taken from a preliminary study that aims at measuring the different bulk moduli (or compressibility) using low amplitude (i.e.  $\sim 0.2$  MPa) and low frequency (i.e.  $\sim 10^{-2}$  Hz) pressure oscillations. Details on the experimental set-up may be found in next **part III**, and details on the experimental protocol are given in **Appendix A**. Here, we only investigate the measured drained bulk moduli  $K_d$  using different saturating fluids.

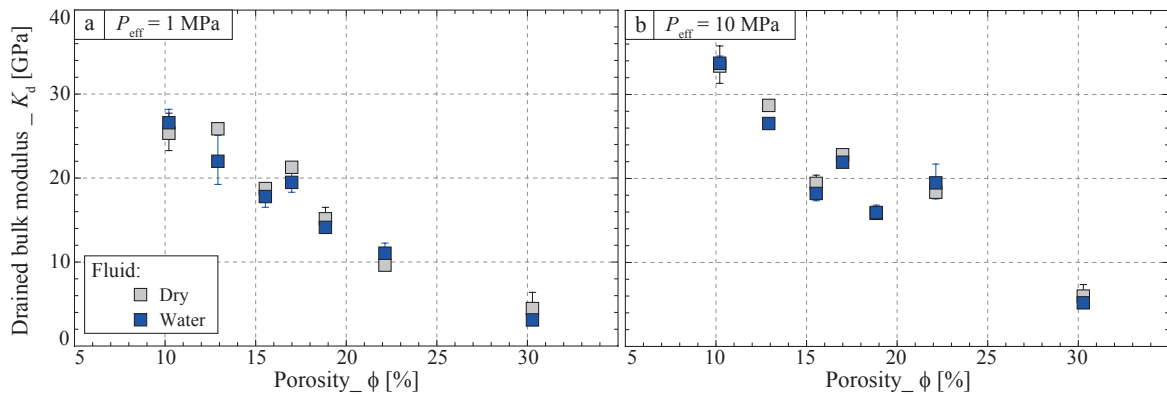


**Figure 3.4 :** Dry and (water-saturated) drained bulk moduli as a function of porosity for the seven limestone samples at two effective pressures of 1 and 10 MPa.

Because  $K_d$  should be independent of fluid if no rock-fluid physico-chemical interaction occurs, it is of interest to investigate the dependence of this property to the saturating fluid.

### 3.2.1 Case of the limestone samples

Out of the sample dataset presented in table (1.2), only seven limestone samples could be measured. The rocks are (i) a Chauvigny oolitic and micritic limestone samples, (ii) samples of Anstrude and Massangis limestone, (iii) a Tavel limestone sample, and (iv) samples of Lavoux and Euville limestone. The sample dataset have a porosity that is in the range of  $\phi \in [10;30]\%$ . All samples' drained bulk moduli  $K_d$  were measured under both dry and water full-saturated conditions for different effective pressures in the range of  $[1;30]$  MPa.

#### Dependence to porosity

For the seven samples, the measurements are reported as a function of porosity for two differing effective pressure of 1 MPa (Fig. 3.4a) and 10 MPa (Fig. 3.4b).

The drained bulk modulus under either dry or water-saturated conditions shows a consistent decrease as the porosity increases. At  $P_{eff} = 1$  MPa, the lowest porosity Tavel Limestone (TaL) has a value of  $K_d \sim 25$  GPa and the highest porosity Chauvigny micrite (ChmL) has a value of  $K_d \sim 4$  GPa. As pressure increases, the drained bulk moduli increase, leading to a second trend of porosity dependence at  $P_{eff} = 10$  MPa (Fig. 3.4b). Note that pressure dependence still remains beyond 10 MPa for two samples, which properties result independent of pressure only for pressures beyond 30 MPa.

#### Dependence to fluid

Comparing the dry and water-saturated bulk moduli, no much change are observed. In both Bierry limestone (ByoL) and ChmL,  $K_d$  are however smaller under water-saturated

conditions than under dry conditions. To better investigate such fluid effect, the water-saturated drained bulk modulus is compared to the dry one (Fig. 3.5).

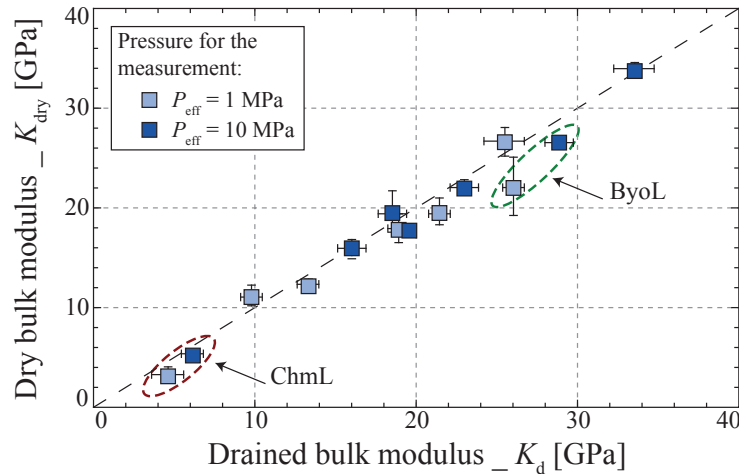


**Figure 3.5 :** Comparison between dry and (water-saturated) drained bulk moduli for the seven limestone samples at two effective pressures of 1 and 10 MPa.

The reported measurements range in values between 3 GPa and 34 GPa. Overall, all samples follow a linear trend indicating a good correspondence between dry and water-saturated drained measurements. The measurements on both ByoL and ChmL indicate a departure from the trend. However, the effect remains small and may relate more to the measurement accuracy.

### 3.2.2 Case of the Berea sample

$C_{bc}$  and  $C_{bp}$  were measured as a function of effective pressure on the Berea sample under dry conditions and saturated by either glycerine or a water-glycerine mixture. No dependence to the saturating fluid is observed from the measurements, and the measurements of  $C_{bc}$  under glycerine or water-glycerine saturation fit the dry measurement. More details are given in Appendix A. We investigate the effect of water saturation at lowest effective pressure for this sandstone sample.

#### Pore pressure variation

For this experiment, the static measurements were made to complement the oscillatory ones so that two sets of measurements are available. The properties of interest are here the drained bulk compressibility coefficients  $C_{bc}$  (or  $C_d$ ) and  $C_{bp}$ . These properties are reported as a function of pore pressure for the water-saturated Berea sandstone sample (Fig. 3.6).

Overall, no dependence to pore pressure is observed for both  $C_{bc}$  and  $C_{bp}$ . It indicates that the effective pressure coefficient does not vary with pore pressure. Note the large

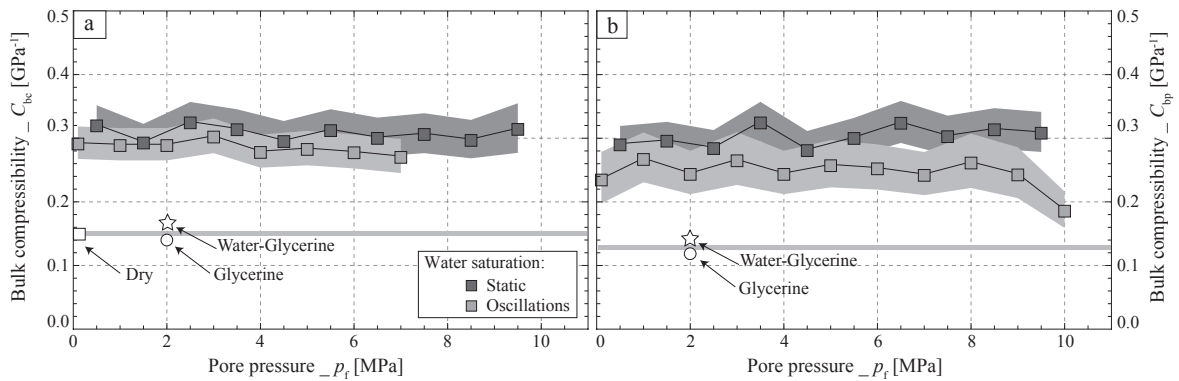


**Figure 3.6** : Drained compressibility coefficients  $C_{bc}$  and  $C_{bp}$  measured as a function of pore pressure for the water-saturated Berea sandstone. The measurements under dry, glycerine and water-glycerine saturated conditions corresponding to the first experiment are reported as white symbols.

change in the coefficients' magnitude between the first and second experiment. Under dry, glycerine and water-glycerine saturations, the values found for  $C_{bc}$  and  $C_{bp}$  are clearly smaller than under water-saturated conditions. The values remain constant for all pore pressures, thus indicating the good accuracy of the measurement.

### Comparison of the drained compressibility

Measurements of the drained  $C_d$  (or  $C_{bc}$ ), undrained  $C_u$ , unjacketed  $C_s$  compressibility and Skempton  $B$  coefficient coefficients can be considered as standard measurements that have already been reported in the literature. In particular, Hart and Wang (2010) have reported the measurements of these properties in case of the Berea sandstone sample. Although the measuring methods differ, it is of interest to investigate the comparison between the present data and the ones they reported. The drained compressibility  $C_d$  is reported as a function of Terzaghi effective pressure (Fig. 3.7) for the two Berea samples.

Overall, a similar dependence to  $P_{eff}$  is observed from both datasets. However, the magnitude differs. While the measurements fit at pressures beyond 20 MPa, the increase in compressibility for the Berea sandstone of Hart and Wang (2010) is much larger than the one measured here. Note however that the saturating fluid differed for the measurements. The reported  $C_d$  was measured under dry conditions, but the one from Hart and Wang (2010) was under water full saturation.

Although the compressibility was not measured for all effective pressures during the first experiment, a measurement was made under water-glycerine saturation at lowest pressure of  $P_{eff} = 1$  MPa during the first experiment. From the second experiment, the property was measured at  $P_{eff} = 1$  MPa under water full saturation. The measurement under water saturation during the first experiment results higher than the dry (and glycerine-saturated)  $C_d$ , yet remains lower than the measurements of Hart and Wang (2010). However, during the second experiment, the value reaches about  $C_d = 0.27$ , a value in the range of the ones

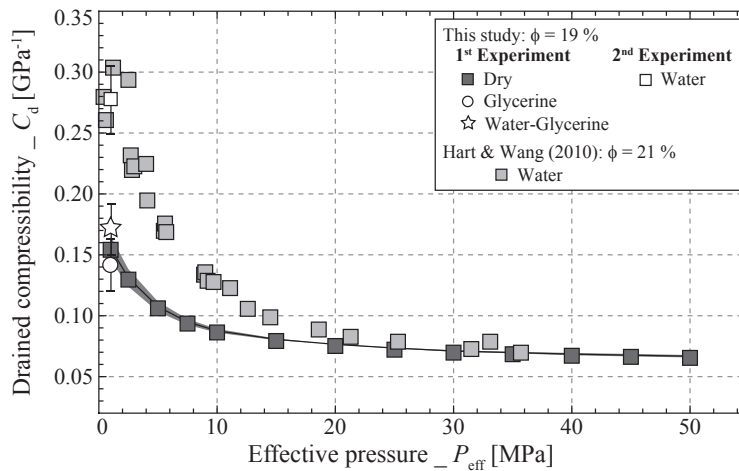


**Figure 3.7 :** Pressure dependence of the drained compressibility. Comparison between the present dataset and the one reported by Hart and Wang (2010)

measured by Hart and Wang (2010).

### Elastic weakening in the Berea sample

All adds-up to directly imply that the water saturation affected the measured property. The first point may point out to a possible elastic weakening from the water-rock interaction. A strong water-weakening effect is evidenced, which remains constant for all pore pressures. The bulk modulus appears to decrease by about 40 % upon water full saturation. Note that such magnitude of weakening was in fact observed from the adsorption study.

Note also that another interesting effect is also highlighted : no or small fluid-rock interaction seems to occur in case of the water-glycerine mixture. It probably originates from the fact that, although dissolved by water, glycerine remained as dissolved species in the pore water. This dissolved specie may have acted like a surfactant, thus cancelling the adsorption effect of the pure/polar water.

### 3.3 General conclusion

New results are obtained from the study of the drained bulk moduli under differing full saturations that add up with the measurements from **chapter II.2**. The drained bulk modulus was measured on a set of limestone samples ranging from 10 % to about 30 % porosity. No clear evidence for an elastic weakening is obtained from the measured drained bulk moduli. Reversely, an increase in the bulk compressibilities (or decrease in  $K_d$ ) of the Berea sample occurs upon water saturation. The amount of decrease in  $K_d$  upon water full saturation appears to be very similar to the one obtained from the RH study (Fig. (3.3)).

All these results may thus imply that the so-called "shear weakening" upon water satu-

ration relates to an adsorption phenomenon that not solely affect shear modulus but also the bulk moduli/compressibilities. This phenomenon is expected to occur only in unce-mented granular material, which is typically the case of sandstone but relatively rare for carbonate rocks. A model that accounts for this physico-chemical effect was developed. It proves to consistently account for the parameters ruling elastic weakening from adsorption in the samples investigated.



## PARTIE III

# Oscillations de la pression de confinement : Calibrations & Mesures

|          |  |            |
|----------|--|------------|
| <b>1</b> | <b>Introduction &amp; Principes de mesure</b>                            | <b>71</b>  |
| <b>2</b> | <b>Bulk modulus dispersion and attenuation (<i>Geophysics, 2015</i>)</b> | <b>77</b>  |
| 2.1      | Introduction . . . . .   | 78         |
| 2.2      | Samples, experimental apparatus & procedure . . . . .                    | 79         |
| 2.3      | Calibration Results . . . . .  | 87         |
| 2.4      | Results on Fontainebleau sandstone . . . . .                             | 89         |
| 2.5      | Interpretation . . . . .   | 95         |
| 2.6      | Conclusion . . . . .   | 102        |
| <b>3</b> | <b>Additional Calibrations &amp; Results</b>                             | <b>105</b> |
| 3.1      | Measured Ultrasonic properties . . . . .                                 | 105        |
| 3.2      | Strain amplitude effects . . . . .                                       | 109        |
| 3.3      | Evidence of a macroscopic fluid flow out of the sample . . . . .         | 112        |
| 3.4      | Measurements on a Berea sample . . . . .                                 | 113        |
| <b>4</b> | <b>Conclusion &amp; Perspectives</b>                                     | <b>115</b> |
| 4.1      | Conclusion . . . . .   | 115        |
| 4.2      | Perspectives . . . . .   | 115        |



## Summary

**Résumé :** Cette partie s'intéresse à la dépendance à la fréquence du module d'incompressibilité, mesuré par des oscillations de la pression de confinement. Le système et le principe de mesure sont tout d'abord calibrés grâce à des standards, permettant une mesure précise du module  $K$  et de son atténuation dans des gammes de pression et de fréquence de  $P_c \in [1; 50]$  MPa et  $f \in [10^{-3}; 10^0]$  Hz.

Deux grès de Fontainebleau, totalement saturés en fluide, sont mesurés pour différentes pressions et fréquences avec ce système. La viscosité du fluide prenant une part dominante dans la fréquence caractéristique des phénomènes de dispersion/atténuation, une glycérine de forte viscosité est utilisée en complément de l'eau. La gamme de fréquence apparente est ainsi étendue à  $f^* \in [10^{-3}; 10^3]$  Hz, ce qui permet de mesurer clairement la transition entre deux régimes élastiques. Une procédure additionnelle permet une mesure des surpressions de pore en sortie d'échantillon, appelée coefficient de pseudo-Skempton. La dépendance à la fréquence de cette propriété est un indicateur direct de l'écoulement fluide et donc de la transition entre domaines drainé et non-drainé.

Ce travail a permis de mesurer simultanément la cause et la conséquence de la transition élastique drainé/non-drainé.

**Abstract :** This part investigates the frequency dependence of the bulk modulus, measured thanks to oscillating the oil confining pressure. Both experimental set-up and measuring principle are first calibrated using standard samples, allowing for a precise measurement of bulk modulus and attenuation in the pressure and frequency ranges of  $P_c \in [1; 50]$  MPa and  $f \in [10^{-3}; 10^0]$  Hz.

Two fully saturated Fontainebleau sandstone samples are measured as a function of pressure and frequency with this set-up. The fluid's viscosity being a ruling parameter in the characteristic frequency of the dispersion/attenuation phenomena, a highly viscous glycerine is used as a complement to water. The range in apparent frequency reached is of  $f \in [10^{-3}; 10^3]$  Hz, allowing to observe a clear transition between two elastic regimes. An added procedure allows for measurements of build-up pore pressure in the dead volume, addressed as the Pseudo-Skempton coefficient. Its frequency-dependent decrease point out to the transition between drained and undrained regimes.

This work thus allowed to measure both the cause and the consequence of the drained/undrained elastic transition.



---

## Introduction & Principes de mesure

---

### Calibration du système de mesure

#### Principe de mesure

On considère un échantillon cylindrique plein, isotrope et homogène de longueur  $L$  et rayon  $r$ . Supposons que l'on y exerce une oscillation de la pression de confinement  $\Delta P$  (i.e. oscillations isotropes) sur l'échantillon, les déformations mesurées  $\epsilon_{ax}$  et  $\epsilon_{rad}$  sont alors données par :

$$\epsilon_{ax} = \epsilon_{rad} = \frac{1}{3K} \Delta P \quad (1.1)$$

Dans ce cas d'étude, le seul le module élastique considéré est donc le module d'incompressibilité, noté  $K$ .

#### Mise en oeuvre expérimentale

Cette méthode d'étude est en pratique mise en place dans une cellule triaxiale, permettant d'appliquer une pression sur un matériau donné. Pour le cas d'étude, une particularité importante que doit posséder une telle presse est de pouvoir exercer de manière instantanée une pression purement isotrope sur le matériau d'étude. Une seule des deux presses présentes à l'ENS permet donc cette étude. La pression isotrope est appliquée sur l'échantillon à l'aide de l'huile de confinement.

La variation périodique de pression de confinement est appliquée à l'aide d'une pompe hydraulique et d'un logiciel créé à cet effet. Une consigne de volume injecté pour un laps de temps donné permet de faire varier le volume d'huile dans le système. Le système étant fermé, cette variation de volume crée la variation de pression désirée. Ce système

avait préalablement été mis en place, et a donné lieu à des publications s'intéressant à la comparaison entre des mesures quasi-statiques et des mesures ultrasoniques de  $K$  (Adelinet et al., 2010; David et al., 2013).

L'intérêt est ici d'étudier la dépendance en fréquence du module  $K$ , des calibrations supplémentaires ont été faites dans le but de déterminer la gamme de fréquence que permettait le système. De plus, ces calibrations ont aussi permis d'atteindre une seconde propriété, caractéristique d'un phénomène de dispersion : l'atténuation  $Q_K^{-1}$  associée au module  $K$ .

### Travaux antérieurs et protocole additionnel

Une claire distinction est visible entre les mesures faites précédemment avec cet outil de mesure (Adelinet et al., 2010; David et al., 2013) et les mesures reportées par les autres équipes étudiant l'effet de fréquence (Batzle et al., 2006; Adam et al., 2006; Mikhaltsevitch et al., 2011; Madonna et al., 2011; Tisato and Madonna, 2012). Les études faites précédemment à l'ENS s'attachaient à l'étude du module d'incompressibilité dans des conditions expérimentales drainées. Au contraire, les autres équipes ont choisi d'étudier des échantillons initialement non-drainés, en empêchant expérimentalement le fluide de sortir de la roche.

Considérant qu'il était intéressant de comprendre la transition en fréquence vers l'état non-drainé, la solution de bloquer artificiellement le fluide dans la roche a été rejetée. Le protocole utilisé consiste à introduire un volume mort relativement important aux deux extrémités de l'échantillon. Grâce à ce système, il est donc possible de mettre en évidence expérimentalement la transition entre l'état drainé et l'état non-drainé. Comme le montre la suite, ce système permet aussi une mesure de la pression de pore en sortie de l'échantillon, et donc de l'écoulement fluide hors de cet échantillon.

### Oscillation due à la température

#### Observation de l'effet

Des mesures de déformation statique ou en oscillation montrent une mesure de déformation périodique additionnelle. Cette perturbation est de basse fréquence, de l'ordre de  $f \sim 10^{-3}$  Hz (Fig. 1.1b). Différents procédés de traitement du signal ont été testés pour comprendre puis annuler ce biais. Néanmoins, il reste intéressant d'essayer de comprendre l'origine de cette oscillation. Une mesure de la température du bain de confinement (Fig. 1.1a) montre que cette oscillation de déformation est en fait corrélée à une oscillation en température. Cette variation provient du régulateur de température présent dans la salle d'expérience.

Connaissant le coefficient de dilatation de l'échantillon, il est possible de déterminer la déformation volumique induite par la variation en température (Fig. 1.1b). En soustrayant

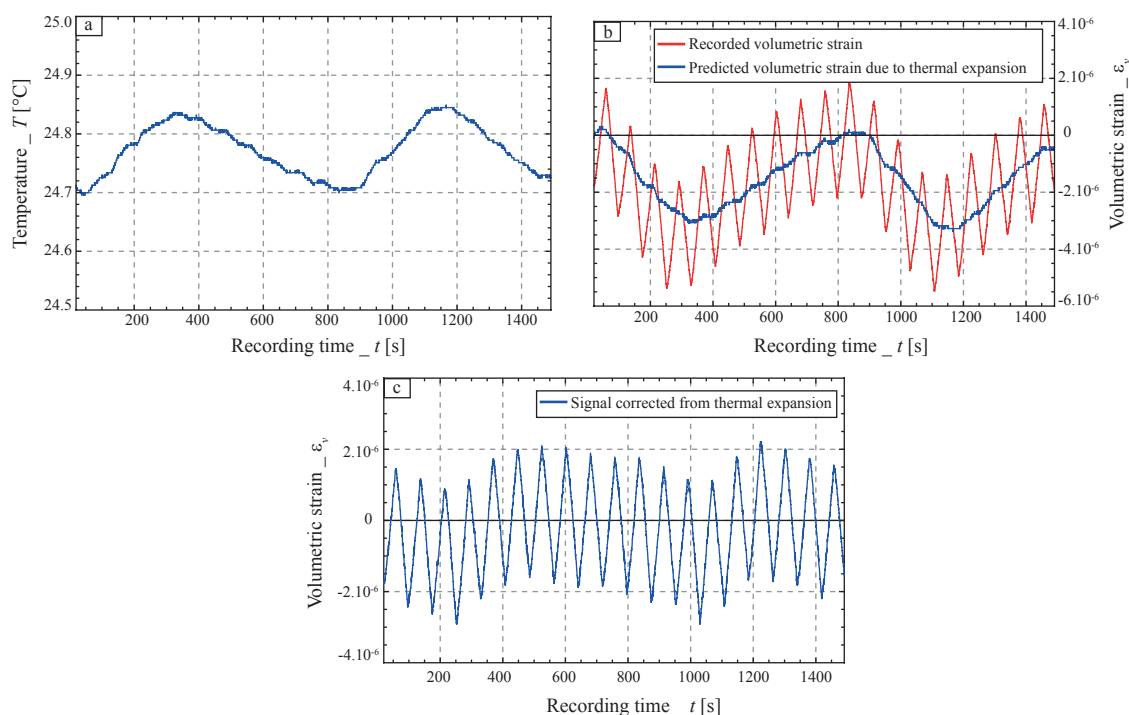


**Figure 1.1 :** (a) Exemple d'une mesure de l'oscillation en température lors d'une expérience. (b) Comparaison entre la déformation par dilatation thermique calculée et la déformation mesurée. (c) Correction de la déformation par soustraction entre la déformation mesurée et la déformation thermique calculée.

la déformation additionnelle calculée à celle mesurée, on obtient un signal beaucoup moins affecté par cette modulation en température (Fig. 1.1c).

### Effet de la correction sur le signal à l'étude

Néanmoins, une oscillation résiduelle est observable après correction (Fig. 1.1c), impliquant que la correction n'est pas parfaite et doit être complétée par un traitement supplémentaire. De plus, cette correction induit aussi une perte d'amplitude du signal, directement observable dans le domain de Fourier (Fig. 1.2).

Dans le domaine de Fourier, une amplitude correspond à une fréquence d'oscillation donnée. La comparaison entre le signal initial et le signal traité montre directement que le traitement affecte l'amplitude initiale du signal (Fig. 1.2). A très faible fréquence, correspondant à l'oscillation en température, une large diminution est observée, ce qui est cohérent. Néanmoins, une légère diminution est aussi observée sur l'amplitude du signal à la fréquence d'intérêt, i.e. correspondant à l'oscillation de pression.

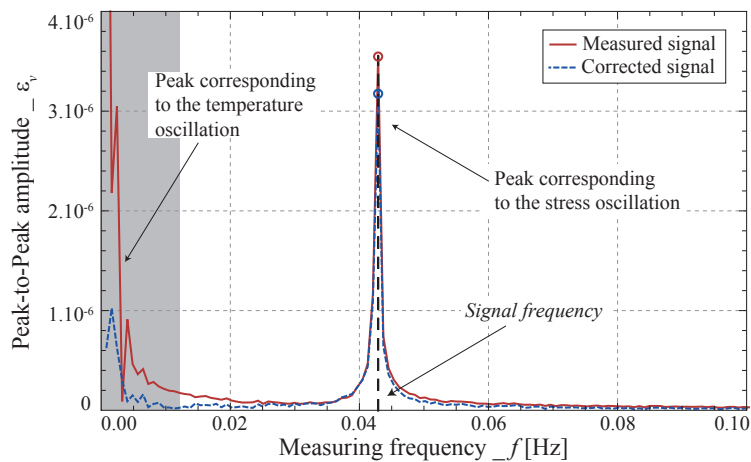


**Figure 1.2 :** Amplitude pic-à-pic dans le domaine de Fourier pour la déformation mesurée (i.e. en rouge) et la déformation corrigée (i.e. en bleu).

## Traitement du signal

Comme montré dans la section précédente, le signal doit être préalablement traité avant de pouvoir en déduire les propriétés recherchées. Trois informations d'importance sont contenues dans les oscillations mesurées : leur fréquence  $f$ , leur phase  $\phi$  et leur amplitude  $A$ . Ces trois informations peuvent être obtenues soit dans le domaine temporel, soit dans le domaine fréquentiel.

### Filtrage dans le domaine fréquentiel

Il a été montré précédemment qu'une correction de dilatation thermique du matériau n'est pas totalement satisfaisante, il est donc nécessaire de filtrer le signal. Un traitement préliminaire utilisait une fonction en ondelette pour séparer hautes et basses fréquences. Cette méthode a été rapidement remplacée par une étude dans le domaine de Fourier. Le signal est d'abord passé dans le domaine fréquentiel à l'aide d'une transformée de Fourier. Il est ensuite filtré par une fonction passe-bande. Puis il est repassé dans le domaine temporel par transformée inverse.

La technique de filtrage introduit des effets de bord sur le signal final. Ce biais est supprimé en ne considérant pas les premières et dernières oscillations dans les traitements finaux.

## Mesures finales

### Déphasage & Atténuation

Dans le domaine fréquentiel, la norme du signal montre un pic de large amplitude. Ce pic correspond à l'amplitude "pic-à-pic"  $A$  de l'oscillation, et est mesurée à la fois pour l'oscillation de pression et pour celle de déformation. Cette valeur permet la connaissance directe des déformations appliquées sur le matériau. La fréquence caractéristique auquel ce pic est observé correspond à la fréquence  $f$  de ce maximum d'amplitude (Fig. 1.2). On obtient alors directement la phase du signal à la fréquence d'étude  $f$ , notée  $\phi$ .

L'atténuation est directement obtenue par la tangente du déphasage entre contrainte ( $\phi_P$ ) et déformation ( $\phi_\epsilon$ ) :

$$Q_K^{-1} = \text{Tan}[\phi_P - \phi_\epsilon]. \quad (1.2)$$

### Module élastique

La détermination du module d'incompressibilité  $K$  nécessite les mesures de la pression exercée  $\Delta P$  sur l'échantillon ainsi que de la déformation volumique  $\epsilon_v$  subie par ce même échantillon. La mesure de déformation volumique de l'échantillon est une moyenne des déformations axiales et radiales de l'échantillon, i.e.  $\epsilon_v = 3.Moy(\epsilon_{ax}, \epsilon_{rad})$ . Le module d'incompressibilité  $K$  est alors obtenu par une régression linéaire entre déformation (i.e. abscisse) et contrainte (i.e. ordonnée).



---

### Bulk modulus dispersion and attenuation (*Geophysics*, 2015)

---

L. Pimienta, J. Fortin and Y. Guéguen, Bulk modulus dispersion and attenuation in sandstone, (2014), *Geophysics*, 80(2), D111-D127.

---

#### Abstract

We report experimental data on the frequency dependence of bulk elastic modulus in porous sandstones. A new methodology is developed to investigate the dispersion/attenuation phenomena on a rock's bulk modulus ( $K$ ) for varying confining pressures in the range of  $[1 - 50]$  MPa and fluids of varying viscosities (i.e. air, glycerine and water). This methodology combines (i) ultrasonic (i.e.  $f \sim 0.5$  MHz) P- and S-wave velocity measurements, leading to the High Frequency (HF)  $K_{HF}$ ; (ii) stress-strain measurements from forced periodic oscillations of confining pressure at Low Frequency (LF) ranges (i.e.  $f \in [4.10^{-3}; 4.10^{-1}]$  Hz), leading to  $K_{LF}$  and  $Q_K^{-1}$ ; and (iii) pore pressure measurement to document the induced fluid-flow in the LF range (i.e.  $f \in [4.10^{-3}; 4.10^{-1}]$  Hz).

The stress-strain method is first checked using three standard samples : glass, gypsum and plexiglass samples. Over the frequency and pressure range of the apparatus, (i)  $K_{LF}$  is stable and accurate; and (ii) the lowest measurable LF attenuation is  $Q_K^{-1} \sim 0.01$ . The methodology is applied to investigate Fontainebleau sandstone samples of 7% and 9% porosity.  $K_{LF}$  and  $Q_K^{-1}$  exhibit correlated variations, which also correlate with an experimental evidence of frequency-dependent fluid-flow out of the sample. Attenuation peaks as high as  $Q_K^{-1} \sim 0.15$  and  $Q_K^{-1} \sim 0.25$  are measured.

The attenuation/dispersion measured under glycerine saturation is compared to Biot-

Gassmann predictions. The overall behaviour of one sample is consistent with a dispersion/attenuation characteristic of the drained/undrained transition. On the reverse, the other sample exhibit exotic behaviours as the measurements are underestimated by the drained/undrained transition and indicate a direct transition from drained to unrelaxed domain. These different behaviours are consistent with the values of the critical frequencies expected for the drained/undrained (i.e.  $f_1$ ) and relaxed/unrelaxed (i.e.  $f_2$ ) transitions.

---

## 2.1 Introduction

Comparing rocks elastic properties inferred from either laboratory ultrasonic (i.e.  $f \sim 1$  MHz) or field sonic (i.e.  $f \in [1; 10^3]$  Hz) velocities is not straightforward because of the frequency range (i.e. up to 5 orders of magnitude). Frequency effects are expressed in terms of dispersion and attenuation of a wave travelling through a medium. Various theories were developed to understand and account for these effects in fluid-saturated porous rocks (e.g., O'Connell and Budiansky, 1974; Cleary, 1978; Winkler and Murphy III, 1995; Le Ravalec et al., 1996; Mavko et al., 2003; Müller et al., 2010; Adelinet et al., 2011). Overall, these theories aim at predicting (i) the characteristic frequencies of the effect; and (ii) the amplitude of attenuation and dispersion.

Even though frequency effects are shown to be important in partially saturated media (e.g., Tisato and Madonna, 2012; Madonna and Tisato, 2013), only fully-saturated rocks are investigated here. In a fully-saturated rock, three flow regimes are expected to take place in the frequency range of  $f \in [10^{-2}; 10^6]$  Hz (e.g., Cleary, 1978; Sarout, 2012). The first regime is the drained one. It corresponds to a macroscopic fluid flow, and is thus associated to very low frequency. The second regime is the undrained one. At a scale of a Representative Elementary Volumes (REV), there is an isobaric state but no macroscopic flow can occur. Both drained and undrained regimes are well accounted for through quasi-static poroelasticity. By comparison with the two first regimes, both relaxed, the third regime is an unrelaxed one. It corresponds to a non-isobaric REV. It follows from the existence of these three regimes of fluid flow that two transitions are expected : from drained to undrained regimes, and from relaxed to unrelaxed regimes.

Several experiments aiming at measuring such effects in the laboratory have been performed in the recent years (Subramaniyan et al., 2014). In particular, a "stress-strain" forced oscillation method has been introduced (e.g., Spencer Jr., 1981). Axial forced oscillations have widely been used for measuring Young modulus and attenuation for a frequency range of about  $f \in [10^{-2}; 10^3]$  Hz (e.g., Batzle et al., 2006; Adam et al., 2006; Tisato and Madonna, 2012; Madonna and Tisato, 2013; Mikhaltsevitch et al., 2014). A similar method was used by Jackson and Paterson (1987) to determine shear dispersion and attenuation in the range of  $f \in [0.01; 0.3]$  Hz with torsional forced oscillations. Measuring bulk modulus

was made possible using confining pressure forced oscillations (Adelinet et al., 2010; David et al., 2013; Fortin et al., 2014). Adelinet et al. (2010) and (David et al., 2013) compared the HF (i.e.  $f \sim 1$  MHz) and LF (i.e.  $f \sim 0.1$  Hz) bulk modulus of dry and fluid-saturated rocks. However, these authors did not investigate the variation of bulk modulus with frequency nor did they measure attenuation in this pressure oscillation mode.

The present contribution reports new results on frequency dependent dispersion and attenuation on the bulk modulus. The experimental set-up is first presented and calibrated using three standard samples. Then, results are reported for two Fontainebleau samples fully-saturated with different fluids. The results are interpreted on the basis of the three fluid-flow regimes and their characteristic frequencies.

## 2.2 Samples, experimental apparatus & procedure

### 2.2.1 Samples studied

#### 2.2.1.1 Calibration samples

Three standard samples were chosen to test the experimental set-up and procedure : (i) a synthetic glass sample made of amorphous silica (Ougier-Simonin et al., 2011; Mallet et al., 2013); (ii) a pure gypsum sample (Brantut et al., 2012); and (iii) a plexiglass (PMMA) sample (e.g., Batzle et al., 2006). These were chosen as : (i) They are homogeneous and isotropic media at the sample scale. (ii) Their elastic properties are known, and they show a large range in compressibilities from  $K = 4.5$  GPa for plexiglass (e.g., Barrau and Laroze, 1988) to  $K = 60$  GPa for glass (e.g., Ougier-Simonin et al., 2011); (iii) These samples have a negligible porosity, and their elastic properties are not expected to change with confining pressure; and (iv) While glass and gypsum elastic properties are independent of frequency, plexiglass is a viscoelastic material whose elastic properties are frequency-dependent. Plexiglass is often used as a mean to test an attenuation apparatus (e.g., Batzle et al., 2006; Tisato and Madonna, 2012; Madonna and Tisato, 2013).

#### 2.2.1.2 Fontainebleau samples

Fontainebleau sandstone is a well-known reference rock. Both framework grains and cement are pure quartz, making up a clean sandstone of about  $\sim 99.9\%$  qtz (Bourbie and Zinszner, 1985; Gomez et al., 2010). As the rock was formed from aeolian quartz grains deposited, the rock possess a random grain orientation and is well sorted, with an average grain radius of about  $r = 100 \mu\text{m}$ . Figure 2.1 shows a Fontainebleau typical thin section. From figure 2.1(a), the rock can consistently be assumed to be homogeneous at the Representative Elementary Volume (REV) scale (i.e. volume  $\gg$  grains' volume). Furthermore, by adding a polarising prism (Fig. 2.1b), it is shown that the different quartz grains have each a different orientation, making the isotropic assumption consistent for this rock.

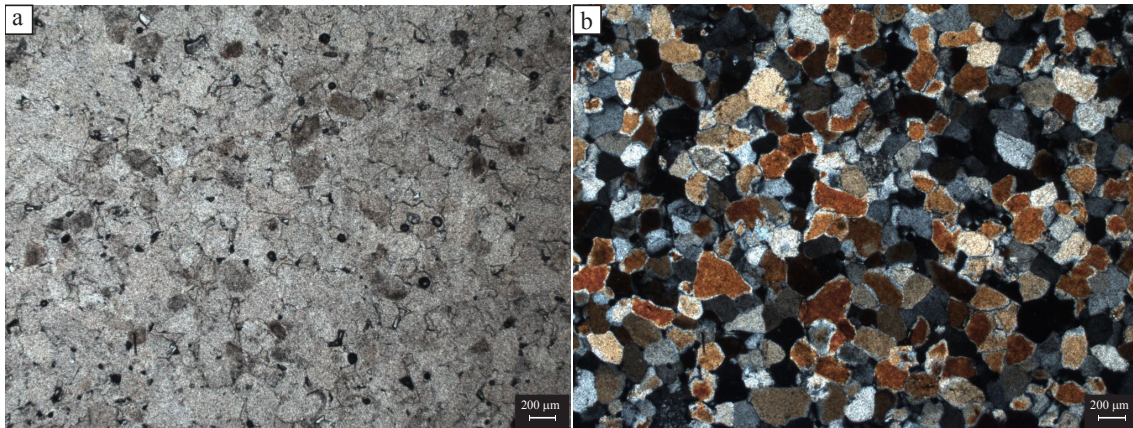


**Figure 2.1** : Microscopic image of a thin section of the  $\sim 7\%$  Fontainebleau sandstone without (a) and with (b) a polarising prism. In (a), grains appear in grey and pores in black. In (b), colours come from the polarising direction.

Depending on the amount of quartz cement, Fontainebleau sandstone porosity ranges from about  $\phi \sim 2\%$  for highly cemented samples to about  $\phi \sim 25\%$  for ill cemented samples. The main differences between samples are the pores entry diameters, leading to variations in permeability of about 4 to 5 orders of magnitude (Bourbie and Zinszner, 1985) between the extreme cases.

The two samples chosen have respectively porosities of about  $\phi = 7.3\%$  (i.e. Fo7) and of about  $\phi = 8.8\%$  (i.e. Fo9). Their total pore volume, measured from total fluid injection at lowest effective pressure, is respectively of  $V_{Fo7} \sim 7.2$  mL and  $V_{Fo9} \sim 8.6$  mL. This is consistent with the samples' dimensions of 40 mm diameter and 80 mm length, i.e. rock volume of about  $\sim 100$  mL. As documented by Bourbie and Zinszner (1985), these samples of slightly different porosities are expected to fall in almost the same permeability range of about  $\kappa \in [10^{-14}; 10^{-15}]$  m<sup>2</sup>.

## 2.2.2 Experimental apparatus & procedure

### 2.2.2.1 Cell and confining set-up

The apparatus aims at measuring simultaneously High Frequency (HF) and Low Frequency (LF) elastic properties. To investigate these properties at different pressures, measurements are conducted in an oil-confining triaxial apparatus (Fortin et al., 2005) that can be used in two different set-ups thanks to an axial piston that can be shifted vertically. Only the first set-up, in which the axial piston is not in contact with the end-platen (and thus the sample) is used here. It allows for studying the sample under pure isotropic conditions. For the sample to be isolated from the surrounding confining oil, it is jacketed radially and enclosed in two end-platens.

A servo-controlled confining pump is linked to the bottom of the cell chamber to deliver the confining pressure. The applied pressure is directly measured by a Keller pressure

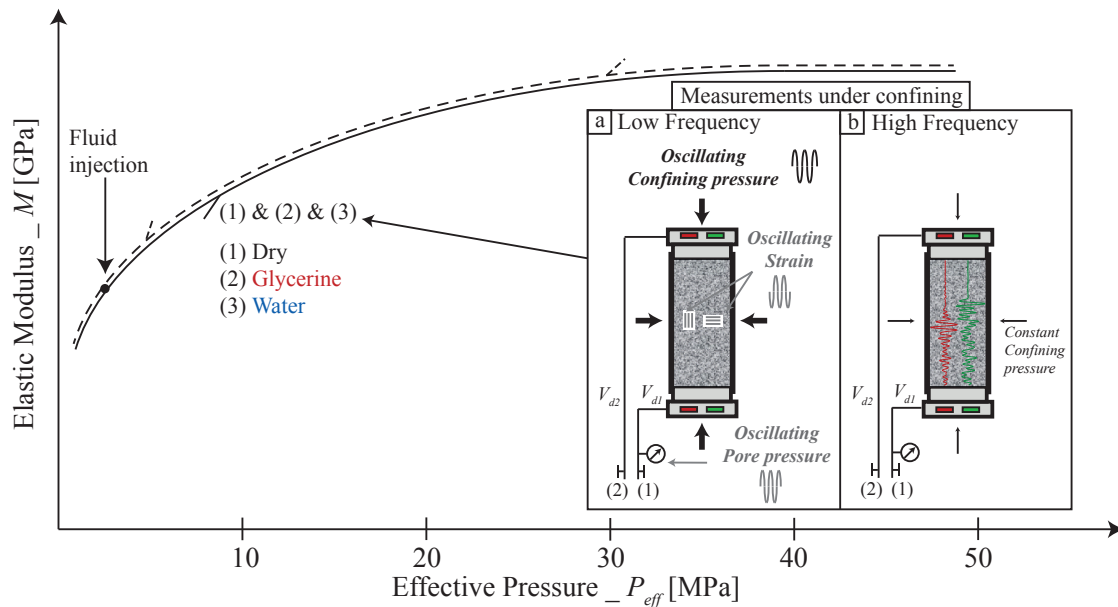


**Figure 2.2 :** Schematic view of the experimental procedure. Under isotropic stress conditions (a) LF measurements originate from a confining pressure oscillation that induces both strain and pore pressure oscillations; and (b)  $K_{HF}$  is obtained from ultrasonic wave velocity measurement, from a travelling pulse between two piezo-electric transducers.

transducer with an accuracy down to about  $P_c \sim 0.01$  MPa. This pressure transducer is placed at the top of the chamber so that the pressure measurement is strictly equal to that applied to the sample.

### 2.2.2.2 Experimental procedure

A procedure (Fig. 2.2) is devised to measure the rocks' bulk moduli using different fluids at different confining pressures. Starting from a pressure of about  $\sim 1$  MPa, elastic moduli are measured at each loading step of confining pressure up to the maximum confining of  $\sim 50$  MPa. For fluid saturation, the confining pressure is slowly decreased down to a pressure of about  $\sim 3$  MPa. At this low pressure, a fluid (i.e. glycerine then water) is introduced in the sample. After pore pressure stabilization (i.e.  $P_p \sim 2$  MPa), the properties are measured again. For the sandstone samples in fluid saturated conditions, Terzaghi effective pressure  $P_{eff} = P_c - P_p$  is used that allows for comparison between dry and fluid-saturated conditions. This approximation of the effective pressure is chosen in order to report in a simple way the data.

The standard non-porous samples are measured in dry conditions only (i.e. step (1) in Fig. 2.2). The Fontainebleau samples are measured under (1) dry; (2) glycerine full saturation; and (3) water full saturation conditions. Starting from the initial pressure of measurement, a controlled rate of about 0.01 MPa/s is used for both loading and unloading as to allowing for complete/instantaneous relaxation of the fluid-filled sample (Fortin et al.,

2007; David et al., 2013).

At each confining pressure, LF and HF properties are obtained using two different methods (Fig. 2.2). HF elastic properties (Fig. 2.2b) are deduced from the measured ultrasonic wave velocities. LF properties (Fig. 2.2a) are measured using confining pressure oscillations around a mean effective pressure value. The induced strain and pore pressure oscillations are recorded. The LF bulk modulus is deduced from the ratio of volumetric strain  $\Delta\epsilon$  over confining  $\Delta P_c$  oscillations. These oscillations are very small, i.e.  $\Delta P_c \sim 0.2$  MPa.

The glycerine full saturation of the sample is ascertained by an injection procedure : (1) vacuum is applied with a vacuum pump at the sample upper end until the measured  $P_p$  reaches a stable negative value; (2) the fluid is injected at the sample bottom while maintaining the vacuum up to full saturation; and (3) the sample is flushed again by a full volume of fluid, i.e. equal to the system "*Sample + Dead Volume*" total volume. Water saturation is then obtained by directly injecting water in the glycerine-filled sample. As glycerine immediately and fully dissolves in water, thus losing its viscosity, the water full saturation is obtained by flushing two to three times the pore volume.

### 2.2.2.3 Pore fluid set-up

Pore pressure is controlled externally, and independently of the confining pressure, by a pair of connected *Quizix* volumetric servo-pumps. The pore volume and pressure measurements' accuracies are respectively of about  $V_p \sim 0.1$   $\mu$ L and  $P_p \sim 0.001$  MPa. Additionally, another pressure transducer of  $P_p \sim 0.01$  MPa accuracy is placed near the sample. Valves are placed at both ends of the sample (Fig. 2.2a) to decrease as much as possible the pipes' dead volumes (i.e. (1) and (2) in Fig. 2.2a), and the pressure sensor is placed near the bottom end-platen (i.e. inside the dead volume). The measured dead volumes are  $V_{d1} = 3.433$  mL and  $V_{d2} = 3.205$  mL, leading to a total dead volume of about  $V_d \sim 6.6$  mL.

The valves can either be open or closed. The first configuration is chosen when changing the confining pressure in the range of  $P_c \in [1; 50]$  MPa, so that the fluid is kept at a constant pressure of  $P_p \sim 2$  MPa. The second configuration is chosen, and the valves are closed, during LF measurements, i.e. during the small pressure oscillation  $\Delta P_c$ . In this configuration, the fluid mass is kept constant in the system (i.e. *Sample + Dead Volume*). This system is experimentally undrained, and fluid pressure changes are tracked by the pore pressure sensor.

This configuration was found to be the most appropriate as it discards any possible bias from an extrinsically-induced differed fluid-flow (i.e. from the slow regulation of the pump). This configuration has often been chosen for measuring frequency effects (e.g., Batzle et al., 2006; Tisato and Madonna, 2012; Madonna and Tisato, 2013; Mikhaltsevitch et al., 2014). In such set-up, one would assume that the resulting measurement is intrinsically undrained. This is actually not the case here owing to the existence of the dead volume (i.e.  $V_d \sim 6.6$  mL). In particular,  $V_d$  is close to the samples' total pore volumes  $V_p$

(i.e.  $V_{F07} \sim 7.2$  mL and  $V_{F09} \sim 8.6$  mL). It follows that  $V_p + V_d$  is undrained, but  $V_p$  is not necessarily undrained.

#### 2.2.2.4 High frequency set-up

High-frequency moduli are measured from the travel-time of an ultrasonic wave through the sample's length (i.e.  $l \sim 80$  mm). For this purpose, a pair of P- and S-wave piezoelectric transducers (PZT5A, *Boston Piezo-Optics Inc.*) are glued in the end platens, at both ends of the sample. The recorded travel-time is directly corrected from the added travel-time in the end platens.

P- & S-wave arrival-time  $\Delta t$  are obtained using a cross-correlation procedure by picking the arrival-time of the P- or S-waveform's maximum amplitudes. The waves velocities (i.e.  $V$ ) are then inferred knowing the sample length  $l$  such that  $V = l/\Delta t$ . High-frequency moduli  $K_{HF}$  and  $G_{HF}$  are obtained from the sample's density  $\rho$  and the measured P- & S-wave velocities assuming the material isotropic such that :

$$\begin{cases} V_p = \sqrt{\frac{K_{HF} + \frac{4}{3}G_{HF}}{\rho}}, \\ V_s = \sqrt{\frac{G_{HF}}{\rho}}, \end{cases} \quad (2.1)$$

with the density  $\rho$  defined from the known quartz (i.e.  $\rho_{qtz}$ ) and fluid (i.e.  $\rho_f$ ) densities, and sample's porosity (i.e.  $\phi$ ) such that  $\rho = \rho_f \cdot \phi + \rho_{qtz} \cdot (1 - \phi)$ .

Note that the sample's length varies with the confining pressure. A length correction  $l = l_0 - \Delta l$  is thus introduced in the measurement of the wave velocities. In a same way, the sample density varies due to the porosity change  $\phi = \phi_0 - \Delta \phi$  so that a second correction is also introduced to obtain the HF elastic moduli (e.g.  $K_{HF}$ ).

The relative elastic waves velocities values obtained from cross-correlation measurements have accuracies of 0.1 %. However, owing to the uncertainty to precisely determine the arrival time on the reference waveforms, absolute P- and S-wave velocities have lower accuracy, of about  $\sim 1\%$  and  $\sim 3\%$  respectively. As the aim of the present contribution is to compare HF and LF moduli, and not the sole effect of the fluid on the P- and S-wave velocities, absolute measurements are needed. As the elastic moduli are deduced from the square of the ultrasonic wave velocities, they bear much larger measurement error. As  $G_{HF}$  is inferred from  $V_s$  only, the low accuracy on the  $V_s$  only affects its absolute value, with an accuracy as low as about  $\sim 6\%$ . On the reverse,  $K_{HF}$  is inferred from a combination of both  $V_p$  and  $V_s$ . The absolute accuracy on  $K_{HF}$  is thus lower than for  $G_{HF}$ , i.e. accounting for errors on both P- and S-wave velocities. Its error is assumed to be higher than about  $\sim 8\%$ .

### 2.2.2.5 Low frequency set-up

As discussed above, the LF measurements rely on the stress-strain method. A low amplitude pressure oscillation at a given frequency is applied on the sample, thus inducing a strain oscillation. Three pairs of axial and radial  $350\ \Omega$  strain gauges (*Tokyo Sokki TML, FCB-6-350-11*) of  $6\text{ mm}$  length are directly glued on the sample. Each of the six strain gauges are mounted in a one-fourth Wheatstone bridge. Pressure (i.e.  $\Delta P_c$ ) and strain (i.e.  $\Delta \epsilon$ ) oscillations are transformed from electric to pressure and strain signals using Catman recording system (*HBM inc.*), able to record at frequencies up to 2400 Hz.

Two different approaches are used for the sample's investigation. First, properties are measured as a function of effective pressure, at a chosen frequency of  $f \sim 0.1\text{ Hz}$ . Secondly, properties are measured as a function of frequencies at various confining pressures.

### 2.2.3 Processing method for the low frequency set-up

At a given effective pressure, an oscillating confining pressure  $\Delta P_c$  (Fig. 2.3a) leads to strain  $\Delta \epsilon$  oscillations (Fig. 2.3c), and, in the case of porous samples saturated by a liquid, to a pore pressure  $\Delta P_p$  oscillation (Fig. 2.3b). The recorded strains account for a solid response to the applied pressure oscillation. The pore pressure oscillations, recorded at the outlet of the pipes' dead volume, account for a fluid response induced by the sample's response.

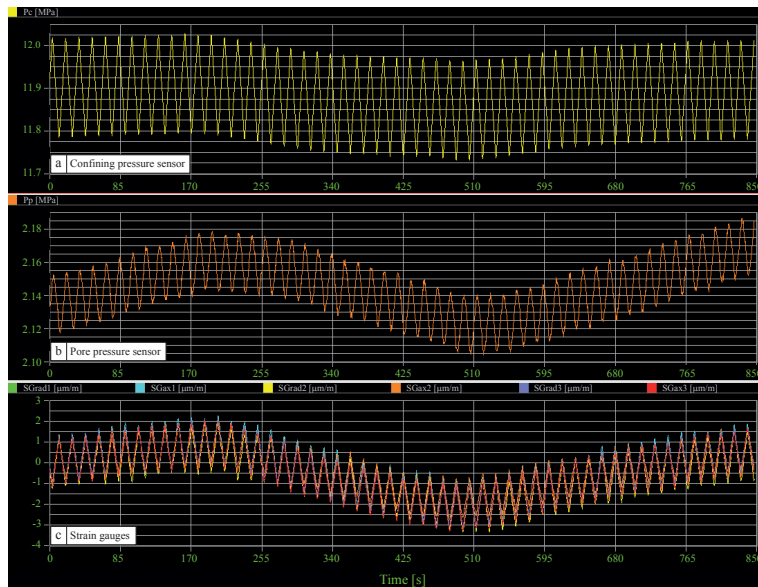


**Figure 2.3 :** Recorded measurement of (a) confining pressure oscillations (i.e.  $\Delta P_c$ ), and induced (b) pore pressure (i.e.  $\Delta P_p$ ) and (c) axial and radial strains (i.e.  $\Delta \epsilon_{rad}$  and  $\Delta \epsilon_{ax}$ ) oscillations prior to signal processing. Example for Fo7 under glycerine saturation at an effective pressure of 10 MPa (i.e.  $P_c = 12\text{ MPa}$  and  $P_p = 2\text{ MPa}$ ). For this example, the signal frequency is  $f = 0.01\text{ Hz}$  and the sampling frequency is  $f = 1\text{ Hz}$ . Note the low frequency modulation due to the air-conditioning system.

The applied confining pressure oscillations  $\Delta P_c$  (Fig. 2.3a) are triangular periodic si-

gnals. As a direct consequence, the output registered signals for both strain  $\Delta\epsilon_v$  (Fig. 2.3c) and pore pressure  $\Delta P_p$  (Fig. 2.3b) have the same triangular form. The signal is a periodic function characterized by its frequency  $f$ , phase  $\phi$  and amplitude  $A$ .

### 2.2.3.1 Volumetric strain measurement

As Madonna and Tisato (2013) pointed out, the sample intrinsic heterogeneity may induce an error as the total rock volumetric strain may differ from the local strain recorded by the gauge. To discard such error (i) the samples (i.e. reference and Fontainebleau samples) used have been chosen to be homogeneous media; and (ii) large strain gauges (i.e. 6 mm length) have been used so that the measurement area is larger than a REV average area.

The volumetric strain  $\epsilon_v$  is theoretically obtained from both axial  $\epsilon_{ax}$  and radial  $\epsilon_{rad}$  strains such that  $\epsilon_v = \epsilon_{ax} + 2\epsilon_{rad}$ . However, under pure isotropic conditions, the measured  $\epsilon_{ax}$  and  $\epsilon_{rad}$  are equal (e.g. Fig. 2.3c). It is thus possible to deduce  $\epsilon_v$  either from  $\epsilon_{ax}$  (David et al., 2013) or  $\epsilon_{rad}$  only. In order to minimize the possible bias, the volumetric strain is here measured from the mean of all gauges so that  $\epsilon_v = 3\bar{\epsilon}$ , where  $\bar{\epsilon}$  is the mean value of all the strain gauges (i.e.  $\epsilon_{ax}$  and  $\epsilon_{rad}$ ).

### 2.2.3.2 Strain measurement

In an automatic procedure, (i) the signals (e.g., Fig. 2.3) are Fourier transformed; (ii) the frequency  $f$ , corresponding to the dominant amplitude peak  $A$ , is picked; and (iii) the phase  $\phi$ , corresponding to the picked frequency  $f$ , is in turn picked. The bulk phase shift  $\Delta\phi_K$  is simply obtained from the phase difference between stress and strain (Batzle et al., 2006; Madonna and Tisato, 2013), such that the bulk attenuation  $Q_K^{-1} = \tan[\Delta\phi_K]$  is obtained.

During the experiment, the air-conditioning of the experimental room results in an extrinsic oscillation (Fig. 2.3) of low frequency (i.e.  $f \sim 10^{-3}$  Hz). The recorded signal is then filtered in Fourier domain to suppress this noise. As shown for the gypsum sample (Fig. 2.4a), after filtering, stress and strain oscillations have the same frequency  $f$ . Because strain is negative in compression, stress and strain are in phase opposition.

Under purely isotropic conditions, the Low Frequency (LF) bulk modulus  $K_{LF}$  is obtained from measured stress  $\Delta P_c$  and strain  $\Delta\epsilon_v$  such that  $\Delta P_c = K_{LF} \cdot \Delta\epsilon_v$ .  $K_{LF}$  is obtained by a linear regression constrained with a 99% confidence interval. The data scatter around this linear regression is used to infer a statistical error, noted  $\Delta K_{LF}$ . An example is reported (Fig. 2.4b) for the three standard samples measured under the same conditions of (i) a low confining pressure (i.e.  $P_c = 1$  MPa); and (ii) an oscillating pressure of  $\Delta P_c = 0.2$  MPa at a frequency of 0.1 Hz. Because the signal-to-noise ratio decreases when the strain amplitude decreases, thus decreasing the strain gauge accuracy, the error is larger for the stiffer Glass and Gypsum than for the soft Plexiglass. Yet, this statistical error remains lower than about

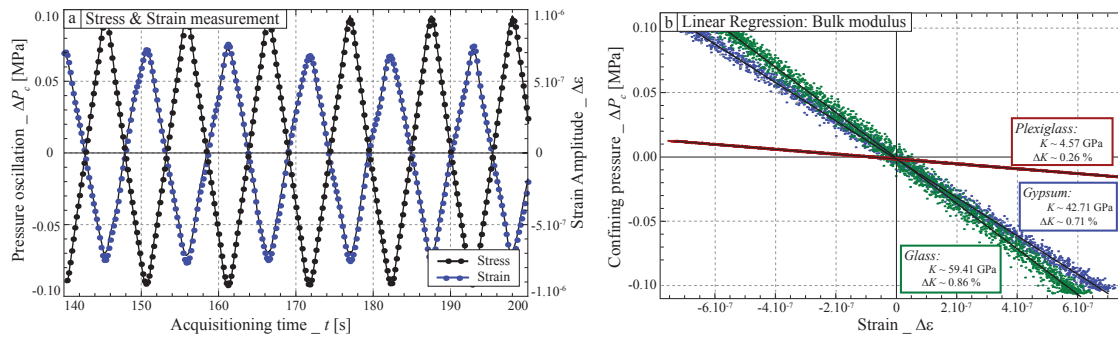


**Figure 2.4 :** Example of stress-induced strain oscillations at a frequency of  $f = 0.1$  Hz and a confining pressure of  $P_c = 1$  MPa : (a) stress (i.e. black) and induced strain (i.e. blue) oscillations for the gypsum sample ; and (b) linear regressions for the three standard samples. The  $\Delta K_{LF}$  values correspond to the statistical error on the measured  $K_{LF}$ .

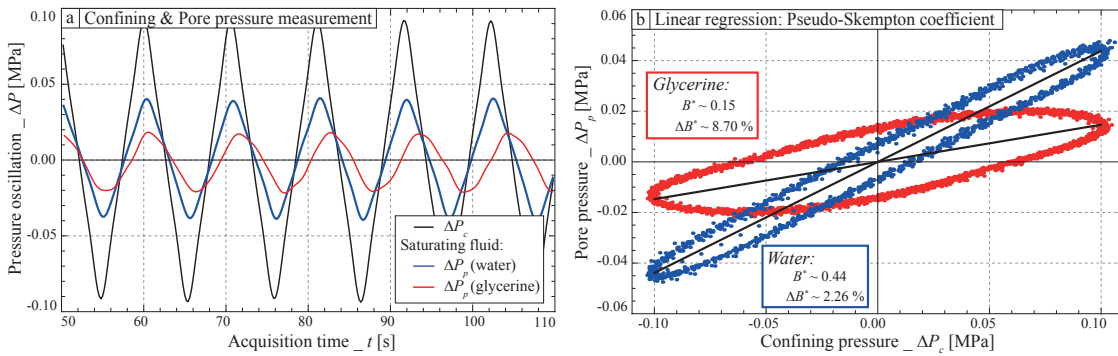


**Figure 2.5 :** Example of stress-induced pore pressure oscillations at  $f = 0.1$  Hz and  $P_{eff} = 1$  MPa for the water- and glycerine-saturated Fo9 : (a) confining (i.e. black) and induced pore (i.e. blue and red) pressure oscillations ; and (b) linear regressions for the water (i.e. blue) or glycerine (i.e. red) saturations.

1% of the measured modulus.

### 2.2.3.3 Pore pressure measurement

Again, the temperature oscillation is filtered to obtain the pore pressure oscillations measurements. An example is shown (Fig. 2.5) for Fo9 fully saturated by either water or glycerine. Pore pressure oscillations (i.e.  $\Delta P_p$ ) can be measured (Fig. 2.5a) for a given effective pressure and frequency.

From  $\Delta P_p$  measurements under purely isotropic oscillations it is possible to obtain a pseudo-Skempton coefficient ( $B^*$ ) of our undrained system (i.e. *Sample + Dead Volume*) such that  $\Delta P_p = B^* \cdot \Delta P_c$ . Because the undrained volume corresponds to  $(V_p + V_d)$ , and not  $V_p$  only, this coefficient  $B^*$  may not equal  $B$ . Using a linear regression, with a 99% confidence interval,  $B^*$  is obtained (Fig. 2.5b). It is clear from figure 2.5b that an hysteresis is present. This means that there is a phase shift between  $\Delta P_c$  and  $\Delta P_p$ . The data scatter around this linear regression, noted  $\Delta B^*$ , is in fact directly related to this phase shift.

Measuring pore pressure oscillation at the outlet of the dead volume implies that the

overpressure caused in the poral fluid by the oscillation induces a fluid flow out of the sample. In other words, the  $\Delta P_p$  oscillations are induced by a fluid flow out of the sample. Conversely, if no fluid pressure oscillations  $\Delta P_p$  are observed, the implication is that there is no time for fluid to flow out of the sample into the dead volume, i.e. the sample is undrained. Note that, for same effective pressure (i.e.  $P_{eff} \sim 1$  MPa) and oscillating frequency (i.e.  $f \sim 0.1$  Hz), the pore pressure response shows a dependence to the saturating fluid in case of Fo9 (Fig. 2.5b). This difference exists for  $B^*$  and  $\Delta B^*$ . It simply implies that, under the same measuring conditions, less fluid flow is allowed in case of glycerine saturation, and that the phase shift is larger. This is consistent with a higher viscosity value for glycerine as compared to water.

## 2.3 Calibration Results

The detailed procedure and processing methods are first tested on the three reference/standard samples in order to assess the behaviours of both apparatus and oscillating system, and thus the accuracy of the reported measurements.

### 2.3.1 Limitations of the apparatus

The oscillating system is first tested to determine the range of pressure values that give reliable data. In particular, one needs to check that strain amplitudes are low enough to avoid inelastic effects. As discussed by Winkler and Murphy III (1995), dependence of elastic properties on amplitude could be observed even at strain amplitudes as low as  $\Delta\epsilon \sim 10^{-6}$  (Winkler, 1985). Yet, these inelastic effects prove to be negligible (i.e. less than about  $\sim 1\%$ ) for strain amplitudes lower than about  $\Delta\epsilon \sim 10^{-5}$  (See Fig.6 from Winkler and Murphy III (1995)).

Using plots of  $\Delta P_c-f$  (Fig. 2.6a) and  $\Delta\epsilon_v-f$  (Fig. 2.6b), the domain where the apparatus is reliable can be constrained. For this apparatus,  $\Delta P_c$  amplitudes (Fig. 2.6a) originate from pump piston oscillations and thus directly correlate with the frequency of oscillation. As measurements prove not to be accurate for strain variations lower than about  $\Delta\epsilon \sim 3 \cdot 10^{-7}$  (Fig. 2.6b), measuring frequencies higher than about  $f \sim 1$  Hz is out of the reliable range. The domain where inelastic effects are present is also discarded (Fig. 2.6b).

Strains of  $\Delta\epsilon \sim 1 - 3 \cdot 10^{-6}$  have been chosen for the measurements at each confining pressure for all samples. Note that the strains measured in the samples can be predicted knowing their bulk modulus. Sandstones bulk moduli range between about  $K \sim 10$  GPa and  $K_s \sim 38$  GPa, so that, from figure (2.6), the maximum frequency is  $f \sim 0.4$  Hz. Owing to these limitations (Fig. 2.6), the frequency range of interest for the reported experiment on Fontainebleau sandstone samples is  $f \in [4 \cdot 10^{-3}; 4 \cdot 10^{-1}]$  Hz.

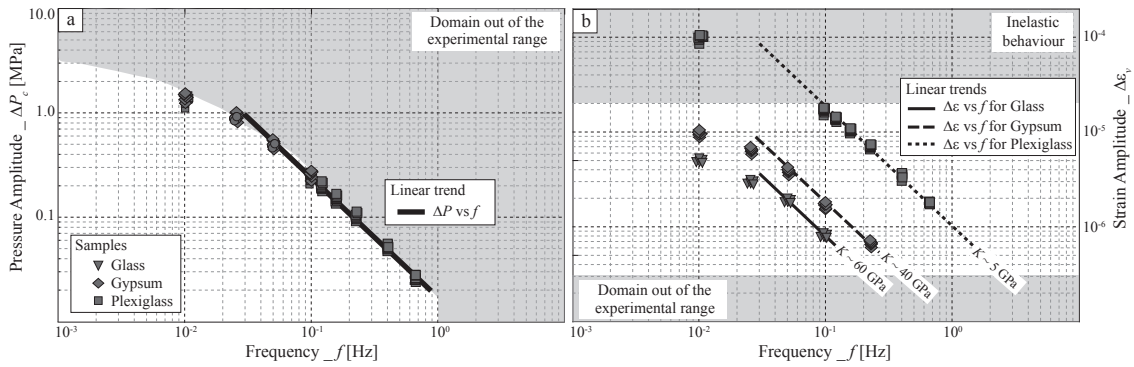


**Figure 2.6 :** Measurement of stress (a) and strain (b) amplitudes for a given frequency. Symbols correspond to measurements on Glass (i.e. triangles), Gypsum (i.e. diamonds) and Plexiglass (i.e. squares). In (a), the gray zone corresponds to a domain out of the experimental range. In (b), the upper grey area corresponds to the inelastic behaviour, and the lower grey area to a domain out of the experimental range.

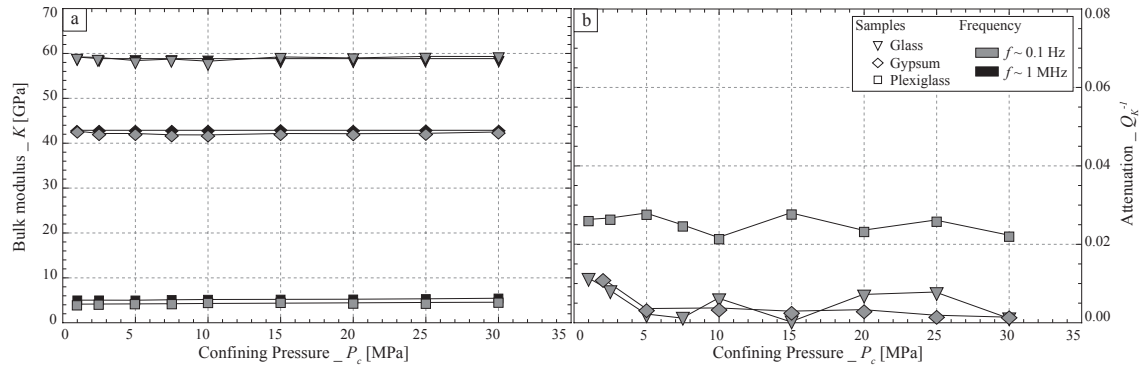


**Figure 2.7 :** Measured Bulk modulus (a) and attenuation (b) on three reference samples for different confining pressures. Low (i.e.  $f = 0.1$  Hz) and High (i.e.  $f \sim 0.5$  MHz) frequencies are represented in grey and black respectively for the samples of Glass (i.e. triangles), Gypsum (i.e. diamonds) and Plexiglass (i.e. squares).

### 2.3.2 Confining pressure effect for the reference samples

As discussed in the experimental procedure,  $K_{LF}$  and  $K_{HF}$  have been measured simultaneously at each confining pressure step starting from  $P_c = 1$  MPa up to  $P_c = 50$  MPa. The measurements at frequencies of  $f \sim 0.1$  Hz and  $f \sim 0.5$  MHz are reported (Fig. 2.7a) as a function of confining pressure. No pressure variation is observed for all three standards (i.e. glass, gypsum and plexiglass). This shows that both LF and HF measurements are reliable at all pressures. Furthermore,  $K_{LF}$  and  $K_{HF}$  have the same values, which are the ones known for these standard samples.

Attenuation has also been measured from the LF periodic signal (Fig. 2.7b). For all confining pressures, values of  $Q_K^{-1} \sim 0.02$  are found for the PMMA, and values of  $Q_K^{-1} \sim 0.01$  are found for both Glass and Gypsum samples. The larger value of the PMMA is consistent with the viscoelastic dispersive properties of this material (e.g., Batzle et al., 2006). Overall, the measurements indicate that the apparatus is able to detect variations as small as  $Q_K^{-1} \sim 0.01$ .

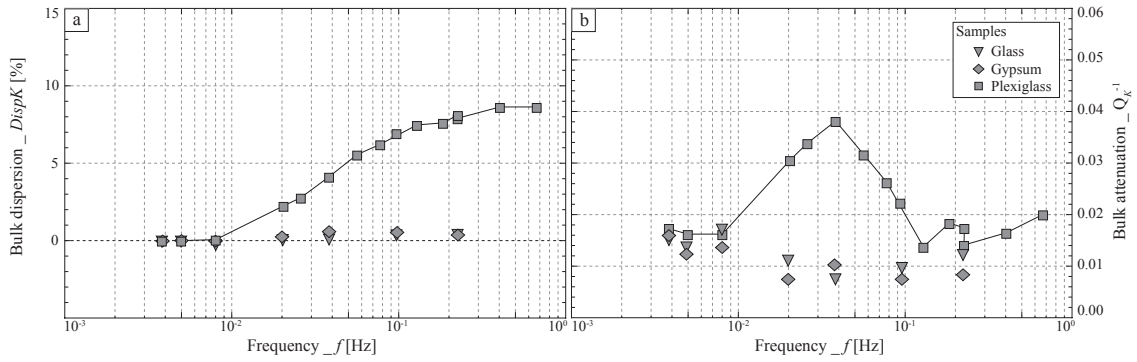


**Figure 2.8 :** Measured Bulk modulus (a) and attenuation (b) on the three reference samples as a function of the oscillation frequency for a confining pressure of  $P_c \sim 1$  MPa.

### 2.3.3 Frequency effect for the reference samples

For a chosen confining pressure, the standard samples have been measured at the different frequencies in the range allowed by the apparatus (i.e.  $f \in [4 \cdot 10^{-3}; 4 \cdot 10^{-1}]$  Hz). As  $K_{LF}$  largely differs from one sample to the other (Fig. 2.7), the values are normalised to evidence a possible frequency effect (i.e. dispersion). The  $K_{LF}$  at the lowest frequencies (i.e.  $K_0$ ) is thus chosen as a reference to define a dispersion coefficient  $DispK_{LF}$  such that :

$$DispK_{LF} = \frac{K_{LF} - K_0}{K_0}. \quad (2.2)$$

The frequency dependence of  $DispK_{LF}$  (Fig. 2.8a) and  $Q_K^{-1}$  (Fig. 2.8b) is presented for the three standard samples, for a fixed confining pressure of 1 MPa. While no variation is observed for glass and gypsum samples, plexiglass  $DispK_{LF}$  values appear to increase with frequency. This evolution directly correlates to a peak in attenuation of  $Q_K^{-1} \sim 0.04$ . All measurements result consistent as (i) glass and gypsum are purely elastic media in the investigated pressure and frequency range ; and (ii) plexiglass is known to be a viscoelastic solid (e.g., Batzle et al., 2006).

Note that, in the case of the plexiglass sample, the measured dispersion (i.e.  $DispK_{LF} \sim 9\%$ ) is a small effect that corresponds to an increase in bulk modulus from 4.32 GPa up to 4.71 GPa at highest frequencies. It implies that the apparatus allows for measurement of effects as small as the one presented here.

## 2.4 Results on Fontainebleau sandstone

Experiments similar to those described for the three standard samples were performed on the two Fontainebleau sandstone samples. These samples are porous, and the measurements were performed at full saturation (i.e. dry, water and glycerine).

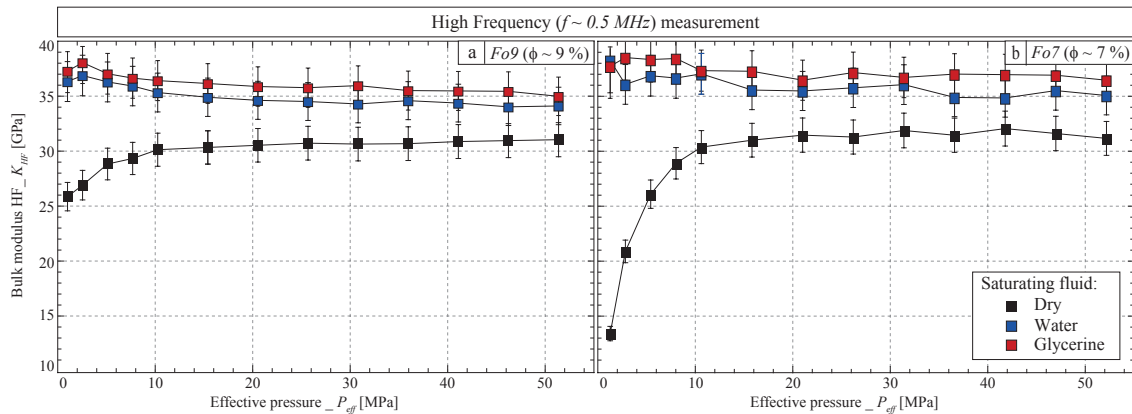


**Figure 2.9** : Measurement of the pressure dependence of Fo9's and Fo7's HF bulk moduli ( $K_{HF}$ ).  $K_{HF}$  is measured for the three different saturating fluids and effective pressures up to about  $P_{eff} \sim 50$  MPa.

### 2.4.1 Pressure dependence of the samples' elastic properties

The HF bulk modulus ( $K_{HF}$ ), inferred from  $V_p$  and  $V_s$ , is reported (Fig. 2.9a-b) as a function of  $P_{eff}$ . Under dry conditions, both samples show a pressure dependent increase in  $K_{HF}$ . Yet, the magnitude in variation is much higher in Fo7, starting from  $\sim 14$  GPa at lowest confining up to  $\sim 33$  GPa at 50 MPa. Under both water and glycerine saturation, however, a small decrease in  $K_{HF}$  is inferred for an increase in effective pressure. This small decrease remains smaller than the error of measurement, so that we may consider the  $K_{HF}$  of these fluid-saturated samples to be constant with pressure.

LF bulk modulus ( $K_{LF}$ ) and attenuation ( $Q_K^{-1}$ ) were obtained from pressure oscillations  $\Delta P_c$  at  $f \sim 0.1$  Hz following the same protocol as above. For both rocks, the measured  $K_{LF}$  (Fig. 2.10a-b) and  $Q_K^{-1}$  (Fig. 2.10c-d) are reported as a function of effective pressure. Overall, one observes a clear dependence to both effective pressure and fluid nature. Both samples show very similar behaviours. Under dry conditions, the measured  $K_{LF}$  (Figs. 2.10a & 2.10b) and  $K_{HF}$  (Figs. 2.9a & 2.9b) have similar values and follow the same pressure dependence in the range of  $P_{eff} \in [1 - 50]$  MPa. A larger pressure dependence is measured in Fo7. Beyond  $P_{eff} \sim 10$  MPa, the pressure dependence is negligible for Fo9 and very small for Fo7.

In fluid saturated conditions,  $K_{LF}$  (Figs. 2.10a & 2.10b) and  $K_{HF}$  (Figs. 2.9a & 2.9b) have different values. For both glycerine and water saturations,  $K_{HF}$  values are higher and almost not fluid or pressure dependent. On the reverse,  $K_{LF}$  varies with effective pressure and its values are different in water- or glycerine-saturated conditions. The difference between dry and water-saturated LF values is very small. In the glycerine-saturated case,  $K_{LF}$  value is higher. Beyond 10 MPa, the pressure dependence is negligible for Fo9 and very small for Fo7.

$K_{LF}$  plots (Figs. 2.10a & 2.10b) tightly correlate to the attenuation  $Q_K^{-1}$  plots (Figs. 2.10c & 2.10d). In particular, (i) no attenuation is observed for dry and water-saturated conditions; and (ii) a large increase in attenuation under glycerine saturation is observed at low

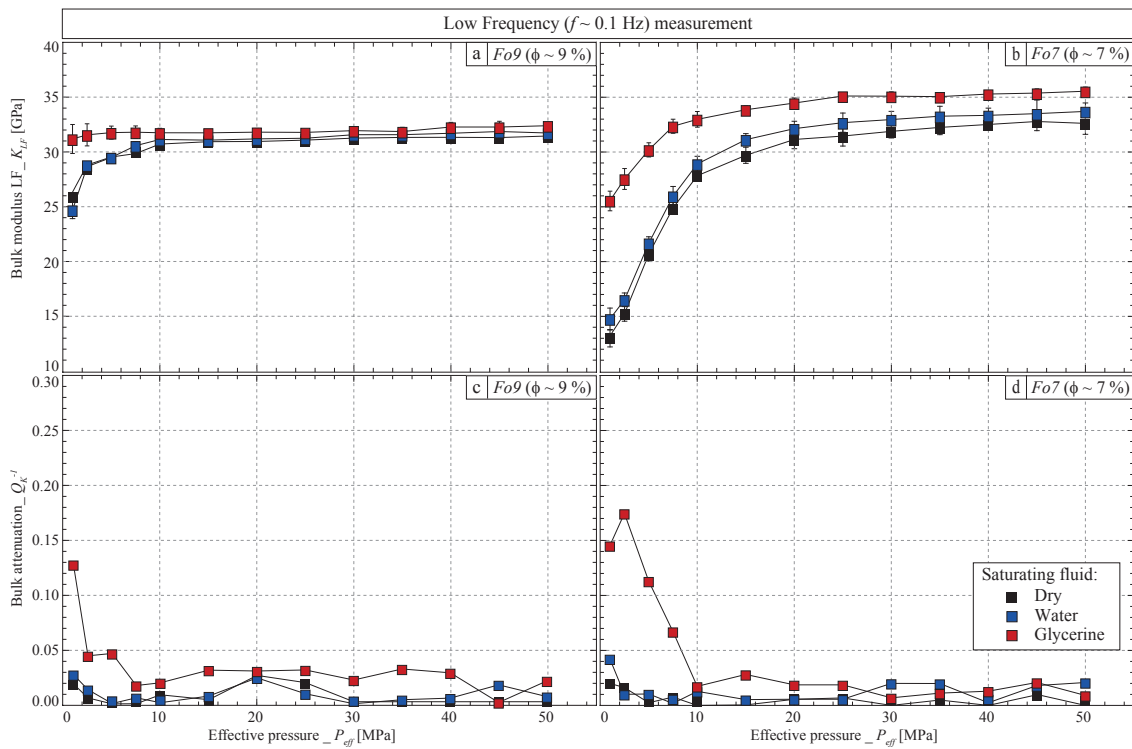


**Figure 2.10** : Measurement of the pressure dependence of Fo9 and Fo7 LF elastic properties. For both samples, the LF bulk moduli  $K_{LF}$  (a & b) and attenuation  $Q_K^{-1}$  (c & d) are measured for the three different saturating fluids for effective pressures up to about  $P_{eff} \sim 50$  MPa.

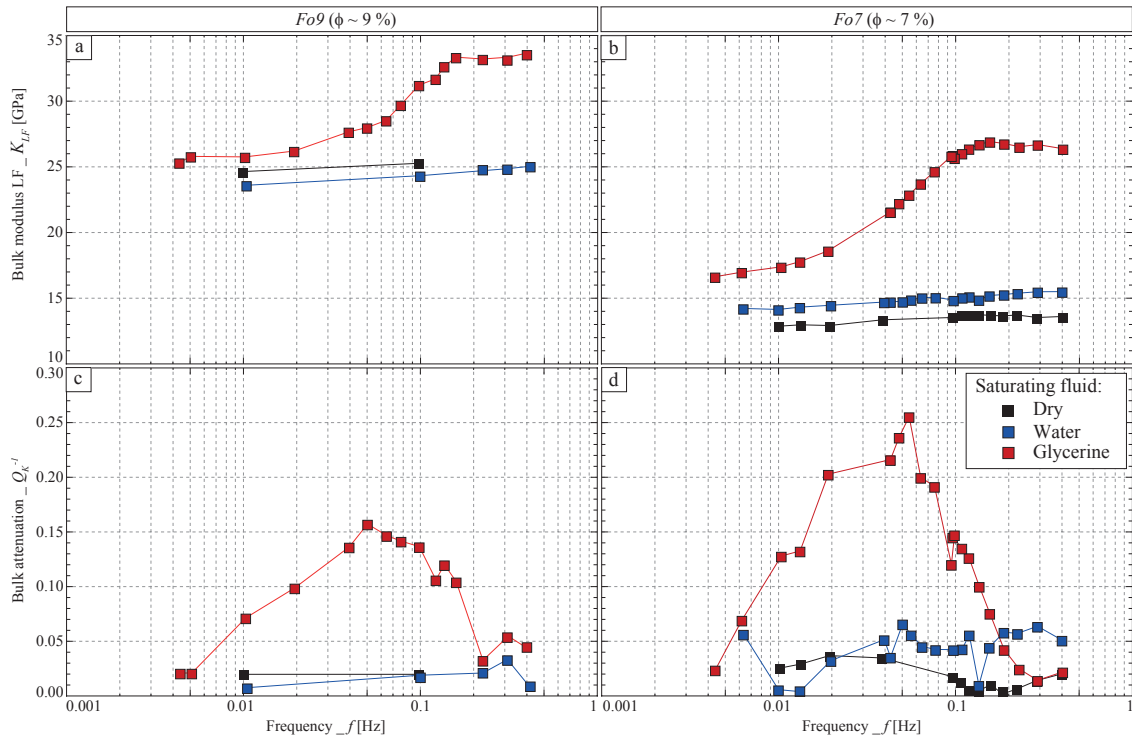


**Figure 2.11** : Measurement of the frequency dependence of Fo9 and Fo7 elastic properties at  $P_{eff} \sim 1$  MPa. For both samples, the bulk modulus  $K_{LF}$  (a & b) and attenuation  $Q_K^{-1}$  (c & d) are measured for the three different saturating fluids in the frequency range of  $f \in [4.10^{-3}; 4.10^{-1}]$  Hz.

effective pressures (i.e.  $P_{eff} < 10$  MPa).

## 2.4.2 Frequency dependence in the LF range at 1 MPa

At a fixed pressure (i.e.  $P_{eff} \sim 1$  MPa),  $K_{LF}$ ,  $Q_K^{-1}$  and  $B^*$  have been measured over the frequency range of  $f \in [4.10^{-3}; 4.10^{-1}]$  Hz allowed by the apparatus (Fig. 2.6).

### 2.4.2.1 Strain measurement : $K_{LF}$ and $Q_K^{-1}$

For both samples, the effects of the different fluids full-saturation on the LF bulk moduli  $K_{LF}$  (Figs. 2.11a & 2.11b) and attenuations  $Q_K^{-1}$  (Figs. 2.11c & 2.11d) are compared. As in the pressure dependence study (Fig. 2.10), measurements under glycerine saturation differ from the ones under dry or water-saturated conditions.

Almost no frequency dependence is observed on  $K_{LF}$  (Figs. 2.11a & 2.11b) under dry and water-saturated conditions, and both Fo7 (i.e.  $K_{LF} \sim 14$  GPa) and Fo9 (i.e.  $K_{LF} \sim 25$  GPa) values are constant. On the reverse, a large frequency dependence is observed for the glycerine-saturated samples. In this last case,  $K_{LF}$  increases with frequency up to a value of 34 GPa for Fo9 and 26 GPa for Fo7 at  $f \sim 4.10^{-1}$  Hz.

These results correlate well with  $Q_K^{-1}$  data (Figs. 2.11c & 2.11d). The measured  $Q_K^{-1}$  show very low values and almost no variation under dry or water-saturated conditions. On

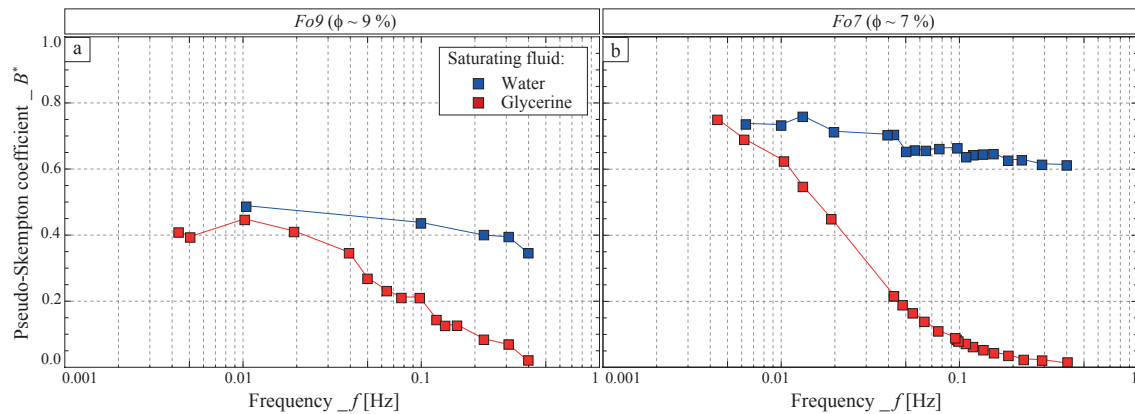


**Figure 2.12** : Measurement at  $P_{eff} \sim 1$  MPa of the frequency dependence of the pseudo-Skempton coefficients  $B^*$  in Fo9 (a) and Fo7 (b) saturated by either water (i.e. blue symbols) or glycerine (i.e. red symbols).

the reverse, a large frequency-dependent variation is observed under glycerine saturation. For this case, an attenuation peak of  $Q_K^{-1} \sim 0.15$  and  $Q_K^{-1} \sim 0.25$  is observed for Fo9 and Fo7 respectively at intermediate frequencies.

#### 2.4.2.2 Pore pressure variations

The frequency dependence of  $B^*$  is reported (Figs. 2.12a & 2.12b) for the water- and glycerine-saturated conditions. For both samples, the measured  $B^*$  values under water saturation differ from the ones under glycerine-saturated conditions. In the water-saturated case,  $B^*$  is almost constant for both samples. In the glycerine-saturated case,  $B^*$  values show a large decrease with frequency, down to about 0 at higher frequencies.

Under water-saturated conditions, the pressure oscillations are observed for all frequencies in the dead volume. It implies that a fluid-flow in and out of the sample occurs under water-saturation whatever the frequency is. Under glycerine-saturated conditions, while the pressure oscillations are observed in the dead volume at lower frequencies, no oscillations are transmitted to the dead volume as  $f$  approaches 0.4 Hz. In agreement with that observation, one notes that, for both rocks, the frequency dependent variations in  $B^*$  (Fig. 2.12) directly correlate with the independently measured increase in  $K_{LF}$  (Fig. 2.11) in both glycerine-saturated samples. It implies that fluid is less and less squeezed out from the sample to the pipes' volume as frequency increases, up to a frequency for which no fluid is allowed to flow out of the sample. In other words, the samples are undrained at these higher frequencies.

#### 2.4.3 Frequency dependence in the LF range at four effective pressures

The measurements have been done for Fo7 for which the frequency dependence has been found to be the largest (Figs. 2.11 & 2.12). The frequency dependent properties are measured for  $P_{eff} = [1; 2.5; 10; 30]$  MPa.

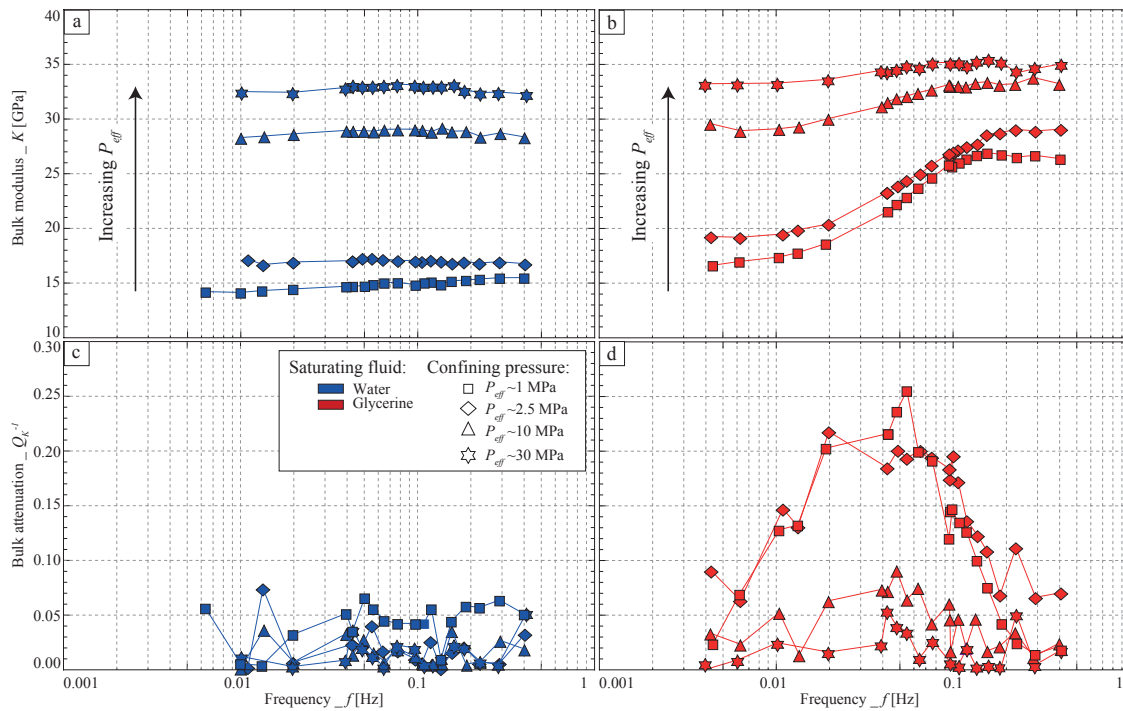


**Figure 2.13** : Measurement of the frequency dependence of Fo7 elastic properties under water (i.e. blue symbols) or glycerine (i.e. red symbols) saturations for 4 different confining pressures. LF bulk modulus  $K_{LF}$  (a & b) and attenuation  $Q_K^{-1}$  (c & d) are measured at the different frequencies allowed by the apparatus for the three different fluids.

#### 2.4.3.1 Strain measurements : $K_{LF}$ and $Q_K^{-1}$

A strong pressure dependence is measured for the water-saturated  $K_{LF}$  (Fig. 2.13a). Again, no frequency dependence is observed. At low frequencies, all glycerine-saturated  $K_{LF}$  (Fig. 2.13b) have values close to the water-saturated ones. Increasing the frequency leads to an increase in the glycerine-saturated  $K_{LF}$  values. This frequency dependence is largely damped by the increase in effective pressure. However, at all effective pressures, the variation takes place in the same frequency range.

Again, the measured frequency dependences of  $K_{LF}$  and  $Q_K^{-1}$  show a good correlation. The water-saturated  $Q_K^{-1}$  (Fig. 2.13c) is low ( $< 0.05$ ) for all effective pressures. Under glycerine saturation (Fig. 2.13d), a large frequency dependent attenuation peak is measured. Increasing the effective pressure results in a clear  $Q_K^{-1}$  decrease.

#### 2.4.3.2 Pore pressure variations

For both water- and glycerine-saturated conditions, a large decrease in  $B^*$  (Figs. 2.14a & 2.14b) is measured when increasing effective pressure. As for the measured  $K_{LF}$ , for a given effective pressure,  $B^*$  values measured under glycerine saturation at lowest frequency are close to the water-saturated (Fig. 2.14a) ones. Only in the glycerine saturated case (Fig. 2.14b),  $B^*$  shows a large decrease with frequency. This frequency dependence decreases

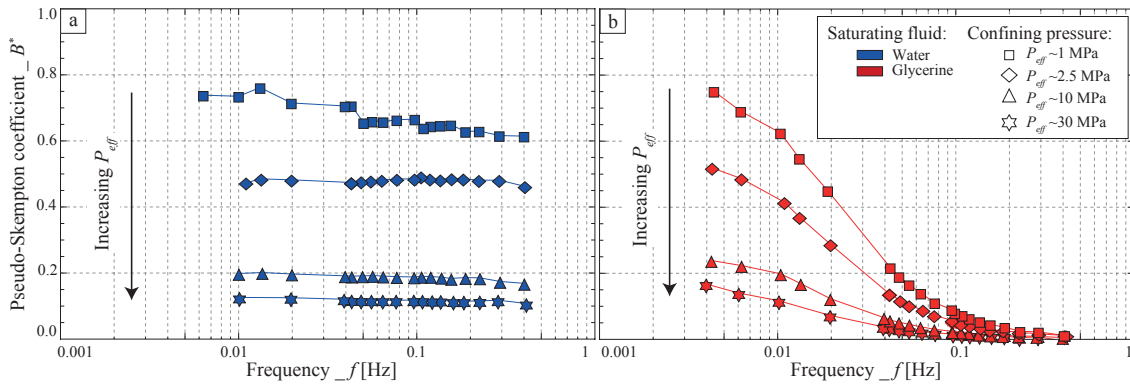


**Figure 2.14** : Measurement of the frequency dependence of the Pseudo-Skempton coefficients  $B^*$  in Fo7 saturated by either water (a) or glycerine (b) for 4 different effective confining pressures.

with increasing effective pressure because the magnitude of  $B^*$  decreases.

Comparing the measured  $K_{LF}$  (Figs. 2.13a & 2.13b) and  $B^*$  (Figs. 2.14a & 2.14b) shows a direct correlation between both the frequency and pressure dependence. The observed pressure and frequency dependence of  $B^*$  correspond to a decreasing fluid flow out of the sample with increasing frequency and effective pressure.

## 2.5 Interpretation

### 2.5.1 Rock physics framework

Dispersion and attenuation effects in porous rocks have been discussed by Cleary (1978) in terms of three fluid-flow regimes (Fig. 2.15a). The transitions between these flow regimes are characterised by two critical frequencies, which values depend on the specific rock/fluid system (Sarout, 2012). Using Zener viscoelastic model (e.g., Nowick and Berry, 1972), the  $K$  and  $Q_K^{-1}$  expected behaviours for these two transitions is summarised in figure (2.15b).

At low frequencies, following Cleary (1978), one can expect to observe the drained and undrained regimes of quasistatic poroelasticity (Gassmann, 1951). Biot-Gassmann equation relates the undrained elastic modulus  $K_u$  to the drained bulk modulus  $K_d$ , the sample porosity  $\phi$ , the fluid bulk modulus  $K_f$  and the skeleton (i.e. quartz in our case) bulk modulus  $K_s$  such that (Gassmann, 1951) :

$$K_u = K_d + \frac{\alpha^2 K_f}{\phi + (\alpha - \phi) \frac{K_f}{K_s}}, \quad (2.3)$$

where  $\alpha$  is the Biot coefficient, defined as  $\alpha = 1 - \frac{K_d}{K_s}$ .

The drained regime is that of a macroscopic fluid flow. Typically, that means a fluid flow over one wavelength at the field scale. Because at low frequencies the wavelength is large (i.e. a few km at 1 Hz) and the rock permeability is low, seismic waves cannot "see"

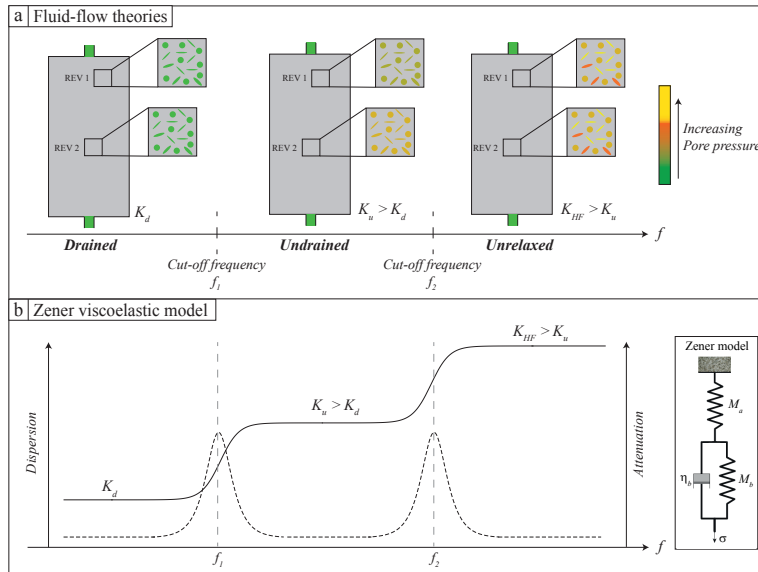


**Figure 2.15 :** (a) Schematic view of the three elastic regimes for a fully-saturated rock : Drained, Undrained and Unrelaxed. Each transition between two regimes corresponds to a critical frequency  $f$ . (b) Schematic representation of the dispersion and attenuation expected from a fluid-flow mechanism between Drained, Undrained and Unrelaxed domains.

this regime. At the laboratory scale however, the forced oscillations mode can correspond to a drained regime because the sample length  $L$  is much smaller than the wavelength  $\lambda$ . As discussed by Cleary (1978), the time constant for fluid flow over the sample length  $L$  depends on the hydraulic diffusivity ( $d$ ) :

$$d = K_d \frac{k}{\eta}, \quad (2.4)$$

where  $k$  is the rock permeability and  $\eta$  is the fluid viscosity. It results that the critical frequency for the drained/undrained transition is  $f_1 = d/(L/2)^2$ , or :

$$f_1 = \frac{4kK_d}{\eta L^2}. \quad (2.5)$$

At higher frequencies, poroelasticity may not be applicable. This will be the case if the REV (Representative Elementary Volume) is not isobaric, i.e. the fluid has not enough time to reach an isobaric state within a REV. In that case, a third flow regime is present that is called "unrelaxed". Since, in general, a porous rock contains inclusions of different shapes (i.e. pores and microcracks), fluid can flow from a compliant microcrack to a neighbouring less compliant pore (O'Connell and Budyanskiy, 1977). This squirt-flow phenomenon is associated with a critical frequency that depends on  $K_d$ , on the microcrack aspect ratio  $\zeta$  and

on the fluid viscosity  $\eta$  such that (O'Connell and Budiansky, 1977) :

$$f_2 = \frac{\zeta^3 K_d}{\eta}. \quad (2.6)$$

Note that owing to this form,  $f_2$  depends highly on the aspect ratio  $\zeta$  so that, for a given fluid's viscosity, a variation in  $\zeta$  of one order of magnitude would lead to a variation of three order of magnitudes on  $f_2$ . The frequency  $f_2$  corresponds to the undrained/unrelaxed transition, i.e.  $f_2$  cannot be lower than  $f_1$ . This is because the "relaxed" state is that where quasistatic poroelasticity does apply, i.e. the fluid pressure is isobaric within the REV.

## 2.5.2 Interpretation of the frequency effects at 1 MPa

### 2.5.2.1 Accounting for fluid and frequency through the "apparent frequency" concept

As shown above,  $f_1$  (Eq. 3.1) and  $f_2$  (Eq. 3.2) both depend on  $\eta^{-1}$ . The viscosity effect may thus be accounted for in the same manner as frequency (Batzle et al., 2001) by defining an apparent frequency :

$$f_f^* = f \cdot \frac{\eta_f}{\eta_0}, \quad (2.7)$$

with  $\eta_0 = 10^{-3} \text{ Pa.s}^{-1}$ . For the frequency range allowed by the apparatus (i.e.  $f \in [4.10^{-3}; 4.10^{-1}] \text{ Hz}$ ), the range in apparent frequencies is (i)  $f_{wat}^* \in [3.5 \cdot 10^{-3}; 3.5 \cdot 10^{-1}] \text{ Hz}$  for the measurements under water (i.e.  $\eta_{wat} = 0.89 \cdot 10^{-3} \text{ Pa.s}^{-1}$ ) full saturation; and (ii)  $f_{gly}^* \in [4.3 \cdot 10^0; 4.3 \cdot 10^2] \text{ Hz}$  for the measurements under glycerine (i.e.  $\eta_{gly} = 1.087 \text{ Pa.s}^{-1}$ ) full saturation. The corresponding apparent cut-off frequencies  $f_1^*$  and  $f_2^*$  may also be defined within this framework such that :

$$f_1^* = \frac{4\kappa K_d}{\eta_0 L^2}, \quad \& \quad f_2^* = \frac{\zeta^3 K_d}{\eta_0}. \quad (2.8)$$

Using the specific parameters values for our experiments, it is finally possible to calculate these cut-off frequencies for both rocks. The sample water permeabilities and drained bulk moduli at  $P_{eff} \sim 1 \text{ MPa}$  are measured (Tab. 2.1). The diffusion length (i.e.  $L/2$ ) has been chosen as equal to the sample's half length or length (e.g.  $L \sim 40 - 80 \text{ mm}$ ). The aspect ratio values can be inferred from the pressure dependence of the dry moduli (Walsh, 1965). Inferred aspect ratio for Fo9 and Fo7 are of about  $\zeta \sim 1 - 2 \cdot 10^{-4}$  and  $\zeta \sim 4 - 5 \cdot 10^{-4}$  respectively. The resulting properties and deduced cut-off frequencies are given in table 2.1.

It appears directly from table 2.1 that the two samples have different apparent cut-off frequencies. While  $f_1^*$  and  $f_2^*$  are separated by one or two orders of magnitude in the case of Fo7, they fall in a similar range for Fo9. As discussed in the following, this fact is unusual and has important consequences.

**Table 2.1** : Specific properties measured for both samples at an effective pressure of  $P_{eff} \sim 1$  MPa

| Sample #                       | Fo9              | Fo7              |
|--------------------------------|------------------|------------------|
| Porosity ( $\phi$ )            | 8.7 %            | 7.2 %            |
| Diffusion Length ( $L$ )       | 40 – 80 mm       | 40 – 80 mm       |
| Permeability ( $\kappa$ )      | $1.10^{-14} m^2$ | $4.10^{-15} m^2$ |
| Drained Bulk modulus ( $K_d$ ) | 25 GPa           | 15 GPa           |
| aspect ratio ( $\zeta$ )       | $1 - 2.10^{-4}$  | $4 - 5.10^{-4}$  |
| Frequency $f_1^*$              | 156 – 625 Hz     | 35 – 140 Hz      |
| Frequency $f_2^*$              | 25 – 200 Hz      | 1000 – 2000 Hz   |

### 2.5.2.2 Case of Fo7 sample : A standard behaviour

Measured values of  $K_{LF}$  and  $Q_K^{-1}$  at  $P_{eff} \sim 1$  MPa are reported as a function of  $f^*$  (Fig. 2.16). An increase in  $K_{LF}$  with  $f^*$  is clearly evidenced.

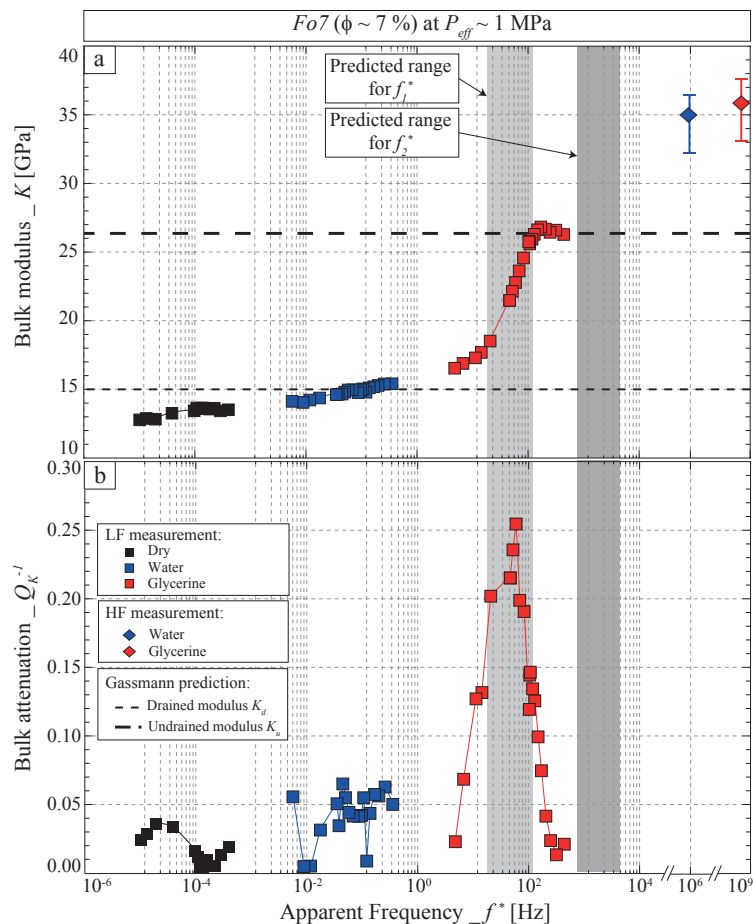


**Figure 2.16** : Fo7 LF bulk (a) modulus  $K_{LF}$  and (b) attenuation  $Q_K^{-1}$  versus  $f^*$  at an effective pressure of  $P_{eff} \sim 1$  MPa. Biot-Gassmann theory for drained and undrained bulk moduli prediction (i.e. dashed lines) and the measured  $K_{HF}$  (i.e. diamonds) are also reported. The ranges for the theoretical cut-off frequencies  $f_1^*$  and  $f_2^*$  are shown by means of greyish zones.

Considering the low  $f^*$  value of  $K_{LF}$  (i.e.  $\sim 15$  GPa) to be the value for the drained modulus  $K_d$ , Biot-Gassmann undrained prediction is  $K_u = 26$  GPa. This value is very close to the measured  $K_{LF}$  at higher apparent frequencies of  $f^* = 200$  Hz. The transition from drained to undrained domains is evidenced in that case. The predicted  $K_u$  and  $f_1^*$  values are consistent with the data. One can conclude that the drained/undrained transition is observed for a critical frequency of  $f_1^* \sim 100$  Hz. This conclusion is further confirmed by both (i) the large attenuation peak of about  $Q_K^{-1} \sim 0.25$  at  $f^* = 100$  Hz; and (ii) the absence of fluid flow out of the sample (i.e.  $B^* \rightarrow 0$ ) at  $f^* = 200$  Hz (i.e. Fig. 2.12b).

From table 2.1, the undrained/unrelaxed transition's cut-off frequency can also be calculated. Its value is  $f_2^* \sim 1$  kHz. The apparatus does not allow to measure  $K_{LF}$  at such a high frequency. Yet,  $K_{HF}$  was measured using the ultrasonic velocity set-up at  $f \sim 0.5$  MHz. Its much higher value (i.e. about  $\sim 34$  GPa) is likely to be related to a transition from undrained to unrelaxed regimes.

### 2.5.2.3 Case of Fo9 sample : An exotic behaviour

Fo9 data measured at  $P_{eff} \sim 1$  MPa are reported as a function of  $f^*$  (Fig. 2.17). Again, a clear increase in  $K_{LF}$  is observed as  $f^*$  increases (Fig. 2.17a).

However, considering the low  $f^*$  value of  $K_{LF}$  (i.e., 25 GPa) to be the value for the drained modulus  $K_d$ , Biot-Gassmann undrained prediction is  $K_u = 29$  GPa. In this case, the Biot-Gassmann prediction underestimates the increase in  $K_{LF}$  with  $f^*$ . In addition, ultrasonic data lead to a  $K_{HF}$  value close to the one of  $K_{LF}$  at  $f^* = 500$  Hz. It implies that no frequency effect exists in the range of  $f^* \in [500 \text{ Hz} - 0.5 \text{ MHz}]$ . This behaviour shows that the bulk modulus increases directly from the drained modulus (at lowest frequency) up to the unrelaxed modulus (at  $f^* \sim 500$  Hz). For this sandstone, the undrained regime does not seem to exist. This behaviour implies that  $f_1^*$  and  $f_2^*$  values overlap in the frequency range of  $K_{LF}$  variation, which is consistent with the values predicted for  $f_1^*$  and  $f_2^*$  (Tab. 2.1). This is unusual since one expects in general  $f_1^* \ll f_2^*$ . This is however because  $L \ll \lambda$  in our case, where  $\lambda$  is the wavelength, so that it can be possible to have a "drained" sample. Our result implies that Fo9 presents a special case for which the undrained regime does not exist (in our experimental conditions). This unusual case has been considered previously by Cleary (1978).

### 2.5.3 Variation of attenuation with frequency

From figures 2.11a and 2.11b, a progressive increase in  $K_{LF}$  with frequency is measured in Fo9 and Fo7 that indicates a progressive transition between domains, and  $Q_K^{-1}$  data show a good correlation with  $K_{LF}$  variations with frequency. At that point, the Zener viscoelastic model (e.g., Nowick and Berry, 1972) can be used. Parameters are the springs moduli  $M_a$  and  $M_b$  and the dashpot viscosity  $\eta_b$  (Figs. 2.15), which can be directly inferred from the

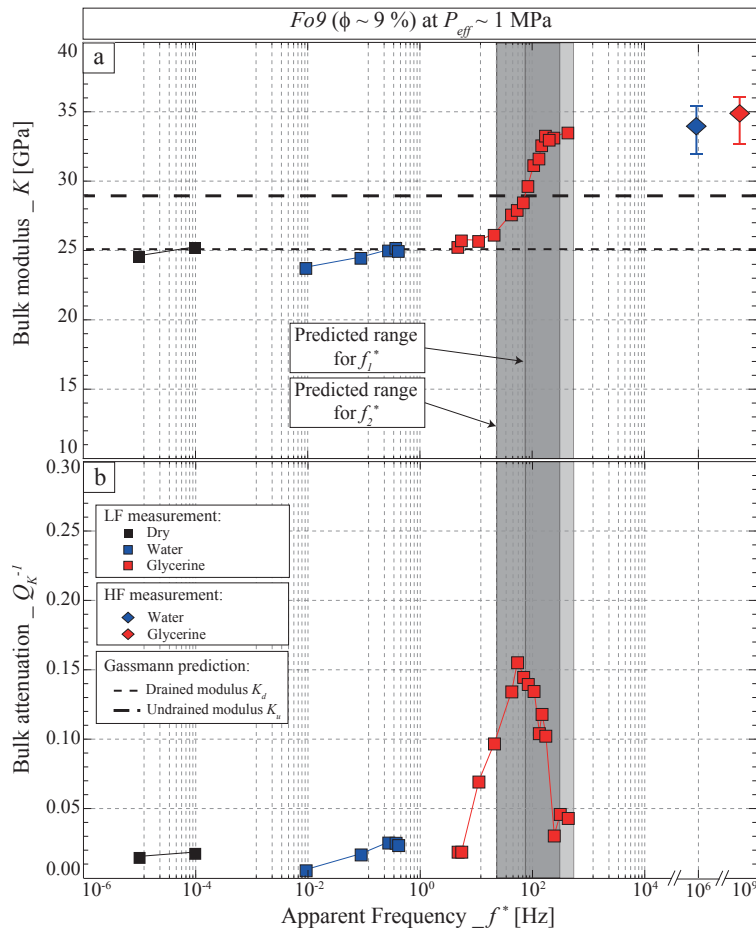


**Figure 2.17** : Fo9 LF bulk (a) modulus  $K_{LF}$  and (b) attenuation  $Q_K^{-1}$  versus  $f^*$  at an effective pressure of  $P_{eff} \sim 1$  MPa. Biot-Gassmann theory for drained and undrained bulk moduli prediction (i.e. dashed lines) and the measured  $K_{HF}$  (i.e. diamonds) are also reported. The ranges for the theoretical cut-off frequencies  $f_1^*$  and  $f_2^*$  are shown by means of greyish zones.

problem's parameters. The dashpot viscosity  $\eta_b$  could be derived from the relaxation time  $\tau_0 = \eta_b / M_b$ , which directly relates to the critical frequency such that  $\tau_0^{-1} = 2\pi f_c$ .

By combining Zener model and Biot-Gassmann prediction, one obtains a possible transition in bulk modulus dispersion and attenuation from drained to undrained conditions (Fig. 2.18).  $M_b$  is taken as the drained modulus  $K_d$ , i.e. 16 GPa and 25 GPa for Fo7 and Fo9 respectively. Knowing  $M_b$ ,  $M_a$  is deduced from the undrained modulus ( $K_u$ ) determined from Biot-Gassmann equation (Eq. 2.3) in the case of glycerine full saturation. A value of  $\eta_b$  is chosen as a best fit of the characteristic frequency of measurements' variations. For Fo7, both  $K_{LF}$  and  $Q_K^{-1}$  variations with frequency indicate a typical Zener-like drained/undrained transition (Figs. 2.18b & 2.18d). For Fo9, however, the Zener-like drained/undrained transition underestimate the dispersion and attenuation measured. This may originate from the overlapping critical frequencies (Tab. 2.1 & Fig. 2.17).

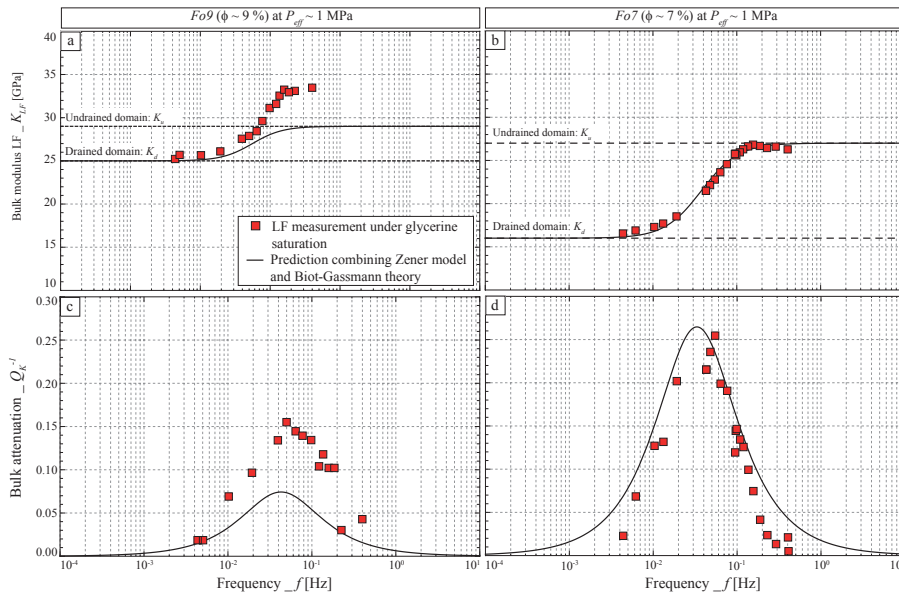


**Figure 2.18** : Comparison between measured and predicted (a) bulk modulus and (b) attenuation variations with frequency in the glycerine-saturated Fo7. The prediction is obtained by combining Zener rheological model and Biot-Gassmann theory.

The Zener model can also be used to describe the transition from undrained to unrelaxed conditions. This result is presented for Fo7 at four different  $P_{eff}$  (Fig. 2.19) : the predicted attenuation curves are obtained assuming that (i) the drained/undrained frequency effect relates to a  $K$  increase from  $K_d$  to  $K_u$  ; and (ii) the relaxed/unrelaxed frequency effect relates to a  $K$  increase from  $K_u$  up to  $K_{HF}$ . At  $P_{eff} \sim 1$  MPa (Figs. 2.18d & 2.19a), predicted and measured attenuation are in good agreement for the first transition. It appears also that  $Q_K^{-1}$  peak due to the drained/undrained transition is larger than the one associated with the relaxed/unrelaxed transition.

Attenuation is progressively damped by the pressure increase up to  $P_{eff} \sim 30$  MPa (Fig. 2.19d). Comparing drained/undrained and relaxed/unrelaxed transitions,  $P_{eff}$  modifies particularly the drained/undrained transition, with a variation in attenuation peak from  $Q_K^{-1} \sim 0.25$  down to about  $Q_K^{-1} \sim 0.03$ . This strong effect of pressure is the result of cracks' closure. The undrained  $K_u$  depends on the drained  $K_d$ , which in turn highly depends on pressure-sensitive cracks (e.g., Guéguen and Kachanov, 2011). As pressure increases,  $K_d$  increases and the difference between  $K_u$  and  $K_d$  decreases. This pressure effect on dispersion corresponding to the drained/undrained is thus expected and implicitly accounted for by Biot-Gassmann theory. Using Zener model proves to be satisfactory. Attenuation peak amplitudes and modulus variations are indeed consistent, and they both decrease when  $P_{eff}$  increases. At higher  $P_{eff}$  values, the agreement between Biot-Gassmann model predictions and data is not as good as at low  $P_{eff}$ . Note however that the effects are much smaller.

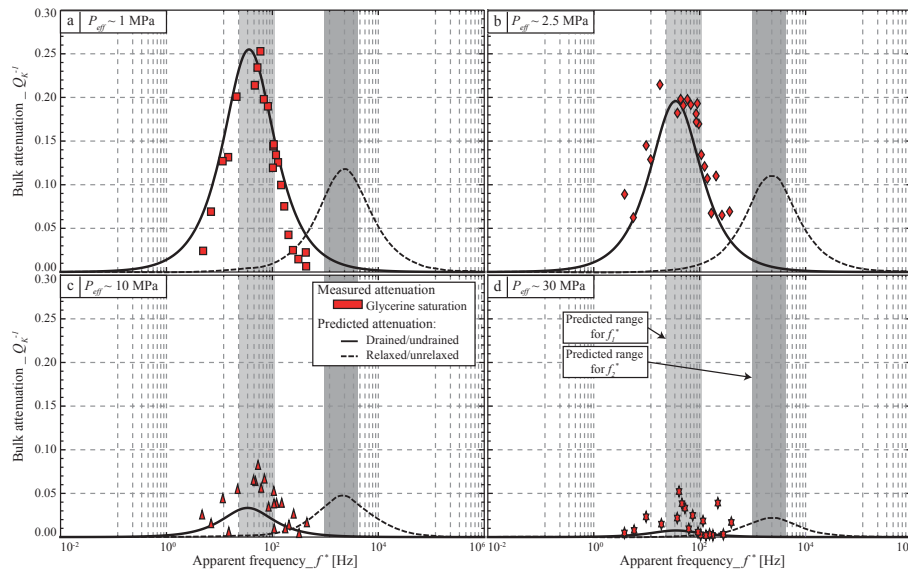


**Figure 2.19** : Comparison between predicted and measured attenuation curves for Fo7 for  $P_{eff} \sim 1$  MPa (a),  $P_{eff} \sim 2.5$  MPa (b),  $P_{eff} \sim 10$  MPa (c) and  $P_{eff} \sim 30$  MPa (d). The theoretical cut-off frequencies are introduced by means of greyish zones.

## 2.6 Conclusion

We report new data on bulk modulus dispersion and attenuation in fully-saturated sandstone samples. The capabilities of the apparatus have been checked using three reference samples : glass, gypsum and plexiglass. The frequency range allowed for the measurement is  $f \in [4 \cdot 10^{-3}; 4 \cdot 10^{-1}]$  Hz. The set-up has been used to measure frequency effects in two Fontainebleau samples of  $\sim 9\%$  (Fo9) and  $\sim 7\%$  (Fo7) porosity. In addition to the measurement under dry conditions, two different saturating fluids have been used : water and glycerine. Owing to their relative viscosities, the apparent frequency range of study has been extended for these sandstone samples to  $f^* \in [3.5 \cdot 10^{-3}; 4.3 \cdot 10^2]$  Hz.

The measured frequency dependence of bulk modulus and attenuation varies with the saturating fluid. Under dry and water-saturated conditions, the sample is fully drained. Under glycerine saturation, a large frequency-dependent increase is measured on both  $K_{LF}$  and  $Q_K^{-1}$ , with attenuation peaks as high as about  $\sim 0.15$  and  $\sim 0.25$  for Fo9 and Fo7 respectively. Confining pressure appears to highly damp these frequency effects. Monitoring the fluid flow out of the samples, in terms of a pseudo-Skempton coefficient, allows to gain further insights on the frequency effect. Fluid is observed to flow out of the samples under water and glycerine saturation at lower frequency, implying that the samples are drained. On the reverse, in glycerine-saturated samples, the flow is observed to decrease with frequency and even vanish at higher frequency. In other words, the samples are undrained.

Combining Zener viscoelastic model and Biot-Gassmann theory, the measurements on the glycerine-saturated samples are compared to predictions for the drained/undrained

transition. Fo7 data are in good agreement with the predictions, implying that the frequency effect measured corresponds to the drained/undrained transition. On the reverse, the prediction clearly underestimates the dispersion and attenuation measured on Fo9, indicating that the measurement can not be strictly related to a drained/undrained transition but involves the relaxed/unrelaxed transition.

Fo7 and Fo9 bulk moduli and attenuation show critical frequency values in agreement with the data. In the case of Fo9, an unusual result is reported : a direct transition from drained to unrelaxed. Attenuation associated with the drained/undrained transition is larger in Fo7 than the one associated with the relaxed/unrelaxed transition (i.e. squirt-flow). Attenuation associated with the drained/undrained transition is more pressure sensitive than the one associated with the relaxed/unrelaxed transition. At  $P_{eff} \sim 30$  MPa, these effects are vanishingly small for both Fo7 and Fo9.

## Acknowledgements

The authors would like to thank Dr. Alexandre Schubnel and Yves Piquier for their help on the experimental set-up. Dr. Maxim Lebedev, Dr. Joel Sarout and an anonymous reviewer are thanked for their constructive comments. The first author also wishes to thank Dr. Pauline Maury for her help on the data processing.



Additional Calibrations & Results

3.1 Measured Ultrasonic properties

3.1.1 Ultrasonic properties of the standard samples

Using a cross-correlation on the ultrasonic waves dominant amplitude, the waves travel-time is measured for the different confining steps on the three standard samples. Using the length correction due to confining pressure, the P- and S-wave velocities are then measured as a function of confining pressure (Fig. 3.1). No pressure dependence is observed on the measurements, which is consistent for these non-porous samples.

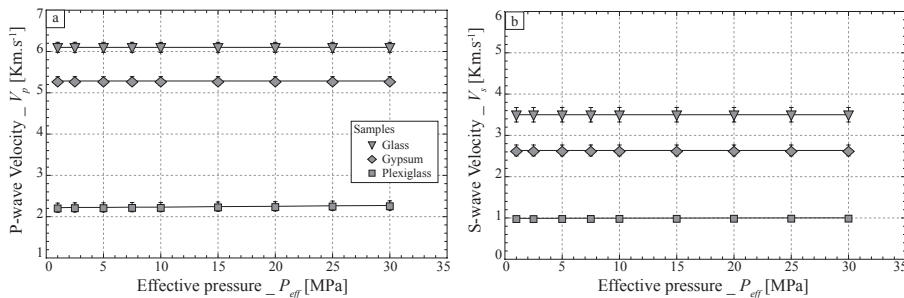
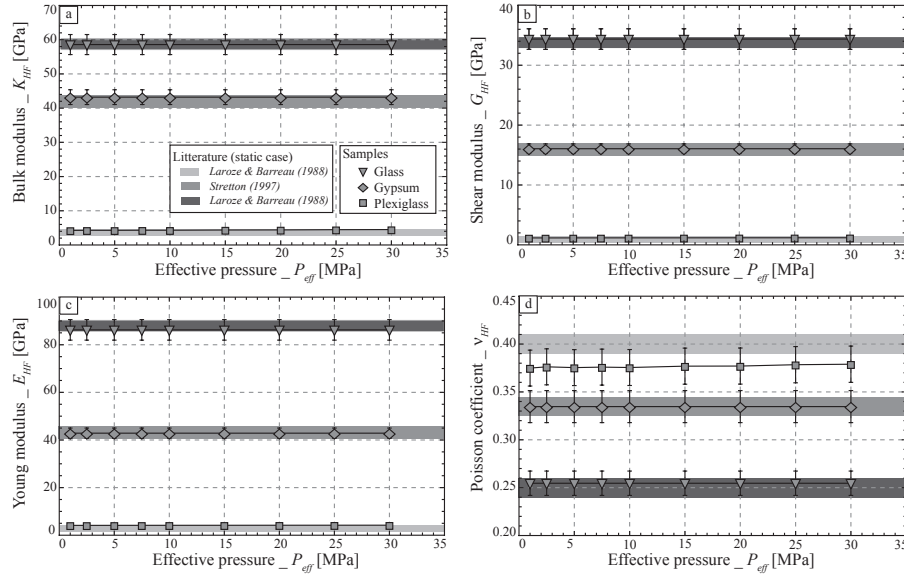


Figure 3.1 : Measured pressure dependent P- and S-wave velocities (a & b) at High Frequency (i.e.  $f \sim 0.5$  MHz) on the three standard samples.

The HF elastic moduli are finally inferred from the the wave velocities using the samples known density by assuming the samples isotropic. While isotropic, purely elastic, solids can be defined from two independent elastic moduli (e.g.,  $K_{HF}$  and  $G_{HF}$ ), four elastic properties may be of interest in terms of mechanical measurements. The bulk modulus ( $K_{HF}$ ), the shear

modulus ( $G_{HF}$ ), and Young modulus ( $E_{HF}$ ) and Poisson ( $\nu_{HF}$ ) ratio are inferred (Fig. 3.2). A comparison with the mechanical/static data from the literature is given for these three standard samples.



**Figure 3.2 :** HF bulk modulus  $K_{HF}$  (a), shear modulus  $G_{HF}$  (b), Young modulus  $E_{HF}$  (c), and Poisson ratio  $\nu_{HF}$  (d) for the three standard samples.

### 3.1.2 Ultrasonic wave velocities for the Fontainebleau samples

As discussed earlier, P- and S-waves arrival times for all effective confining pressures ( $P_{eff}$ ) and fluid conditions (i.e. dry, water- or glycerine-saturations) are measured from an automatic picking of the maximum amplitude of each P- or S-waveform. As a direct consequence, maximum amplitudes (i.e.  $A_p$  and  $A_s$ ) are also obtained from the waveforms. From hand-picking the reference P- and S-waves velocities (i.e.  $V_p$  and  $V_s$ ) at higher confining under dry conditions, the absolute  $V_p$  and  $V_s$  are obtained for all  $P_{eff}$  and saturating conditions. The measurements are reported for both Fo9 (Fig. 3.3) and Fo7 (Fig. 3.4) as a function of  $P_{eff}$  for the three saturating conditions. While the relative cross-correlation measurements lead to accuracies as low as about  $\sim 0.1\%$ , the absolute  $V_p$  and  $V_s$  accuracies are of about  $\sim 1\%$  and  $\sim 3\%$  respectively. The error-bars account for accuracies on the absolute measurements.

Overall, a clear  $P_{eff}$  dependent increase in both amplitudes (Fig. 3.3a & 3.3b) and velocities (Fig. 3.3c & 3.3d) is observed for Fo9 under dry conditions. P-waves (i.e.  $A_p$  and  $V_p$ ) are clearly affected by the introduction of fluid (i.e. water and glycerine). On the reverse, S-waves (i.e.  $A_s$  and  $V_s$ ) show almost no change with the saturating fluid.

The same observations are made for the dry Fo7 amplitudes' (Fig. 3.4a & 3.4b) and velocities' (Fig. 3.4c & 3.4d) dependence to  $P_{eff}$ . Under saturation by water and glycerine,

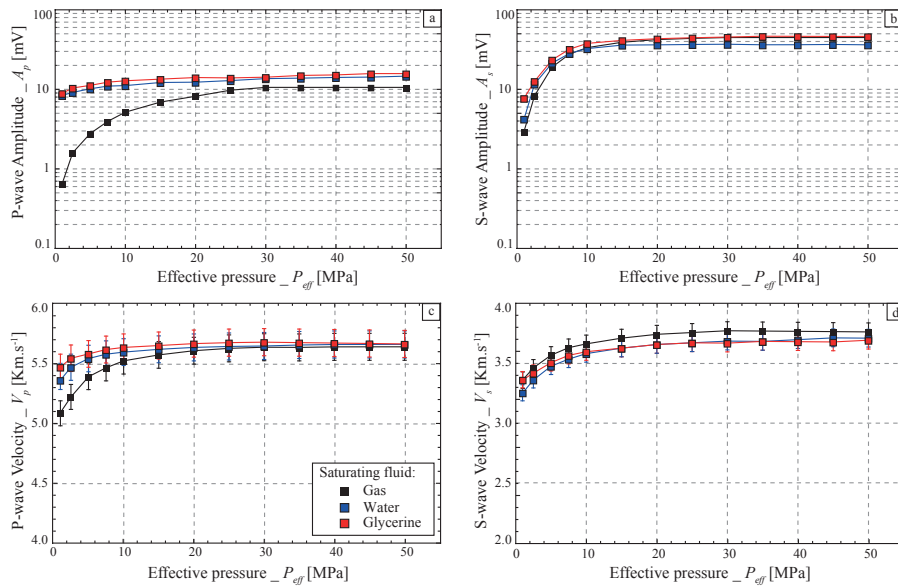


**Figure 3.3 :** Measured pressure dependent P- and S-wave maximum amplitudes (a & b) and P- and S-wave velocities (c & d) at High Frequency on Fo9 for the three different saturating fluids.

$A_p$  and  $V_p$  show again a large increase at low  $P_{eff}$ . However, a deviation from Fo9 behaviour is observed from  $A_s$  and  $V_s$  that show an increase under water- and glycerine-saturation at low  $P_{eff}$ . This difference in behaviours relates to a large density of cracks with thin aspect ratio in Fo7.

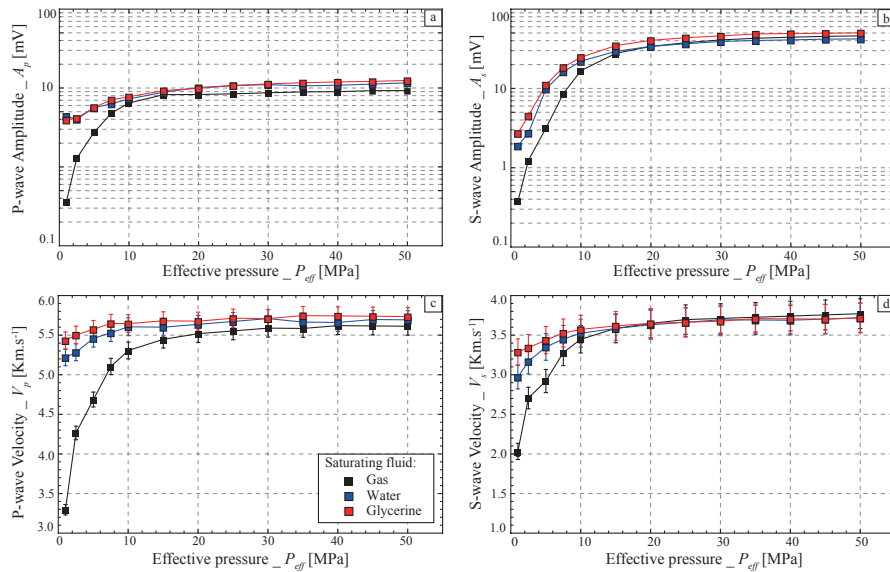


**Figure 3.4 :** Measured pressure dependent P- and S-wave maximum amplitudes (a & b) and P- and S-wave velocities (c & d) at High Frequency on Fo7 for the three different saturating fluids.

### 3.1.3 Porosity variation from confining pressure

As discussed earlier, two important informations are needed prior to deducing elastic wave velocities and HF elastic moduli : the pressure-induced length and porosity (i.e. density) variations of the sample. These can be inferred from the strain measurements during the pressure ramps (Fig. 3.5). Note that, to measure accurately the volume change, the rate of the stress-strain ramp is particularly important when under saturation by an incompressible fluid as the sample needs to remain drained.

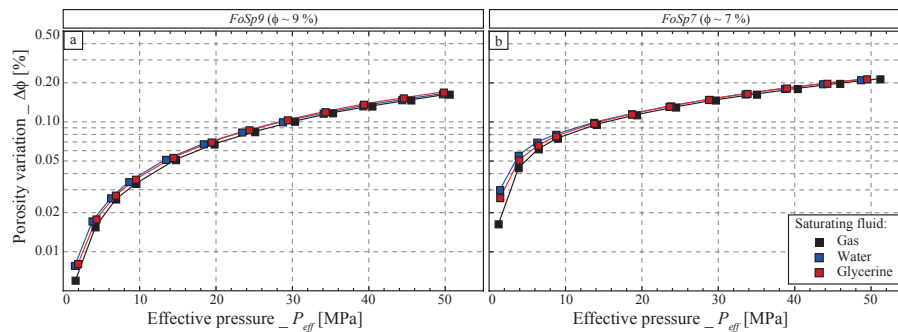


**Figure 3.5** : Measured porosity variations  $\Delta\phi$  with confining pressures on (a) Fo9 and (b) Fo7 for the three different saturating fluids.

As shown in figure 3.5, the porosity variations  $\Delta\phi$  bear almost no dependency on the saturating fluid. It implies that the sample is probably in drained conditions during all stress-strain ramps. Note that  $\Delta\phi$  was plotted in logarithmic scale as to highlight two different variation tendencies of (i) large variations at pressures lower than about  $P_{eff} \sim 20$  MPa, and (ii) constant ones starting from this pressure. This value of slope change may relate to the closure of the more compliant microcracks initially present in the rock.

### 3.1.4 Inferred ultrasonic moduli for the Fontainebleau samples

Assuming the rock isotropic, two independent HF elastic moduli (e.g.  $K_{HF}$  and  $G_{HF}$ ) can then be inferred from the measured  $V_p$  and  $V_s$ . As these moduli are deduced from the ultrasonic wave velocities, they bear much larger measurement errors. As  $G_{HF}$  is inferred from  $V_s$  only, the accuracy on  $V_s$  only affects its absolute value, and is of about  $\sim 6\%$ .  $K_{HF}$  is however inferred from a combination of both  $V_p$  and  $V_s$ . The absolute accuracy on  $K_{HF}$  is thus higher than about  $\sim 8\%$ .

The inferred  $K_{HF}$  (Figs. 3.6a & 3.6b) and  $G_{HF}$  (Figs. 3.6c & 3.6d) are reported for both Fo9 and Fo7 as a function of  $P_{eff}$  for the three saturating conditions. Under dry conditions,  $K_{HF}$  and  $G_{HF}$  of both samples show a typical increase with increasing  $P_{eff}$ , interpreted as the crack closure. Furthermore, under fluid saturation, a large increase is observed on  $K_{HF}$  of both samples.  $G_{HF}$  of Fo9 shows no fluid effect for all  $P_{eff}$ , which is consistent with Gassmann assumption that fluid does not affect the rock effective shear modulus. It

implies that the decrease observed on  $V_s$  is a density effect. Finally,  $G_{HF}$  of Fo7 shows a fluid-strengthening that disappears when increasing  $P_{eff}$ , which is consistent in case of an highly cracked medium.

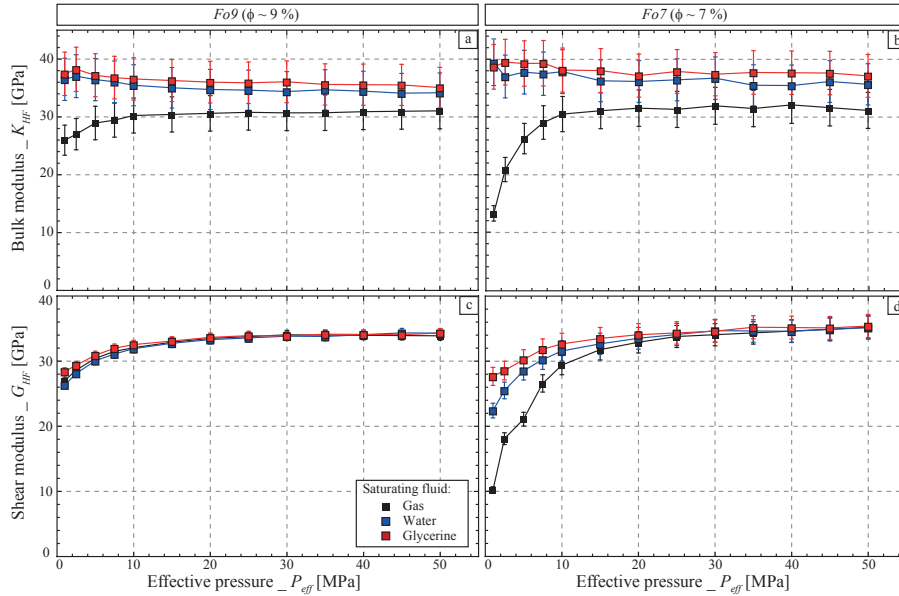


**Figure 3.6 :** Deduced pressure dependent  $K_{HF}$  (a & b) and  $G_{HF}$  (c & d) for Fo9 and Fo7 under three different saturating conditions.

However,  $K_{HF}$  is observed to slightly decrease with increasing  $P_{eff}$ , which is inconsistent with the usual theories. This behaviour is thought to occur from the large measurement error of  $V_s$ .  $K_{HF}$  of both rocks is in the range of  $K_{HF} \in [33;35]$  GPa and  $K_{HF} \in [32;36]$  GPa for Fo9 and Fo7 respectively.

## 3.2 Strain amplitude effects

While the discussion on the role of the strain amplitude was discarded from the main results, it remain of interest to investigate this effect. As stated, this effect leads to small variations only. Furthermore, owing to the system limitations, this strain amplitude effect can only be studied for small stress variations (in order not to spend months for one measurement). A weak material is thus chosen to test such effect : a loosely cemented Fontainebleau sandstone of 18% porosity. The effect is expected to be considerably lower in the well-cemented sandstone samples chosen above.

### 3.2.1 Amplitudes of strains reached

In order to investigate the dependence to the strain amplitude, the sample need to be measured for different values of oscillating pressure  $\Delta P$ . Assuming that the strain ampli-

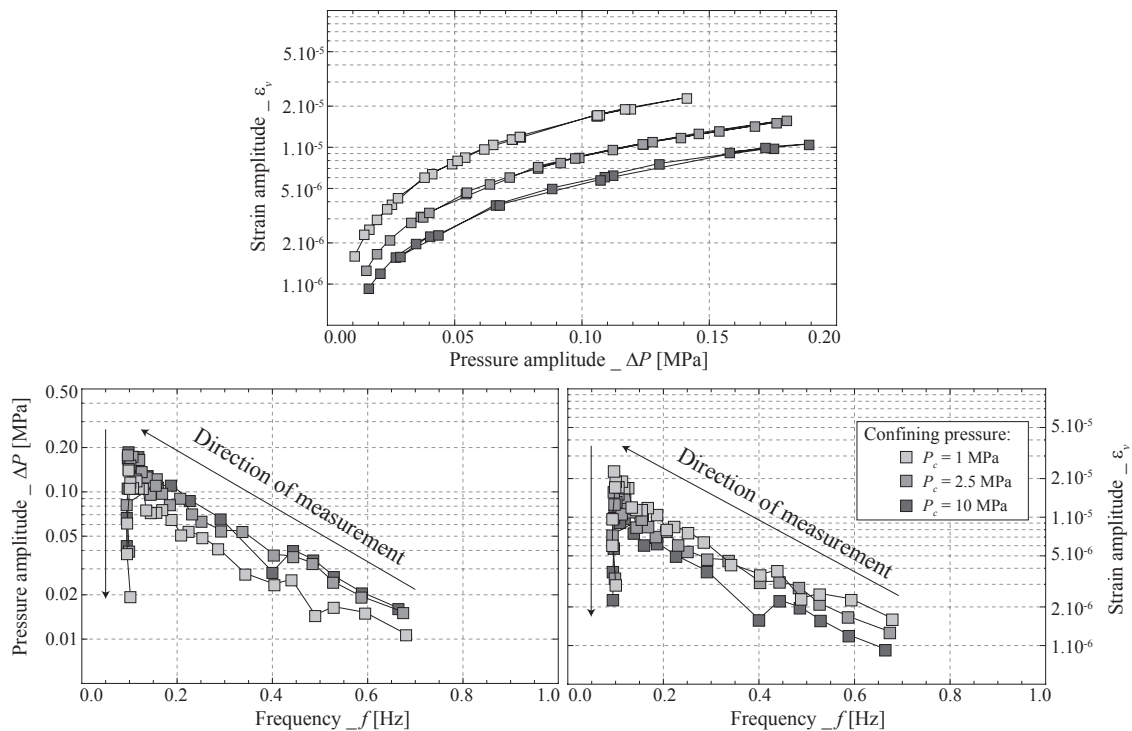


**Figure 3.7 :** (a) Amplitudes in volumetric strains reached for the stress amplitudes applied. Overview of the experimental protocol to test the reversibility of the measured values, highlighted by showing the (b) stresses and (c) strains measured at the different frequencies of measurement. Three confining pressures of  $P_c = [1; 2.5; 10]$  MPa are tested.

tude plays a role, this is expected to occur from slippage at the grain contact. It would then be possible that the grains do not come back to their original place after deforming at a given strain. To check this, two procedures are adopted. First, the starting confining pressure is  $P_c = 10$  MPa, then pressure is decreased to  $P_c = 2.5$  MPa and finally to  $P_c = 1$  MPa for the measurements. Secondly, the properties are measured starting from the lowest pressure amplitudes and then increasing. When the highest amplitude of oscillation is reached, it is again progressively decreased for a same oscillating frequency of  $f = 0.1$  Hz. This second approach also allows to ascertain that the frequency of measurement do not take a role in the amplitude loss. The procedure used for this measurement is illustrated in Fig.3.7.

Plotting first the strain amplitude induced by the applied oscillating pressure amplitude (Fig.3.7a) for the different pressures of measurement shows that (i) the amplitude of the applied stress slightly increases with increasing the confining pressure; and, conversely, (ii) the amplitude of the induced strain decreases as confining pressure increases. Both aspects are consistent. The first possibly occurs from an experimental artefact, i.e. from possibly few gas bubbles in the confining cell's volume. The second from the rock's micro-structure, which is less stress-sensitive as pressure increases. Plotting stress (Fig.3.7b) and strain (Fig.3.7c) amplitudes as a function of the oscillating frequency shows the same

behaviour. The protocol of measurement used is illustrated by an arrow.

### 3.2.2 Effect of the strain amplitude on the rock's elastic response

The resulting bulk modulus of the 18% porosity Fontainebleau sandstone is reported as a function of the applied stress amplitude for the three confining pressures (Fig.3.8a). A consistent increase with increasing confining pressure is observed. The bulk modulus of this rock sample remains particularly low, i.e. from 2 GPa at  $P_c = 1$  MPa up to  $K = 6$  GPa at  $P_c = 10$  MPa. A larger scattering is somewhat observed by increasing the confining pressure, which is within the obtained measurement errors.

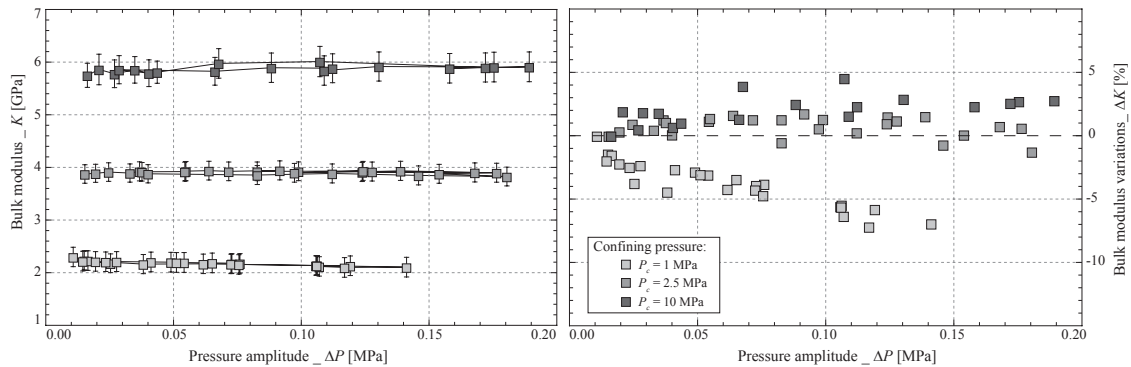


**Figure 3.8** : Dependence to the stress amplitude of the (a) bulk modulus; and (b) relative variation. Three confining pressures of  $P_c = [1; 2.5; 10]$  MPa are tested.

Note however that a small decrease in  $K$  can be observed as the amplitude of the oscillation increases. To better highlight this behaviour, the relative variation  $\Delta K$  as compared to the measurement at lowest stress/strain amplitude is calculated for each confining pressure. This  $\Delta K$  is again reported as a function of the stress amplitude for the three confining pressures (Fig.3.8b). Overall, no tendencies can be observed from the measurements at  $P_c = 2.5$  MPa and  $P_c = 10$  MPa. It implies that no inelastic effect is measured for these two confining pressures. On the reverse, a clear decrease  $\Delta K$  is observed for  $P_c = 1$  MPa. That is independent of frequency is this low frequency range, i.e. it falls in the definition given for an inelastic effect. This inelastic effect thus proves to occur for this rock sample. The decrease is as high as about 7% at higher strain amplitudes, i.e. of about  $2 \cdot 10^{-5}$ . The reason behind the disappearance of this inelastic effect is the intrinsic stiffening effect of confining pressure, i.e. the pressure induces a strength on the grains' contact thus preventing a possible slippage.

As shown from this measurement, inelastic effects related to the large stress/strain amplitudes are expected to occur only in the very loosely cemented samples. For samples holding initially bulk moduli larger than about 10 GPa, such effect would not be measured or would fall in the measurement error of the system.

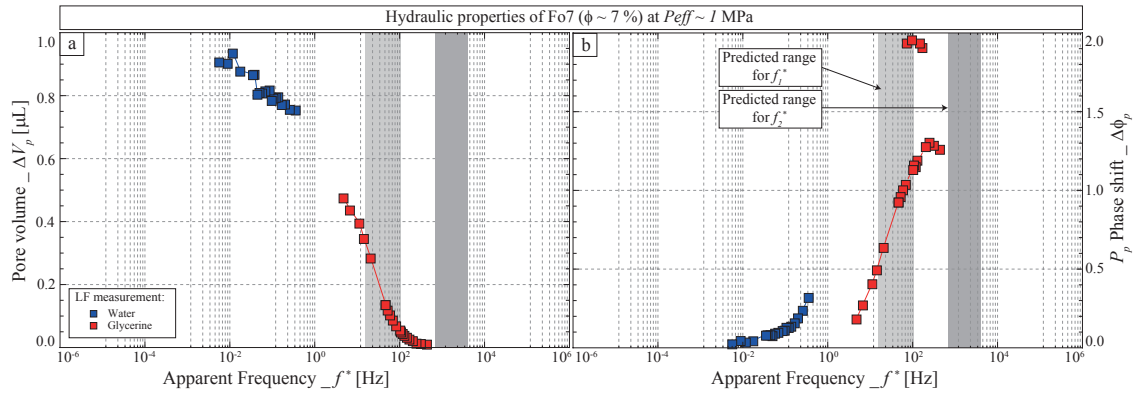


**Figure 3.9 :** Measurement of the dependence to the apparent frequency  $f^*$  of Fo7 pore volume variations  $\Delta V_p$  (a) and pore pressure phase shift  $\Delta\phi_p$  (b) at an effective pressure of  $P_{eff} \sim 1$  MPa. The theoretical cut-off frequencies are introduced by means of greyish zones.

### 3.3 Evidence of a macroscopic fluid flow out of the sample

Note that the pore pressures variations in the dead volume relate to a stress-induced fluid-flow in and out of the sample. The measured  $B^*$  thus relates directly to fluid mass (or volume) oscillations  $\Delta V_p$ . Owing to the small pressure variations (i.e. lower than  $\Delta P_c 0.2$  MPa), the dead volume can consistently be considered incompressible and  $\Delta V_p$  can directly be reached such that :

$$\Delta V_p = V_{tot} \cdot \frac{\Delta P_c \cdot B_p}{K_f}, \quad (3.1)$$

with  $V_{tot} = V_{d1} + V_{d2} + V_p$  the total volume of fluid in the system,  $K_f$  the fluid bulk modulus, and  $\Delta P_c \sim 0.2$  MPa the confining pressure oscillation amplitudes. For Fo7, the pore volume was measured of about  $V_p \sim 7.2$  mL. Note that, as it relates to a normalisation by the fluid intrinsic compressibility, introducing this parameter also allows for a comparison of the sole frequency dependence of water and glycerine saturation measurements.

The resulting pore volume oscillations  $\Delta V_p$ , along with the pore pressure/volume phase shift  $\Delta\phi_p$ , are represented as a function of  $f^*$  in figure 3.9. Furthermore, the predicted cut-off frequencies  $f_1^*$  and  $f_2^*$  are also introduced in the figure.

The pore volume evolution shows a characteristic evolution : (i) for  $f^* < 200$  Hz, large decrease in  $\Delta V_p$  and increase in  $\Delta\phi_p$  are observed that correspond to a change from drained to undrained conditions; and (ii) for  $f^* > 200$  Hz,  $\Delta V_p$  and  $\Delta\phi_p$  reach a plateau at about  $\Delta V_p \sim 0$  and  $\Delta\phi_p \sim 1.3$ . At such stage, no fluid goes out of the sample any more. Note finally from figure 3.9(a) that a large fluid flow is observed below  $f^* < 5$  Hz, with a flow from  $\Delta V_p \sim 1 \mu\text{L}$  to  $\Delta V_p \sim 0.5 \mu\text{L}$ .

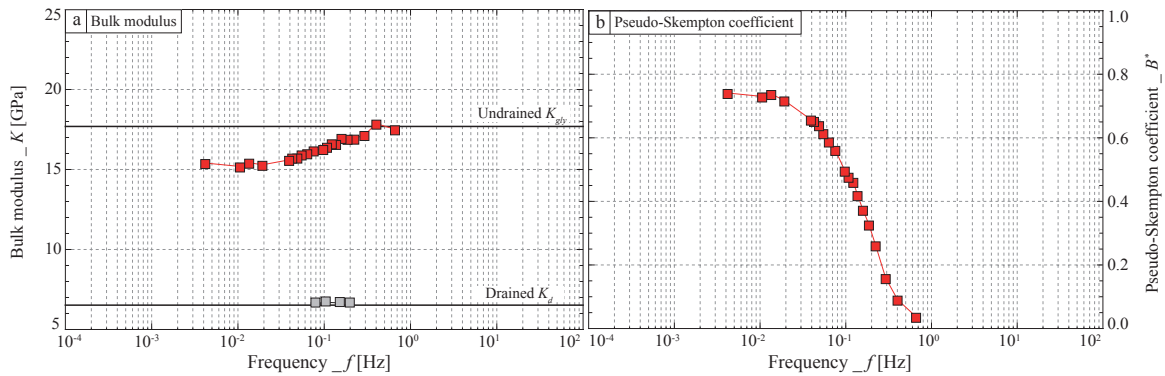


**Figure 3.10** : Measured frequency-dependent (a) bulk modulus and (b) Skempton coefficient of a 19 % Berea sample.

### 3.4 Measurements on a Berea sample

In addition to the Fontainebleau samples, a Berea sandstone sample was also measured. The rock is of about 19 % porosity and  $\kappa = 5 \cdot 10^{-14} \text{ m}^{-2}$  permeability. The sample is measured under dry and glycerine-saturated conditions using low-amplitude confining pressure oscillations (?). Although the sample was measured as a function of pressure and frequency, in a similar way as the Fontainebleau samples reported before, only the frequency dependence for a given  $P_{eff}$  is of interest here. The frequency-dependence of the measured solid (Fig. 3.10a) and hydraulic (Fig. 3.10b) response are reported for an effective pressure of  $P_{eff} = 1 \text{ MPa}$ .

Although the measured  $K_{LF}$  (Fig. 3.10a) remains constant at lowest frequencies, its value is three times larger than  $K_d$ . As frequency increases,  $K_{LF}$  slightly increases, of about 2 GPa, to reach the value of  $K_{ud}$ . In addition, the pseudo-Skempton coefficient  $B^*$  is initially constant, and then decreases as frequency increases to reach a value near zero for  $f \sim 1 \text{ Hz}$ .

Both properties add-up to indicate that the sample is initially drained at lowest frequency. As frequency increases, the transition between drained and undrained regimes is observed. Based on this understanding, the value of  $K_{LF}$  at lowest frequencies is not consistent. It in fact originates from the existing dead volume. Because the Berea sample is very compressible a has a large porosity, it is largely affected by this dead volume.

Note that both attenuation  $Q_K^{-1}$  and fluid pressure phase shift  $\Delta\phi_B$  were also measured for these conditions. Because the results are consistent with both results and interpretations, these are not reported for simplicity.



---

## Conclusion & Perspectives

---

### 4.1 Conclusion

An existing experimental set-up, originally used to measure a quasi-static bulk modulus, has been extensively tested using various standard samples. This work lead to calibration of a protocol allowing to accurately measure the frequency-dependent dispersion and attenuation of samples' bulk modulus in the frequency range of  $f \in [10^3; 10^0]$  Hz. Using this set-up to measure Fontainebleau samples, large dispersions are measured that fully relate to measured attenuations as large as  $Q_K^{-1} = 0.25$ .

An additional procedure has been tested and used : The fluid is allowed to flow in and out of the sample, i.e. the sample is not experimentally undrained. Yet, valves are placed to let an additional fluid volume (i.e. dead volume) near the sample where the variations of pore pressure are measured. Doing so allowed for measuring a frequency-dependent global fluid-flow out of the sample.

Combining these measurements/informations on Fontainebleau samples lead to conclude that the large frequency-dependent dispersion/attenuation measured fully relates to a global fluid-flow in and out of the sample, which is consistent with the drained/undrained transition.

### 4.2 Perspectives

**Measuring limitations** Owing to either large permeability of the rocks studied or to the limitations of the apparatus, the measurements allowed to study only the drained/undrained transition under glycerine saturation. As a matter of fact, the apparatus allows measurements only in a frequency range of  $f \in [10^3; 10^0]$  Hz, and the rock samples

used have permeabilities of about  $\kappa \in [10^{-16}; 10^{-13}] \text{ m}^2$ . Comparing this frequency range to the obtained characteristic frequency for the effect of interest shows that, consistently, only by saturating the sample by glycerine is this transition observable (Fig. 4.1a).

Two main points are thus missed using this apparatus. First, it is not possible to measure this transition under water saturation. Thus the effect of the fluid's bulk modulus on the drained/undrained transition is not investigated. Furthermore, as shown earlier, the relaxed/unrelaxed transition unfortunately cannot be observed experimentally with this apparatus.

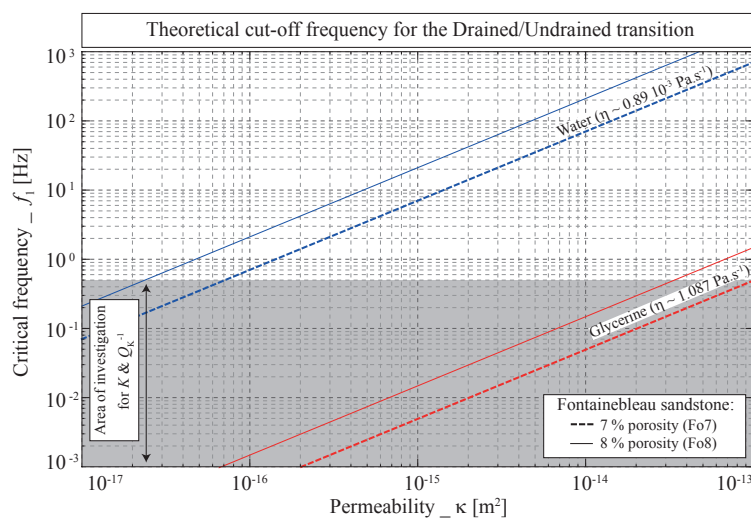


**Figure 4.1 :** Theoretical critical frequency for the Drained/Undrained transition as a function of the sample's permeability and of the fluid's viscosity. The water-saturated (i.e. blue) and glycerine-saturated (i.e. red) case are predicted. The frequency limitation of the apparatus for these confining pressure oscillations is reported as a grey zone.

To counter such limitations, a second system is introduced and calibrated in next chapter. This system, relying on deviatoric stress oscillations, allows to measure samples' elastic properties in the frequency range of  $f \in [10^3; 10^2] \text{ Hz}$ . Applying such apparatus to measure the Fontainebleau sandstone samples of interest, it may become possible to observe directly both drained/undrained and relaxed/unrelaxed transitions. Even though this added set-up cannot measure directly samples' bulk modulus, the property can be inferred in the framework of linear isotropic elasticity.

**Role of dead volumes on the measurements** Note for the measurements that a small overestimation of the drained bulk modulus is observed under both water and glycerine saturations. This effect is much larger for more porous and compressible rocks (e.g. Berea sandstone). Furthermore, the measured pore pressure in the dead volume denotes a pore pressure build-up inside the sample, implying that the sample is not perfectly drained at lowest frequencies. To go further, one needs to physically understand and determine the

causes of these effects. This is the aim of **part V**.



## PARTIE IV

# Oscillation de la contrainte déviatorique : Calibrations & Mesures

|          |  |            |
|----------|--|------------|
| <b>1</b> | <b>Introduction &amp; Principes de mesure</b>                                    | <b>123</b> |
| <b>2</b> | <b>Effect of fluids and frequencies on Young modulus (<i>Geophysics</i>)</b>     | <b>131</b> |
| 2.1      | Introduction . . . . .   | 132        |
| 2.2      | Experimental apparatus and Samples studied . . . . .                             | 133        |
| 2.3      | Calibration Results : Measurements under dry conditions . . . . .                | 139        |
| 2.4      | Effect of fluids on sandstone samples' Young modulus . . . . .                   | 145        |
| 2.5      | Interpretation & Discussion . . . . .  | 148        |
| 2.6      | Conclusion . . . . .   | 155        |
| <b>3</b> | <b>Effect of fluids and frequencies on Poisson ratio (<i>GRL, submitted</i>)</b> | <b>157</b> |
| 3.1      | Introduction . . . . .   | 158        |
| 3.2      | Samples & Experimental procedure . . . . .                                       | 158        |
| 3.3      | Results : Effect of pressure and frequency on Poisson ratio . . . . .            | 160        |
| 3.4      | Interpretation : Fluid flow and effective medium theories . . . . .              | 164        |
| 3.5      | Conclusion . . . . .   | 168        |
| <b>4</b> | <b>Discussions &amp; Perspectives</b>  | <b>169</b> |
| 4.1      | Effect of fluids on Poisson ratio of sandstone samples . . . . .                 | 169        |
| 4.2      | Effect of the boundary conditions . . . . .                                      | 171        |
| 4.3      | Conclusions . . . . .  | 175        |



## Summary

**Résumé :** Les mesures par oscillation de la pression de confinement restent limitées à une gamme de fréquence faible. Une deuxième méthode est donc testée : la méthode par oscillation axiale. Après calibration sur des standards, cette méthode permet de mesurer à la fois le module d'Young et le coefficient de Poisson sur une gamme de pression et de fréquence de  $P_c \in [1; 30]$  MPa et  $f \in [10^{-3}; 10^2]$  Hz.

L'utilisation de fluides visqueux permet d'étendre la gamme de fréquence à  $f \in [10^{-3}; 10^5]$  Hz. Dans le cas d'un échantillon de grès de Fontainebleau étudié, un second phénomène de dispersion/atténuation est observé, attribué à la transition entre régimes relaxé et non-relaxé. Grâce à cette méthode, les deux transitions entre les trois régimes élastiques sont donc directement mesurées pour ces deux propriétés élastiques. Le module d'Young montre une augmentation claire pour une augmentation de la fréquence, et semble indiquer deux transitions élastiques. Les variations sont cohérentes avec les théories usuelles. La dispersion mesurée sur le coefficient de Poisson est particulièrement intéressante car directement reliée au rapport  $V_p/V_s$ . Une variation en forme de cloche est mesurée pour cette propriété, ce qui est expliqué par une valeur en régime non-drainé supérieure au régime non-relaxé pour le cas particulier de cet échantillon. Les théories usuelles permettent de nouveau d'expliquer qualitativement ce résultat.

Certaines complexités du système de mesure, comme par exemple l'effet du volume mort ou de la position de la mesure, sont finalement étudiées.

**Abstract :** The measuring set-up using confining pressure oscillations bears an important flaw : only a narrow range of frequencies can be investigated. A second method is thus tested : The axial oscillations method. From extensive calibrations using different standard samples, the apparatus allows to measure both Young modulus and Poisson ratio over pressure and frequency ranges of  $P_c \in [1; 30]$  MPa and  $f \in [10^{-3}; 10^2]$  Hz. Using viscous fluids, the range in apparent frequency reached is  $f \in [10^{-3}; 10^5]$  Hz.

In case of a particular Fontainebleau sandstone, a second dispersion/attenuation phenomenon is observed that is attributed to the transition between relaxed and unrelaxed regimes. Using this set-up and procedure, both transitions between the three elastic regimes for the two elastic properties. Young modulus shows a clear frequency dependent increase for both elastic transitions that is consistent with the usual theories. The reported dispersion on Poisson ratio has a particular interest because it directly relates to the usually sought  $V_p/V_s$  ratio. A bell-shaped variation is measured for this property as, for this sample, the undrained regime results larger than the unrelaxed one. The existing theories allow to qualitatively explain those measurements.

Some complexities of the measuring set-up, such as the effect of the dead volume or the measuring position, are finally investigated.



## Introduction & Principes de mesure

Alors que le système d'oscillation de la pression de confinement ne permet d'étudier qu'une gamme de fréquence relativement faible, il est possible d'utiliser un second système de mesure pour étendre la gamme de fréquence d'étude : le système d'oscillations axiales. Ce système permet de mesurer les propriétés élastiques d'une roche sur une gamme de fréquence de l'ordre de  $f \in [10^{-3}; 10^2]$  Hz (Fig. 1.1).

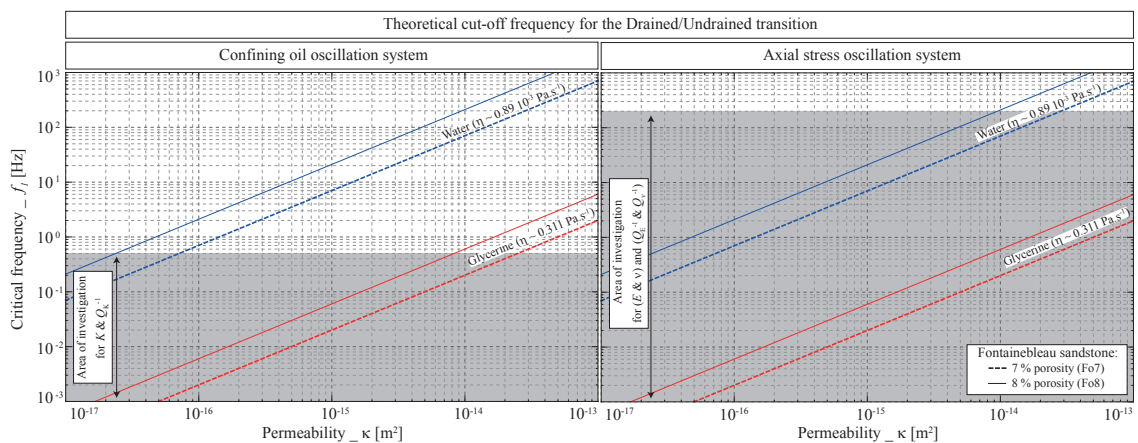


**Figure 1.1 :** Theoretical critical frequency for the Drained/Undrained transition as a function of the sample's permeability and of the fluid's viscosity. The water-saturated (i.e. blue) and glycerine-saturated (i.e. red) case are predicted. The frequency limitations of the apparatus for (a) isotropic and (b) axial measurements are reported.

Grace à ce nouveau système, il semble possible d'étudier dans les mêmes échantillons que précédemment la transition entre régimes drainé et non-drainé pour une saturation en eau. De plus, il semble aussi possible d'atteindre un deuxième effet de fréquence : la tran-

sition entre régimes relaxé et non-relaxé. Avant d'introduire les résultats, rapportés en chapitres 2 et 3, il est nécessaire de comprendre le principe la mesure ainsi que les complexités expérimentales à prendre en compte.

## Principe & Problématiques de mesure

Dans ce chapitre, les mêmes procédés de traitement que précédemment sont utilisés. En particulier, l'oscillation en température est filtrée de la même manière, et a un effet seulement sur les fréquences inférieures à 0.1 Hz.

### Oscillation axiale : Principe

#### Modules élastiques étudiés

Dans le cas d'oscillations axiales, la contrainte radiale est maintenue constante (i.e.  $\Delta\sigma_{rad} = 0$ ), alors que la contrainte axiale est mise en oscillation (i.e.  $\Delta\sigma_{ax} \neq 0$ ). En supposant que les amplitudes de déformation sont suffisamment faibles pour rester dans le domaine de l'élasticité linéaire, on obtient :

$$\begin{cases} \epsilon_{ax} = \frac{1}{E} \Delta\sigma_{ax} \\ \epsilon_{rad} = -\frac{\nu}{E} \Delta\sigma_{ax} \end{cases} \quad (1.1)$$

Par combinaison entre déformation axiale et radiale, il est possible d'obtenir le coefficient de Poisson  $\nu$  :

$$\frac{\epsilon_{rad}}{\epsilon_{ax}} = -\nu \quad (1.2)$$

#### Atténuation associée

Comme expliqué dans le chapitre I.1, un facteur de qualité ( $Q^{-1}$ ) peut être associé à chaque module élastique.  $Q_E^{-1}$  est associé au module d'Young  $E$ ,  $Q_K^{-1}$  est associé au module d'incompressibilité  $K$ , et  $Q_G^{-1} = Q_s^{-1}$  est associé au module d'incompressibilité  $G$ .

Dans le cas d'un matériau isotrope, d'après les relations d'élasticité, des relations entre ces facteurs de qualité peuvent alors être obtenues (Winkler and Nur, 1979) :

$$\frac{(1-\nu)(1-2\nu)}{Q_p} = \frac{(1+\nu)}{Q_E} - \frac{2\nu(2-\nu)}{Q_s} \quad (1.3)$$

$$\frac{(1-2\nu)}{Q_K} = \frac{3}{Q_E} - \frac{2(1+\nu)}{Q_s} \quad (1.4)$$

$$\frac{(1+\nu)}{Q_K} = \frac{3(1-\nu)}{Q_p} - \frac{2(1-2\nu)}{Q_s} \quad (1.5)$$

$\nu$  étant le coefficient de Poisson.

Dans l'étude d'un matériau isotrope, une autre propriété élastique est d'intérêt : le coefficient de Poisson  $\nu$ . Par analogie avec les autres modules élastiques, il est rigoureusement possible d'associer à cette propriété élastique son facteur de qualité propre :  $Q_\nu^{-1}$ . Il est alors intéressant de relier ce facteur de qualité avec ceux déterminés précédemment. Reprenant la procédure utilisée par Winkler and Nur (1979), on définit le coefficient complexe tel que  $\nu^* = \nu_1 + i\nu_2$ . En prenant par exemple la relation d'élasticité linéaire dans le cas isotrope entre  $\nu$ ,  $E$  et  $G$ , la relation complexe devient :

$$\nu^* = \frac{(E_1 + iE_2) - 2(G_1 + iG_2)}{2(G_1 + iG_2)}. \quad (1.6)$$

En multipliant par la partie conjuguée, puis extrayant parties réelle et imaginaire de  $\nu^*$ ,  $Q_\nu^{-1}$  est donc obtenu tel que :

$$Q_\nu^{-1} = \frac{\nu_2}{\nu_1} = \frac{E_2 G_1 - E_1 G_2}{G_1(E_1 - 2G_1) + G_2(E_2 - 2G_2)}. \quad (1.7)$$

Finalement, on obtient une relation entre  $Q_\nu^{-1}$ ,  $Q_E^{-1}$  et  $Q_s^{-1}$  telle que :

$$Q_\nu^{-1} \left[ \nu + \frac{1}{Q_s} \left( \frac{1+\nu}{Q_E} - \frac{1}{Q_s} \right) \right] = \frac{1+\nu}{Q_E} + \frac{1+\nu}{Q_s}. \quad (1.8)$$

De la même manière, il est possible de relier  $Q_\nu^{-1}$ ,  $Q_p^{-1}$  et  $Q_s^{-1}$ . Le facteur de qualité associé au coefficient de Poisson peut donc être directement relié aux atténuations mesurées sur les ondes P et S.

## Oscillation axiale : Mesure

### Mesures de déformations

Pour chaque oscillation du déviateur  $\Delta\sigma_{ax}$ ,  $\epsilon_{ax}$  et  $\epsilon_{rad}$  sont enregistrées. Les signaux sont de nouveau directement filtrés pour supprimer l'effet de la température. Un exemple d'oscillation est donné pour le cas d'un échantillon de gypse soumis à une pression  $P_c = 1$  MPa et une contrainte statique  $\sigma_{ax} = 0.2$  MPa (Fig. 1.2).

Pour cette méthode d'oscillation, la forme d'oscillation est purement sinusoidale (Fig. 1.2a). La mesure de  $\epsilon_{alu}$  permet d'obtenir la valeur de la contrainte sinusoidale exercée telle que  $\Delta\sigma_{ax} = E_0 \epsilon_{alu}$ , avec  $E_0 = 72.5$  GPa. La contrainte est ici de l'ordre de  $\Delta\sigma_{ax} = 0.15$  MPa. La mesure de  $\epsilon_{rad}$  est en opposition de phase avec les mesures de  $\epsilon_{alu}$  et  $\epsilon_{ax}$ .

### Traitement du signal

La même méthode de traitement du signal que pour les oscillations isotropes est utilisée ici. Pour chaque signal caractérisant une propriété élastique, deux paramètres sont de nouveau étudiés : l'amplitude et la phase.

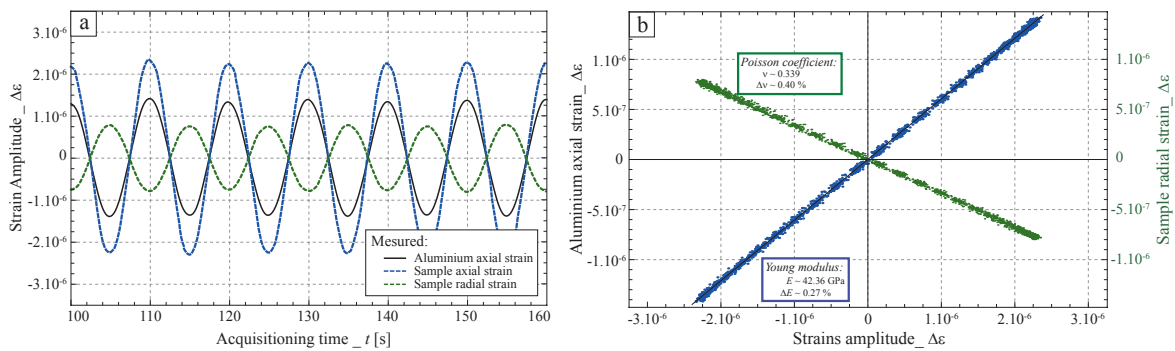


**Figure 1.2 :** Example of measurements from a stress oscillation in case of the gypsum sample. (a) The standard's (i.e.  $\epsilon_{alu}$ ) and sample's (i.e.  $\epsilon_{ax}$  and  $\epsilon_{rad}$ ) strains are recorded as a function of time. (b) Linear regressions are obtained from the recorded and inferred signals so that the elastic moduli are obtained.

L'amplitude du signal permet d'accéder au module élastique. Les modules élastiques sont de nouveau obtenus par une régression linéaire (Fig. 1.2b). Les module d'Young ( $E$ ) et coefficient de Poisson ( $\nu$ ) sont respectivement obtenus par régression entre  $\Delta\sigma_{ax}$  et  $\epsilon_{ax}$ , et entre  $\epsilon_{rad}$  et  $\epsilon_{ax}$ .

Dû à l'opposition de phase notée précédemment, la regression linéaire associée à la mesure de  $\nu$  a une pente inversée en comparaison avec les modules élastiques. La pente varie pour chaque propriété élastique, indiquant différentes amplitudes de modules. La dispersion statistique par rapport à la régression est utilisée pour indiquer un ordre d'erreur sur la mesure. Pour cette mesure, la valeur obtenue ne dépasse pas 1 % quel que soit la mesure étudiée.

La phase du signal est déterminée dans le domaine de Fourier. Dans le cas de  $E$ ,  $K$  et  $G$ , la phase obtenue sur la mesure de déformation associée est comparée à la phase de la contrainte (i.e.  $\Delta\sigma_{ax}$ ). La tangente du déphasage ainsi obtenu donne une mesure de l'atténuation reliée au module mesuré, i.e.  $Q_E^{-1}$  :

$$Q_E^{-1} = \text{Tan}[\phi_{\epsilon_{alu}} - \phi_{\epsilon_{ax}}]. \quad (1.9)$$

Dans le cas du coefficient de Poisson, le même principe d'étude est utilisé.  $\nu$  étant obtenu par le rapport entre déformation axiale et déformation radiale, le déphasage entre ces deux déformations est mesuré. La tangente de ce déphasage est utilisée pour le calcul du facteur de qualité du coefficient de Poisson, noté  $Q_\nu^{-1}$  :

$$Q_\nu^{-1} = \text{Tan}[\phi_{\epsilon_{ax}} - \phi_{\epsilon_{rad}}]. \quad (1.10)$$

### Problématiques de mesures

Comme indiqué précédemment, il est nécessaire de connaître la valeur de la force exercée sur l'échantillon pour déduire la valeur du module d'Young  $E$ . La contrainte oscillante est ici délivrée par un oscillateur mécanique/piezo-électrique. Cet oscillateur transforme

un signal électrique en un déplacement, et donc en une force exercée sur l'échantillon. Une des difficultés de cette méthode est de connaître avec précision la valeur de la force appliquée. Différentes approches successives ont été testées pour parvenir à contraindre ce paramètre.

Finalement la mesure est obtenue en mesurant la déformation de l'embase inférieure en aluminium. Ce matériau étant purement élastique, la déformation enregistrée est indépendante de la fréquence et se relie directement à la force appliquée. Deux jauges axiales sont collées, diamétralement opposées sur l'embase. Dans le cas idéal, la mesure est stable et les jauges diamétralement opposées mesurent des déformations de même amplitude et phase.

## Effet de l'amplitude de déformation sur les modules

Comme pour la mesure du module d'incompressibilité, il est important de vérifier que les variations des propriétés élastiques mesurées ne proviennent pas d'un biais expérimental tel que l'effet de l'amplitude. Ici, la valeur de contrainte axiale est décidée par le voltage d'entrée de l'oscillateur mécanique. La roche étudiée est un grès de Béréa, possédant une porosité d'environ 20%.

Ces mesures ont en fait été effectuées en collaboration avec une équipe de *Los Alamos, USA* (Dr. Jacques Riviere & Pr. Paul Johnson) dans le but d'étudier l'"Acousto-Elasticité" dans les roches. Les données "mécaniques" présentées ici feront partie d'une publication ultérieure, actuellement en préparation.

### Amplitudes de contrainte et de déformation

Pour une contrainte donnée, l'amplitude pic-à-pic est mesurée par la valeur d'amplitude du pic dans le domaine de Fourier. L'amplitude de déformation axiale de l'embase inférieure est directement transformée en contrainte axiale. Les amplitudes de contrainte et de déformation (axiale et radiale) de l'échantillon sont donc obtenues pour différentes fréquences (Fig. 1.3a) et pressions de confinement (Fig. 1.3b). Une échelle semi-log est utilisée pour pouvoir reporter déformations axiale et radiale dans la même figure. La variation non-linéaire entre contrainte et déformations observée est un effet direct de cette échelle.

Comme énoncé précédemment, l'oscillateur utilisé applique un déplacement correspondant à un voltage d'entrée. L'échantillon ayant un module plus élevé quand la pression de confinement augmente, l'amplitude de contrainte axiale doit être plus élevée pour atteindre le même déplacement.

### Effet sur les modules élastiques

Il est intéressant d'étudier la variation des propriétés élastiques avec une variation de la contrainte appliquée. Tout comme pour les mesures de déformation (Fig. 1.3), la variation

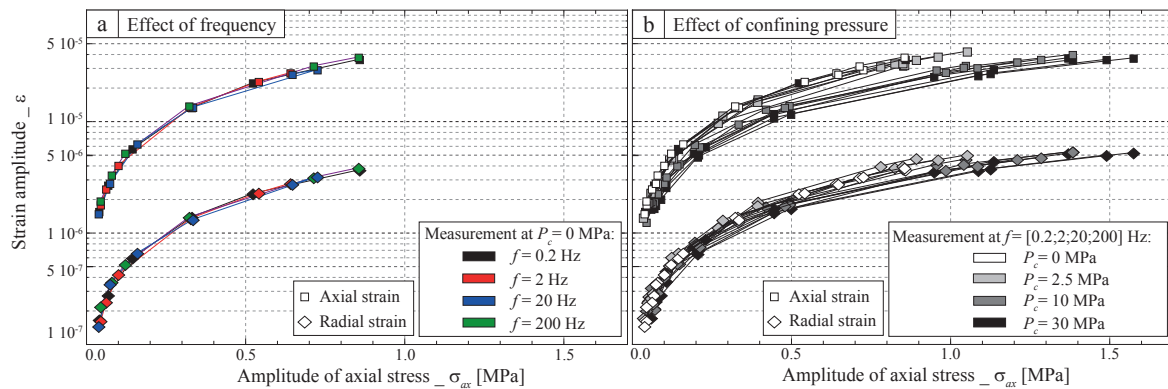


**Figure 1.3 :** Measured axial (i.e. squares) and radial (i.e. diamonds) strains as a function of the applied stress for different (a) frequencies and (b) confining pressures. The sample investigated is a Berea sample of 20% porosity. Note that a semi-log scale was used in order to introduce simultaneously both axial and radial strains.

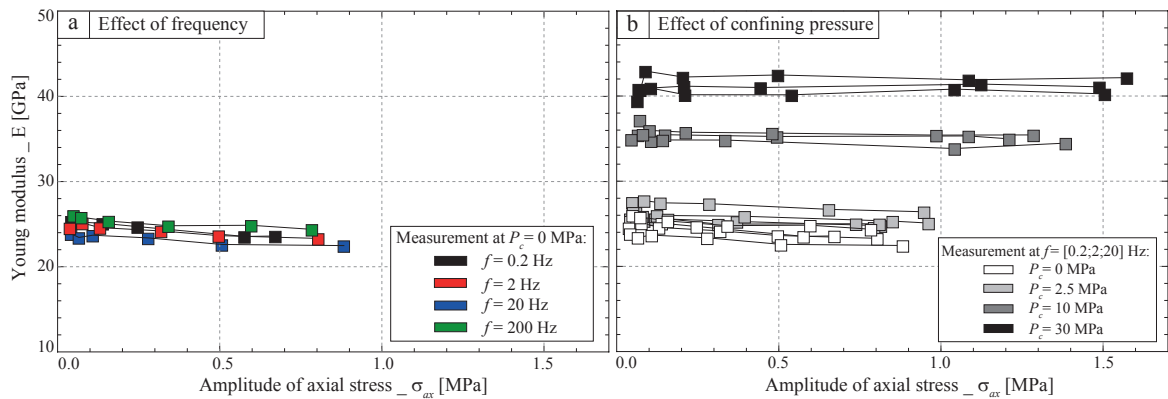


**Figure 1.4 :** Measured Young modulus as a function of the applied stress for different (a) frequencies and (b) confining pressures. The sample investigated is a Berea sample of 20% porosity.

du module d'Young (Fig. 1.4a) et du coefficient de Poisson (Fig. 1.5b) sont étudiés pour différentes fréquences (Figs. 1.4a & 1.5a) et pressions de confinement (Fig. 1.4b & 1.5b). Tout comme pour le module  $K$ , une dépendance à l'amplitude de déformation semble être observée sur  $E$  pour cette roche. Une faible diminution, de l'ordre de quelques pourcents, est mesurée sur  $E$  avec une augmentation de la contrainte (et donc de la déformation) axiale entre 0 et 1.5 MPa. Cette variation est mesurée pour toutes les fréquences d'étude. Néanmoins, la variation semble appartenir à la barre d'incertitude de la mesure.

Dans le cas du coefficient de Poisson, aucune dépendance à l'amplitude est mesurée. Le coefficient de Poisson varie entre 0.1 et 0.14. Ce résultat est proche des valeurs habituellement obtenues dans des grès (de l'ordre de 0.1). Une augmentation du coefficient de Poisson avec la pression de confinement est mesurée, tendant à montrer que la roche est isotrope (Wang et al., 2012). La valeur 0.14 obtenue pour le coefficient de Poisson à plus haut confinement est supérieure à celle pour le quartz (i.e. 0.07), ce qui peut être dû à la forte porosité ( $\sim 20\%$ ) ou à un taux d'argile important ( $\sim 15\%$ ) dans l'échantillon.

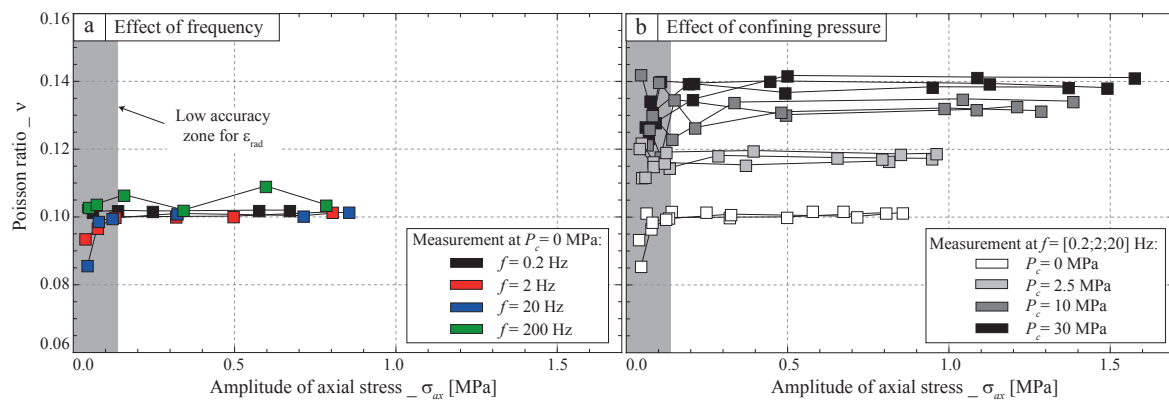


**Figure 1.5 :** Measured Poisson ratio as a function of the applied stress for different (a) frequencies and (b) confining pressures. The sample investigated is a Berea sample of 20% porosity.

En conclusion, un effet de l'amplitude de déformation peut être attendu dans des échantillons granulaires peu cimentés. Cet effet est néanmoins négligeable pour des amplitudes de contrainte inférieures à 0.5 MPa.



---

### Effect of fluids and frequencies on Young modulus (*Geophysics*)

---

L. Pimienta, J. Fortin and Y. Guéguen, Experimental evidence for Young modulus dispersions associated with the drained/undrained and undrained/unrelaxed transitions in sandstone, (2015), *Geophysics*, Accepted.

---

#### Abstract

Seismic wave dispersions and attenuations were shown to occur in sedimentary rocks. However, it remains challenging to observe experimentally these effects. This article reports measurements of Young modulus dispersions and attenuations from the drained/undrained and undrained/unrelaxed transitions. A new experimental set-up has been developed to measure rocks' Young modulus and Poisson ratio over a wide range in pressure ( $P_c \in [0;30]$  MPa) and frequency ( $f \in [5.10^{-3};10^2]$  Hz). Calibration with standard samples shows that (i) no pressure and frequency dependency of the apparatus is observed; and (ii) the measured and inferred elastic properties fit well with published data. Additional measurements of plexiglass' Young modulus dispersion and attenuation are also consistent with published data. The plexiglass' Poisson ratio shows a frequency-dependent decrease that fits both static and ultrasonic data. Young modulus and attenuation are measured as a function of effective pressure and frequency for Fontainebleau sandstone samples saturated by water and glycerine. While little variations are observed for one sample, the second one exhibit strong pressure- and frequency-dependent variations of both Young modulus and attenuation. An evidence for a frequency-dependent fluid-flow is simultaneously measured. The characteristic frequency for these variations is

highly fluid-dependent. Accounting for the in-situ fluids' viscosity using an apparent frequency parameter, this article reports Young modulus and attenuation of a fluid-saturated Fontainebleau sandstone over an apparent frequency band of  $f^* \in [10^{-3}; 10^5]$  Hz. The measurements under water and glycerine saturation compare favourably, and two frequency-dependent phenomena are observed that may relate to the drained/undrained and undrained/unrelaxed transitions. The undrained/unrelaxed transition occurs in a large frequency range, which is attributed to a distribution in aspect ratio of the rock's microcracks. The measurements are then compared to reported bulk modulus dispersion/attenuation on the same Fontainebleau sandstone. The frequency-dependent dispersions in Poisson ratio and shear modulus are inferred.

---

## 2.1 Introduction

Sedimentary rocks saturated by fluids are known to be dispersive materials. Their frequency-dependent behaviours originate from fluid movements in the rock's porous network induced by the elastic waves. When comparing field and laboratory measurements, the frequency dependence of the elastic properties is to be considered. For fully-saturated rocks, two transitions between three elastic domains are expected (e.g., Cleary, 1978; Sarout, 2012) in the frequency range of interest (i.e.  $f \in [10^{-1}; 10^6]$  Hz). The first transition is that from drained to undrained regimes. Both regimes are within the field of poroelasticity. This transition is expected to occur at low frequencies. The second transition, occurring at higher frequency, is that from relaxed to unrelaxed regimes. This last situation is out of the validity domain of poroelasticity as the Representative Elementary Volume is not in an isobaric state anymore.

Owing to the experimental complexities, very few laboratory apparatus allow for measuring such frequency-dependent transitions. The stress-strain method is promising as it allows for measurement of elastic properties over wide frequency and pressure ranges up to about  $f \in [10^{-3}; 10^3]$  Hz and  $P_c \in [0; 100]$  MPa respectively (e.g., Subramaniyan et al., 2014). Apparatus for measurements of confining pressure (Adelinet et al., 2010; David et al., 2013; Fortin et al., 2014; ?) or shear stress (e.g., Jackson and Paterson, 1987) oscillations were developed, but the stress-strain method applied to axial stress oscillations is by far the most used (e.g., Batzle et al., 2001, 2006; Adam et al., 2006, 2009; Mikhaltsevitch et al., 2011; Tisato and Madonna, 2012; Madonna and Tisato, 2013). To the authors' knowledge, data from the literature however do not report clear transitions between the expected elastic regimes. First, the boundary conditions are most of the time chosen so that the fluid-saturated medium's elastic properties are directly undrained, thus discarding the transition from drained to undrained regimes. Second, a clear transition from undrained to unrelaxed domain is yet to be clearly reported.

Using three standard samples, this work reports a new experimental set-up allowing for measuring frequency-dependent Young modulus, Poisson ratio and Young attenuation in the frequency and pressure ranges of  $f \in [5 \cdot 10^{-3}; 10^2]$  Hz and  $P_c \in [0; 30]$  MPa. Young modulus and its intrinsic attenuation are measured as a function of pressure and frequency on two Fontainebleau sandstone samples saturated by water and glycerine. Simultaneously, hydraulic properties are measured. The results are interpreted in the light of the usual fluid-flow theories and using published results on the  $K$  modulus of the same rock samples (?).

## 2.2 Experimental apparatus and Samples studied

### 2.2.1 Samples studied

#### 2.2.1.1 Calibration samples

Three standard samples were chosen to test the experimental set-up and procedure : (i) A synthetic glass sample made of amorphous silica (Mallet et al., 2013); (ii) A pure gypsum sample (Brantut et al., 2012); and (iii) A plexiglass (PMMA) sample (e.g., Batzle et al., 2006). These samples were chosen as (i) they are homogeneous and isotropic media at the sample scale; (ii) their static and dynamic elastic properties are known, and they show a large range in elastic moduli; (iii) these samples have no porosity, and their elastic properties are not expected to change with confining pressure or added axial stress; and (iv) while glass and gypsum elastic properties are independent of frequency, plexiglass is a viscoelastic material whose elastic properties are frequency-dependent. Plexiglass is often used as a mean to test an attenuation apparatus (e.g., Batzle et al., 2006; Tisato and Madonna, 2012; Madonna and Tisato, 2013; ?).

#### 2.2.1.2 Fontainebleau sandstone

Fontainebleau sandstone is a well-known reference rock. Both framework grains and cement are pure quartz, making up a clean sandstone of about  $\sim 99.9\%$  qtz (Bourbie and Zinszner, 1985; Gomez et al., 2010). As the rock was formed from deposited aeolian quartz grains, the rock possess a random grain orientation and is well sorted, with an average grain size of about  $\sim 200 \mu\text{m}$ . The rock can consistently be assumed homogeneous and isotropic at the Representative Elementary Volume (REV) scale (i.e. volume  $\gg$  grains' volume).

Depending on the amount of cementing quartz, Fontainebleau sandstone samples' porosity ranges from about  $\phi \sim 2\%$  for highly cemented samples to about  $\phi \sim 25\%$  for ill cemented samples. The main differences between samples are the pores entry diameters. These diameters decrease from  $d \sim 20 \mu\text{m}$  (high porosity) to about  $d \sim 5 \mu\text{m}$  (low porosity), which leads to variations in permeability of about 4 to 5 orders of magnitude (Bourbie and Zinszner, 1985). The two samples used in this study have respectively porosities of about

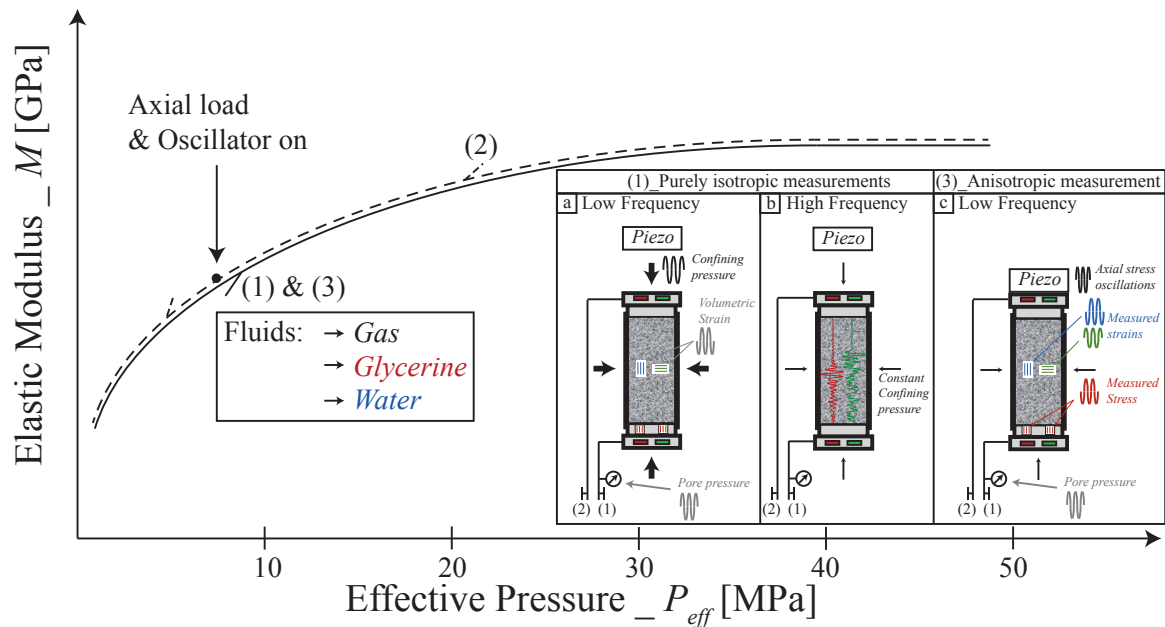


**Figure 2.1 :** Schematic view of the experimental set-up and procedure for measuring the whole set of HF (b) and LF (a & c) elastic moduli under different fluids' saturation. (1) Under no deviatoric stress, (a) LF confining pressure oscillations lead to measuring bulk modulus; and (b) ultrasonic velocities are measured to infer the HF moduli. Under a small deviatoric stress, LF deviatoric oscillations are applied to measure Young modulus and Poisson coefficient. The cylindrical sample is isolated laterally from the confining oil using a rubber jacket.

$\phi \sim 7.2\%$  (i.e. Fo7) and of about  $\phi \sim 8.3\%$  (i.e. Fo8), and originate from the same blocks as in ?.

## 2.2.2 Experimental apparatus & procedure

### 2.2.2.1 Cell and confining set-up

The apparatus aims at measuring simultaneously the complete set of elastic properties at High Frequency (HF) and Low Frequency (LF). To investigate these properties at different pressures, measurements are conducted in an oil-confining triaxial apparatus (Fortin et al., 2005). The sample is radially enclosed in a rubber jacket to be separated from the confining medium (i.e. oil). This oil-confining triaxial apparatus can be used in two different set-ups thanks to an axial piston that can be shifted vertically (Fig. 2.1).

In the first set-up, the axial piston is not in contact with the end-platen (and thus the sample), allowing for studying the sample under pure isotropic conditions. As shown (?), this set-up allows to measure (i) LF bulk modulus (i.e.  $K_{LF}$ ) and attenuation (i.e.  $Q_K^{-1}$ ), using confining pressure oscillations (Fig. 2.1a) at different frequencies; and (ii) ultrasonic P- and S-wave velocities (i.e.  $V_p$  and  $V_s$ ) travelling through the sample (Fig. 2.1b).

A second set-up has been built in order to measure the LF Young modulus (i.e.  $E_{LF}$ ) and Poisson ratio (i.e.  $\nu_{LF}$ ) using axial stress oscillations (Fig. 2.1c) as a function of frequency.

This second set-up is the focus of the present contribution. As shown from the schematics, in order to exert axial stress oscillations  $\Delta\sigma_{ax}$  on the sample, an added deviatoric load  $\sigma_{ax}$  is needed to ascertain the stability of the measuring set-up. Yet, the magnitude of  $\sigma_{ax}$  may affect the sample's properties during the measurement. The effect of this added deviatoric load is further investigated below, prior to introducing the measurements under fluid-saturated conditions.

### 2.2.2.2 Pore fluid set-up

Pore pressure is controlled externally, and independently of the confining pressure, by a pair of connected *Quizix* servo-pumps. The pore volume and pressure measurements accuracies are respectively of about  $V_p \sim 0.1 \mu\text{L}$  and  $P_p \sim 0.001 \text{ MPa}$ . Additionally, another pressure transducer of  $P_p \sim 0.001 \text{ MPa}$  accuracy is placed near the sample. Valves are placed at both ends of the sample (Fig. 2.1) to decrease as much as possible the pipes' dead volumes, and the pressure sensor is placed near the bottom end-platen (i.e. inside the dead volume). The measured dead volumes are  $V_{d1} = 3.433 \text{ mL}$  and  $V_{d2} = 3.205 \text{ mL}$ , leading to a total dead volume of about  $V_d \sim 6.6 \text{ mL}$ .

The valves can either be open or closed. The first configuration is chosen when changing the confining pressure, so that the fluid is kept at a constant pressure of  $P_p = 2 \text{ MPa}$  and the sample is drained during the pressure ramps. Following similar measurements (e.g., Batzle et al., 2006; Tisato and Madonna, 2012; Madonna and Tisato, 2013; Mikhaltsevitch et al., 2014; ?), the second configuration is chosen, and the valves are closed during the axial stress oscillation  $\Delta\sigma_{ax}$ . In this configuration, the fluid mass is kept constant in the system (i.e. *Sample + Dead Volume*). This system is experimentally undrained, and fluid pressure changes are tracked by the pore pressure sensor in the dead volume. This configuration was found to be the most appropriate as it discards any possible bias from an extrinsically-induced differed fluid-flow, i.e. from the delayed regulation of the pore pressure pump. Owing to the existence of the large dead volume and of the sample's intrinsic storage capacity (e.g., Ghabezloo and Sulem, 2010), the samples used prove to remain drained under quasi-static conditions (?).

### 2.2.2.3 Low frequency set-up

As discussed above, the LF measurements rely on the stress-strain method. An axial stress oscillation at a given frequency is applied to the sample, thus inducing a strain oscillation. The axial stress is exerted by a *PI* piezo-electric actuator scheduled to function in the range of  $f \in [10^{-3}; 10^2] \text{ Hz}$  and electrical amplitudes of  $A \in [10; 1000] \text{ V}$ , with a maximum displacement of  $30 \mu\text{m}$ . The oscillator is linked to (i) a LF generator sending a continuous sinusoidal electric signal of given amplitude (i.e.  $A \in [0.1; 10] \text{ V}$ ) and frequency (i.e.  $f \in [10^{-3}; 10^8] \text{ Hz}$ ); and (ii) an amplifier. This actuator transforms a volt amplitude in

a mechanical displacement, which directly depends on the sample's stiffness. Thus stress cannot be directly inferred from the input voltage, and is a function of the sample's strain.

To precisely measure the stress applied on the sample, two axial *FCB* 350  $\Omega$  strain gauges (*Tokyo Sokki TML*, FCB-6-350-11) of 6 mm length are glued to the aluminium bottom end-plates. Stress is deduced by knowing the end-plates Young modulus, i.e.  $E_0 = 72.5$  GPa. To measure the sample's strains, three pairs of axial and radial *FCB* 350  $\Omega$  strain gauges of 6 mm length are directly glued on the sample. All the strain gauges used are the same and are mounted in a one-fourth Wheatstone bridge, allowing to discard possible bias by using different gauges (e.g., Adam et al., 2006). All strains and the pore pressure oscillations are transformed from electric to strain and pressure signals using Catman recording system (*HBM inc.*), able to record at frequencies up to 2400 Hz.

#### 2.2.2.4 Experimental procedure

A procedure (Fig. 2.1) is devised to measure the frequency and pressure dependence of the whole set of elastic moduli of rocks saturated by different fluids. Starting from an effective pressure of about  $P_{eff} \sim 1$  MPa, the frequency-dependence of the properties is measured at each confining pressure step up to the maximum confining of  $P_{eff} = 30$  MPa. When changing the confining pressure, a controlled rate of about 0.01 MPa/s is used to allow for complete/instantaneous relaxation of the fluid-filled sample (Fortin et al., 2007). The same procedure is followed for the three different saturating conditions, i.e. (1) dry, (2) water- and (3) glycerine-saturation. For the sandstone samples in fluid saturated conditions, Terzaghi effective pressure  $P_{eff} = P_c - P_p$  is used that allows for an approximate yet simple comparison between dry and fluid-saturated conditions.

The glycerine full saturation is ascertained by a precise injection procedure : (1) vacuum is applied with a vacuum pump at the sample upper end until the measured  $P_p$  (at the sample's bottom) reaches a stable negative value of  $\sim -0.8$  MPa; (2) then, the fluid is injected at the sample bottom while maintaining the vacuum with the vacuum pump. This injection procedure (using the vacuum pump) complements the density effect (i.e. air pushed up by the denser fluid), and was shown to allow for a 100% fluid saturation (e.g., ?). Water saturation is then obtained by directly injecting water in the glycerine-filled sample. As glycerine immediately and fully dissolves in water, thus losing its viscosity, the water full saturation is obtained by flushing two to three times the pore volume.

### 2.2.3 Processing method

#### 2.2.3.1 Permeability measurement

To understand the fluid-flow effects at the sample scales, the rocks' transport properties have to be measured. The pressure gradient method (Figs. 2.2a & 2.2b) is here used. It consists in applying a pressure gradient (Fig. 2.2a) and measuring the fluid flow (Fig.

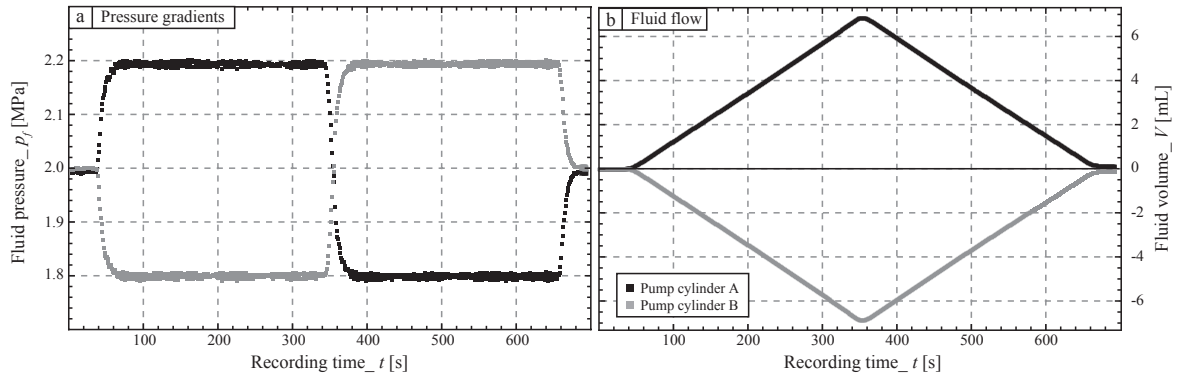


**Figure 2.2** : Example of a permeability measurement for Fo7, by (a) applying a pressure gradient and (b) measuring the fluid flow at both ends of the sample. Here, Pump A is linked to the sample's top, and Pump B is linked to the sample's bottom.

2.2b). Knowing both pressure gradient and fluid flow allows one to measure the hydraulic conductivity across the sample, which is obtained for each confining step. Permeability is then directly inferred using Darcy's law, taking the sample's dimensions and the fluid viscosity as input parameters.

### 2.2.3.2 Strains oscillations : mechanical (elastic) response

At a given effective pressure, the confining pressure is maintained constant (i.e.  $\Delta P_c = 0$ ) and an added oscillating axial stress is exerted on the sample (i.e.  $\Delta \sigma_{ax} \neq 0$ ). This oscillating stress  $\Delta \sigma_{ax}$  leads to axial (i.e.  $\Delta \epsilon_{ax}$ ) and radial (i.e.  $\Delta \epsilon_{rad}$ ) strain oscillations (Fig. 2.3a). Following the elastic theory for a homogeneous/isotropic cylindrical sample, LF Young modulus ( $E_{LF}$ ) and Poisson ratio ( $\nu_{LF}$ ) may be inferred from such measurements (e.g., Batzle et al., 2006) :

$$\Delta \epsilon_{ax} = \frac{1}{E_{LF}} \Delta \sigma_{ax} \quad \& \quad \frac{\Delta \epsilon_{rad}}{\Delta \epsilon_{ax}} = -\nu_{LF}. \quad (2.1)$$

For each frequency of applied  $\Delta \sigma_{ax}$ , axial and radial strains are recorded. A typical processing method is applied on the recorded signals (?), namely : (i) Phase picking in Fourier domain (e.g., Batzle et al., 2006; Madonna and Tisato, 2013) to obtain the phase shift between the axial stress (i.e. end-platen's axial strain) and the sample's axial strain, which tangent is the attenuation on Young modulus (i.e.  $Q_E^{-1}$ ); (ii) filtering in Fourier domain ; and (iii) linear regressions, to obtain the relevant elastic moduli.

An example of strain oscillation is reported (Fig. 2.3a) for the Gypsum sample measured at a confining pressure of  $P_c = 10$  MPa and axial added load of  $\sigma_{ax} = 2$  MPa. The amplitude and frequency of the axial oscillation are here of  $\Delta \sigma_{ax} \sim 0.2$  MPa (i.e. about  $\Delta \epsilon_{alu} \sim 2.5 \cdot 10^{-6}$ ) and  $f = 0.1$  Hz respectively, leading to sample's strains of about  $\Delta \epsilon_{ax} \sim 4.5 \cdot 10^{-6}$  and  $\Delta \epsilon_{rad} \sim 1.5 \cdot 10^{-6}$ . The sample's Young modulus (i.e.  $E_{LF}$ ) and Poisson ratio (i.e.  $\nu_{LF}$ ) are then obtained (Fig. 2.3b) from a linear regression constrained with a 99% confidence interval. The data scatter around the linear regressions (i.e.  $E_{LF}$  and  $\nu_{LF}$ ) are used to infer a statistical

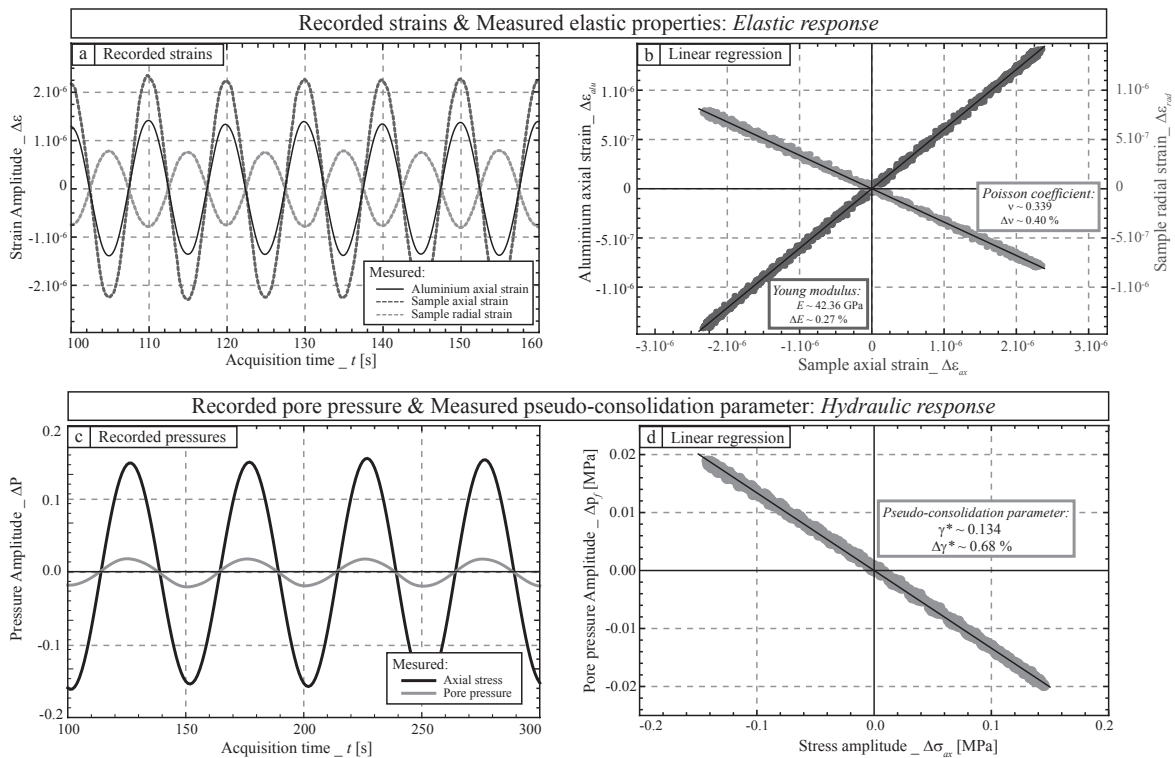


**Figure 2.3 :** Example of a standard measurement of Young modulus ( $E_{LF}$ ) and Poisson ratio ( $\nu_{LF}$ ) for the gypsum sample for a confining pressure of 10 MPa and an axial stress of 2 MPa. (a) The oscillating aluminium's axial strain, and sample's axial and radial strains are recorded ; and, knowing the aluminium Young modulus ( $E_0$ ), (b) linear regressions are calculated between the recorded strains to obtain  $E_{LF}$  and  $\nu_{LF}$ . Example of a measurement of the pseudo-consolidation parameter for Fo7 under water saturation at an effective pressure of 1 MPa and an axial stress of 0.2 MPa. (c) Oscillating stress (inferred from the recorded axial strain and  $E_0$ ) and pore pressure are recorded ; and (d) the linear regression between both signals is calculated.

error, noted respectively  $\Delta E_{LF}$  and  $\Delta \nu_{LF}$ . Note that, the applied strains in the sandstone samples of study are lower than about  $10^{-5}$  in order to remain in the elastic domain.

### 2.2.3.3 Pore pressure oscillations : hydraulic response

Following ? an additional information is obtained by measuring the fluid pressure oscillations at the outlet of the dead volume. Applying an oscillating deviatoric stress  $\Delta \sigma_{ax}$  results in an oscillating pore fluid pressure (Fig. 2.3c), which relates to both the rock's compressibility and to the fluid's diffusivity. The relevant parameter to understand a rock's hydraulic response in the case of an isotropic undrained loading is Skempton coefficient. In case of a deviatoric loading, the consolidation coefficient ( $\gamma$ ) is the appropriate parameter (Wang, 2000). A pseudo-consolidation parameter ( $\gamma^*$ ) is introduced here, defined as the ratio of pore fluid pressure at the dead volume outlet ( $\Delta p_f$ ) to the deviatoric applied stress ( $\Delta \sigma_{ax}$ ) such that :

$$\gamma^* = \frac{\Delta p_f}{\Delta \sigma_{ax}} \quad (2.2)$$

As for  $E_{LF}$  and  $\nu_{LF}$  (Fig. 2.3b),  $\gamma^*$  is obtained from a linear regression between  $\Delta p_f$  and  $\Delta \sigma_{ax}$ . An example of a low frequency (i.e.  $f = 0.1$  Hz) stress oscillation inducing a pore pressure oscillation is reported (Fig. 2.3c) for the water-saturated Fo7 sample. For this measurement, the static conditions applied are an effective pressure of  $P_{eff} = 1$  MPa (i.e.  $P_c = 3$  MPa and  $p_f = 2$  MPa) and an added deviatoric load of  $\sigma_{ax} = 0.2$  MPa. The sample appears to be in a purely drained state so that an instantaneous response is observed on the pore pressure signal. As a direct consequence, the linear regression (Fig. 2.3d) is almost a straight line. By increasing frequency, a phase shift between applied  $\Delta \sigma_{ax}$  and induced  $\Delta p_f$  appears.

## 2.3 Calibration Results : Measurements under dry conditions

The calibration is carried out following a step-wise procedure to assess the measuring accuracy of the apparatus. First, using the purely elastic glass and gypsum samples, the pressure and frequency dependence of both apparatus and procedure are tested. Then, in the particular case of the plexiglass sample, the accuracy of the frequency dependence set-up is tested. Finally, the role/effect of an added axial load on a rock's elastic response is tested using (i) the dependence to confining pressure of the dry Fontainebleau samples' elastic moduli for different values of axial load ; and (ii) a comparison between bulk moduli obtained using the three different measuring set-ups (Fig. 2.1).

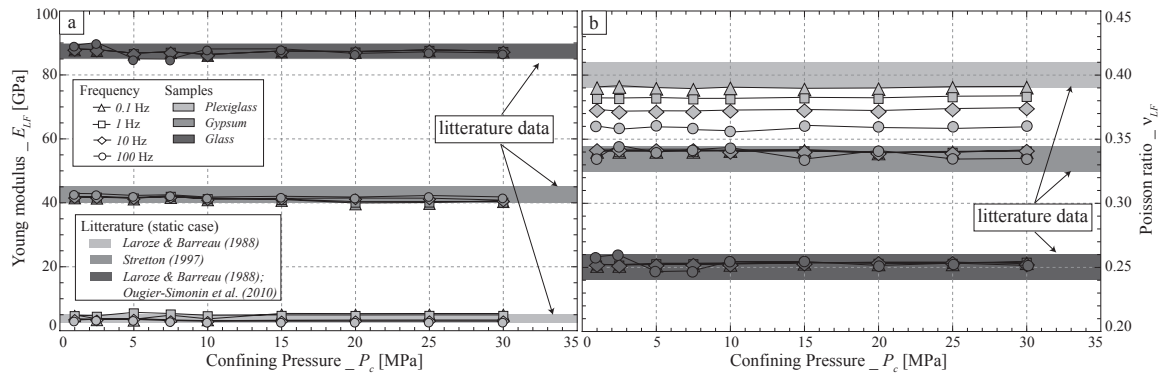


**Figure 2.4 :** Measured pressure dependence of the elastic properties of the three reference samples from axial oscillations at four different oscillation frequencies of  $f \in [0.1, 1, 10, 100]$  Hz. (a) Young modulus  $E_{LF}$  and (b) Poisson ratio  $\nu_{LF}$  are directly measured for all confining pressures up to  $P_c \sim 30$  MPa.

### 2.3.1 Confining pressure effect for the reference samples

#### 2.3.1.1 Measured Young modulus and Poisson ratio

Prior to measuring pressure-dependent rock samples, the pressure dependence of the axial set-up needs to be assessed. The three standard samples are measured as a function of confining pressure (Fig. 2.4) for given frequencies of  $f \in [0.1, 1, 10, 100]$  Hz. To ascertain the measurement stability, an axial stress of about  $\sigma \sim 2$  MPa is applied for all measurements. The measurements are compared to the static values found in the literature for all three samples.

For the three samples,  $E_{LF}$  (Fig. 2.4a) and  $\nu_{LF}$  (Fig. 2.4b) are independent of confining pressure. The result is consistent with earlier  $K$  measurements on these non-porous standard samples (?). Furthermore, for all measuring frequencies in the range of  $f \in [10^{-2} - 10^2]$  Hz,  $E_{LF}$  (Fig. 2.4a) and  $\nu_{LF}$  (Fig. 2.4b) of both glass and gypsum samples fit and are in good agreement with the published static data. Note from the plexiglass sample, that a frequency dependence is observed for all confining pressures. This effect is investigated in next subsection.

#### 2.3.1.2 Inferred bulk modulus

In the framework of linear elasticity, under the assumption of an isotropic material, it is possible to infer bulk (i.e.  $K_{ax}$ ) by combining the measured  $E_{LF}$  and  $\nu_{LF}$ . For all three samples, the pressure dependence of  $K_{LF}$  (Fig. 2.1a) and  $K_{HF}$  (Fig. 2.1b) have been measured in a previous study (?). For the three standard samples, the previously measured (i.e.  $K_{LF}$  and  $K_{HF}$ ) and inferred from this work (i.e.  $K_{ax}$ ) bulk moduli are compared as a function of pressure (Fig. 2.5).

For the three standard samples,  $K_{ax}$  fits with measurements using the different measuring set-ups (Fig. 2.1) for all confining pressures (Fig. 2.5). It thus indicates the reproducibility

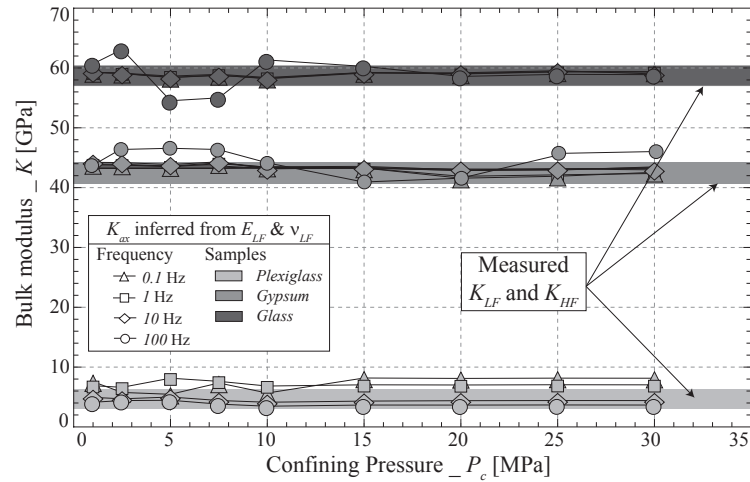


**Figure 2.5** : Pressure dependence of the standard samples' bulk modulus  $K_{ax}$ , inferred from  $E_{LF}$  and  $\nu_{LF}$ , for different frequencies of  $f = [0.1; 1; 10; 100]$  Hz. The  $K_{LF}$  and  $K_{HF}$  measured on the same samples (?) are reported for comparison

bility of the measurements using the different set-ups.

### 2.3.2 Frequency effect for the plexiglass sample

The frequency dependence of the plexiglass sample is further investigated to test the accuracy of the apparatus. Young modulus ( $E_{LF}$ ), Young attenuation ( $Q_E^{-1}$ ), and Poisson ratio ( $\nu_{LF}$ ) are measured as a function of frequency in the range  $f \in [10^{-2}; 10^2]$  Hz that is allowed by the apparatus. Although the frequency dependence of this material is known to vary from sample to sample (e.g., Madonna and Tisato, 2013), the measurements are compared to existing data (Batzle et al., 2006; Madonna et al., 2011; Tisato and Madonna, 2012) on plexiglass samples.

#### 2.3.2.1 Attenuation of plexiglass' Young modulus

To the authors' knowledge, Young attenuation ( $Q_E^{-1}$ ) is the plexiglass' elastic property that was the most measured (Batzle et al., 2006; Madonna et al., 2011; Tisato and Madonna, 2012). The frequency-dependent measurements of this property, compared to the existing datasets, are thus reported first (Fig. 2.6). The measured  $Q_E^{-1}$  shows values ranging between 0.04 and 0.08 over the frequency range of study.

A large attenuation peak, of about  $Q_E^{-1} = 0.08$ , is observed from the measurements at  $f = 15$  Hz. Comparing the present  $Q_E^{-1}$  data to reported data (Fig. 2.6), very similar behaviours are observed. Data reported by Madonna et al. (2011) and Tisato and Madonna (2012) show a similar peak at about  $\sim 0.08$  and the same frequency of  $\sim 15$  Hz. For the different temperatures (i.e. 23 deg C and 40 deg C) of measurement, the  $Q_E^{-1}$  peaks measured by Batzle et al. (2006) are slightly higher (i.e. 0.09 and 0.1) and at higher frequencies

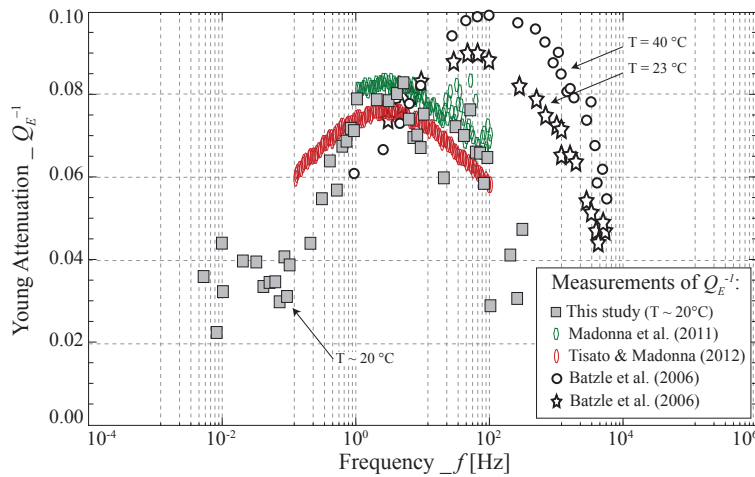


**Figure 2.6 :** Measured frequency dependence of Young attenuation  $Q_E^{-1}$  of the Plexiglass sample for a confining pressure of 10 MPa and an axial stress of 2 MPa. Existing LF measurements of  $Q_E^{-1}$  found in the literature (Batzle et al., 2006; Madonna et al., 2011; Tisato and Madonna, 2012) are reported for comparison.

(i.e.  $\sim 50$  Hz and  $\sim 100$  Hz). It indicates that the plexiglass investigated here and the ones of Madonna et al. (2011) and Tisato and Madonna (2012) are very similar and were measured under very similar "in-situ" conditions. Comparison with Batzle et al. (2006) results shows that the plexiglass they used and/or the "in-situ" measuring conditions are slightly different. As shown by Batzle et al. (2006), the  $Q_E^{-1}$  peak is shifted to higher magnitudes and higher frequencies as the temperature increases. The temperature during the present measurements was of about  $T = 20$  deg C, which could explain the lower magnitude in the  $Q_E^{-1}$  peak measured.

Finally, a small peak of  $Q_E^{-1} \sim 0.04$  (Fig. 2.6) appears at lower frequencies (i.e.  $f \in [5 \cdot 10^{-3}; 10^{-1}]$  Hz). Studies from the literature do not report measurements at frequencies lower than  $f = 10^{-1}$  Hz, so that no comparison can be made for this second peak. Note however that this second frequency-dependent variation correlates to the  $K_{LF}$  and  $Q_K^{-1}$  variations measured in the same frequency range (i.e.  $f \in [5 \cdot 10^{-3}; 5 \cdot 10^{-1}]$  Hz) for this plexiglass sample (?).

### 2.3.2.2 Elastic Dispersion on the plexiglass sample

Frequency dependent  $E_{LF}$  (Fig. 2.7a) and  $\nu_{LF}$  (Fig. 2.7b) are reported for the plexiglass sample. To understand the frequency-dependent variations, the measurements are compared to limit cases of (i) HF measurements (i.e.  $E_{HF}$  and  $\nu_{HF}$ ); and (iii) the static values found in the literature (e.g., Boudet and Ciliberto, 1998). In case of the frequency-dependent  $E_{LF}$ , an existing dataset is found in the literature that is also reported for comparison (Batzle et al., 2006).

A large frequency-dependent increase is observed on  $E_{LF}$  (Fig. 2.7a) that correlates to

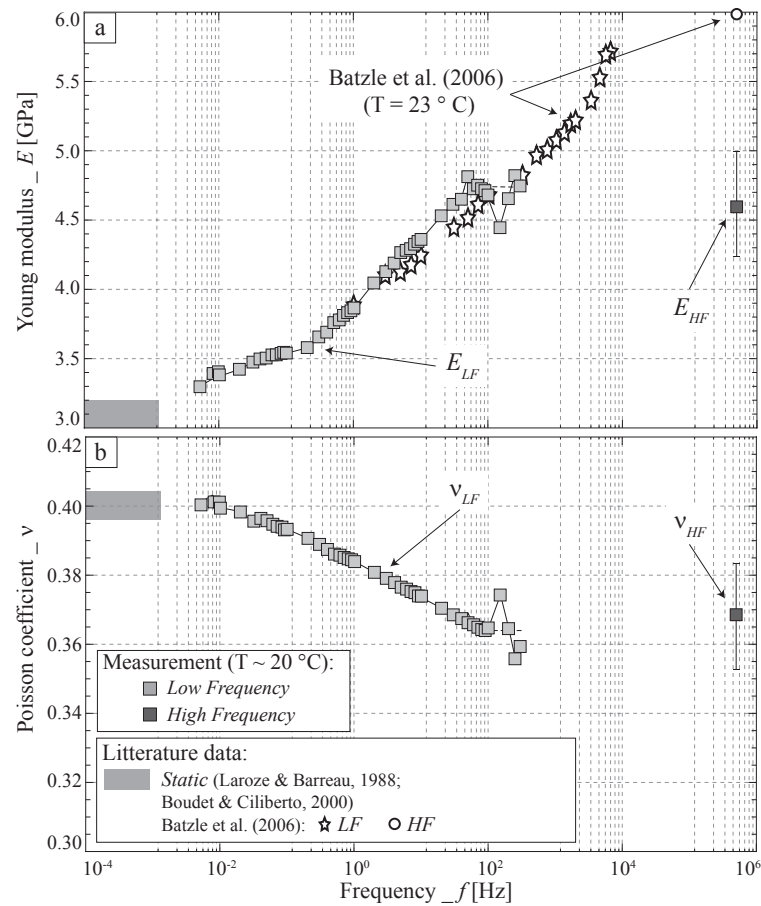


**Figure 2.7** : Measured frequency dependence of the (a) Young modulus  $E_{LF}$ ; (b) Poisson ratio  $\nu_{LF}$  of the Plexiglass sample for a confining pressure of 10 MPa and an axial stress of 2 MPa. HF measurements and static data from the literature are reported. In addition, existing data on  $E_{LF}$  and  $E_{HF}$  (Batzle et al., 2006) are reported for comparison.

the measured  $Q_E^{-1}$  (Fig. 2.6). Comparing to the end-values reported shows an overall consistency.  $E_{LF}$  at very low frequency is close to the static value from the literature (Boudet and Ciliberto, 1998). It increases with increasing frequency, up to a value at  $f = 10^2$  Hz close to that from ultrasonic measurement  $E_{HF}$ . This may indicate that no dispersion effect is expected in this sample at higher frequencies. As for  $Q_E^{-1}$  (Fig. 2.6),  $E_{LF}$  slightly differs from the one measured by Batzle et al. (2006) that keeps on increasing at frequencies higher than about  $f = 10^2$  Hz. The difference is to be related to the difference in the plexiglass used and/or the measuring conditions (e.g. temperature). Note finally that a slope change is observed at about  $f = 10^{-1}$  Hz, which correlates with the behaviour of  $Q_E^{-1}$  (Fig. 2.6).

In case of frequency-dependent Poisson ratio (i.e.  $\nu_{LF}$ ), the authors do not know of any existing measurement for plexiglass. The measurements are thus only compared to HF measurements and to the published static value (e.g., Boudet and Ciliberto, 1998). Overall,  $\nu_{LF}$  (Fig. 2.7b) shows a continuous decrease with increasing frequency. At low frequency

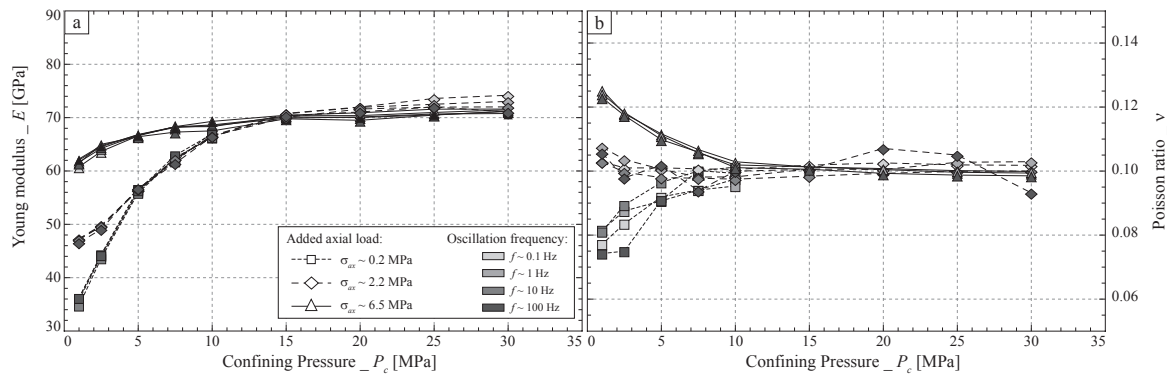


**Figure 2.8** : Measured pressure dependence of the (a) Young modulus ( $E_{LF}$ ) and (b) Poisson ratio ( $\nu_{LF}$ ) of the dry Fo7 for different values of axial load. Four different oscillation frequencies (i.e. symbols) of  $f \in [0.1, 1, 10, 100]$  Hz are chosen.

(i.e.  $f \sim 10^{-2}$  Hz), it is close to the literature static value of  $\nu_{stat} \sim 0.4$  (Boudet and Ciliberto, 1998). As frequency increases, it progressively decreases down to a value at  $f \sim 10^2$  Hz close to the one inferred from ultrasonic velocities of  $\nu_{HF} \sim 0.36$ . Consistently with the measured  $E_{LF}$  (Fig. 2.7a), no dispersion is thus expected in the frequency band of  $f \in [10^2; 10^6]$  Hz for this sample.

### 2.3.3 Effect of the static axial load on dry rock samples

As introduced earlier, the reported standard samples' properties were measured under a small deviatoric load of about  $\sigma_{ax} = 2$  MPa. This small axial load is needed (e.g., Subramanian et al., 2014) to (i) ascertain parallelism; and (ii) provide stable measurements. Since the standard samples are neither porous nor microcracked, this deviatoric load does not affect the sample's internal microstructure. However, sedimentary rocks contain microcracks that are sensitive to pressure. In that case, what is the effect of this  $\sigma_{ax}$ ?

#### 2.3.3.1 Change in overall behaviours with static axial load

The pressure dependence of  $E_{LF}$  and  $\nu_{LF}$  is reported (Fig. 2.8) for the dry Fo7 for three different axial loads of  $\sigma_{ax} = [0.2; 2.2; 6.5]$  MPa. Consistently, no frequency dependence is measured under dry conditions, and a dependence to confining pressure is observed. It appears that a small deviatoric load (i.e.  $\sigma_{ax} < 6.5$  MPa) strongly affects the resulting sample's elastic properties for confining pressures lower than about 10 MPa. For both  $E_{LF}$  (Fig. 2.8a) and  $\nu_{LF}$  (Fig. 2.8b), three distinct pressure-dependent curves are observed. At low confining pressures (i.e.  $P_c < 10$  MPa),  $E_{LF}$  appears to increase for an increasing value of  $\sigma_{ax}$ . Interestingly,  $\sigma_{ax}$  induces a clear change in  $\nu_{LF}$  (Fig. 2.8b) pressure dependency.

This shift in pressure dependencies measured on  $\nu_{LF}$  can be explained by a change in the rock's overall isotropic properties. Following Wang et al. (2012), the measured dry  $V_p/V_s$  ratio (i.e.  $\nu$ ) is expected to increase with increasing  $P_c$  for isotropic rocks. However,

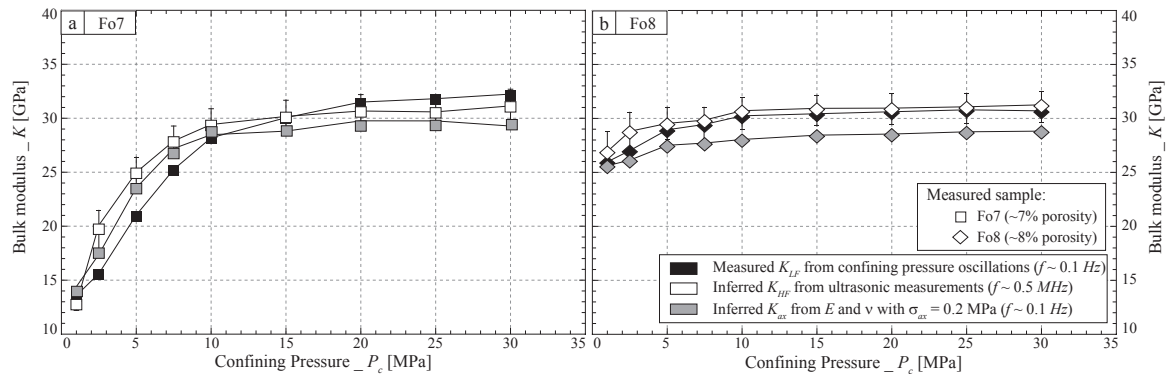


**Figure 2.9 :** Pressure dependence for the dry (a) Fo7 and (b) Fo8 samples of the bulk modulus measured using the different experimental set-ups (Fig. 2.1). The  $K_{ax}$ , inferred from  $E_{LF}$  and  $\nu_{LF}$  (Fig. 2.1c) at lowest axial load (i.e.  $\sigma_{ax} = 0.2$  MPa), is compared to the  $K_{LF}$  (Fig. 2.1a) and  $K_{HF}$  (Fig. 2.1b) measured under purely isotropic conditions (?).

it could decrease with increasing  $P_c$  for an anisotropic rocks if measured in the appropriate orientation. The rock is initially isotropic, the axial pressure (i.e.  $\sigma_{ax}$ ) closes the horizontal small aspect ratio microcracks, thus inducing an anisotropy.

### 2.3.3.2 Testing the sample's isotropy

In order to check the isotropy using the present measuring set-up, it is possible to compare the measurements to the ones measured under zero deviatoric stress. For that purpose, one can use  $K_{LF}$  and  $K_{HF}$ , measured under pure isotropic conditions (Fig. 2.1a & 2.1b). For dry Fo7 (Fig. 2.9a) and Fo8 (Fig. 2.9b) samples,  $E_{LF}$  and  $\nu_{LF}$  have been measured under the lowest added axial load (i.e.  $\sigma_{ax} = 0.2$  MPa). The inferred  $K_{ax}$  are compared to  $K_{LF}$  and  $K_{HF}$  measured on the same Fontainebleau samples (?).

At all confining pressures,  $K_{ax}$  falls in the uncertainty range of measured  $K_{LF}$  and  $K_{HF}$ . It implies that this added axial load is low enough, and that no stress-induced anisotropy effect is visible. As a consequence we choose to fix this static axial load in the following at  $\sigma_{ax} = 0.2$  MPa.

## 2.4 Effect of fluids on sandstone samples' Young modulus

The frequency and pressure dependence of the three main parameters have been investigated in both sandstone samples : (i) Young modulus ( $E_{LF}$ ); (ii) Young attenuation ( $Q_E^{-1}$ ); and (iii) Pseudo-consolidation parameter ( $\gamma^*$ ).

### 2.4.1 Pressure dependence of the samples' Young modulus

For both Fo8 (Figs. 2.10a & 2.10b) and Fo7 (Figs. 2.10c & 2.10d), the pressure dependence of  $E_{LF}$  has been investigated in case of the glycerine-saturated and water-saturated samples

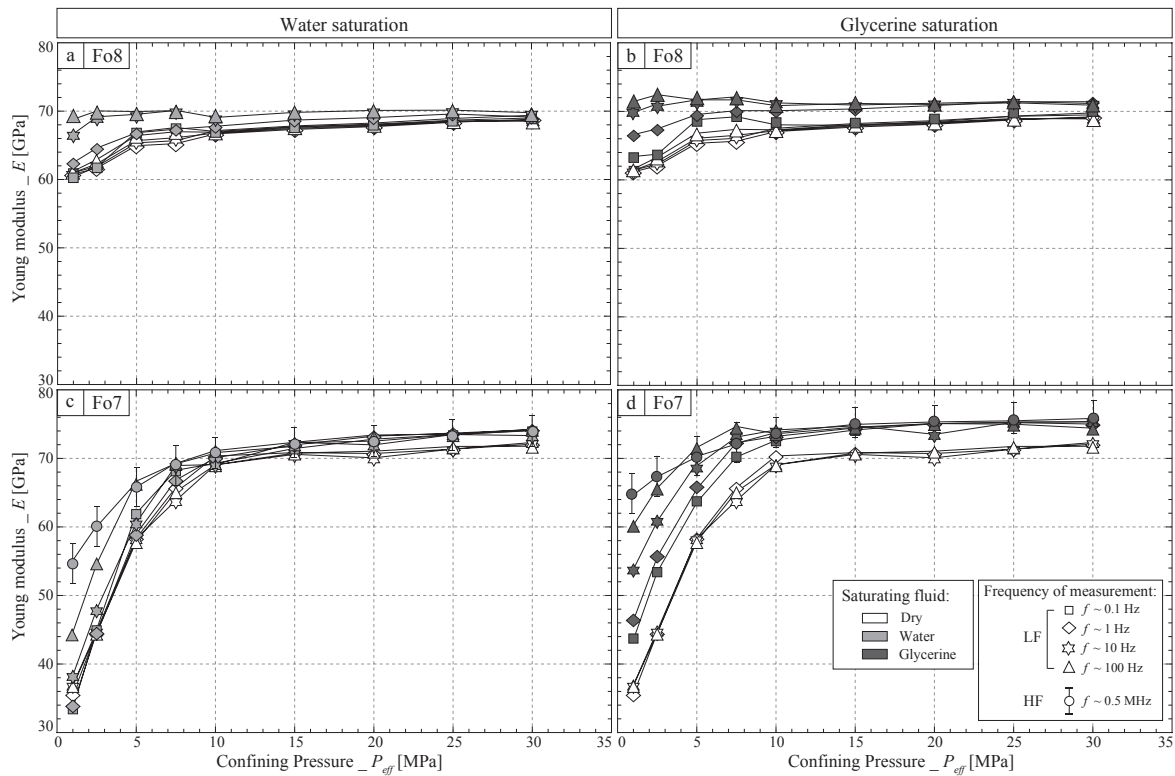


**Figure 2.10** : Measured pressure dependence of the Young modulus ( $E_{LF}$ ) of the dry and fluid-saturated (a-b) Fo8 and (c-d) Fo7. Four different oscillation frequencies (i.e. symbols) of  $f = [0.1; 1; 10; 100]$  Hz are chosen for the  $E_{LF}$  measurement. The fluid-saturated  $E_{HF}$  is also reported for Fo7 sample.

for four measuring frequencies of  $f = [0.1; 1; 10; 100]$  Hz. The dry  $E_{LF}$  are reported for comparison. The values of  $E_{HF}$  measured under fluid-saturated conditions are also reported for comparison in case of Fo7. Overall, the pressure dependence is very strong for Fo7 and weak for Fo8. Under fluid saturation, increasing the frequency leads to a large decrease in this pressure dependence for both rocks. At effective pressures beyond  $\sim 10$  MPa, the measurements are only slightly higher than the dry  $E_{LF}$  for all frequencies.

The Fo8 sample (Figs. 2.10a & 2.10b) shows no measurable pressure dependence under fluid-saturated conditions for frequencies higher than about  $f = 10$  Hz. Almost no difference between glycerine and water saturation is measured. Fo7 shows much larger effects. A clear distinction between fluid, pressure and frequency effects is observed. At confining pressures below 10 MPa, the fluid-saturated Young modulus increases with frequency, up to the measured  $E_{HF}$ . For any frequency, the glycerine-saturated Young modulus results higher than the water-saturated one.

## 2.4.2 Frequency dependence of Young modulus for Fo7 sample

The frequency dependence of Young modulus (i.e.  $E_{LF}$ ) and attenuation (i.e.  $Q_E^{-1}$ ), measured on Fo7 saturated by either water (Figs. 2.11a & 2.11c) or glycerine (Figs. 2.11b &

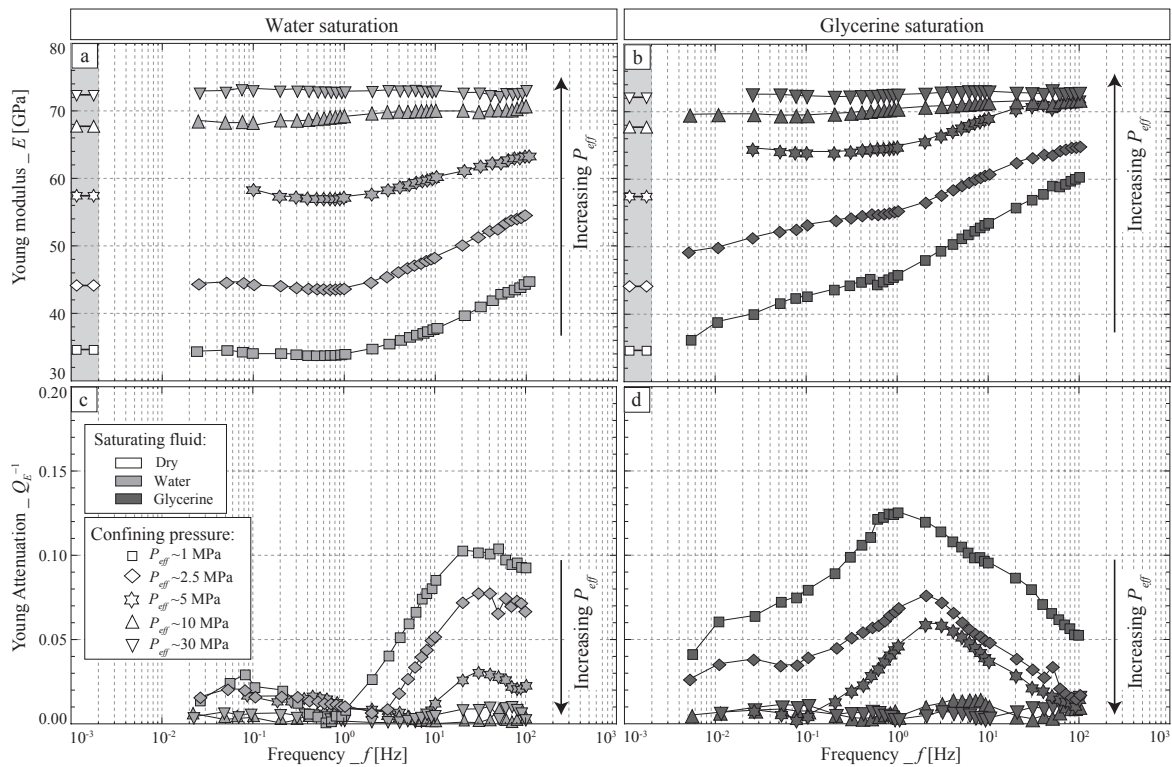


**Figure 2.11** : Measured frequency dependence of the Young (a-b) modulus  $E_{LF}$  and (c-d) attenuation  $Q_E^{-1}$  of Fo7 fully saturated by water or glycerine at different confining pressures.

2.11d) is reported for five different effective pressures up to  $P_{eff} = 30$  MPa. A large effect of frequency is measured on  $E_{LF}$  (Figs. 2.11a & 2.11b) that varies with both fluid and pressure. For a given  $P_{eff}$ , the increase of  $E_{LF}$  occurs at higher frequency and is of lower magnitude for the water-saturated case as compared to the glycerine one.

Furthermore, for both saturated cases,  $P_{eff}$  appears to damp the frequency dependence of  $E_{LF}$  and  $Q_E^{-1}$ . In particular, at  $P_{eff} \sim 30$  MPa, no frequency dependence is measured on both water- and glycerine-saturated  $E_{LF}$  and  $Q_E^{-1}$ . On the reverse, at the lowest  $P_{eff}$  conditions (i.e.  $P_{eff} = [1; 2.5]$  MPa) a large increase with frequency is observed. In the particular case of the glycerine-saturated sample at 1 MPa,  $E_{LF}$  increases from 38 GPa to about 60 GPa. A large  $Q_E^{-1}$  peak is associated with that increase. The  $Q_E^{-1}$  peak has a maximum of 0.12 at about  $f \sim 1$  Hz. The same observations are made at a  $P_{eff}$  of 2.5 MPa.

### 2.4.3 Frequency dependence of hydraulic properties

As introduced earlier, the stress-induced pore pressure oscillations in the dead volume are described through a pseudo-consolidation parameter  $\gamma^*$ . The frequency dependence of this property is investigated for Fo7 saturated by either water (Fig. 2.12a) or glycerine (Fig. 2.12b). The different effective pressures of  $P_{eff} = [1; 2.5; 5; 10; 30]$  MPa are investigated.

$\gamma^*$  decreases with increasing effective pressure at low frequency. Furthermore, for a gi-

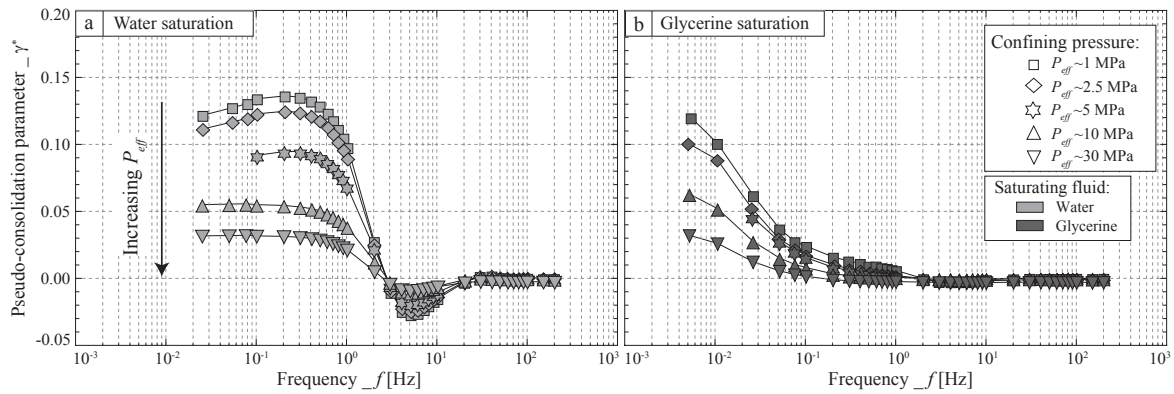


**Figure 2.12** : Measured frequency dependence of the pseudo-consolidation parameter for Fo7 fully saturated by (a) water or (b) glycerine at different confining pressures.

ven effective pressure,  $\gamma^*$  decreases when frequency increases in both water- and glycerine-saturated conditions. The glycerine case (Fig. 2.12b) shows a monotonous decrease down to  $\gamma^* = 0$  at about  $f = 1$  Hz. On the reverse, the water-saturated case (Fig. 2.12a) shows a sharp decrease between 0.2 Hz and 2 – 20 Hz.

The frequency-dependent decrease of  $\gamma^*$  corresponds to a decreasing fluid flow out of the sample (?). Under both water- and glycerine-saturated conditions, a frequency can be reached for which no flow out of the sample can be observed. In agreement with measurements of  $E_{LF}$  (Fig. 2.11a), the frequency of the observed decrease in fluid flow (i.e.  $\gamma^*$ ) occurs at much lower frequencies in case of the glycerine saturation.

## 2.5 Interpretation & Discussion

Large frequency-dependent variations in Young modulus and attenuation are measured that depend on the saturating fluid. In addition, the variations in  $\gamma^*$  indicate the existence of frequency-dependent fluid flow, which also depend on the saturating fluid. First, the role of the fluid's viscosity in these frequency-dependent variations is questioned and accounted for. Then, the measurements are interpreted in terms of fluid flow at different scales. Finally, the frequency-dependent  $E_{LF}$  and  $Q_E^{-1}$  measured on Fo7 are compared to the reported measurements of bulk modulus dispersion and attenuation on the same rock (?).

### 2.5.1 Viscosity effect and Apparent frequency

In the framework of the fluid flow theories, apparent frequency ( $f^*$ ) that accounts for fluid's viscosity ( $\eta_f$ ) and frequency ( $f$ ) in the same manner is a key parameter. It is defined as :

$$f_f^* = f \cdot \frac{\eta_f}{\eta_0}, \quad (2.3)$$

with  $\eta_0 = 10^{-3} \text{ Pa}\cdot\text{s}^{-1}$ , and  $\eta_f$  the fluid's viscosity.

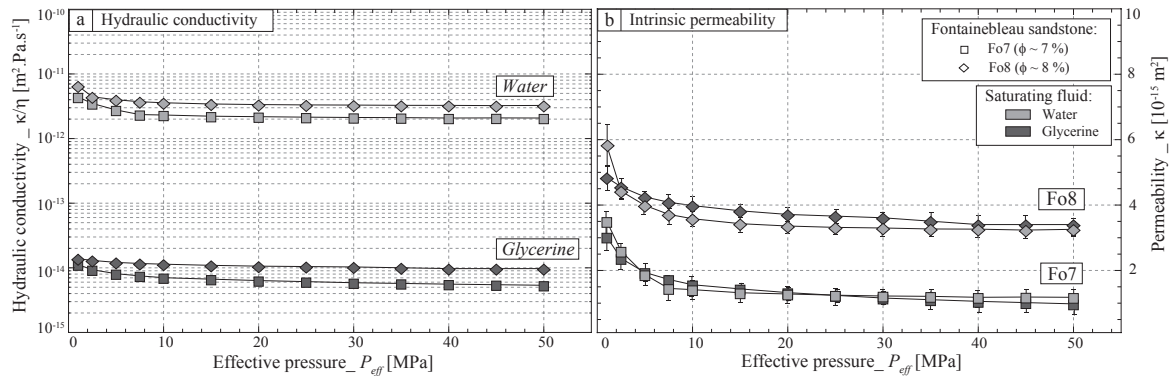


**Figure 2.13 :** (a) Measured hydraulic conductivities as a function of effective pressure for Fo7 (i.e. squares) and Fo8 (i.e. diamonds) saturated by either water or glycerine. (b) Inferred samples' intrinsic permeabilities as a function of effective pressure for Fo7 and Fo8. For both samples, the glycerine's viscosity chosen for the fit between water and glycerine is of  $\eta_{gly} = 350\eta_{wat} = 0.312 \text{ Pa} \cdot \text{s}^{-1}$ .

### 2.5.1.1 Assessment of fluids' in-situ viscosity

The samples' hydraulic conductivities are measured using the pressure gradient method (Figs. 2.2a & 2.2b) for the different  $P_{eff}$  under both glycerine and water saturation. Under quasi-static conditions, allowing for Darcy's law to apply, one directly obtains hydraulic conductivity ( $\kappa/\eta$ ) as a function of effective pressure (Fig. 2.13a).

From the measured hydraulic conductivities, about two-three orders of magnitudes separate the water-saturated measurements from the glycerine-saturated ones (Fig. 2.13a). Assuming the same permeability values for both fluids (Fig. 2.13b), the difference between fluids' "in-situ" viscosities does not correspond to the theoretical ratio (i.e.  $\eta_{wat}/\eta_{gly} \sim 1221$ ) but to the ratio  $\eta_{wat}/\eta_{gly} \sim 350$ . This ratio between water's and glycerine's viscosities (i.e.  $\eta_{gly} = 350\eta_{wat}$ ) fits for both Fo7 and Fo8 (Fig. 2.13b). The "in-situ" water viscosity is assumed to be  $\eta_{wat} = \eta_0$ . The resulting "in-situ" glycerine's viscosity is thus of  $\eta_{gly} = 350\eta_0$ . The values of "in-situ" viscosities being assessed for each fluid (i.e.  $\eta_f$ ), the apparent frequency  $f^*$  can be obtained. Considering the range of frequencies measured of  $f \in [5 \cdot 10^{-3}; 10^2]$  Hz, the apparent frequency range (i) for water saturation (i.e.  $\eta_{wat} = 10^{-3} \text{ Pa} \cdot \text{s}^{-1}$ ) is of  $f_{wat}^* \in [5 \cdot 10^{-3}; 10^2]$  Hz; and (ii) for glycerine saturation (i.e.  $\eta_{gly} = 0.35 \text{ Pa} \cdot \text{s}^{-1}$ ) is of  $f_{gly}^* \in [1.75; 0.35 \cdot 10^5]$  Hz.

### 2.5.1.2 Young modulus and attenuation variations with apparent frequency

The Young modulus and attenuation are plotted as a function of apparent frequency (Fig. 2.14) for different effective pressures of  $P_{eff} = [1; 2.5; 5; 10]$  MPa. No variations are observed for  $P_{eff} = 30$  MPa so that this case is not considered here. The frequencies allowed by the apparatus lead to measurements over the apparent frequency range of  $f^* \in [10^{-3}; 10^5]$  Hz. Furthermore, some measurements under different saturation conditions have the same apparent frequency.

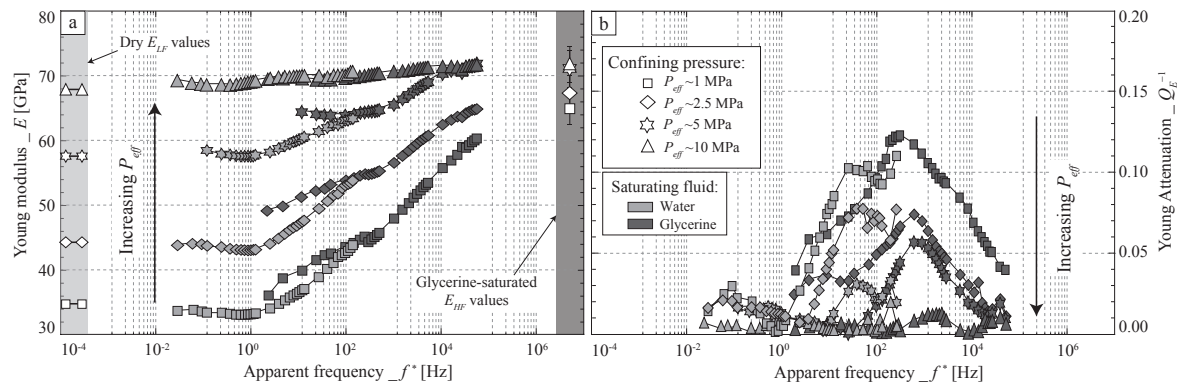


**Figure 2.14** : Inferred dependence to apparent frequency of the (a) Young modulus  $E_{LF}$ ; and (b) Young attenuation  $Q_E^{-1}$  of the fully saturated Fo7. The water's and glycerine's viscosities, allowing to fix the apparent frequency, are respectively of  $\eta_{wat} = 10^{-3} \text{ Pa}\cdot\text{s}^{-1}$  and  $\eta_{gly} = 0.35 \text{ Pa}\cdot\text{s}^{-1}$ . Different effective pressures of  $P_{eff} = [1; 2.5; 5; 10] \text{ MPa}$  are reported. Dry  $E_{LF}$  and glycerine-saturated  $E_{HF}$  values are reported for comparison.

Overall, a good fit is obtained between measurements of Young moduli (Fig. 2.14a) under either water or glycerine saturation. At low effective pressure  $P_{eff} \in [1; 2.5; 5] \text{ MPa}$ , a progressive increase in modulus is measured with increasing apparent frequency. At lowest effective pressure, this increase is as large as about 30 GPa over the range of apparent frequencies. For all effective pressures, the increase in  $E_{LF}$  with apparent frequency shows a slope change at a frequency of 100 Hz. In addition,  $Q_E^{-1}$  (Fig. 2.14b) presents a large peak for  $f^*$  close to  $10^2 \text{ Hz}$ . The peak shows the same magnitude for both water- and glycerine-saturated cases, but occurs at slightly higher  $f^*$  for the glycerine-saturated case. At  $P_{eff} = 10 \text{ MPa}$  and beyond, very little variations are measured on both  $E_{LF}$  and  $Q_E^{-1}$ .

In the low  $P_{eff}$  range and for  $f^* \in [1; 50] \text{ Hz}$ ,  $E_{gly} > E_{wat}$ . This could be related to the fluids' intrinsic bulk modulus, which is higher for glycerine (i.e. 4.4 GPa) than for water (i.e. 2.2 GPa).

## 2.5.2 Fluid flow at different scales in Fo7

As reported in ?, both drained/undrained and undrained/unrelaxed transitions are expected in the investigated frequency range (i.e.  $f^* \in [10^{-3}; 10^5] \text{ Hz}$ ) for Fo7 sample. How well do the present results fit with this previous interpretation ?

### 2.5.2.1 Observed transitions between regimes

In the drained regime, fluid has time to flow in and out of a given Representative Elementary Volume (REV), so that this case corresponds to the dry one. Measurements under water-saturated conditions at frequencies lower than  $f^* = 1 \text{ Hz}$  (Fig. 2.14a) also prove to correspond to such regime. In the undrained regime, fluid mass is constant within a REV, and  $K_{ud}$  results higher than the drained  $K_d$ . The data from ? fit to the drained/undrained transition in the range of  $f^* \in [1; 10^2] \text{ Hz}$ , the undrained  $K_{ud}$  being reached at frequencies

below  $f^* = 10^2$  Hz. This same theoretical transition could explain the increase of  $E_{LF}$  observed at frequencies below  $f^* = 10^2$  Hz (Fig. 2.14a). Furthermore, a small plateau might be observed at about  $f^* = 10^2$  Hz, that could indicate an undrained regime. If, in agreement with poroelasticity, the shear modulus is constant (i.e.  $G_{ud} = G_d$ ), it is indeed expected that  $E_{ud}$  should be higher than  $E_d$ . The observed variations are consistent with the predicted cut-off frequency for this transition, expected to take place at  $f_1^* = 10$  Hz (?).

In the unrelaxed domain, fluid has no time to flow from one inclusion (i.e. pore or crack) to the neighbouring one. The relaxed/unrelaxed transition is expected to take place at higher frequency than the drained/undrained one, and lead to larger elastic moduli. This second transition could explain the increase in  $E_{LF}$  starting from the plateau at  $f^* = 10^2$  Hz up to the large  $E_{HF}$  value (Fig. 2.14a). This interpretation is consistent with the predicted cut-off frequency for this second transition that is expected to take place at  $f_2^* = 10^3$  Hz (?).

One may thus consider that the data for  $E_{LF}$  variations (Fig. 2.14a) could be related to the (i) drained to undrained transition, in the range of  $f^* \in [10^0; 10^2]$  Hz; and (ii) relaxed to unrelaxed transition, in the range of  $f^* \in [10^2; 10^5]$  Hz. Then, the attenuation data is expected to show two distinct attenuation peaks, at the frequencies of  $f_1^*$  and  $f_2^*$  respectively. This is not the case (Fig. 2.14b). A possible explanation is that the two transitions are too close, so that the two attenuation peaks overlap. The pressure has a strong effect on these two transitions, so that at  $P_{eff} = 10$  MPa and beyond, no variation is observed.

### 2.5.2.2 Dispersion and attenuation in terms of Zener model

Using Zener viscoelastic model, it is possible to infer the frequency-dependent dispersions and attenuations expected in case of the drained/undrained and relaxed/unrelaxed transitions. From the general theory of linear viscoelastic response (e.g., Nowick and Berry, 1972), a transition between two regimes associated with a change in elastic modulus (i.e. modulus dispersion) should also be associated to some energy absorption (i.e.  $Q^{-1}$  peak). Within such framework, dispersion and attenuation phenomena correlate. Their frequency dependence can be investigated using a specific viscoelastic model. Zener model uses a combination of a spring (of stiffness/modulus  $M_a$ ) in series with a parallel assemblage of a spring (of stiffness/modulus  $M_b$ ) and a dashpot (of viscosity  $\eta_b$ ). Noting that  $M_0^{-1} = M_a^{-1} + M_b^{-1}$  and  $\tau_0 = \eta_b (M_a + M_b)^{-1}$ , it can be shown that the complex modulus  $\bar{M}(\omega)$  takes the form :

$$\bar{M}(\omega) = \frac{M_0 + i\omega\tau_0 M_a}{1 + i\omega\tau_0}, \quad (2.4)$$

where  $\omega = 2\pi f$  is the pulsation, and  $\tau_0$  is the characteristic relaxation time. Noting that  $\bar{M}(\omega) = M_R(\omega) + iM_I(\omega)$ , one determines the magnitude  $M(\omega) = \sqrt{M_R^2 + M_I^2}$  and attenuation  $Q^{-1}(\omega) = M_I/M_R$ .

To apply such viscoelastic model, three parameters (i.e.  $M_a$ ,  $M_b$  and  $\eta_b$ ) need to be inferred. From limits considerations,  $M_a$  and  $M_0$  are obtained respectively at highest and lowest

frequencies of the transition of interest. Furthermore,  $\eta_b$  may be obtained from the knowledge on the characteristic relaxation time  $\tau_0$  (or critical frequency  $f_c$ ) of the effect. Finally, one may infer these parameters either from direct measurements or from assumed theories. In particular, Zener model allows to predict the dispersion/attenuation curves expected in the case of drained/undrained or relaxed/unrelaxed transitions if the elastic properties of the three regimes are known. For these two transitions, the two critical frequencies  $f_c$  chosen are assumed to be  $10^1$  Hz (i.e.  $f_1^*$ ) and  $10^3$  Hz (i.e.  $f_2^*$ ).

We apply the Zener model (Eq. 4) to our data using for  $E_{ud}$  either the measured value at  $10^2$  Hz (i.e.  $E_{ud}^{meas}$ ) or that predicted from Biot-Gassmann equation (i.e.  $E_{ud}^{th}$ ). Note that, for each prediction, we use Zener model twice because we have two transitions. We assume that the drained (i.e.  $E_d$ ) and unrelaxed (i.e.  $E_{ur}$ ) Young moduli are known. They are obtained from the data, i.e.  $E_d = E_{dry}$  and  $E_{ur} = E_{HF}$ . We calculate for  $E$  and  $Q_E^{-1}$  two distinct curves depending on the choice of  $E_{ud}$ . The first one, using only the data, corresponds to a transition from  $E_d$  to  $E_{ud}^{meas}$  (i.e. drained/undrained) and from  $E_{ud}^{meas}$  to  $E_{ur}$  (i.e. relaxed/unrelaxed). The second one, using Biot-Gassmann prediction, relates to a transition from  $E_d$  to  $E_{ud}^{th}$  (i.e. drained/undrained) and from  $E_{ud}^{th}$  to  $E_{ur}$  (i.e. relaxed/unrelaxed). The two dispersion and attenuation curves are compared to the dataset (Fig. 2.15) for two effective pressures of  $P_{eff} = [1; 2.5]$  MPa. The Biot-Gassmann prediction of the undrained Young modulus is shown for comparison.

In case of Young modulus dispersion (Figs. 2.15a & 2.15b), the measurements at 1 and 2.5 MPa show the same overall behaviours and lead to the same interpretations. The Zener plot using Biot-Gassmann prediction is slightly below the Zener plot using the data for the drained/undrained transition. The Zener plot using  $E_{ud}^{meas}$  fits the data frequency dependence for the drained/undrained transition, but deviates from it in case of the undrained/unrelaxed transition. For all  $f^* > 10^2$  Hz, the plot overestimates the measurements, indicating that the measured dispersion is "slower" than expected in case of an unique frequency effect. This effect may be explained by a distribution in microcracks of differing aspect ratio inside this natural rock.

The measured  $Q_E^{-1}$  (Figs. 2.15c & 2.15d) show a peak similar in amplitude to the ones predicted by Zener plots in the case of the drained/undrained transition. For the relaxed/unrelaxed transition, both Zener plots overestimate the peak.

### 2.5.3 Young modulus and bulk modulus variations

Bulk modulus  $K_{LF}$  and attenuation  $Q_K^{-1}$  were measured on the same sample (?). The two datasets are reported in Fig. (2.16a). As in the previous section, the measurements are plotted as a function of apparent frequency and compared to two Zener plots. Again, both drained regime (i.e.  $K_d$  and  $E_d$ ) and unrelaxed regime (i.e.  $K_{ur}$  and  $E_{ur}$ ) are directly measured. The sole difference between the two Zener plots is in the choice for the value of the undrained regime. The first Zener plot is obtained using the measured undrained

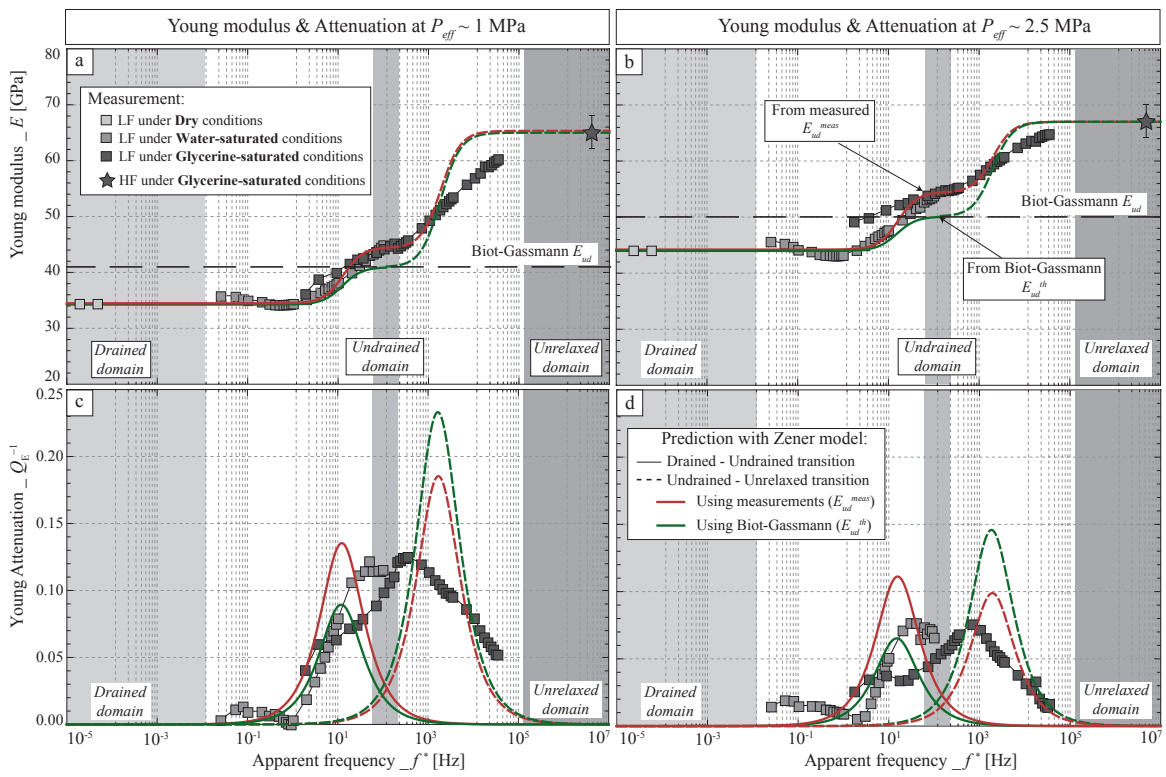


**Figure 2.15** : Measured (a-b) Young modulus and (c-d) attenuation of the fluid-saturated Fo7 as a function of  $f^*$  for  $P_{eff} = [1; 2.5]$  MPa. Measurements are compared to the Zener-like variations expected for the drained/undrained (i.e. filled curve) and relaxed/unrelaxed (i.e. dashed curve) transition. Two curves are predicted using the measured  $E_{ud}^{meas}$  (i.e. red) and predicted  $E_{ud}^{th}$  (i.e. green) undrained Young modulus.

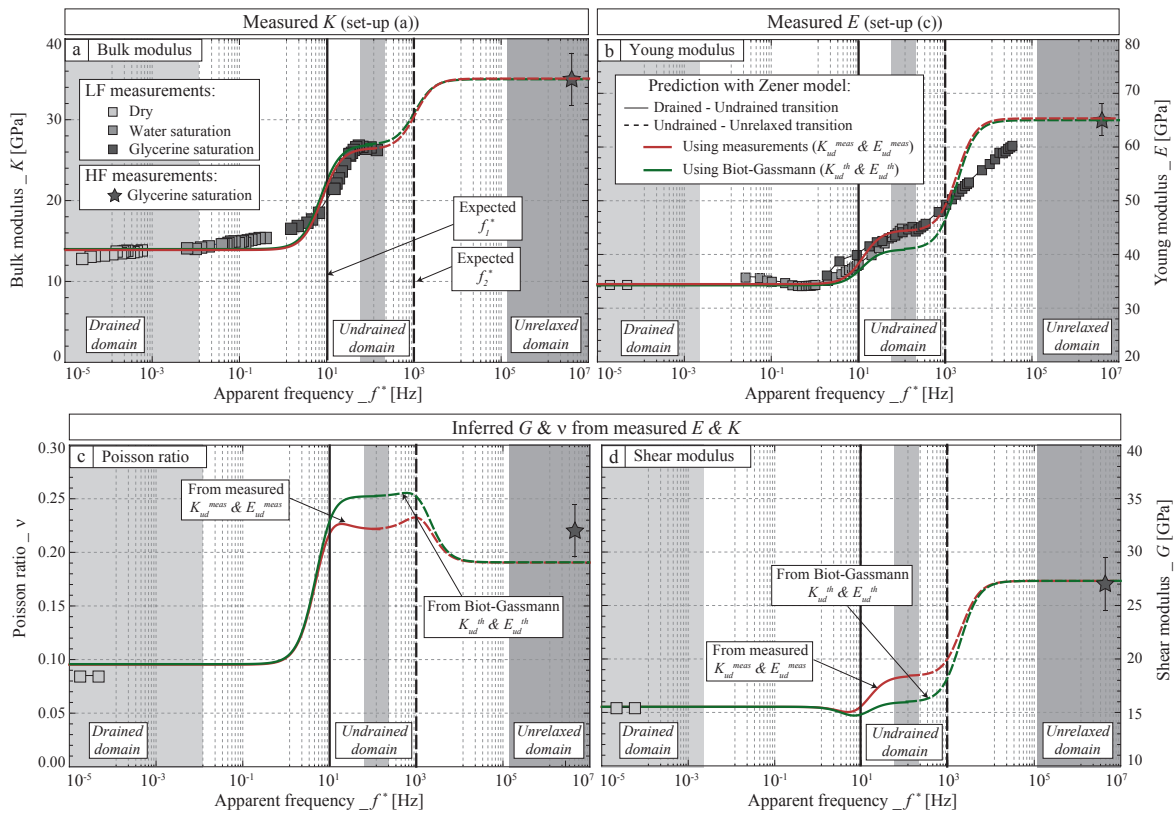


**Figure 2.16 :** (a-b) Measured and (c-d) inferred elastic properties of Fo7 as a function of  $f^*$  for  $P_{eff} = 1$  MPa. The measured (i.e. symbols) (a) Bulk modulus (?) and (b) Young modulus are compared to Zener-like predicted drained/undrained (i.e. filled curves) and undrained/unrelaxed (i.e. dashed curves) transitions. (c) Poisson ratio and (d) shear modulus inferred from the Zener-like predictions of  $K$  and  $E$ .

modulus (i.e.  $E_{ud}^{meas}$  and  $K_{ud}^{meas}$ ). The second Zener plot is obtained using Biot-Gassmann prediction (i.e.  $E_{ud}^{th}$  and  $K_{ud}^{th}$ ).

### 2.5.3.1 Dispersions in elastic moduli

Assuming linear isotropic elasticity, it is possible to infer from  $E$  and  $K$  both the Poisson ratio  $\nu$  and the shear modulus  $G$ . As the bulk and Young modulus datasets do not cover the same frequency range,  $\nu$  and  $G$  are inferred using the calculated Zener plots (Figs. 2.16c & 2.16d). Measured data on dry  $\nu_d$  and glycerine-saturated  $\nu_{HF}$  and  $G_{HF}$  are reported, along with  $G_d$  inferred from the measured  $\nu_d$  and  $E_d$ . For both  $\nu$  and  $G$ , an increase is observed between the dry LF and glycerine-saturated HF data. Yet, the two elastic properties show different behaviours at intermediate frequencies.

For the shear modulus (Fig. 2.16d), both Zener plots show a monotonous increase with frequency. Using Biot-Gassmann theory (i.e.  $E_{ud}^{th}$  and  $K_{ud}^{th}$ ), no change in  $G$  for the drained/undrained transition is predicted. The little variation observed corresponds to a numerical artefact from combining  $K$  and  $E$  Zener plots. The  $G$  dispersion is expected to occur during the relaxed/unrelaxed transition. Using the direct data fit (i.e.  $E_{ud}^{meas}$  and  $K_{ud}^{meas}$ ), a

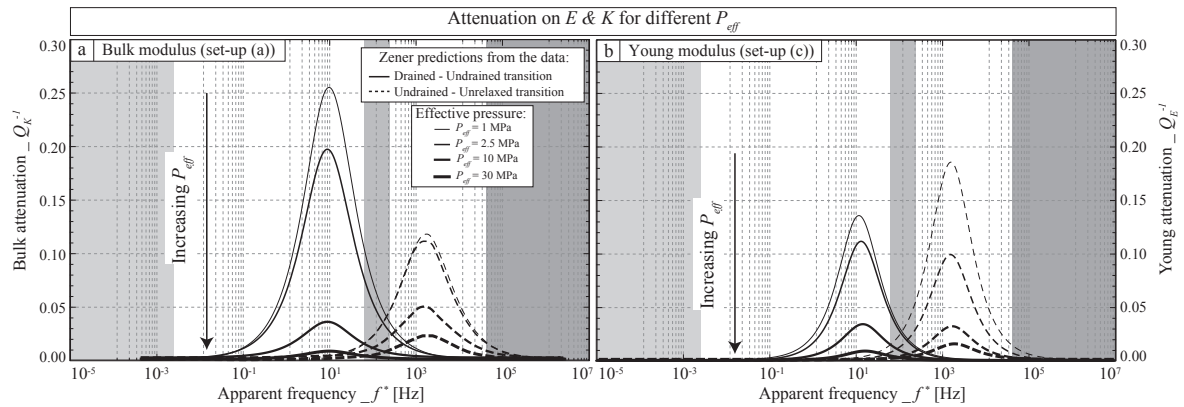


**Figure 2.17** : Comparison between the frequency-dependent attenuations on  $K$  and  $E$  for varying pressures of  $P_{eff} = [1; 2.5; 10; 30]$  MPa. The attenuations are obtained using Zener model from the measured dispersions in  $K$  and  $E$ .

slight increase of  $G$  is however predicted for the drained/undrained transition such that  $G_{ud} > G_d$ . The relaxed/unrelaxed transition is again predicted to result in a large increase of  $G$ . Note that this result for the relaxed/unrelaxed transition is expected from effective medium theories for a fully-saturated rock.

Both Zener plots for  $\nu$  (Fig. 2.16c) show an increase from 0.1 up to 0.25 at intermediate frequencies, corresponding to the drained/undrained transition. As frequency increases, a decrease is then inferred down to 0.19 at higher frequencies. This bell-shaped curve indicates that the undrained  $\nu_{ud}$  is predicted to be higher than the unrelaxed  $\nu_{ur}$ . This behaviour is in fact consistent with Effective Medium Theories calculations for a microcracked rock.

### 2.5.3.2 Attenuations for the different transitions

Using Zener plots fitted to the dispersion data, a comparison can be proposed for  $Q_K^{-1}$  (Fig. 2.17a) and  $Q_E^{-1}$  (Fig. 2.17b) for different pressures of  $P_{eff} = [1; 2.5; 10; 30]$  MPa.

Two strong attenuation peaks are predicted for both  $Q_K^{-1}$  and  $Q_E^{-1}$  at low effective pressures. Both attenuation peaks decrease when increasing  $P_{eff}$ , which is consistent with the fact that the microcracks progressively close when increasing the confining pressure. At  $P_{eff} = 1$  MPa,  $Q_K^{-1}$  (Fig. 2.17a) is predicted to be larger for the drained/undrained transition than for the relaxed/unrelaxed one. The reverse is predicted for  $Q_E^{-1}$  (Fig. 2.17a). This difference originates from the fact that  $E$  combines both  $K$  and  $G$ . As  $G$  is not expected to show any dispersion for the drained/undrained transition,  $Q_E^{-1}$  should consistently be lower than  $Q_K^{-1}$  for this transition.

## 2.6 Conclusion

Calibration of a new set-up with two standard samples (i.e. glass and gypsum) shows that Young modulus and Poisson ratio can be measured in the frequency range of  $f \in$

$[5 \cdot 10^{-3}; 10^2]$  Hz. Bulk and shear moduli can be inferred from these data. The results, fit well with previously published data. No pressure and frequency dependency of the apparatus is observed. Using the plexiglass sample, measurements on Young modulus dispersion and attenuation are consistent with previous measurements. The new set-up is accurate over the frequency range of  $f \in [5 \cdot 10^{-3}; 10^2]$  Hz.

The pressure dependence of Young modulus has been measured at different frequencies on well-known sandstone samples saturated by water and glycerine. One sample shows small variations. The other one exhibits strong pressure- and frequency-dependent variations. This second sample has been further investigated as a function of frequency for both saturating fluids. Large frequency-dependent variations have been measured on Young modulus and attenuation. The key parameter for these effects, defined as the apparent frequency  $f^*$ , combines frequency and the fluids' viscosity in the same manner. The frequency-dependence of Young modulus and attenuation have been investigated over the frequency range of  $f^* \in [10^{-3}; 10^5]$  Hz. The measurements using different fluids compare favourably, and both drained/undrained and relaxed/unrelaxed transitions have been measured on Young modulus. Combining present results with previous ones on bulk modulus, Poisson ratio and shear modulus have been inferred over the frequency range. Poisson ratio appears to be strongly frequency dependent and shows a large bell-shaped variation. The shear modulus shows a slight evidence of a dispersion associated to the drained/undrained transition, and a stronger variation associated with the relaxed/unrelaxed transition.

## Acknowledgements

Yves Pinquier and Dr. Alexandre Schubnel are thanked for their technical help in setting up the measuring system.

---

### Effect of fluids and frequencies on Poisson ratio (*GRL, submitted*)

---

L. Pimienta, J. Fortin and Y. Guéguen, Effect of fluids and frequencies on the Poisson ratio of a sandstone sample, (2015), *Geophysical Research Letters*, Submitted.

---

#### Abstract

Poisson ratio is an important parameter when interpreting measured geophysical and seismic data. For an isotropic medium, it directly relates to the ratio of P- and S-wave velocities. Using the stress-strain method, Poisson ratio  $\nu$  is measured as a function of fluid nature, pressure and frequency on a Fontainebleau sandstone. Strong dependencies to the three parameters are observed, and bell-shaped variations of  $\nu$  are measured as a function of frequency. Two clear  $Q_\nu^{-1}$  peaks are observed that correlate to these variations. A good agreement between the water- and glycerine-saturated measurements is obtained. A clear bell-shaped dispersion is observed, which holds for all effective pressures. Using effective medium theories, it is shown that the frequency-dependent bell-shaped variation can be expected in porous microcracked rocks if both drained/undrained and relaxed/unrelaxed transitions occur. For this rock,  $V_p/V_s$  ratio is also expected to show a frequency-dependent bell-shaped variation.

### 3.1 Introduction

Sedimentary rocks saturated by fluids are known to be dispersive materials. Their frequency-dependent behaviours originate from fluid movements in the rock's porous network induced by the seismic waves. When comparing field and laboratory measurements, the frequency dependence of the measured P- and S-wave velocities needs to be considered (e.g., Mavko and Nur, 1975; O'Connell and Budiansky, 1977; Cleary, 1978; Winkler and Nur, 1979; Le Ravalec and Guéguen, 1996). The velocity ratio  $V_p/V_s$ , known as a good fluid indicator, may be frequency-dependent (e.g., Mavko and Jizba, 1991; Wang et al., 2012). In isotropic materials,  $V_p/V_s$  depends only on Poisson ratio, an intrinsic material's property. Yet, little is known on the effect of frequency on this property.

To measure and understand experimentally these dispersion/attenuation effects in the laboratory, the stress-strain method is promising. It usually allows for elastic measurements over wide frequency and pressure ranges up to about  $f \in [10^{-3}; 10^3]$  Hz and  $P_c \in [0; 100]$  MPa respectively (e.g., Subramaniyan et al., 2014). The method applied to axial stress oscillations is by far the most used (e.g., Spencer Jr., 1981; Batzle et al., 2001, 2006; Adam et al., 2009; Tisato and Madonna, 2012; Madonna and Tisato, 2013; Mikhaltsevitch et al., 2014). Yet, only the frequency dependence of Young modulus and attenuation is usually reported. Only Mikhaltsevitch et al. (2013) report a Poisson ratio measured on a limestone sample, which is in their case frequency independent.

In this study, Poisson ratio  $\nu$  and  $Q_v^{-1}$  are measured in the frequency and pressure ranges of  $f \in [5 \cdot 10^{-3}; 10^2]$  Hz and  $P_c \in [0; 30]$  MPa in a fluid-saturated sandstone sample. The results are interpreted in terms of fluid-flow theories, and using Effective Medium Theories.

### 3.2 Samples & Experimental procedure

#### 3.2.1 Samples

Three standard samples were chosen to test the measuring set-up : (i) A synthetic glass sample made of amorphous silica (Mallet et al., 2013); (ii) A pure gypsum sample (Brantut et al., 2012); and (iii) A plexiglass (PMMA) sample (e.g., Batzle et al., 2006). All three are homogeneous and isotropic media of known static and dynamic elastic properties, and have no porosity. In addition, plexiglass is a viscoelastic material whose elastic properties are frequency-dependent (e.g., Batzle et al., 2006).

Fontainebleau sandstone is a well-known reference rock. Both framework grains and cement are pure quartz, making up a clean sandstone of about  $\sim 99.9\%$  qtz (Bourbie and Zinszner, 1985; Gomez et al., 2010). The rock can consistently be assumed homogeneous and isotropic at the Representative Elementary Volume (REV) scale. The sample investigated has a porosity of about 7% (i.e. Fo7), and permeability of  $4 \cdot 10^{-15}$  m<sup>2</sup>. It originates from

the same block as in ?.

### 3.2.2 Experimental apparatus & procedure

#### 3.2.2.1 Apparatus & Low frequency set-up

The sample is radially enclosed by a rubber jacket to be separated from the confining medium (i.e. oil). Lateral fluid flow is thus prevented. Measurements are conducted in an oil-confining triaxial apparatus (Fortin et al., 2005) that can be used in two different set-ups thanks to an axial piston that can be shifted vertically. In the first set-up, the axial piston is not in contact with the end-platen (and thus the sample), allowing for studying the sample under pure isotropic conditions. LF bulk modulus (i.e.  $K_{LF}$ ) and attenuation (i.e.  $Q_K^{-1}$ ), and ultrasonic P- and S-wave velocities can be measured with this set-up (?). A second set-up has been built in order to measure the LF Young modulus (i.e.  $E_{LF}$ ) and Poisson ratio (i.e.  $\nu_{LF}$ ) in the frequency range of  $f \in [10^{-3}; 10^2]$  Hz. This second set-up is the focus of the present contribution. For each pressure step in the pressure range of  $[1; 30]$  MPa, small axial stress oscillations were applied. The same experiment was conducted for three cycles, i.e. under room dry, glycerine-saturated then water-saturated conditions. Under fluid (i.e. glycerine and water) full saturation, a pore pressure of  $p_f = 2$  MPa is maintained. For each measurement under fluid saturation, valves are closed so that the experimental system, composed of the sample's pore volume and the tubing's dead volume (i.e.  $V_d = 6.6$  mL), is undrained. Owing to the existence of the large dead volume and of the sample's intrinsic storage capacity (e.g., Ghabezloo and Sulem, 2010), the sample is not necessarily undrained (?). Terzaghi effective pressure  $P_{eff} = P_c - p_f$  is used that allows for comparison between dry and fluid-saturated conditions.

The axial stress is exerted by a **PI** piezo-electric actuator scheduled to function in the range of  $f \in [10^{-3}; 10^2]$  Hz and electrical amplitudes of  $A \in [10; 1000]$  V, with a maximum displacement of  $30 \mu\text{m}$ . This actuator transforms the electric amplitude in a stress-dependent displacement/strain. To measure the samples' axial and radial strains, three pairs of axial and radial **FCB**  $350 \Omega$  strain gages of 6 mm length are directly glued to the samples' half-length. All the strain gages used are the same and are mounted in a one-fourth Wheastone bridge, allowing to discard possible bias by using different gages (e.g., Adam et al., 2006). Strains oscillations are recorded using **Catman** recording system.

#### 3.2.2.2 Strains' amplitude : Poisson ratio $\nu$

The confining pressure is maintained constant (i.e.  $\Delta P_c = 0$ ) and an added oscillating axial stress is exerted to the sample (i.e.  $\Delta \sigma_{ax} \neq 0$ ). For each frequency of axial stress oscillation, axial and radial strains are recorded. Following the elastic theory for a homogeneous/isotropic cylindrical sample, LF Young modulus ( $E_{LF}$ ) and Poisson ratio ( $\nu_{LF}$ ) may be inferred from such measurements (e.g., Batzle et al., 2006). A typical processing method

is applied to the signal (?), namely (i) Phase picking in Fourier domain following a usual procedure (e.g., Batzle et al., 2006; Madonna and Tisato, 2013; Mikhaltsevitch et al., 2014) to obtain the phase shifts ; (ii) Filtering in Fourier domain ; and (iii) Linear regression, and its related accuracy assessment.

In this article, Poisson ratio is of interest. The sample's Poisson ratio (i.e.  $\nu_{LF}$ ) is obtained from a linear regression between radial and axial strains. The data scatter around the linear regressions (i.e.  $\nu_{LF}$ ) is used to infer a statistical error, noted  $\Delta\nu_{LF}$ . Because the quartz Poisson ratio  $\nu_{qtz}$  is of  $\sim 0.1$  (e.g., Mavko et al., 2003) and the radial strains cannot be measured for strains lower than  $\Delta\epsilon \sim 5 - 8.10^{-7}$ , axial strains are fixed to be lower than  $5 - 8.10^{-6}$ . This value is expected to remain in the elastic domain, i.e. lower than about  $\sim 10^{-5}$ .

### 3.2.2.3 Strains' phase : Factor $Q_v^{-1}$

Assuming an isotropic linear viscoelastic medium in which the imaginary parts remain small (Winkler and Nur, 1979), Young modulus attenuation  $Q_E^{-1}$  and bulk modulus attenuation  $Q_K^{-1}$  can be defined. Relations between  $Q_K^{-1}$ ,  $Q_E^{-1}$ ,  $Q_p^{-1}$  and  $Q_s^{-1}$  (i.e. P- and S-waves attenuations), and the material's Poisson ratio  $\nu$  are found (see Winkler and Nur (1979) for instance) by further assuming that (i) the complex moduli can be substituted for their corresponding real moduli in the linear elasticity relations ; and (ii) the attenuation (i.e.  $Q^{-1}$ ) is equal to the modulus' imaginary part (i.e.  $Im(M)$ ) to real part (i.e.  $Re(M)$ ) ratio. The shear modulus (i.e.  $G$ ) attenuation is in fact  $Q_G^{-1} = Q_s^{-1}$ .

Under the same considerations, the quality factor  $Q_v^{-1}$  can be defined for the Poisson ratio. In practice,  $Q_E^{-1}$  and  $Q_K^{-1}$  are defined as the tangent of the phase shift (i.e. difference) between stress and strain. Similarly,  $\nu_{LF}$  being measured as the ratio of the radial over axial strain, its  $Q_v^{-1}$  factor is obtained as the tangent of the phase shift between axial and radial strains.

## 3.3 Results : Effect of pressure and frequency on Poisson ratio

### 3.3.1 Poisson ratio of standard samples

For the three standard samples, the pressure dependence of  $\nu_{LF}$  and  $Q_v^{-1}$  is investigated (Figs. 3.1a & 3.1b) for the measuring frequencies of  $f = [0.1; 1; 10; 100]$  Hz. Consistently, the measured  $\nu_{LF}$  (Fig. 3.1a) in both glass and gypsum samples fits with the literature data, and  $Q_v^{-1}$  (Fig. 3.1b) remains lower than 0.01 for all frequencies and pressures. Only for the viscoelastic plexiglass sample a deviation from the static measurement is observed on  $\nu_{LF}$ . In addition,  $\nu_{LF}$  and  $Q_v^{-1}$  show a clear dependence to frequency that holds for all pressures.

For the viscoelastic Plexiglass sample,  $\nu_{LF}$  and  $Q_v^{-1}$  are measured (Figs. 3.1c & 3.1d) in

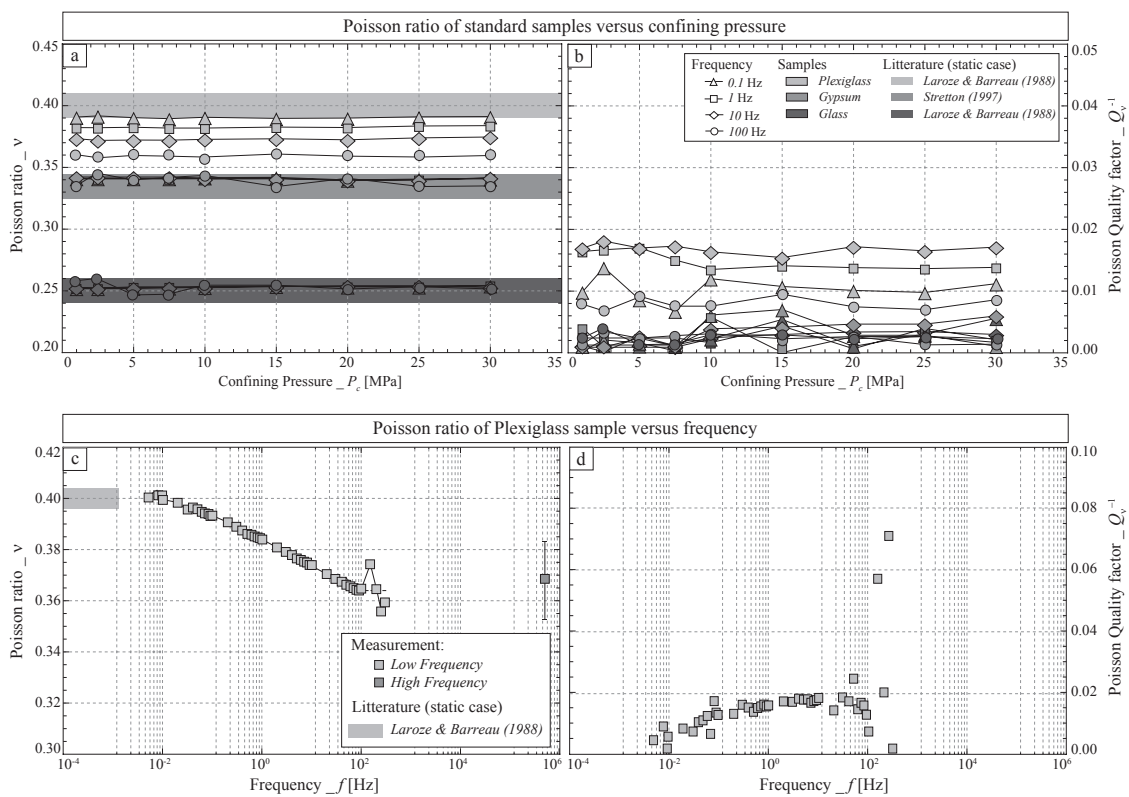


**Figure 3.1 :** Measured pressure dependent (a) Poisson ratio and (b) its intrinsic attenuation of the three standard samples for four frequencies of  $f = [0.1; 1; 10; 100]$  Hz. Data from the literature, measured under static conditions, is reported for comparison. The frequency-dependent (c) Poisson ratio and (d) Poisson quality factor is also reported for the Plexiglass sample.

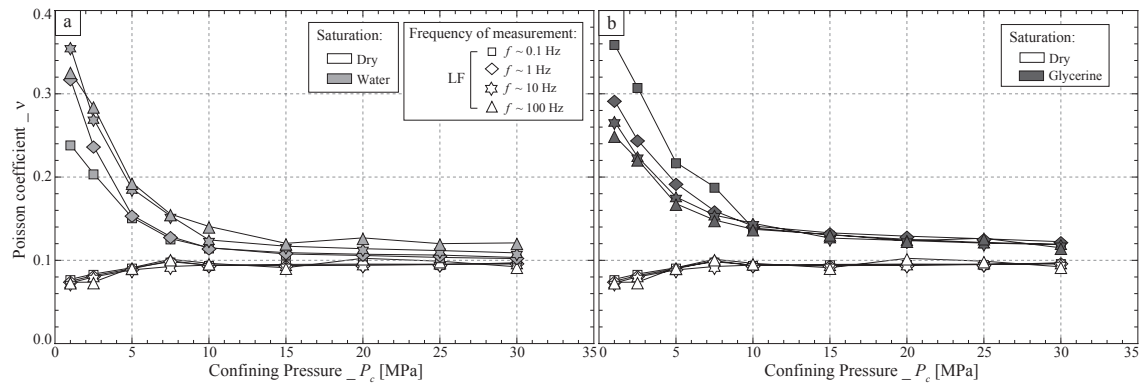


**Figure 3.2 :** Measured pressure dependent Poisson ratio of Fo7 saturated by either (a) water or (b) glycerine. The added axial load applied for the measurement's stability was  $\sigma_{ax} = 0.2$  MPa.

the frequency range of  $f \in [10^{-3}; 10^2]$  Hz. The measured  $\nu_{LF}$  (Fig. 3.1c) shows a frequency-dependent decrease that is consistent with both the static value reported (Boudet and Ciliberto, 1998) and the value  $\nu_{HF}$  inferred from ultrasonic velocities (?). It correlates to the frequency dependence of  $Q_v^{-1}$  (Fig. 3.1d).

### 3.3.2 Dependence to fluids and pressure

The pressure dependence of Poisson ratio  $\nu_{LF}$  of the 7% Fontainebleau sample under dry, water- and glycerine-saturated conditions is reported (Fig. 3.2) for four measuring frequencies of  $f = [0.1; 1; 10; 100]$  Hz. The dry measurements are compared to either water-saturated (Fig. 3.2a) and glycerine-saturated (Fig. 3.2b) conditions.

Under dry conditions, an increase in  $\nu_{dry}$  (Fig. 3.2) is measured with increasing confining pressure. This behaviour is expected if microcracks are progressively closed by the increasing pressure (Wang et al., 2012). When saturating the rock by an incompressible fluid (i.e. water or glycerine), large increases are observed on  $\nu_{LF}$ . Effective pressure strongly damps the differences between dry and fluid-saturated  $\nu_{LF}$ , so that all measurements converge to a value near 0.1 at  $P_{eff} = 30$  MPa. At low  $P_{eff}$ , the frequency dependence however differs for the two saturating fluids. Under water saturation,  $\nu_{LF}$  shows an increase with increasing frequency, up to  $f = 10$  Hz beyond which it decreases. Under glycerine saturation,  $\nu$  decreases with increasing frequency.

### 3.3.3 Dependence to fluids and frequencies

The frequency dependence of Poisson ratio is investigated (Fig. 3.3) in the case of the Fo7 sandstone sample saturated by either water or glycerine. The pressures of measurements are  $P_{eff} = [1; 2.5; 5; 10; 30]$  MPa. For both saturating fluids, large frequency-dependent variations of both  $\nu_{LF}$  and  $Q_v^{-1}$  are observed and the evolutions show some similarities.

When frequency increases,  $\nu_{LF}$  first increases and then decreases beyond some cha-

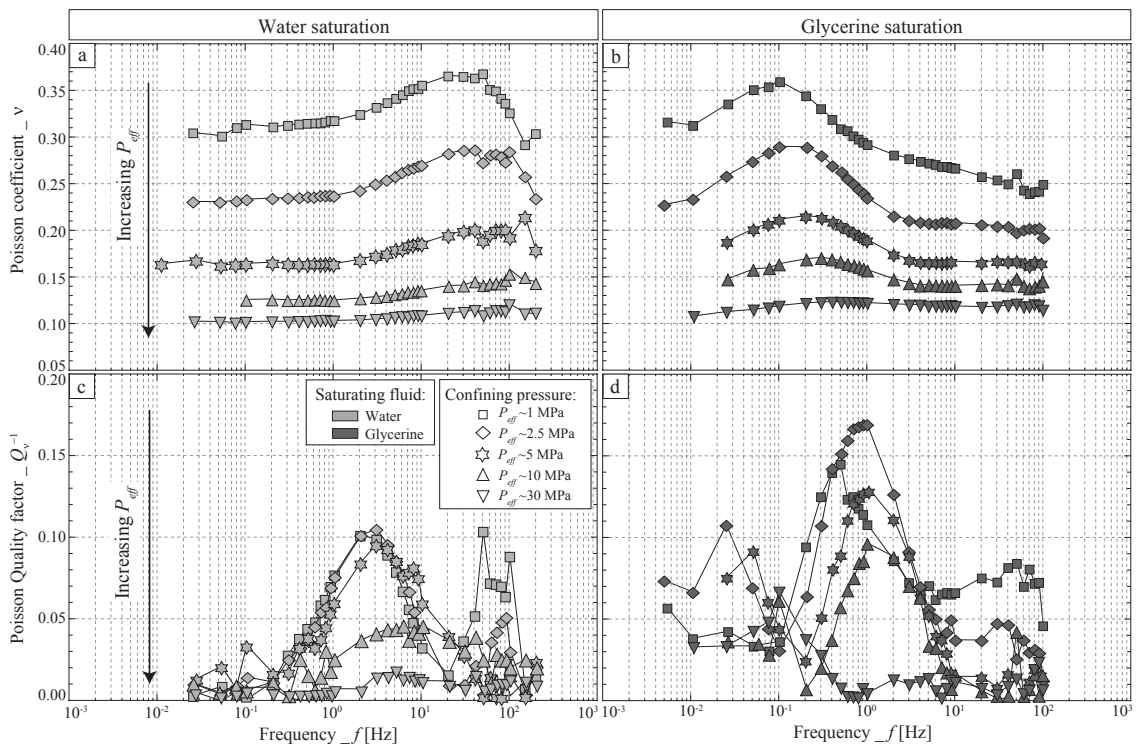


**Figure 3.3 :** Frequency dependence of the (a) Poisson ratio  $\nu_{LF}$  and (b)  $Q_v^{-1}$  factor of the 7% porosity Fontainebleau sandstone sample (i.e. Fo7) saturated by either water or glycerine. The measurements are obtained at different effective pressures of  $P_{eff} = [1; 2.5; 5; 10; 30]$  MPa.

racteristic frequency value. This bell-shaped variation corresponds to the observations of pressure-dependent measurements on Fo7 (Fig. 3.2). For any  $P_{eff}$  below 30 MPa, the frequency-dependent bell-shaped curve of  $\nu_{LF}$  is observed for both fluids' saturations. The amplitudes of the variations are identical with both fluids, but the variations are shifted in frequency. For water saturation (Fig. 3.3a), the bell-shaped's maximum occurs at about 20 – 50 Hz. Under glycerine saturation (Fig. 3.3b), the maximum is observed at lower frequencies, of about 0.1 Hz. Note that the maxima shift to slightly higher frequencies as  $P_{eff}$  increases.

For both fluids' saturations, two  $Q_v^{-1}$  peaks are observed in the investigated frequency range. The first peak takes place at a frequency for which  $\nu_{LF}$  increases. The second one takes place at a frequency for which  $\nu_{LF}$  decreases. The  $Q_v^{-1}$  measured under either water (Fig. 3.3c) or glycerine (Fig. 3.3d) saturation shows peaks of similar magnitudes but at differing frequencies.

### 3.4 Interpretation : Fluid flow and effective medium theories

Frequency dependence of elastic properties in fluid-saturated rocks is understood as fluid flow at different scales that induce transitions between elastic regimes. We discuss below the interpretations in terms of existing theories.

#### 3.4.1 Fluid-flow theories and frequency dependence of elastic properties

In the framework of the fluid flow theories, two transitions between three elastic regimes are expected in the seismic frequency range ( $f \in [10^{-3}; 10^6]$  Hz). A characteristic frequency can be inferred for each transition. The first transition is from drained to undrained regimes, and is ruled by the time constant (or critical frequency  $f_1$ ) for fluid flow over the sample's length  $L$  (Cleary, 1978) :

$$f_1 = \frac{4kK_d}{\eta L^2}, \quad (3.1)$$

where  $k$  and  $K_d$  are the rock permeability and the drained bulk modulus respectively, and  $\eta$  is the fluid viscosity. The second transition is from undrained to unrelaxed regimes, and is ruled by the time constant (or critical frequency  $f_2$ ) for fluid flow out of the rock's microcracks (O'Connell and Budiansky, 1977) :

$$f_2 = \frac{\bar{\zeta}^3 K_d}{\eta}, \quad (3.2)$$

where  $\bar{\zeta}$  is the averaged microcracks' aspect ratio.

Both  $f_1$  and  $f_2$  appear to depend inversely on the fluid's viscosity ( $\eta_f$ ), so that apparent frequency ( $f^*$ ) that accounts for fluid's viscosity ( $\eta_f$ ) and true frequency ( $f$ ) in the same

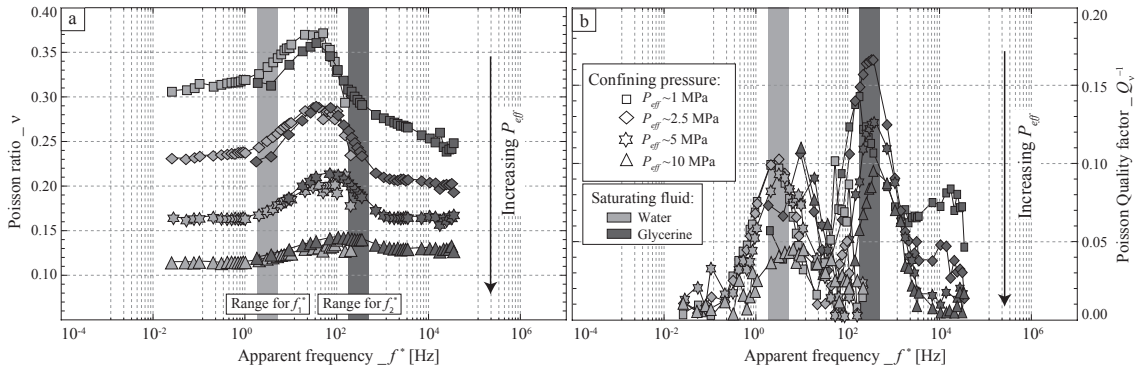


**Figure 3.4 :** Inferred dependence to apparent frequency  $f^*$  of (a)  $\nu_{LF}$  and (b)  $Q_v^{-1}$  for the 7% Fontainebleau sandstone (Fo7). The values are measured for different values of effective pressures of  $P_{eff} = [1; 2.5; 5; 10]$  MPa. The cut-off frequencies  $f_1^*$  and  $f_2^*$  are obtained from the  $Q_v^{-1}$  peaks.

manner is a key parameter. It is defined as :

$$f_f^* = f \cdot \frac{\eta_f}{\eta_0}, \quad (3.3)$$

with  $\eta_0 = 10^{-3} \text{ Pa}\cdot\text{s}^{-1}$ , and  $\eta_f$  the fluid's viscosity. To obtain a direct "in-situ" measurement of this fluid's viscosity parameter, the hydraulic conductivity ( $\kappa/\eta$ ) is measured as a function of effective pressure. Assuming the same permeability values for both fluids, the ratio between fluids' "in-situ" viscosities corresponds to  $\eta_{wat}/\eta_{gly} \sim 350$ . Considering the range of  $f \in [5 \cdot 10^{-3}; 10^2]$  Hz, the apparent frequency range is (i) of  $f_{wat}^* \in [5 \cdot 10^{-3}; 10^2]$  Hz for water saturation (i.e.  $\eta_{wat} = 10^{-3} \text{ Pa}\cdot\text{s}^{-1}$ ); and (ii) of  $f_{gly}^* \in [1.75; 0.35 \cdot 10^5]$  Hz for glycerine saturation (i.e.  $\eta_{gly} = 0.35 \text{ Pa}\cdot\text{s}^{-1}$ ). The critical frequencies can also be redefined as  $f_1^*$  and  $f_2^*$ . Using values for  $K_d$ ,  $k$  and  $\zeta$  obtained for this rock (?),  $f_1^*$  and  $f_2^*$  are at about 10 Hz and 1 kHz respectively for this rock sample.

Poisson ratio  $\nu_{LF}$  and quality factor  $Q_v^{-1}$  are compared to apparent frequency for different pressures of  $P_{eff} = [1; 2.5; 5; 10]$  MPa (Fig. 3.4). The frequencies allowed by the apparatus lead to measurements under different saturation conditions that have the same apparent frequency. A good fit is obtained between measurements. Interestingly, the maximum values of  $\nu_{gly}$  and  $\nu_{wat}$  perfectly fit for all effective pressures (Fig. 3.4a) so that clear bell-shaped curves are observed and a continuum is observed with increasing  $f^*$  on the  $\nu_{LF}$  measurement. No dependence to the fluids' intrinsic compressibility is observed. The measured  $Q_v^{-1}$  (Fig. 3.4b) show a good fit between water and glycerine saturations. The apparent frequencies correlate for both fluids, and two  $Q_v^{-1}$  peaks are observed.

The characteristic frequencies of the  $Q_v^{-1}$  peaks are found to be of 5 Hz and 500 Hz respectively, which are both near the expected value for  $f_1^*$  and  $f_2^*$ . The measured Poisson ratio  $\nu$  dispersions and  $Q_v^{-1}$  seem thus a very good proxy of both transitions between elastic regimes.

As  $P_{eff}$  increases, the magnitude in  $\nu_{LF}$  variations decreases, which may relate to the

closure of pre-existing microcracks (e.g., Adelinet et al., 2011). Note further that the characteristic frequency for the bell-shaped's maximum of  $\nu_{LF}$  slightly increases as  $P_{eff}$  increases. The same variation with frequency is observed on the  $Q_\nu^{-1}$  peaks. It implies that  $P_{eff}$  has a second smaller effect, which leads to an increase in the frequency of both dispersion/attenuation phenomena.

### 3.4.2 Effective medium theories and values of $\nu$ in the three elastic regimes

The approach of Adelinet et al. (2011) can be used to predict the  $\nu$  values for the three elastic regimes expected in the frequency range of study (i.e.  $f \in [10^{-3}; 10^6]$  Hz), i.e. drained, undrained and unrelaxed regimes. This approach combines Biot-Gassmann and effective medium theories. In Adelinet et al. (2010, 2011), the rocks investigated were basalts, composed of a large amount of equant pores and a small quantity of microcracks. Sedimentary rocks exhibit a microstructure that can schematically be considered as bearing pore families of differing compressibilities (e.g., Fortin et al., 2007; Guéguen and Kachanov, 2011).

Using the model of Adelinet et al. (2011), the drained (i.e.  $K_d$  and  $G_d$ ) and unrelaxed (i.e.  $K_{ur}$  and  $G_{ur}$ ) regimes are built by predicting respectively the effective elastic properties of the dry and fluid-saturated medium. The intermediate undrained regime (i.e.  $K_{ud}$  and  $G_{ud} = G_d$ ) is then attained from the drained one using Biot-Gassmann fluid substitution theory. Poisson ratio ( $\nu$ ) is simply inferred from  $K$  and  $G$  for each of the three regimes from the relation :

$$\nu = \frac{3K - 2G}{2(3K + G)}. \quad (3.4)$$

The crack density  $\rho$  variations account for the pressure-dependent elastic properties. Predictions for the three regimes are thus tested as a function of this parameter (Fig. 3.5). For this prediction (i) the sample's porosity (7%) is chosen; (ii)  $K_s$  and  $G_s$  are the ones of the quartz (Mavko et al., 2003); (iii)  $\nu_{ud}$  and  $\nu_{ur}$  are predicted for a glycerine-saturated medium; (iv) different values of  $\xi$  are tested for the unrelaxed prediction.

While  $\nu_d$  decreases, a large increase is observed for both  $\nu_{ud}$  and  $\nu_{ur}$  as  $\rho$  increases (i.e. as  $P_{eff}$  decreases). A strong dependence to the aspect ratio  $\xi$  is observed on the variations predicted for  $\nu_{ur}$ , and an increase is predicted as  $\xi$  decreases. Although the measurements are clearly underestimated by the modelled  $\nu_{ud}$  and  $\nu_{ur}$ , it remains of interest to investigate the different tendencies. The undrained  $\nu_{ud}$  is larger than the unrelaxed  $\nu_{ur}$  if the microcrack's aspect ratio is large enough. Then, the relation  $\nu_d < \nu_{ur} < \nu_{ud}$  holds. Note that the same relation between the three regimes has been previously reported (See Fig.2 from Wang et al. (2012)).

As the unrelaxed regime should always exist at higher frequencies than the undrained one, this relation between regimes explains the measured bell-shaped variations.

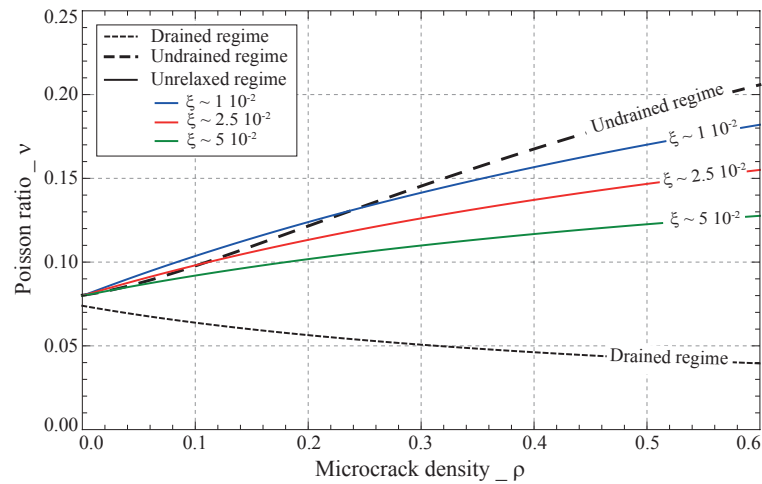


**Figure 3.5 :** Predicted dependence to the microcracks' density  $\rho$  of Poisson ratio of a porous (i.e.  $\phi_p = 7\%$ ) and microcracked rock under dry and glycerine-saturated conditions.  $\nu_d$ ,  $\nu_{ud}$  and  $\nu_{ur}$  are predicted using Adelinet et al. (2011) approach. For  $\nu_{ur}$  predictions, different aspect ratio in the range of  $\zeta \in [5 \cdot 10^{-3}; 1 \cdot 10^{-2}]$  are tested.

### 3.4.3 Experimental limits in the drained regime

At frequencies below 0.5 Hz, a large deviation is observed between  $\nu_{LF}$  measured under water saturation and under dry conditions. The dry  $\nu_{LF}$  should however be equal to the drained  $\nu$  value. This implies that the measured  $\nu_{LF}$  under water saturation is not purely drained. The explanation is that the boundary conditions of the experiment prevent the measurement of the "drained"  $\nu$ . The boundary condition responsible for this effect is found to be in the existence of a dead volume at both sample's ends. Although large (i.e.  $V_d = 6.6$  mL), this dead volume induces a pore pressure increase in the sample that leads to a measured  $\nu_{LF}$  larger than  $\nu_d$ . If the dead volume was very large, the measurement is expected to equal  $\nu_d$ . As shown in Fig. (3.6a), this experimental bias is important, leading to a dispersion from drained to undrained regimes that is underestimated by the measurement.

### 3.4.4 Inferred $V_p/V_s$ ratio

In an elastic isotropic homogeneous medium, a direct relationship links  $V_p/V_s$  to the material's Poisson ratio  $\nu$  (e.g., Wang et al., 2012). Although the boundary conditions affect the measurements for frequencies below 0.5 Hz, the inferred  $V_p/V_s$  ratio can be calculated in the seismic frequency range for the case of  $P_{eff} = 1$  MPa (Fig. 3.6b).

Interestingly, the same bell-shaped variations is calculated for  $V_p/V_s$  ratio as  $f^*$  increases, with a maximum value of 2.2 for the undrained domain. The magnitudes of the variations largely decrease with increasing effective pressure, and are constant at 1.5 beyond 30 MPa.

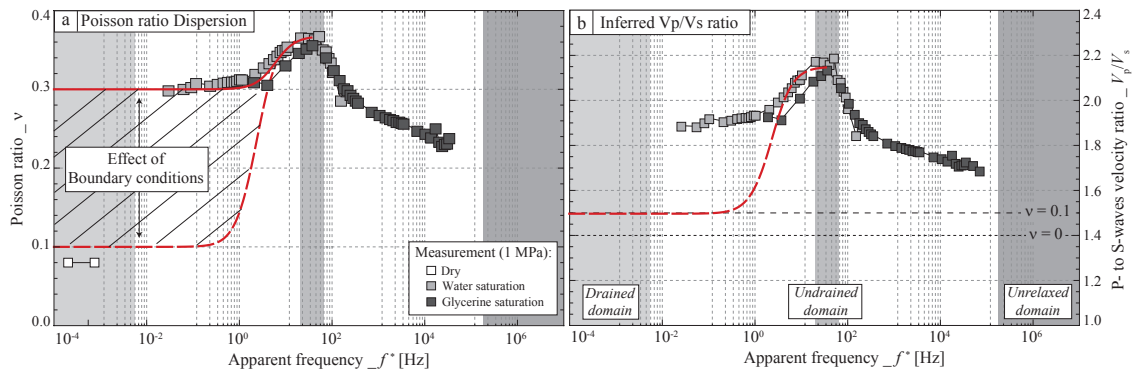


**Figure 3.6 :** (a) Frequency dependence of the measured  $\nu$  under fluid saturation (i.e. symbols and continuous curve) compared to the expected drained/undrained transition using the dry measurement (i.e. dashed curve). (b) Inferred  $V_p/V_s$  ratio as a function of  $f^*$  for the fluid-saturated Fo7 sample. The chosen pressure is of  $P_{eff} = 1$  MPa. Zener model is used to predict the dispersion curves for the drained/undrained transition.

### 3.5 Conclusion

Pressure and frequency-dependent Poisson ratio and  $Q_v^{-1}$  factor are investigated on a Fontainebleau sandstone under dry and fluid-saturated conditions. Large dependences to fluids, pressures and frequencies are observed, and frequency-dependent bell-shaped variations are measured. Accounting for fluids' viscosity in the same manner as frequency, an apparent frequency  $f^*$  is defined, and the frequency range is  $f^* \in [10^{-3}; 10^5]$  Hz. No fluid's compressibility effect is observed. These variations are shown to be consistent with a theoretical interpretation using effective medium theory. At high pressure, cracks are closed and the variations are very small. The ratio of P- and S-wave velocities are finally inferred over the seismic frequency range. Frequency-dependent bell-shaped variations are again observed.

### Acknowledgements

Y. Piquier and A. Schubnel are thanked for their technical help. All the data presented in this paper (Figs. 1, 2 and 3) are available upon request to the corresponding author.

---

## Discussions & Perspectives

---

A strong effect of fluids and frequencies on the measured Poisson ratio has been highlighted. The measurements however show behaviours that need to be better understood. For this purpose, additional measurements on different rocks were made. Furthermore, the use of poroelasticity proved useful in giving a first order interpretation/correction of the effect.

### 4.1 Effect of fluids on Poisson ratio of sandstone samples

While only measurements on the Fo7 sandstone were reported so far, Poisson ratio was measured on different sandstone samples. In addition to Fontainebleau samples of differing porosities (i.e. Fo4, Fo8 and Fo9), the elastic response of Berea sandstone samples has been investigated. The Berea samples used originate from the same block, and have a porosity of about 19.3 % (i.e. Be19) and 19.7 % (i.e. Be20). Their permeability was measured under water saturation, and is of about  $5 \cdot 10^{-14} \text{m}^2$  for both rock samples.

#### Accounting for the fluid's viscosity

The frequency dependence of Poisson ratio (i.e.  $\nu_{LF}$ ) and attenuation (i.e.  $Q_v^{-1}$ ) of Be19, Be20, Fo7 and Fo8 are measured under different fluids' saturations. For all samples, two saturating fluids are used. The first fluid, common for all rock samples, is the highly viscous pure glycerine. In case of the Fontainebleau samples, the second measurement is made for a saturation by pure water. In case of the two Berea samples, the second fluid chosen is a water-glycerine mixture, i.e. of a viscosity lower than glycerine yet higher than water.

From the measured hydraulic conductivities (Fig. 4.1a), and assuming the same per-

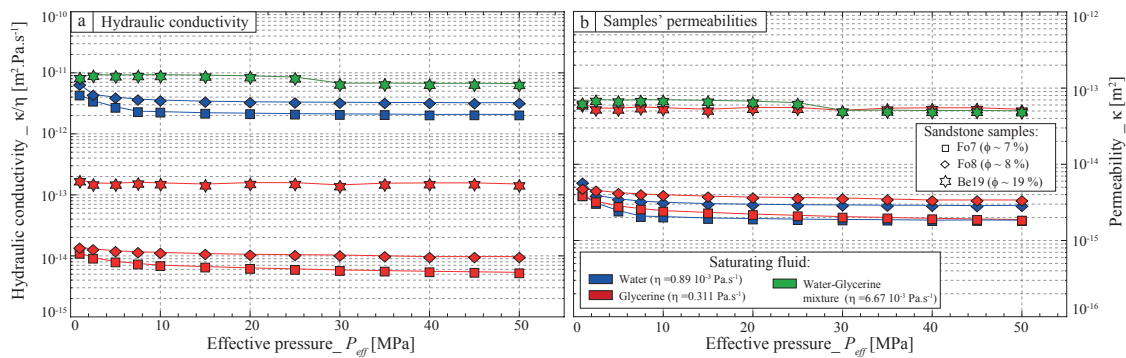


**Figure 4.1 :** Measured samples' hydraulic properties. (a) Hydraulic conductivity measured for the samples saturated under either glycerine, water or a water-glycerine mixture. (b) Inferred samples' permeabilities. The fluids' viscosities are chosen so that the permeabilities fit.

meability values for both fluids (Fig. 4.1b), the fitting fluids' "in-situ" viscosity is obtained. Using the permeability measured under water saturation as a reference, the viscosity ratio are obtained for all samples. Finally, assuming the water's viscosity to be about  $\eta_{wat} = 10^{-3} Pa \cdot s^{-1}$ , the glycerine's viscosity is of  $\eta_{wat} = 350 Pa \cdot s^{-1}$  and the water-glycerine mixture's one is of  $\eta_{mixt} \sim 7.44 \cdot 10^{-3} Pa \cdot s^{-1}$ .

### Poisson ratio as a function of apparent frequency

The apparent frequency  $f^*$  is computed by knowing the obtained viscosities, and  $\nu_{LF}$  and  $Q_v^{-1}$  are reported for the four sandstone samples (Fig. 4.2). For all samples, the measurements under differing fluids' viscosities fit in both magnitude and frequency-dependent variations.

Note first that the fluids' compressibilities do not affect the measured values of  $\nu_{LF}$  so that the magnitude measured fit between both saturating fluids. Differing tendencies are observed on the frequency dependence of  $\nu_{LF}$  for the four samples. Fo8 shows a very small increase at  $f^*$  lower than 10 Hz, then remains constant for frequencies beyond. The absence of variations at higher  $f^*$  is thought to occur as the two transitions fall in the same range of frequency (?). Fo7 shows the characteristic bell-shaped variation noted earlier, which probably relates to the both drained/undrained and undrained/unrelaxed transitions. The Berea samples show an increase, up to about 100 Hz, where the values remain constant. As for Fo7, a decrease is then observed for frequencies beyond 10 kHz.

Such shift to higher frequency as compared to Fo7 is expected to originate from an higher mean aspect ratio of the the sample's microcracks. Using the crack closure theory of ?, the Berea sample's microcracks' mean aspect ratio is indeed expected to be about two times larger than in Fo7 (i.e.  $4 - 5 \cdot 10^{-4}$ ), of about  $8 - 10 \cdot 10^{-4}$ . Because the characteristic frequency for the effect takes the cubic value of the aspect ratio as an input, this could cause the large difference in frequency. Indeed, for a bulk modulus of  $K_d = 5 GPa$  and aspect ratio of  $\zeta \cdot 10^{-3}$ , one obtains  $f_2^* \sim 5 \cdot 10^3 Hz$ .

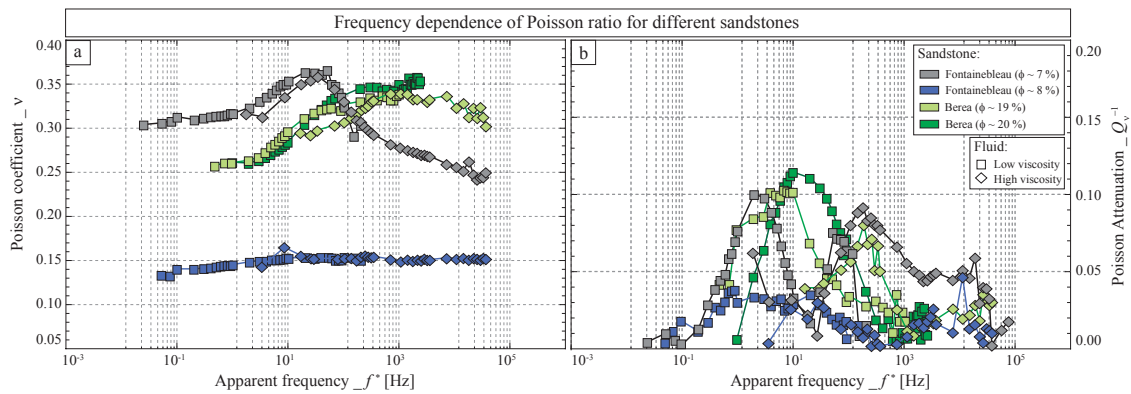


**Figure 4.2 :** Inferred dependence to apparent frequency  $f^*$  of (a)  $\nu_{LF}$  and (b)  $Q_v^{-1}$  for the different sandstone samples. Water (or water-glycerine) saturation and glycerine saturation are reported respectively as squares and diamonds.

When investigating the magnitude of the variations, the samples also differ. While Fo8 sample's  $\nu_{LF}$  never exceeds about 0.16, the values reached by the Berea samples and Fo7 are as high as about 0.33. Furthermore, the measured  $\nu_{LF}$  under undrained conditions fits between Fo7 and the Berea samples under both water (or water-glycerine) and glycerine saturations.

## 4.2 Effect of the boundary conditions

### 4.2.1 Bulk and shear moduli for Fo7

The  $K^{ax}$  and  $G^{ax}$  inferred from  $E_{LF}$  and  $\nu_{LF}$  measured on Fo7 under dry and fluid-saturated conditions (Chaps. 2 & 3) are reported as a function of effective pressure (Fig. 4.3). For both properties, an important difference is observed between the dry and fluid-saturated measurements. Under dry conditions, consistently, an increase is observed as  $P_{eff}$  increases. Under saturation by an incompressible fluid, the inferred  $K^{ax}$  (Fig. 4.3a) shows a particularly large increase at lowest confining pressure. Moreover, the pressure dependence of the fluid-saturated bulk modulus measured is inconsistent as  $K^{ax}$  is expected to increase with increasing effective pressure.

While the pressure dependence of  $G^{ax}$  (Fig. 4.3b) is similar for all measurements, a clear differentiation between fluids is highlighted for this inferred property. At low effective pressure, the shear modulus of the rock shows (i) a decrease from dry to water-saturated conditions; and (ii) an increase from dry to glycerine-saturated conditions. This variation is not consistent with the usual Biot-Gassmann theory that assumes a shear modulus independent of the saturating fluid. The same observation was made in the case of a carbonate rock by Adam et al. (2006), and was related to the largely discussed fluid-induced shear weakening in carbonate rocks (e.g., Baechle et al., 2007).

However, the sample studied is a quartz-pure sandstone. Even though moisture adsorp-

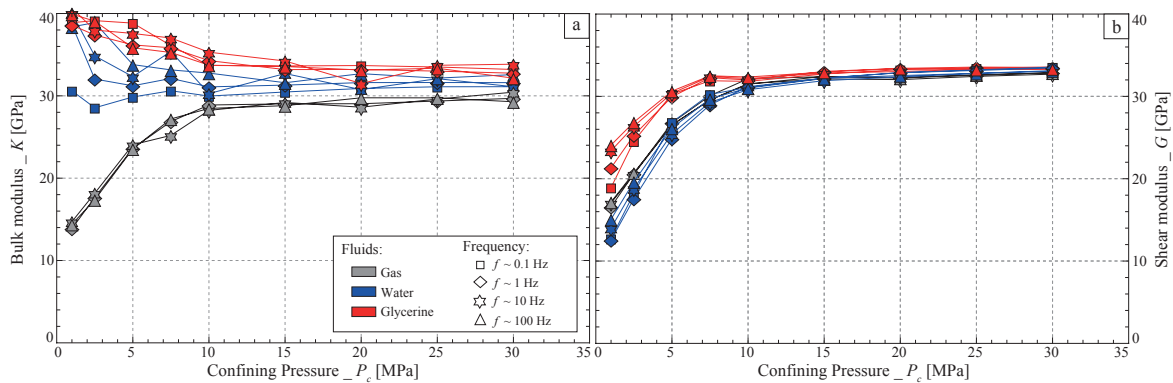


**Figure 4.3 :** Pressure dependence of  $K_{ax}$  and  $G_{ax}$  inferred from the measured  $\nu$  and  $E$  for this rock sample saturated by (a) water or (b) glycerine. The dry measurement is reported for comparison.

tion (i.e. very low saturations) was shown to affect the elastic properties (e.g., Clark et al., 1980) of the loosely cemented sandstones, these samples are relatively well cemented and did not show large elastic weakening (Pimienta et al., 2014a). This apparent fluid effect observed on both inferred bulk modulus (Fig. 4.3a) and shear modulus (Fig. 4.3b) probably originate from the boundary conditions (Dunn, 1986, 1987). A possible interpretation of this effect is introduced below.

#### 4.2.2 Strain gauge position and local pore pressure

For Fo7, Poisson ratio shows interesting trends of increase and decrease with frequency in both water- and glycerine-saturated cases. This variation seems to be consistent with the usual fluid flow theories. Yet, the measured water-saturated Poisson ratio are much higher than the dry measurement, even for frequencies low enough to theoretically allow for drained conditions. This effect may be explained from the experimental boundary conditions (Dunn, 1987), and can be tested using a specific experiment.

Up to this point, strains were always measured at the sample's center as to discard possible barrel's effects. For a Berea sample of about  $6 \cdot 10^{-14} \text{ m}^2$  permeability and 20% porosity, the strain gauges are glued at two given positions on the sample. While the first gauge (i.e. SG1) is again glued at the sample's half-length (i.e. equi-distant from the end-platens), the second one (i.e. SG2) is here glued near the bottom end-platen (Schematic view in Fig. 4.4c).

The frequency dependence of  $\nu$  and  $Q_\nu^{-1}$  is measured on the sample under either dry (Figs. 4.4a & 4.4c) or fluid-saturated (Figs. 4.4b & 4.4d) conditions. As for the Berea sample reported in Fig. (4.2), the saturating fluid is a water-glycerine mixture. In addition, the frequency dependence of  $\nu$  and  $Q_\nu^{-1}$  is measured for varying values of pore fluid pressure (i.e.  $p_f \in [0.1; 2; 9] \text{ MPa}$ ) and a constant Terzhagi effective pressure of  $P_{eff} \sim 1 \text{ MPa}$ .

Consistently, the measurement under dry conditions (Figs. 4.4a & 4.4c) shows a frequency-independent stable measurement that is independent of the strain gage posi-

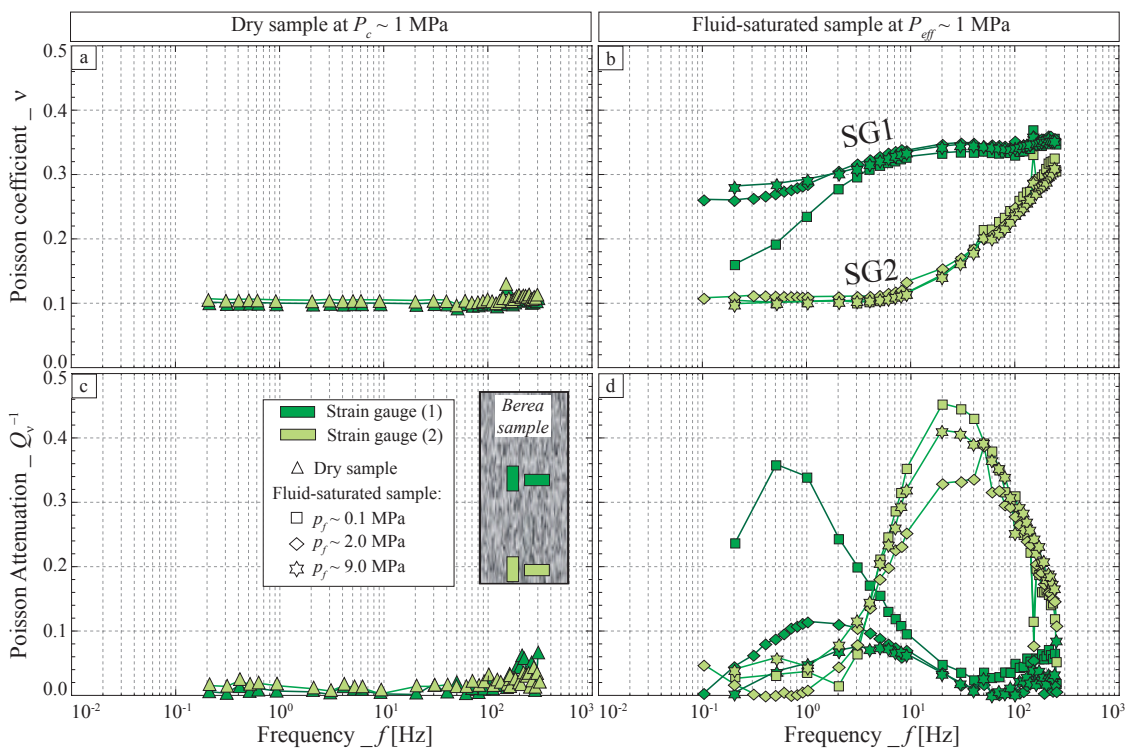


**Figure 4.4 :** Frequency dependence of (a)  $\nu_{LF}$  and (b)  $Q_v^{-1}$  of the Berea sandstone sample. For the same effective pressure of  $P_{eff} \sim 1$  MPa, the measurements are repeated for different pore pressures of  $p_f = [0.1; 2; 9]$  MPa. Two positions are chosen for the strain gauges, SG1 is at the sample’s half-length, and SG2 is at the sample’s bottom.

tion. Poisson ratio remains constant at  $\nu \sim 0.1$  and  $Q_\nu^{-1}$  is almost zero for both SG1 and SG2. On the reverse, large increase and variations are measured under fluid full saturation (Figs. 4.4b & 4.4d). For all values of pore pressures, the measurements from SG1 and SG2 diverge in both their magnitude and their frequency dependence.

For a better understanding, the effect of pore pressure and measuring position are investigated separately.

### Pore pressure effects on SG1 measurements

Noting that SG1 was placed at a same position than in the previously reported measurements (Fig. 4.2), it is of interest to first investigate its measurements. In particular, different pore pressures were tested.

For pressures of  $p_f = [2;9]$  MPa, the measured  $\nu_{LF}$  and  $Q_\nu^{-1}$  are very similar to the ones obtained before. In particular, the measured  $\nu_{LF}$  (i.e. Fig. 4.4b) at low frequencies under fluid saturation remains much higher than the one under dry conditions. When increasing the measuring frequency, a small increase in  $\nu$  is observed from 0.25 up to a stable value of 0.34 at  $f \sim 20$  Hz. This variation correlates with a measured  $Q_\nu^{-1}$  peak (i.e. Fig. 4.4d) of about 0.1 at a frequency of  $f = 1$  Hz. Both magnitudes and variations of the measured  $\nu$  and  $Q_\nu^{-1}$  with SG1 are consistent with earlier measurements (Fig. 4.2).

However, by decreasing the pore fluid pressure to 0.1 MPa, the value of  $\nu_{LF}$  under fluid-saturated conditions at lowest frequency is of 0.16, and it seems decreasing toward the dry value as frequency decrease. Furthermore,  $\nu_{LF}$  increases with frequency up to the value obtained for the measurements at higher  $p_f$ . This large increase correlates with a much larger  $Q_\nu^{-1}$  peak (i.e. Fig. 4.4d). This peak is as large as about 0.35, near to the one that was inferred from the poroelastic correction.

It indicates that no boundary effects are observed when the pore pressure is small enough not to allow for a pressure build-up. It thus confirms the results obtained using the poroelastic correction.

### Effect of the strain gauge position

The measurements from SG2 differ from the ones of SG1. For SG2, no clear effect of  $p_f$  can be observed on  $\nu$  (Fig. 4.4b) so that all measurements are superimposed. Furthermore, the measured  $\nu_{LF}$  shows a clear increase from the purely dry value of  $\nu = 0.1$  up to a value of about  $\nu = 0.32$  at  $f \sim 200$  Hz. In addition,  $Q_\nu^{-1}$  peaks (Fig. 4.4d) as large as about 0.4 are observed. This suggests that, at low frequencies, SG2 is closed to the drained regime, and may imply that SG2 is considerably less sensitive to the dead volume effect.

Although fully consistent in its magnitudes of variation, the measurements from SG2 introduce a new complexity : the critical frequency of the effects largely differ. While the characteristic frequency for the  $Q_\nu^{-1}$  peaks is of about  $f \sim 1$  Hz for SG1, it is at about

$f \sim 20$  Hz for SG2, i.e. one order of magnitude higher.

### 4.3 Conclusions

Young modulus and Poisson ratio were measured as a function of frequency for different sandstone samples. The complexities of the experimental set-up made it so that only few successful experiments could be reported. However, owing to the experimental complexity and the originality of the measurements, two articles were submitted to peer-reviewed journals out of these results. In addition, it allowed for a collaboration with a team from *Los Alamos*. This work will lead to a third manuscript.

As shown from the further discussions, other complexities surface from this set-up :

- First, the static deviatoric load needed to obtain the stability for the measurement may lead to measuring an anisotropic sample, which behaviour are expected to differ from an isotropic one.
- Second, the boundary conditions appear to affect the measurement of both Poisson ratio and Young modulus. The role of the dead volume was accounted for and seemed to give consistent results. A further understanding on this effect is sought from developing a poroelastic model that accounts for the experimental boundary conditions (**part. V**).

All of these aspects are currently investigated.



**Transition Drainé/Non-Drainé  
en fréquence :  
Modélisation de l'expérience**

|          |   |            |
|----------|---|------------|
| <b>1</b> | <b>Introduction : Understanding the experiment</b>                  | <b>181</b> |
| <b>2</b> | <b>General 1D model : Isotropic solicitation</b>                    | <b>183</b> |
| 2.1      | Theoretical boundary conditions . . . . .                           | 183        |
| 2.2      | Role of the dead volume : Experimental boundary condition . . . . . | 191        |
| 2.3      | Direct comparison with the measurements . . . . .                   | 196        |
| <b>3</b> | <b>Conclusion &amp; Perspectives</b>                                | <b>201</b> |
| 3.1      | Conclusions . . . . .   | 201        |
| 3.2      | General 1D model : Deviatoric solicitation . . . . .                | 202        |
| 3.3      | Perspectives : 2D poroelastic model . . . . .                       | 204        |



---

## Summary

**Résumé :** Dispersion et atténuation, attribuées à la transition drainé/non-drainé, ont été mesurées expérimentalement (**parties III & IV**). Néanmoins, des effets de bords affectent les propriétés mesurées. Cette partie a pour but de modéliser l'expérience, et donc de comprendre ces effets de bords.

Un modèle 1D est développé par résolution directe des équations quasi-statique de la poroélasticité, en choisissant différentes conditions de bord. Le modèle permet de prédire quatre propriétés qui sont directement comparables aux mesures : le module d'incompressibilité, son atténuation, le coefficient de Skempton et le déphasage de surpression de pore.

La condition de bord réelle est un système "artificiellement non-drainé", pour lequel un volume mort est présent aux deux extrémités de l'échantillon. De par l'existence du volume mort, une inter-relation entre capacités de stockage de l'échantillon et du volume mort détermine la magnitude et la fréquence des transitions élastiques mesurées. Le modèle est cohérent avec les données.

**Abstract :** A clear elastic dispersion/attenuation was measured in **parts III & IV** that was related to the drained/undrained transition. However, the measurements showed evidences of boundary conditions. This part aims at modelling the experiment, and thus at understanding the different effects brought by the boundary conditions.

A 1D model is developed by solving the equations of quasi-static poroelasticity, and different boundary conditions are tested. The model allows for predicting four properties that can be directly compared to the measurements : bulk modulus, bulk attenuation, Skempton coefficient and pore pressure phase shift.

The realistic boundary condition corresponds to an "experimentally undrained" system, for which a dead volume exists at both ends of the sample. Owing to the existence of a dead volume, an interplay between sample's and dead volumes' storage capacity determines both the magnitudes and the frequency dependence of the measurements. The model is consistent with the measurements.



---

## Introduction : Understanding the experiment

---

Considering the measurements on  $K$  frequency dependence, a clear evidence for the Drained/Undrained transition is observed. Indeed,  $K$  values show an increase from the Drained to Undrained regime predicted by Biot-Gassmann theory. However, a pore pressure build-up is also measured in the dead volume during the experiment that leads to the measurement of a pseudo-Skempton coefficient  $B^*$ . The measurements are in fact exotic as no drained/undrained transition should theoretically be expected for  $K$  if a Skempton coefficient, characteristic property of an undrained medium, is measured (Fig. 1.1).

Furthermore, as noted in **chapter III.3**, measurements on a Berea sample show a value at lowest frequency under fluid saturation that is much larger than the drained/dry value. These inconsistency result from the existence of a dead volume. In order to better understand the experiments, a 1D model is developed based on the typical quasi-static poroelastic theory. Different boundary conditions are tested to better understand the effect. Finally, the 1D model is compared to the measurements to test its applicability.

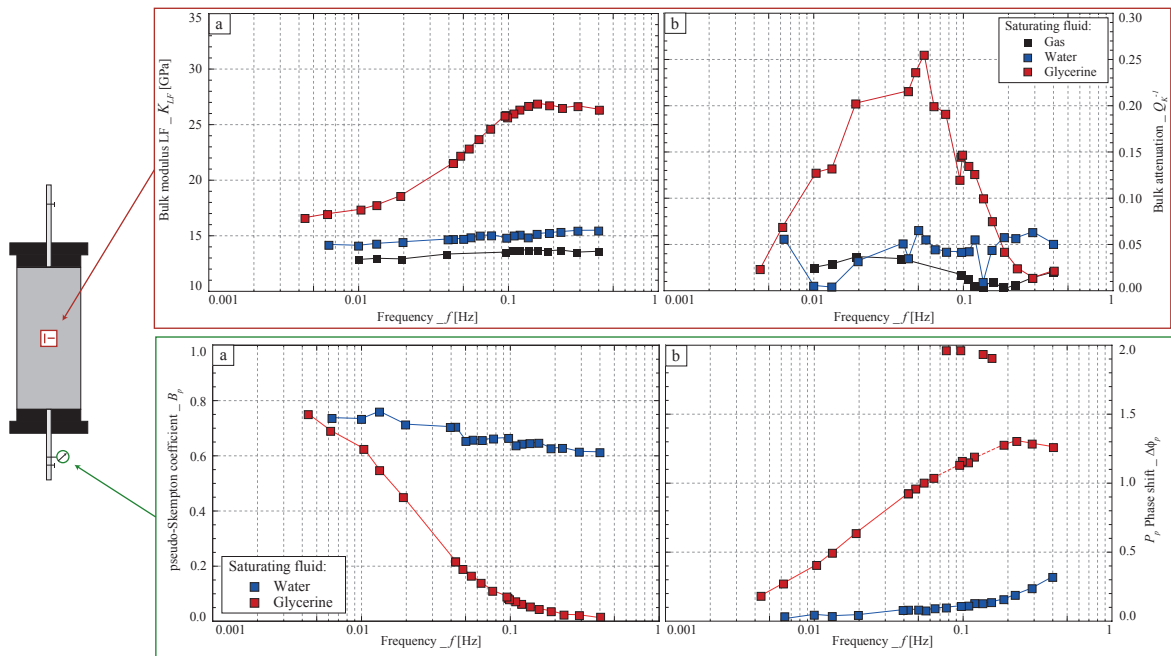


Figure 1.1 : Measurements in case of Fo7 saturated by glycerine measured at  $P_{eff} = 1$  MPa.

---

**General 1D model : Isotropic solicitation**

---

Within the framework of the poroelastic theory, using the equilibrium conditions and the mass conservation, it is possible to define the partial derivative equation satisfied by the pore fluid pressure ( $p_f$ ) such that (e.g. Rice and Cleary, 1976; Zimmerman, 2000; Guéguen and Bouteica, 2004) :

$$\frac{\kappa BK_d}{\eta(1 - \alpha B)} \nabla^2 p_f = \frac{BK_d}{1 - \alpha B} \frac{\partial \epsilon_v}{\partial t} - \frac{\partial p_f}{\partial t}. \quad (2.1)$$

Where  $\kappa$ ,  $K$ ,  $B$  and  $\alpha$  are respectively the rock's permeability, drained bulk modulus, Skempton coefficient and Biot-Willis coefficient.  $\eta$  is the fluid's intrinsic viscosity. Noting that the volumetric strain is  $\epsilon_v = K_d^{-1}(P - \alpha p_f)$ , the source term  $P$  may be introduced in the differential equation.

This source term depends on the condition of stress solicitation chosen. Two cases of stress solicitation are considered in the following. The confining pressure oscillations can be considered as an "isotropic solicitation", i.e. a solicitation that is equal in all directions. The uniaxial stress oscillation can be considered as a "deviatoric solicitation". Because it was easier to consider first the case of confining pressure oscillations, more emphasis is given to the model regarding this solicitation condition.

## 2.1 Theoretical boundary conditions

### 2.1.1 Model derivation

Here, we consider an isotropic solicitation of the rock. An oscillating confining pressure is applied so that  $P(t)$  is a source term that is time-dependent. The equation (Eq. 2.1) is solved in 1 dimension (1D model) by assuming for  $p_f$  to vary as a function of  $z$  only.

Finally, the equation rewrites (Zimmerman, 2000) :

$$\frac{\partial p_f}{\partial t} = \frac{\kappa BK_d}{\eta \alpha} \frac{\partial^2 p_f}{\partial z^2} + B \frac{\partial P}{\partial t}. \quad (2.2)$$

Noting that the rock's storage coefficient writes  $S_s = \alpha / (BK_d)$  (Kümpel, 1991), the equation rewrites :

$$\frac{\partial p_f}{\partial t} = \frac{\kappa}{\eta S_s} \frac{\partial^2 p_f}{\partial z^2} + B \frac{\partial P}{\partial t}. \quad (2.3)$$

In case of no source terms (i.e.  $P = cst$ ), this equation corresponds to the one usually investigated in case of permeability measurement using the "oscillating pulse" method (e.g. Brace et al., 1968; Lin, 1977; Hsieh et al., 1981; Song and Renner, 2006, 2007). The applied confining pressure  $P$  is here supposed to be small variations  $\Delta P$  of a sinusoidal form such that  $P = \Delta P e^{i\omega t}$ . Accounting for this time dependence, and using the theorem of variables separation, the partial derivative equation simplifies to :

$$p_f(z, t) + i \left( \frac{D}{\omega} \right) \frac{\partial^2}{\partial z^2} [p_f(z, t)] = B \Delta P e^{i\omega t}, \quad (2.4)$$

with  $D = \kappa / (S_s \eta)$  being the fluid diffusivity in the sample. The equation being simplified to a typical differential equation of second order, solutions can be found analytically. These are of the form :

$$p_f(z, t) = \left[ B \Delta P + p_f^{\pm} e^{\pm(1-i)\sqrt{\frac{\omega}{2D}}z} \right] e^{i\omega t}, \quad (2.5)$$

with  $p_f^+$  and  $p_f^-$  two constants that are obtained from the chosen problem's boundary conditions.

Finally, the elastic properties may be inferred using the usual theory of poroelasticity. To remain consistent, the applied solicitation being isotropic, the sole modulus being accessible is here the bulk modulus. This property is reached from the volumetric strain, which in turn can directly be obtained from  $\epsilon_v = K_d^{-1}(P - \alpha p_f)$ . Note that the differential equation could have also been solved to directly obtain  $\epsilon_v$ , which is expected to give the exact same results. Here, solving for  $p_f$  has been preferred as it directly allows to highlight the role of the pore pressure on the frequency dependent elastic variations.

## 2.1.2 Drained and Undrained boundary conditions

The two typical boundary conditions that need to be considered are the drained and undrained conditions (Fig. 2.1).

### 2.1.2.1 Theoretical derivation

In the drained conditions (Fig. 2.1a), no pore pressure is applied/maintained to the sample upper (i.e.  $z = L$ ) and lower (i.e.  $z = 0$ ) ends so that  $p_f(0, t) = p_f(L, t) = 0$ . In

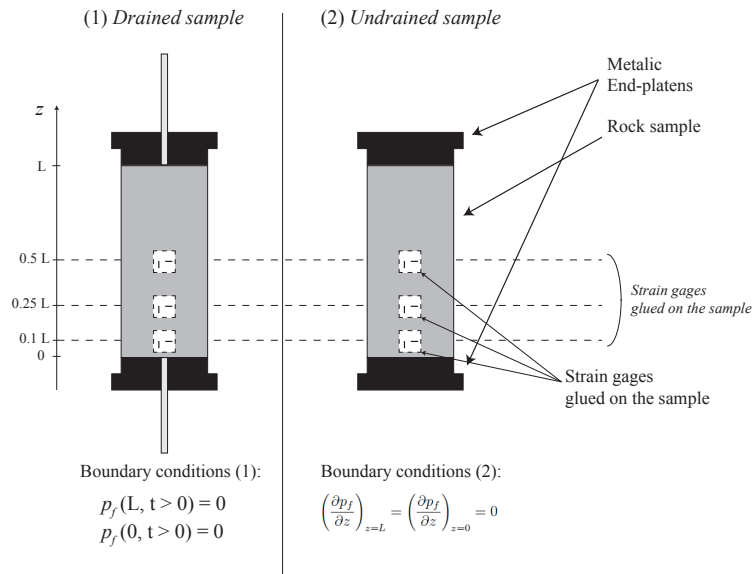


**Figure 2.1 :** Schematic view of the sample associated with the three possible boundary conditions.

the undrained condition (Fig. 2.1b), on the reverse, fluid is not allowed to flow out of the sample so that :

$$\left(\frac{\partial p_f}{\partial z}\right)_{z=L} = \left(\frac{\partial p_f}{\partial z}\right)_{z=0} = 0. \quad (2.6)$$

The undrained boundary condition leads to a constant solution of  $p_f(z, t) = B P(t)$ , i.e. an immediate and frequency-independent response of the pore fluid to the oscillating pressure. In the drained boundary condition, the sample's behaviour depends on the frequency of the applied stress oscillation.

Owing to the simple boundary condition of null pore pressure at both ends, an analytical solution can easily be found such that :

$$p_f(z, t) = B \Delta P e^{i\omega t} \left[ 1 - \frac{\sinh(a(L-z)) + \sinh(az)}{\sinh(aL)} \right], \quad (2.7)$$

with the constant  $a = (1-i)\sqrt{\omega/2D}$ . As shown from this solution, any value of  $p_f(z, t)$  corresponds to the "local" overpressure created by the stress oscillation  $\Delta P$ . Finally, a "local" volumetric strain can be calculated such that :

$$\epsilon_v(z, t) = -\frac{B \Delta P}{K_d} e^{i\omega t} \left[ (1-\alpha) + \alpha \frac{\sinh(a(L-z)) + \sinh(az)}{\sinh(aL)} \right]. \quad (2.8)$$

Note the sign change in the equation that corresponds to the convention chosen of a decrease in strain as pressure increases. Both "local" properties are complex. In the following these are characterized by their norm and phase.

**Table 2.1** : Example of problem parameters in the case of the 7% porosity Fontainebleau sandstone sample.

| Parameter                       | Estimated value  |
|---------------------------------|--|
| Sample length                   | $L = 80 \text{ mm}$  |
| Sample diameter                 | $D = 40 \text{ mm}$  |
| Sample's porosity               | $\phi = 7\%$   |
| Sample's drained bulk modulus   | $K_d = 14 \text{ GPa}$   |
| Sample's permeability           | $\kappa = 4 \cdot 10^{-15} \text{ m}^2$                        |
| Confining oscillation amplitude | $\Delta P = 0.2 \text{ MPa}$                                   |
| Glycerine compressibility       | $K_{gly} = 4.36 \text{ GPa}$                                   |
| Glycerine viscosity             | $\eta_{gly} = 1.087 \text{ Pa.s}$                              |
| Sample's storage capacity       | $S_s = 5.86 \cdot 10^{-2} \text{ GPa}^{-1}$                    |
| Sample's hydraulic diffusivity  | $C_{gly} = 2.20 \cdot 10^{-4} \text{ m}^2 \cdot \text{s}^{-1}$ |
| Water compressibility           | $K_{wat} = 2.25 \text{ GPa}$                                   |
| Water viscosity                 | $\eta_{wat} = 0.89 \cdot 10^{-3} \text{ Pa.s}$                 |
| Sample's storage capacity       | $S_s = 7.36 \cdot 10^{-2} \text{ GPa}^{-1}$                    |
| Sample's hydraulic diffusivity  | $C_{wat} = 6.10 \cdot 10^{-2} \text{ m}^2 \cdot \text{s}^{-1}$ |

### 2.1.2.2 Discussion of the analytical 1D solution

Before investigating the frequency dependence of the modelled properties that can be compared to the measurements, it is of interest to investigate first the different responses of this 1D model.

**Investigating the problem's parameters** As this model is designed to precisely understand and predict the measurements from ? on a 7% Fontainebleau sample (Fo7), the problem's parameters are fixed from the experimental set-up conditions and using this sample's measured properties (Tab. 2.1). The rock's drained bulk modulus was measured to be of about  $K_d \sim 14 \text{ GPa}$  at lowest confining pressure (i.e.  $P_{eff} \sim 1 \text{ MPa}$ ). The Skempton and Biot-Willis coefficients are then deduced, assuming the skeleton bulk modulus to be the one of the quartz crystal (i.e.  $K_{qtz} \sim 37 \text{ GPa}$ ), using the usual relations of poroelastic theory. Finally, the hydraulic diffusivity ( $D$ ) is directly deduced from the measured sample's permeability (i.e.  $\kappa \sim 4 \cdot 10^{-15} \text{ m}^2$ ) and storage capacity (i.e.  $S_s$ ), and the fluid's viscosity ( $\eta$ ).

As shown, for a sample's intrinsic properties, the resulting measurements highly depend on the saturating fluid's intrinsic properties. Viscosity affects the diffusivity of the sample, thus affecting the frequency dependence. On the other hand, the fluid's compressibility affects the saturated sample's overall compressibility and storage capacity, thus affecting the magnitude of the measured/predicted frequency effect.

**Time dependence** The constants being experimentally fixed (Tab. 2.1), the time-dependence of  $p_f$  as compared to the applied  $P$  is investigated (Fig. 2.2). The local  $p_f$  is

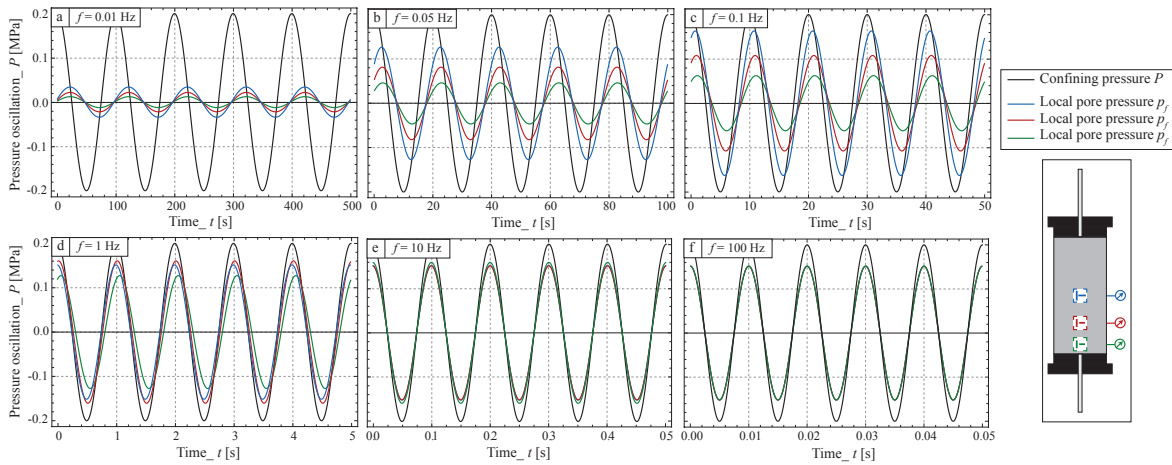


**Figure 2.2 :** Time dependence of the applied confining pressure oscillations and predicted pore pressure response for different frequencies in the range of  $f \in [10^{-2}; 10^2]$ . The properties of this synthetic sample are the ones of a Fontainebleau sandstone of 7% porosity saturated by glycerine.

calculated for different frequencies ( $f \in [10^{-2}; 10^2]$  Hz) and for three sensors' positions (Fig. 2.1) in case of this synthetic sample. The sample is here assumed to be glycerine-saturated.

While low at lowest frequency (Fig. 2.2a), the amplitude of the induced  $p_f$  oscillations increases with increasing frequency, up to  $f \sim 10$  Hz (Fig. 2.2e) where they become independent of frequency. Interestingly, a phase shift between the  $p_f$  and  $P$  oscillations. While the pore pressure response is initially shifted in time (i.e. phase shift) by about  $\pi/2$  at lowest frequency of  $f = 10^{-2}$  Hz (Fig. 2.2a), the phase shift decreases down to zero at  $f \sim 10^2$  Hz (Fig. 2.2e).

The frequency-dependent variation from drained, when no pore pressure variations occur, to undrained conditions, when fluid pressure  $p_f$  directly responds to the applied pressure  $P$  oscillation, appears to occur on a very large frequency band of about  $f \in [10^{-2}; 10^1]$  Hz. Note also that, owing to the boundary conditions, a large dependence to the position is observed. This point is further investigated below.

**Spatial dependence** The position ( $z$ ) dependence of both norm and phase of the "local" pore pressure (i.e.  $p_f$ ) and strain (i.e.  $\epsilon_v$ ) is investigated (Fig. 2.3). The properties are calculated for different frequencies of the applied  $P$  in the range of  $f \in [10^{-2}; 10^2]$  Hz. For the fluid pressure  $p_f$ , norm and phase show a similar monotonous behaviour.

As frequency increases, the norm (Fig. 2.3a) increases and the phase (Fig. 2.3b) decreases. Reversely, norm (Fig. 2.3c) and phase (Fig. 2.3d) of the volumetric strain  $\epsilon_v$  do not correlate. At low frequency, norm and phase increase as frequency increases. However, there exists a critical frequency (i.e.  $f \sim 0.05$  Hz) after which the phase decreases when frequency keeps increasing.

Note that the largest amplitude is first observed at the sample's center. As frequency increases, almost all of the sample shows the same response. By definition, the variations

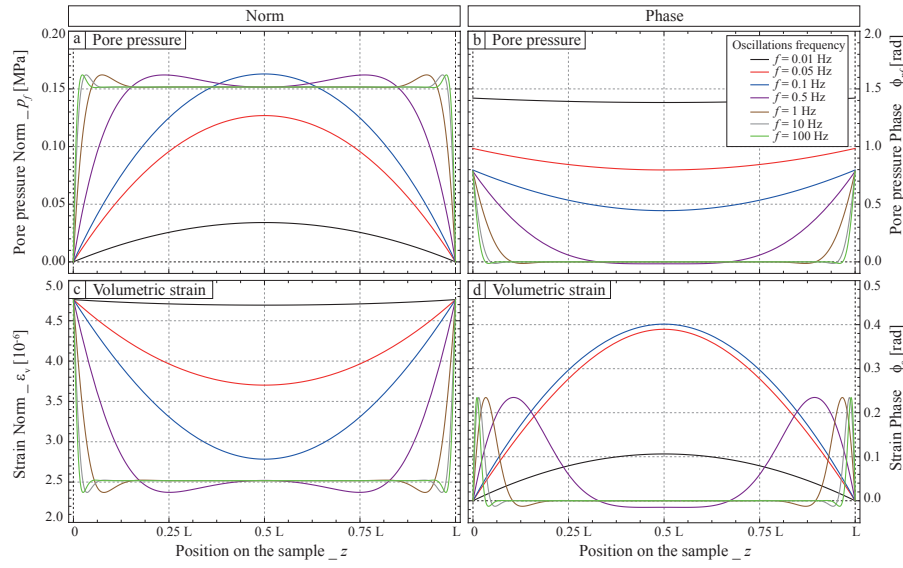


**Figure 2.3 :** Position dependence of the predicted (a-b) pore pressure and (c-d) volumetric strain response to the applied confining pressure oscillations for different frequencies in the range of  $f \in [10^{-2}; 10^2]$ . Both signals' norms and phases are investigated. The properties of this synthetic sample are the ones of a Fontainebleau sandstone of 7% porosity saturated by glycerine.

are symmetric with respect to the sample's center.

**"Local" versus "global" predictions** Assuming that we remain within the bounds for linear poroelasticity, we are here interested in the frequency-dependent variations of the Skempton coefficient and Bulk modulus. As in ?, a local pseudo-Skempton coefficient  $B^*$  is defined. Similarly, a local pseudo-bulk modulus  $K^*$  may be directly deduced from the complex volumetric strain :

$$B^*(z, \omega) = \frac{p_f(z, \omega)}{P(\omega)}, \quad \& \quad K^*(z, \omega) = -\frac{P(\omega)}{\epsilon_v(z, \omega)}. \quad (2.9)$$

The bulk modulus and Skempton coefficient are intrinsic properties of a given rock sample. The locally calculated  $K^*$  and  $B^*$  can be averaged over the sample's length  $L$  to access the global (or volume-averaged) "properties" of the rock (i.e.  $K_g$  and  $B_g$ ) such that :

$$B_g(\omega) = \frac{\frac{1}{L} \int_0^L p_f(z, \omega) \cdot dz}{P(\omega)}, \quad \& \quad K_g(\omega) = -\frac{P(\omega)}{\frac{1}{L} \int_0^L \epsilon_v(z, \omega) \cdot dz}, \quad (2.10)$$

Again, the "local" and "global" predictions can be characterised by their norms (e.g.  $\|B^*\|$  and  $\|K^*\|$ ) and phases (e.g.  $\phi_{B^*}$  and  $\phi_{K^*}$ ). The norms are related to modulus  $K$  and coefficient  $B$ . The phase  $\phi_{B^*}$  (or  $\Delta\phi_p$ ) relates to the delay in oscillating fluid pressure as compared to the applied confining pressure oscillations. In other words, this property directly relates to the

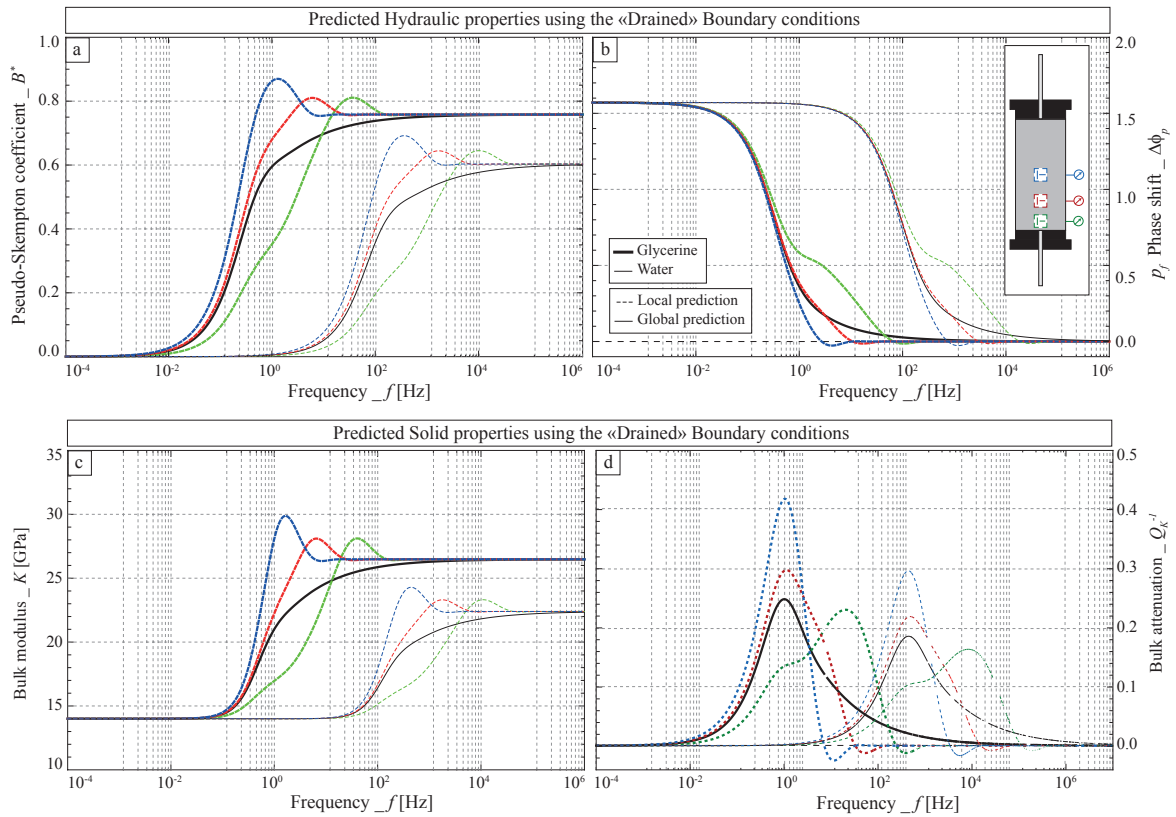


**Figure 2.4 :** Predicted drained to undrained transition of the frequency-dependent (a-b) hydraulic and (c-d) elastic properties of the 7% Fontainebleau sample (i.e. Fo7) saturated by water (i.e. thin curves) or glycerine (i.e. thick curves). Both "local" (i.e. dashed colour curves) and "global" (i.e. continuous black curves) predictions are compared. The cases of saturating conditions are tested.

frequency-dependent hydraulic diffusivity in the sample. The phase  $\phi_{K^*}$  relates to the phase shift between applied stress and induced strain, which tangent is usually characterized as the bulk modulus attenuation (i.e.  $Q_K^{-1}$ ).

Both "local" and "global" hydraulic (Figs. 2.4a & 2.4b) and solid (Figs. 2.4c & 2.4d) response to the applied stress oscillation are investigated as a function of frequency for a Fo7 sample saturated by either water or glycerine. Three positions have been chosen along the sample's length at  $z = [L/2; L/4; L/10]$ . Overall,  $\|B^*\|$  (Fig. 2.4a) and  $\|K^*\|$  (Fig. 2.4c) show a consistent increase from drained to undrained domain, the phase shift  $\Delta\phi_p$  shows large decrease with frequency from  $\pi/2$  down to zero and a large  $Q_K^{-1}$  peak is observed. For all properties, owing to the water intrinsic viscosity, water saturation shift the effect's characteristic frequency upward.

In case of the "local" predictions, while no change is observed at either high or low frequencies, a clear dependence to the position is predicted for all properties in the characteristic frequency for the drained/undrained transition. Furthermore, all curves show non-monotonous variations at high frequency. As shown from the "global" predictions, the non-monotonous variations disappear leading to a progressive frequency-dependent

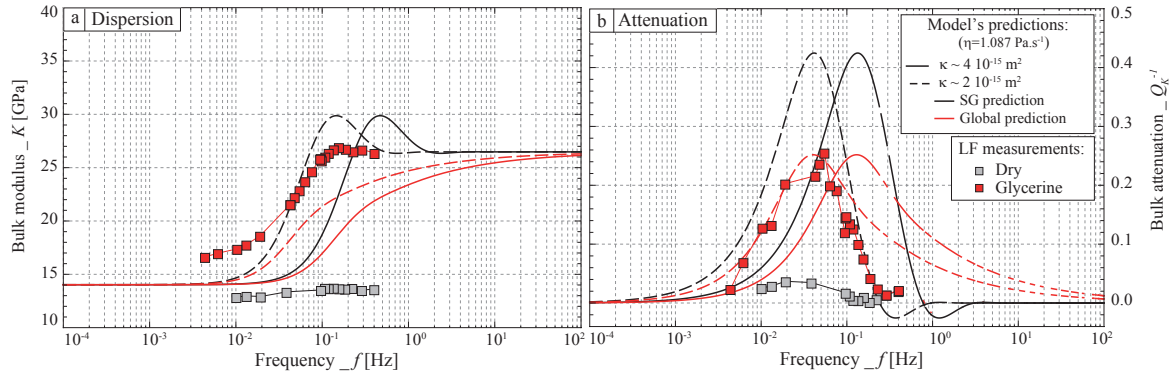


**Figure 2.5 :** Comparison between the dependence to apparent frequency of the predicted (curves) and measured (symbols) bulk modulus  $K$  (a) and bulk attenuation  $Q_K^{-1}$  (b) for Fo7 sample. The predictions for both "SG" (i.e. black curves) and "global" (i.e. red curves) are reported for two slightly differing sample's permeabilities. The fluid's viscosity is one of glycerine, i.e.  $\eta = 1.087 \text{ Pa}\cdot\text{s}^{-1}$ .

increase.

### 2.1.3 Comparison with the measurements on Fo7

As shown by ?, a strong frequency-dependent bulk modulus dispersion and attenuation responses were observed in two glycerine-saturated Fontainebleau sandstone samples. For the 7% Fontainebleau sandstone (Fo7), the measured fluid flow at the sample's end suggests that the dispersion/attenuation measured is caused by the drained/undrained transition.

Because the properties were measured thanks to strain gauges locally glued on the samples, the prediction should be averaged over this length at the position of measurement to build local "SG" predictions (i.e. at the SG scale) such that :

$$B_{SG}(\omega) = \frac{1}{(z_2 - z_1)} \int_{z_1}^{z_2} p_f(z, \omega) \cdot dz, \quad \& \quad K_{SG}(\omega) = - \frac{P(\omega)}{\frac{1}{(z_2 - z_1)} \int_{z_1}^{z_2} \epsilon_v(z, \omega) \cdot dz'} \quad (2.11)$$

with  $z_1$  and  $z_2$  being two positions corresponding to the lower and upper end of the strain gauge. Here, the strain gauges have a length of about 6 mm and are at the sample's half-length so that the "SG" prediction is at the sample's center.

The frequency-dependent measurements of  $K$  and  $Q_K^{-1}$  from ? are compared to the model's predictions for Fo7 (Figs. 2.5a & 2.5b). Noting that, owing to the measurement accuracy, the sample's permeability is in the range of  $2 - 4 \cdot 10^{-15} \text{ m}^2$ , the model's predictions are tested for the two values.

The measurements on Fo7 show similar magnitudes and very similar frequency dependence as the model's predictions. Note directly that the "local" prediction has the same frequency band as the data. It implies that the frequency dependence of the predicted response is very comparable to a Zener-like viscoelastic effect.

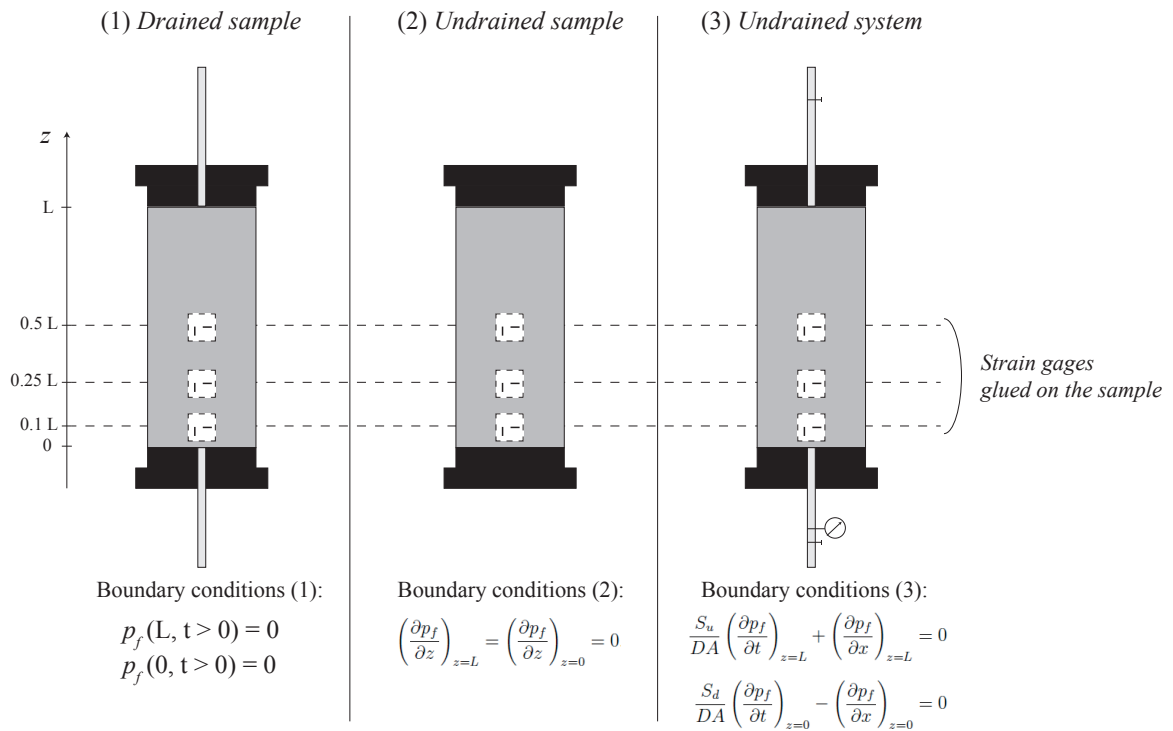


**Figure 2.6 :** Schematic view of the sample associated with the three possible boundary conditions. The usual theoretical "drained" and "undrained" boundary conditions are complemented with a more realistic boundary condition, which in fact combines the two theoretical ones.

## 2.2 Role of the dead volume : Experimental boundary condition

Recalling the solutions obtained in 1 :

$$p_f(z, t) = \left[ B\Delta P + p_f^\pm e^{\pm(1-i)\sqrt{\frac{\omega}{2b}}z} \right] e^{i\omega t}, \tag{2.12}$$

the problem's boundary conditions are changed to obtain the two constants  $p_f^+$  and  $p_f^-$ . The two typical boundary conditions usually considered are the "drained" (Fig. 2.6a) and "undrained" (Fig. 2.6b) conditions (e.g., Dunn, 1986, 1987). They correspond to the extremal cases of fluid either fully blocked or fully unblocked by the system. A third boundary condition may finally be addressed, which combines the purely "drained" and "undrained" conditions : the "experimentally undrained" condition (Fig. 2.6c). This last condition is the most realistic one as it is usually not experimentally possible to attain purely drained or undrained experimental conditions.

### 2.2.1 Role of the dead volumes

The "experimental undrained" boundary condition consists in an undrained system not only constituted of the sample but also of a dead volume at both sample's upper and lower ends. Such boundary condition was in fact largely investigated in case of "oscillating pulse"

measurement (e.g., Brace et al., 1968; Lin, 1977; Hsieh et al., 1981; Song and Renner, 2006, 2007). It can be directly obtained from the mass continuity at both ends of the sample, i.e. the mass of fluid lost by the system equals the fluid compressibility in the dead volume. Following earlier studies, these boundary conditions are found to be (Brace et al., 1968; Lin, 1977) :

$$S_1 \left( \frac{\partial p_1}{\partial t} \right)_{z=L} + \frac{\kappa A}{\eta} \left( \frac{\partial p_f}{\partial z} \right)_{z=L} = 0, S_2 \left( \frac{\partial p_2}{\partial t} \right)_{z=0} - \frac{\kappa A}{\eta} \left( \frac{\partial p_f}{\partial z} \right)_{z=0} = 0. \quad (2.13)$$

Where  $S_1$  and  $S_2$  are respectively the storage capacities of downstream and upstream dead volumes, and  $p_1 = p_f(0, t)$  and  $p_2 = p_f(L, t)$  are the pressures in the downstream and upstream dead volumes.  $A$  is the sample's cross-sectional area.

The dead volumes' properties need to be known. In particular, they contribute through their overall storage capacity. Owing to the very low pressure variations applied (i.e.  $\Delta P = 0.2$  MPa), leading to even lower pore pressure variations, the tubing's compressibility can consistently be neglected so that only the compressibility of the fluid in this dead volume needs to be accounted for. Knowing the values of lower (i.e.  $V_1$ ) and upper (i.e.  $V_2$ ) dead volumes,  $S_1$  and  $S_2$  are obtained. Furthermore, the sample's storage capacity is also needed. It can be reached from the theoretical expression of this property (Kümpel, 1991). The problem's parameters can all be fixed from direct measurements. The usual problem's parameters (Tab. 2.1) need thus to be extended to the case of these experimental set-up conditions (Tab. 2.2). The case of Fo7 sample is again chosen as an example.

## 2.2.2 Quasi-static conditions

Solving  $p_f(z, t)$  for this realistic set of boundary conditions leads to a complex solution that cannot be reported in simplified form. Yet, it has essentially the same form as the equation obtained for the "drained" boundary conditions. Furthermore, it remains possible to investigate the limiting cases. In particular, the assumed quasi-static case (i.e. zero frequency) can easily be reached, and gives :

$$\frac{p_f(z, t)}{P(t)} = B_0 = B_{th} \frac{V_s S_s}{V_s S_s + S_1 + S_2}. \quad (2.14)$$

where  $V_s = AL$  is the sample's total volume.

It has been shown that, in case of an existing dead volume, the measured Skempton coefficient had to be corrected to account for the existing dead volume. In particular, assuming isothermal conditions, it has been shown theoretically that the measured value for Skempton coefficient writes (e.g., Ghabezloo and Sulem, 2010) :

$$B_{mes} = \frac{C_d - C_s}{\phi(C_f - C_\phi) + (C_d - C_s) + \frac{S_1 + S_2}{V_s}}, \quad (2.15)$$

**Table 2.2 :** Example of problem parameters in the case of the 7% porosity Fontainebleau sandstone sample. The dead volume is also accounted for.

| Parameter                       | Estimated value  |
|---------------------------------|--|
| Sample length                   | $L = 80 \text{ mm}$  |
| Sample diameter                 | $D = 40 \text{ mm}$  |
| Sample's porosity               | $\phi = 7\%$   |
| Sample's drained bulk modulus   | $K_d = 14 \text{ GPa}$   |
| Sample's permeability           | $\kappa = 4 \cdot 10^{-15} \text{ m}^2$                        |
| Confining oscillation amplitude | $\Delta P = 0.2 \text{ MPa}$                                   |
| Lower Dead volume (1)           | $V_1 = 3.4 \text{ mL}$   |
| Upper Dead volume (2)           | $V_2 = 3.2 \text{ mL}$   |
| Glycerine compressibility       | $K_{gly} = 4.36 \text{ GPa}$                                   |
| Glycerine viscosity             | $\eta_{gly} = 1.087 \text{ Pa.s}$                              |
| Lower (1) storage capacity      | $S_1 = 7.34 \cdot 10^{-6} \text{ L.GPa}^{-1}$                  |
| Upper (2) storage capacity      | $S_2 = 7.80 \cdot 10^{-6} \text{ L.GPa}^{-1}$                  |
| Sample's storage capacity       | $S_s = 5.86 \cdot 10^{-2} \text{ GPa}^{-1}$                    |
| Sample's hydraulic diffusivity  | $C_{gly} = 2.20 \cdot 10^{-4} \text{ m}^2 \cdot \text{s}^{-1}$ |
| Water compressibility           | $K_{wat} = 2.25 \text{ GPa}$                                   |
| Water viscosity                 | $\eta_{wat} = 0.89 \cdot 10^{-3} \text{ Pa.s}$                 |
| Lower (1) storage capacity      | $S_1 = 1.42 \cdot 10^{-6} \text{ L.GPa}^{-1}$                  |
| Upper (2) storage capacity      | $S_2 = 1.51 \cdot 10^{-6} \text{ L.GPa}^{-1}$                  |
| Sample's storage capacity       | $S_s = 7.36 \cdot 10^{-2} \text{ GPa}^{-1}$                    |
| Sample's hydraulic diffusivity  | $C_{wat} = 6.10 \cdot 10^{-2} \text{ m}^2 \cdot \text{s}^{-1}$ |

where  $C_d$  and  $C_s$  (and  $C_\phi$ ) are the rock drained and skeleton compressibilities, and  $C_f$  is the fluid compressibility. Noting that  $S_s = \phi(C_f - C_\phi) + (C_d - C_s)$  (Kümpel, 1991), and combining with the theoretical expression for the Skempton coefficient ( $B_{th}$ ), this equation rewrites :

$$B_{mes} = B_{th} \frac{V_s S_s}{V_s S_s + S_1 + S_2}, \quad (2.16)$$

which thus equals the limiting case obtained at zero frequency and thus proves the consistency of the present 1D model.

### 2.2.3 Model predictions

Either "global" or "local" hydraulic and elastic responses of the rock can be predicted. Both will be tested in order to assess their correspondence with the measurements. As introduced above, the input parameter of main interest is the value of the dead volumes. The effect of this parameter will thus be tested.

#### "Global" predictions

The model's "global" predictions (over the entire sample's length) are investigated first. They are noted :  $K_g$  and  $Q_{K_g}^{-1}$  for the predicted solid response, and  $B_g$  and  $\Delta\phi_{B_g}$  for the hydraulic response. The frequency-dependent hydraulic (Figs. 2.7a & 2.7b) and elastic (Figs. 2.7c & 2.7d) model's responses are investigated using the parameters measured in the fluid-saturated Fo7 sample (Tab. 2.2). The experimentally measured dead volume  $V_{meas}$ , along with other values of dead volumes, are used in order to investigate the intrinsic effect of this parameter.

We consider first the pseudo-Skempton coefficient  $B_g$  (Fig. 2.7a) in quasi-static conditions (i.e. at lowest frequencies). The case of very large dead volume (i.e.  $10^3 V_{meas}$ ) leads to a prediction that fits with the one of the "Drained" boundary condition. Reversely, the "Undrained" boundary condition is reached at zero dead volume. By increasing the frequency,  $B_g$  shows an increasing value up to the Skempton coefficient theoretically predicted by the poroelastic theory, i.e.  $B = 0.71$ . The magnitude of the frequency-dependent increase thus directly depends on the value of the dead volume.

At large dead volume (i.e. near the "Drained" boundary conditions),  $\Delta\phi_{B_g}$  (Fig. 2.7b) decreases from  $\pi/2$  down to zero at higher frequencies. For intermediate dead volumes, the phase shift increases for  $f < f_c$  and decreases for  $f > f_c$ . The amplitude of variation is directly related to the value of dead volume. Under purely "Undrained" boundary conditions (i.e. null dead volume), no phase shift is observed.

The frequency-dependent variation of  $K_g$  (Fig. 2.7c) and  $Q_{K_g}^{-1}$  (Fig. 2.7d) is investigated for both glycerine and water saturations. Consistently, the dispersion involved under water saturation occurs at much higher frequencies due to the lower viscosity of the fluid. As for the hydraulic properties (Figs. 2.7a & 2.7b), a strong effect of the dead volume is observed

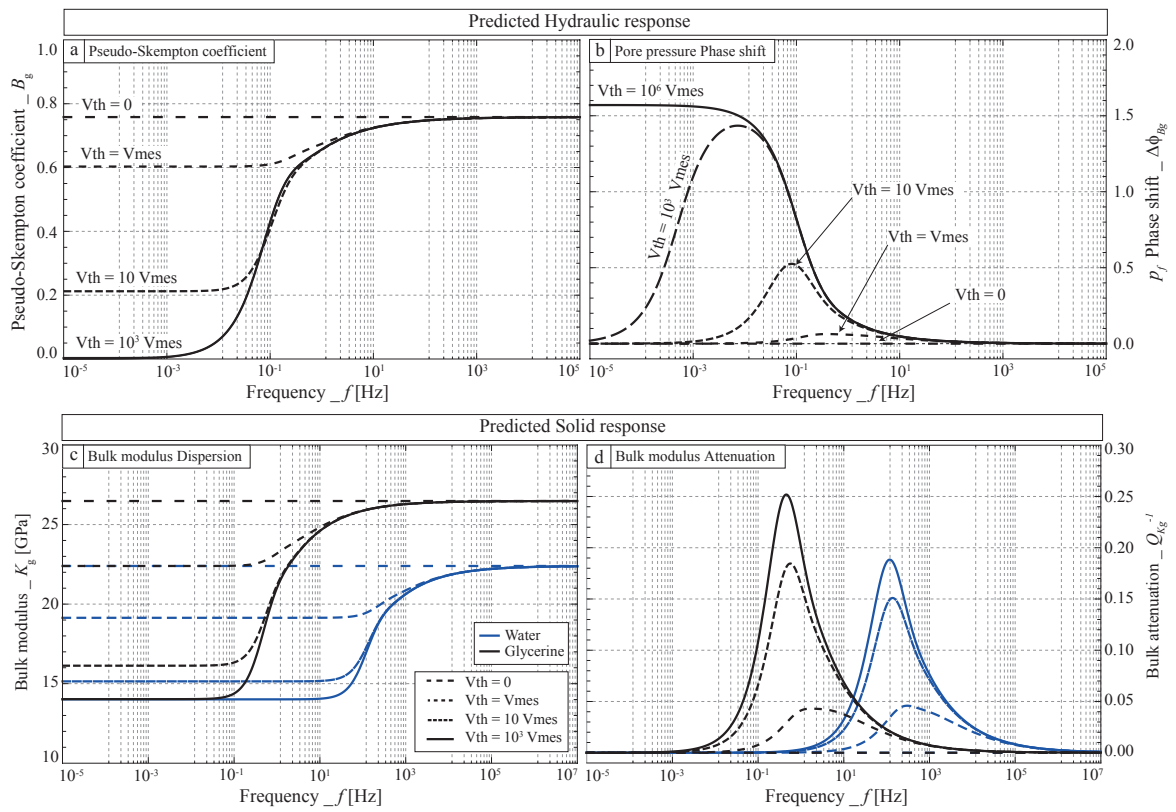


**Figure 2.7** : Predicted frequency dependence of the (a-b) hydraulic and (c-d) elastic response of the fluid-saturated Fo7 sample. Only the "global" prediction are reported, i.e. the response is summed over the sample's length.

on both  $K_g$  and  $Q_{K_g}^{-1}$ . For large dead volumes (i.e.  $10^3 V_{meas}$ ), a clear transition from  $K_d$  to  $K_{ud}$  is observed (Fig. 2.7c). By decreasing the dead volume, the initial value of  $K_g$  at low frequencies (i.e. in the drained domain) is much larger than  $K_d$ , and even equals  $K_{ud}$  when the dead volume equals zero. Dead volume appears to affect mainly the value predicted at low frequency. The magnitude of the variations, differs between glycerine and water owing to a difference between the intrinsic bulk modulus of each fluid.

The predicted variations in  $Q_{K_g}^{-1}$  (Fig. 2.7c) is consistent with  $K_g$  predictions. Decreasing the dead volumes damps the resulting attenuation, starting from the one expected under purely drained conditions, down to no attenuation for the purely "Undrained" conditions. Note that, interestingly, the attenuation peak appears to slightly shift to higher frequencies as the dead volume decreases.

### "Local" and "SG" predictions

For the bulk modulus and pseudo-Skempton coefficient, the model's "SG" predictions (summation over the strain gauge length at the sample's center) are investigated. They are noted  $K_{SG}$  and  $B_{SG}$ . In case of the pseudo-Skempton coefficient, the "local" prediction  $B_l$  is investigated at a position infinitely near to the boundary, so that the frequency-dependent variations in the dead volume can be approached. The frequency-dependent variations of  $K_{SG}$  (Fig. 2.8a), and  $B_{SG}$  and  $B_l$  (Fig. 2.8b) are investigated for the same problem's parameters as before.

Again, a strong effect of the dead volume is observed on the predictions. At lowest frequencies, the values equal the ones of the global predictions. By increasing the frequency, a sharp increase is observed at the sample's half-length. The values predicted for  $K_{SG}$  and  $B_{SG}$  show a small peak above the asymptotic values of the theoretical  $K_{ud}$  and  $B$ , before decreasing to reach these values. This sharp increase is consistent with the measurements from ?, and indicates a similar frequency-dependent transition as the one expected from Zener viscoelastic model. Investigating the position near the dead volume for  $B^*$  predictions (Fig. 2.8b) shows an interesting decrease with increasing the oscillation frequency. It indicates that fluid can less and less flow out of the sample as frequency increases, i.e. the sample becomes undrained.

## 2.3 Direct comparison with the measurements

The comparison of the model with measurements on two sandstone samples is tested. For both rocks, all parameters are known. The dead volume  $V_d$  is measured so that the upper and lower storages capacities are known. The other needed parameters for the model are (i) the drained (i.e. dry) bulk modulus ; (ii) the sample's porosity and permeability ; and (iii) the fluid's viscosity. All of these parameters are directly measured. Finally, Biot-Willis, Skempton and storage coefficients are deduced from the poroelastic relations by knowing

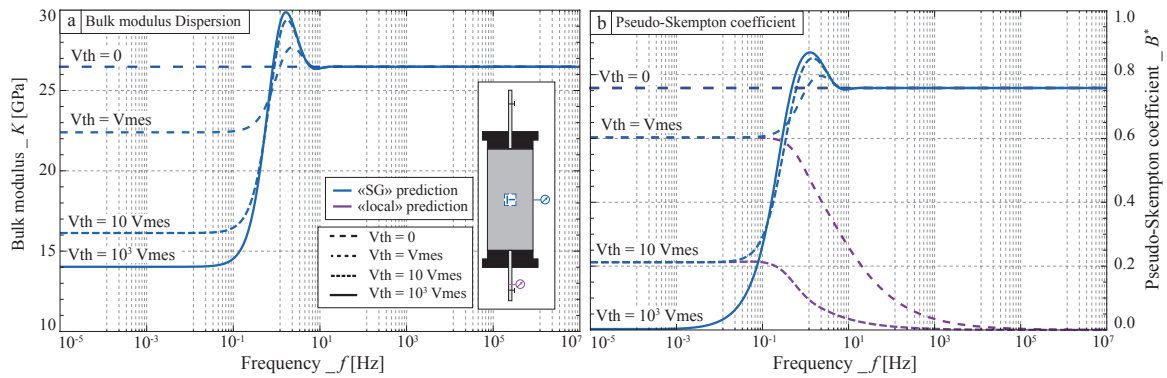


**Figure 2.8 :** Predicted frequency dependence of  $K_{SG}$ ,  $B_{SG}$  and  $B^*$  for the glycerine-saturated Fo7 sample. The sole local response is investigated. Different values of dead volume are chosen, starting from zero, up to a value a thousand time superior than the dead volume measured.

the sample's drained bulk modulus and porosity, and assuming a skeleton bulk modulus of 37 GPa.

For a comparison between model and measurement, the model's predictions are made according to the experimental conditions. While the strains for the solid response's measurement were at the sample's center, the pore pressure sensor for the hydraulic response measurement is placed in the dead volume (Fig. 1.1). Accordingly :

- the "SG" predictions at the sample center, noted  $K_{SG}$  and  $Q_{K_{SG}}^{-1}$ , are calculated for the solid response.
- the "local" predictions infinitely near the dead volume, noted  $B_l$  and  $\Delta\phi_{B_l}$ , are calculated for the hydraulic response.

The notations for the measurements are the ones reported before. The measured bulk modulus and attenuation are noted  $K_{LF}$  and  $Q_K^{-1}$ . The measured pseudo-Skempton coefficient is noted  $B^*$ . For consistency, the pore pressure phase shift is noted  $\Delta\phi_{B^*}$ .

### 2.3.1 Case of Fo7 sandstone

#### 2.3.1.1 Solid response at $P_{eff} = 1$ MPa

The model is compared with the measurements on the Fo7 sample at an effective pressure of  $P_{eff} = 1$  MPa. The frequency dependence of  $K$  (Fig. 2.9a) and  $Q_K^{-1}$  (Fig. 2.9b) is investigated. Different values of dead volume are tested in order to compare model and measurements. Owing to the accuracy of measurement of the permeability, the model's predictions are obtained for two different values of sample's permeabilities of  $2 - 4 \cdot 10^{-15} \text{m}^2$ .

As for before, different values of dead volumes lead to values of  $K_{SG}$  at lowest frequencies largely above the measured dry bulk modulus of 13 GPa. While the measured  $K_{LF}$  (?) also result higher than the dry value, the  $K_{SG}$  predicted for the measured  $V_{meas}$  largely overestimate the  $K_{LF}$ . On the reverse, the fit is obtained for a value of dead volume about 10

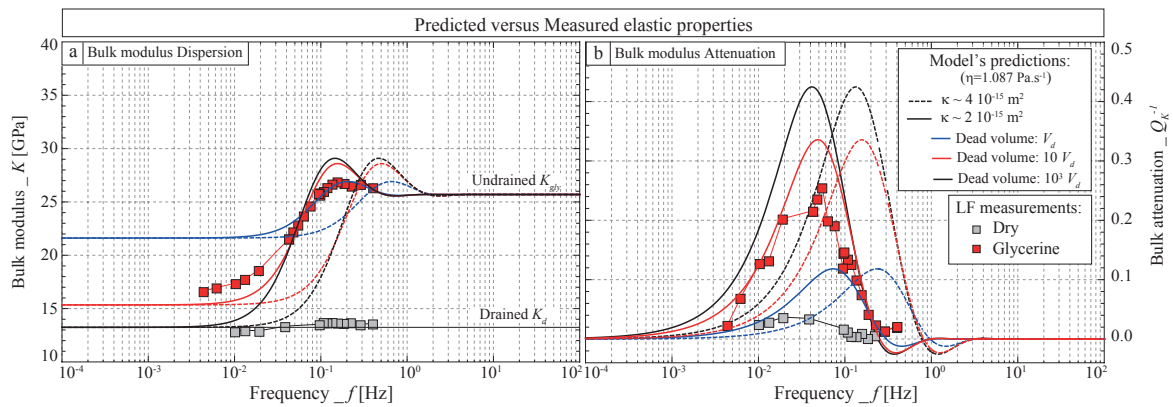


**Figure 2.9 :** Comparison of the frequency dependence of the predicted (curves) and measured (symbols)  $K$  (a) and  $Q_K^{-1}$  (b) for Fo7 sample. The "SG" predictions are calculated for the glycerine saturating conditions. The measured dead volume  $V_{meas}$  is used, along with other values of dead volumes.

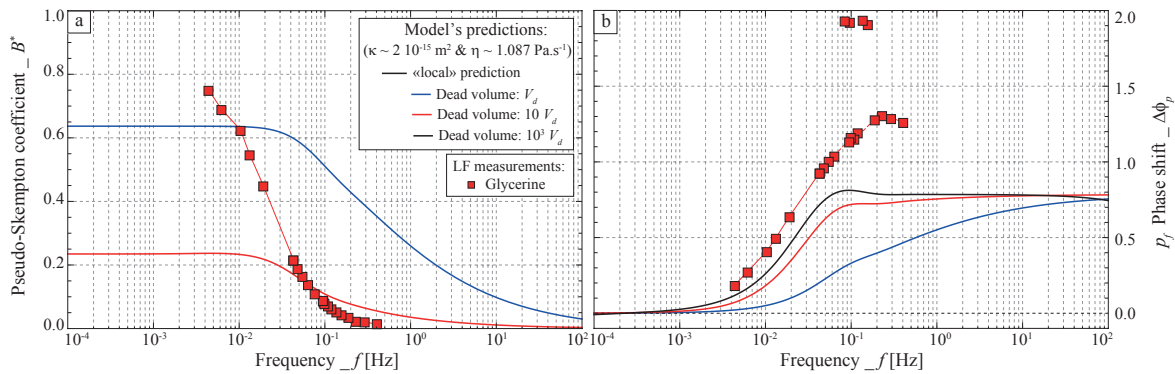


**Figure 2.10 :** Comparison between the frequency dependence of the predicted (curves) and measured (symbols) hydraulic properties for the glycerine-saturated Fo7 sample. The "local" predictions in the sample and at the bottom are calculated. The measured dead volume  $V_{meas}$  is used, along with other values of dead volumes.

times higher than the one measured, i.e. equal to  $10 V_{meas}$ . This result is not consistent and may originate from the problem's parameters used. The measured attenuation  $Q_K^{-1}$  (Fig. 2.9b) falls in between the predicted  $Q_{K_{SG}}^{-1}$  for the values of dead volumes of  $10 V_{meas}$  and  $V_{meas}$ .

### 2.3.1.2 Hydraulic response at $P_{eff} = 1$ MPa

The hydraulic properties predicted are compared to the measurement (Fig. 2.10). Overall, the model's predictions compares favourably with the measurements. As frequency increases, pseudo-Skempton coefficient (i.e.  $B_l$  and  $B^*$ ) decreases and pore pressure phase shift (i.e.  $\Delta\phi_l$  and  $\Delta\phi_{B^*}$ ) increases. However, deviations between prediction and measurement are observed.

In case of the pseudo-Skempton coefficient (Fig. 2.10a), both the amplitude and the frequency dependence differ between the predicted  $B_l$  and the measured  $B^*$ . First, the

measured  $B^*$  is larger than the predicted  $B_l$  for the measured  $V_{meas}$ . This deviation between model and measurements under quasi-static conditions was also observed for the solid responses (Fig. 2.9). Second,  $B^*$  decreases much faster than  $B_l$  as frequency increases. Because the frequency dependence of  $B^*$  is the same as both  $K_{SG}$  and  $K_{LF}$  (Fig. 2.9b), this second effect probably originates from the inaccuracy of the model to precisely predict variations in the dead volume.

### 2.3.2 Case of the Berea sample

Because a strong effect of the dead volume is observed for the Berea sandstone sample, the comparison with the model is tested. The only measurements of interest are here the ones made under glycerine saturation. The input viscosity chosen for the model is thus  $\eta = 1.087 \text{ Pa}\cdot\text{s}^{-1}$ . The frequency-dependence of the measured elastic (Fig. 2.11a) and hydraulic (Fig. 2.11b) properties are compared to model's predictions for an effective pressure of  $P_{eff} = 1 \text{ MPa}$ . For consistency, the measured  $K_{LF}$  and  $Q_K^{-1}$  are compared to "local"  $K_{SG}$  and  $Q_{K_{SG}}^{-1}$  predicted at the sample's center, and the measured  $B^*$  and  $\Delta\phi_B$  are compared to the "local"  $B_{th}^*$  and  $\Delta\phi_{B_{th}}$  predicted at the sample's bottom. In order to better understand the hydraulic properties inside the sample, the "local"  $B_{SG}$  and  $\Delta\phi_{B_{SG}}$  are also reported.

At lowest frequencies, the measured  $K_{LF}$  (Fig. 2.11a) results much higher than  $K_d$ . As shown from the predicted  $K_{SG}$ , this bias results from the dead volume and is theoretically expected. In fact, the measurement correspond particularly well with the model's predictions. As frequency increases, both modelled and measured  $K$  slightly increase, of about 2 GPa, to reach the value of  $K_{ud}$ . A good fit is also observed for the  $Q_K^{-1}$  (Fig. 2.11b) for the measured  $V_{meas}$ . The attenuation thus results much lower than the one expected in case of the ideal transition from  $K_d$  to  $K_{ud}$ .

At lowest frequencies, a good fit is also obtained between  $B^*$  and predicted  $B_l$  (Fig. 2.11c). The magnitude of the measured  $B^*$  is also well predicted by the model. Finally, the predicted  $\Delta\phi_{B_l}$  also fits with the measured  $\Delta\phi_{B^*}$  (Fig. 2.11d),  $\Delta\phi_{B^*}$ . A clear frequency-dependent increase is predicted that fits to the measurements.

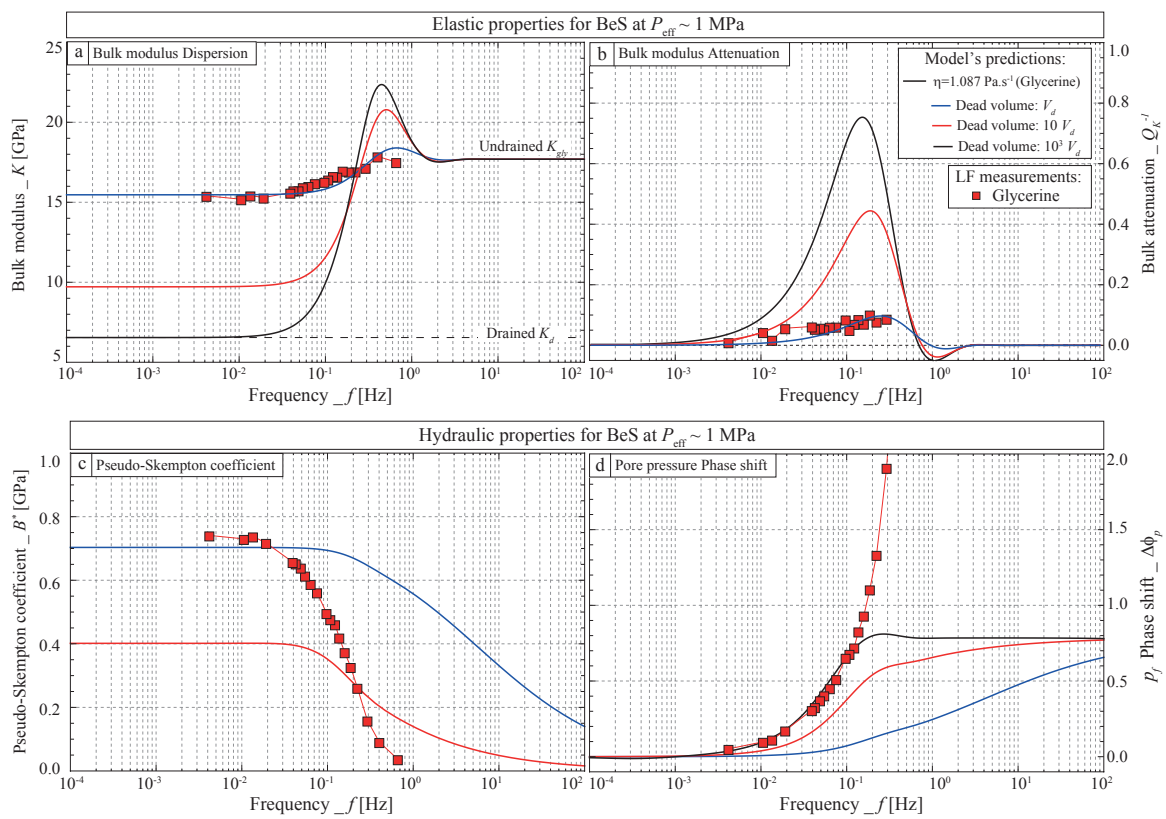


**Figure 2.11** : Comparison between predicted and measured frequency-dependent (a-b) solid and (c-d) hydraulic properties for the Berea sample. Different values of dead volumes are chosen for comparison, starting from the measured  $V_{meas}$ .

---

## Conclusion & Perspectives

---

### 3.1 Conclusions

A 1D model was developed that aimed at predicting the frequency-dependent variations involved in the drained to undrained transition. It is solely developed to understand the variations measured in **part III**, i.e. from the effect of an isotropic solicitation. Four properties may be predicted by this model : (i) the Skempton coefficient  $B$ , defined as the ratio of pore pressure over confining pressure ; (ii) the pore pressure phase shift  $\Delta\phi_B$ , which is assumed to indicate the frequency-dependent hydraulic diffusivity ; (iii) the bulk modulus  $K$ , defined as the ratio of volumetric strain over confining pressure ; and (iv) the bulk attenuation  $Q_K^{-1}$ , obtained from the tangent of the phase shift between stress and strain. This 1D model is tested for different boundary conditions : the theoretical "drained" and the "experimental undrained" boundary conditions.

Using the "drained" boundary condition, and measurable input parameters, the 1D model is tested in terms of its dependence to frequency and to the position of measurement. Comparing the model's predictions to the measurements on a Fontainebleau sandstone, an overall fit is obtained.

Yet, proofs for inconsistency are evidenced from the pore pressure build-up measured in the dead volume and from measurements of  $K$  in the highly compliant Berea sandstone. Noting that the theoretical "drained" and "undrained" boundary conditions may not apply to the reality of the experiment, realistic boundary conditions are sought. The presence of the dead volume is then accounted for to build up a more realistic "experimentally undrained" boundary condition. The effect of the dead volume on the resulting predictions is shown to originate from the interplay between sample's and dead volumes' intrinsic storage capacities. Comparison with the measurements on a Berea sandstone show a good

fit in both frequency dependence and magnitude for the effect. In case of the Fontainebleau sandstone, an overall fit is also obtained.

## 3.2 General 1D model : Deviatoric solicitation

### 3.2.1 Model derivation

It could be of interest to investigate the response of the poroelastic rock to an oscillating uniaxial stress, i.e. a deviatoric solicitation. The basic equation remains Eq. (2.1). Under the assumption of an isotropic response of the porosity to a deviatoric load, the volumetric strain is defined as :

$$\epsilon_v = \frac{1}{K} \left( \frac{\text{Tr}(\sigma)}{3} - \alpha p_f \right), \quad (3.1)$$

Here we assume (i) the stress  $\sigma$  to be positive in compression ; and (ii) the confining (i.e. radial) pressure to be held constant, while an oscillating axial stress (i.e.  $\sigma_{ax}(t)$ ) is applied. Again, we assume here that  $p_f$  varies only in the  $z$ -direction, which originates from the given boundary conditions. Finally, the equation rewrites :

$$\frac{\partial p_f}{\partial t} = \frac{\kappa}{\eta S_s} \frac{\partial^2 p_f}{\partial z^2} + \frac{B}{3} \frac{\partial \sigma_{ax}}{\partial t}. \quad (3.2)$$

The applied stress  $\sigma_{ax}(t)$  is here supposed to be small variations  $\Delta\sigma$  of a sinusoidal form such that  $\sigma_{ax}(t) = \Delta\sigma e^{i\omega t}$ . Accounting for this time dependence, the partial derivative equation simplifies to :

$$p_f(z, t) + i \left( \frac{D}{\omega} \right) \frac{\partial^2}{\partial z^2} [p_f(z, t)] = \frac{B}{3} \Delta\sigma e^{i\omega t}, \quad (3.3)$$

The equation being simplified to a typical differential equation of second order, solutions can be found analytically. As for the case of isotropic solicitation, these are of the form :

$$p_f(z, t) = \left[ \frac{B}{3} \Delta\sigma + p_f^\pm e^{\pm(1-i)\sqrt{\frac{\omega}{2B}}z} \right] e^{i\omega t}, \quad (3.4)$$

with  $p_f^+$  and  $p_f^-$  two constants that are obtained from the chosen problem's boundary conditions.

Again, a straightforward solution is easily found using the same theoretical "drained" or "undrained" boundary conditions, and a solution can also be obtained in case of the "experimentally undrained" boundary conditions. One could finally attain the "local" and "global" predictions for Young modulus and Poisson ratio.

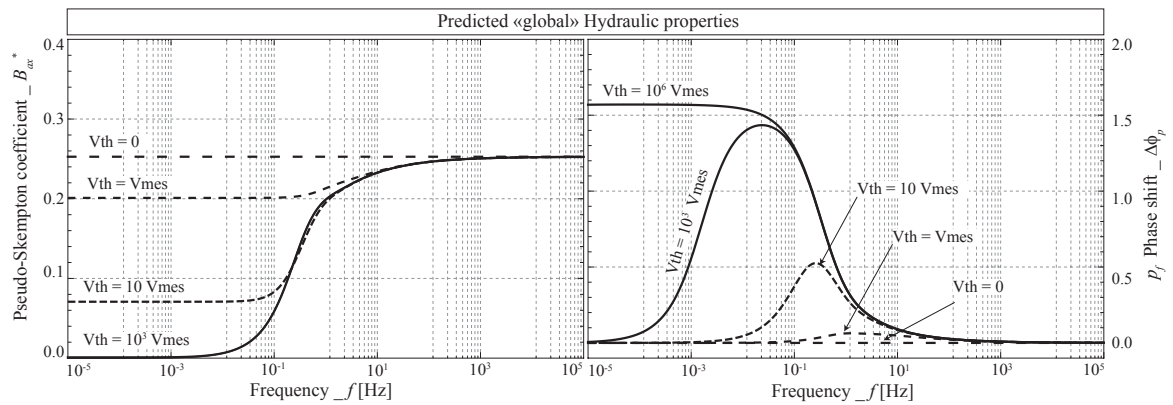


Figure 3.1 : Predicted frequency dependence of (a)  $\gamma$  and (b)  $\Delta\phi_\gamma$ . The sole "global" response is investigated.

### 3.2.2 Effect of the dead volume

We are again interested in both hydraulic and elastic properties. As for the isotropic solicitation, one may infer the pore pressure amplitude normalized by the stress amplitude, i.e. a consolidation parameter  $\gamma$ . The phase shift of the pore pressure as compared to the applied stress oscillation (i.e.  $\Delta\phi_\gamma$ ) is also of interest. For simplicity, only the "global" predictions of the model are investigated. These are again obtained by summing over the sample's length.

The frequency dependence of  $\gamma$  and  $\Delta\phi_\gamma$  is investigated for a synthetic sample that has the properties of the glycerine-saturated Fo7 sample (Fig. 3.1). Different values of dead volumes, related to the measured  $V_{meas}$ , are again tested. Comparing this prediction to the isotropic solicitation predictions shows an overall good fit.  $\Delta\phi_\gamma$  is strictly equal with the predicted  $\Delta\phi_B$ , and  $\gamma$  is strictly equal to one-third of the earlier predicted  $B$ , whichever the frequency. The relation of  $B = 3\gamma$  roots in the defined equation, which considers that only one-third of Skempton coefficient contributes to the pore pressure build-up from a deviatoric solicitation.

The elastic properties of interest are Young modulus  $E$ , Poisson ratio  $\nu$ , and their relative attenuations  $Q_E^{-1}$  and  $Q_\nu^{-1}$ . These could be inferred directly from the calculated pore pressure by applying the equations of poroelasticity.

### 3.2.3 Insight from the measurements : Skempton coefficient versus Consolidation parameter

Before going further in the modelling approach, it is of interest to verify that the developed 1D model applies to the case of a deviatoric solicitation. For this purpose, a comparison between measurements from **part III** and **part IV** is of interest : the sample's hydraulic response to the stress impulsion. Within the framework of poroelasticity, it is indeed expected that the porosity variation from an anisotropic solicitation should remain isotropic, and

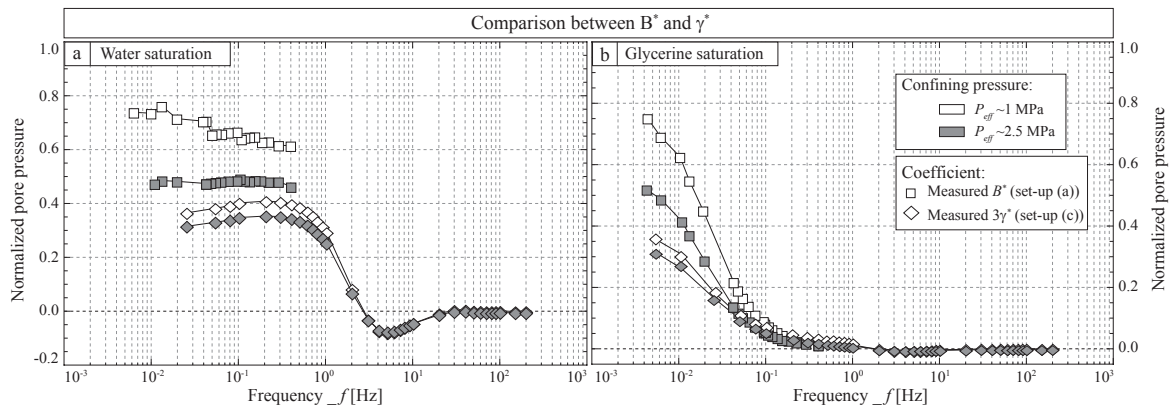


**Figure 3.2** : Comparison between frequency-dependent pseudo-Skempton coefficient  $B^*$  and pseudo-consolidation parameter  $\gamma^*$  measured on Fo7 under either (a) water or (b) glycerine saturation. To account for an isotropic solicitation,  $\gamma^*$  is multiplied by 3 in this comparison. Two confining pressure of  $P_{eff} = [1; 2.5]$  MPa are chosen for the comparison.

that  $B = 3\gamma$ . Similarly, the pseudo-Skempton coefficient  $B^*$  and pseudo-consolidation parameter  $\gamma^*$  measured on the Fo7 sample are compared (Figs. 3.2a & 3.2b).

Consistently, both hydraulic properties show the occurrence of fluid-flow for the same  $f$  under glycerine saturation (Fig. 3.2b). Yet, the magnitudes differ. The measured isotropic  $B^*$  is about twice larger than  $3\gamma^*$ . This implies that the amount of fluid-flow out of the sample during the deviatoric solicitation, is lower than what is theoretically expected. Such difference may have strong implications as the amount of fluid not flowing out of the sample may induce an additional lateral pore overpressure.

It seems possible that such deviation relates from the anisotropy induced from the measuring set-up. Under deviatoric solicitation, the properties may be more affected by the lateral boundary conditions. Owing to both the boundary conditions and the solicitation mechanism, the measured elastic properties are thus prone to differ.

### 3.3 Perspectives : 2D poroelastic model

Up to now, the problem was only solved in one dimension. This 1D problem proved to give consistent results for the isotropic solicitation, yet to deviate in case of the anisotropic solicitation. A possible cause for such deviations is that the strains are measured on the sample's (lateral) edge, which is bounded by the impermeable sleeve. It may result of importance to investigate such effect on the measurements. This is done by solving the equations in two dimensions, and using the two sets of boundary conditions. Below, examples of two different lateral boundary conditions are tested : the "drained" and "undrained" conditions. For this example, the axial boundary conditions are kept to the simplest "drained" boundary condition.

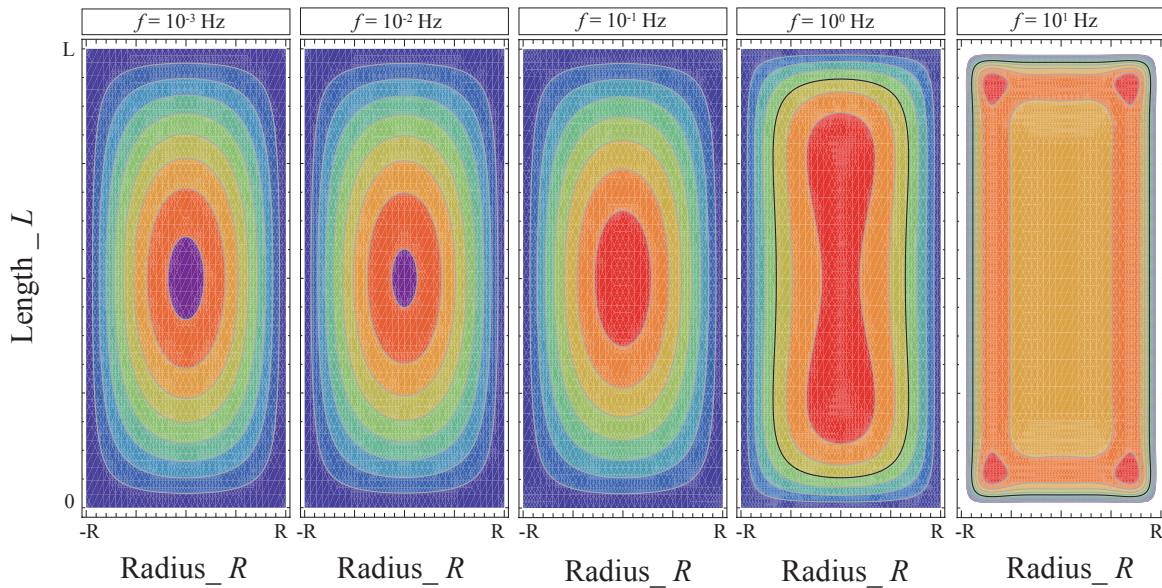


**Figure 3.3 :** Model prediction for the drained lateral and axial boundary conditions. The colour scale is from purple-blue at lowest pressure up to red at highest pressure.

### Laterally drained boundary condition

The case of purely drained axial and lateral boundary conditions corresponds to the ideal case scenario where no boundary effects should affect the measurements. Let us investigate first the pore pressure response to an oscillating axial stress solicitation (Fig. 3.3).

Consistently, a constant fluid response is obtained at the boundary when the wave travels through the medium. At the sample's center, a dependence to frequency occurs. The case of lowest frequency of  $f = 10^{-3}$  Hz corresponds to the standard drained case. As frequency increases, build-up pressure increases locally to reach the center of the sample at  $f = 0.1$  Hz. At  $f = 1$  Hz, the build-up pressure extends axially, to reach the sides at  $f = 10$  Hz.

If one investigates the response for the Poisson ratio (Fig. 3.3), consistently, the model's response is very similar as for the pore pressure.

Initially, while the sample's seems to be partially drained, the edges of the sample remain drained. Poisson ratio then increases as frequency increases. For a strain gauge placed at the sample's edge, one would thus obtain a pure transition from drained to undrained regimes. At the center, it is however expected for the Poisson ratio to show an increase from partially drained to undrained regime.

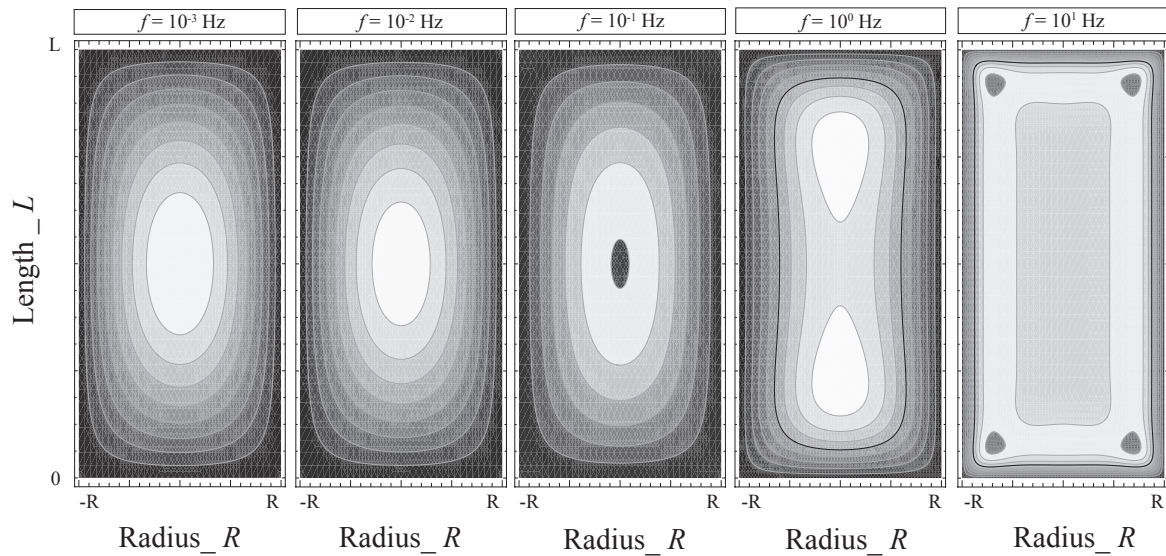


**Figure 3.4 :** Model prediction for Poisson ratio in case of the drained lateral and axial boundary conditions. A grey scale is used, from black for the lowest values to white at the highest ones.

### Laterally Undrained boundary condition

For the radially undrained boundary condition, the pore pressure response to an oscillating axial stress solicitation (Fig. 3.5) differs.

Apart from the chosen boundary condition, the procedure is the same. Yet, large differences are obtained as compared to the laterally drained boundary conditions. It implies that the build-up pressure largely depends to those conditions. In particular, the build-up pressure is initially higher than under purely drained boundary conditions. It implies that, although the axial boundary condition is purely drained, the radially undrained boundary condition directly introduces an experimental bias on the measurement : for a strain gauge placed at the sample's center (on the edge), the property measured will never be purely drained. This is typically what is observed from the measurements.

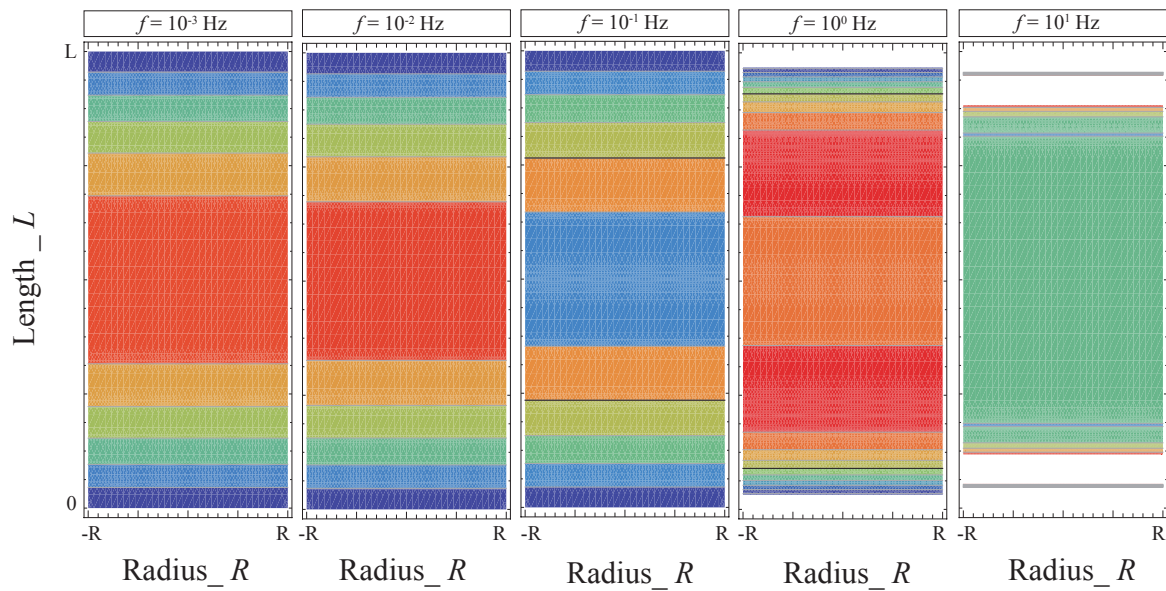


**Figure 3.5 :** Model prediction for the undrained lateral boundary conditions. The colour scale is from purple-blue at lowest pressure up to red at highest pressure.



# **Conclusion & Perspectives**

|          |   |            |
|----------|---|------------|
| <b>1</b> | <b>Summary &amp; Perspectives</b>                                       | <b>211</b> |
| 1.1      | Summary of the results . . . . .  | 211        |
| 1.1.1    | Effect of frequency on the elastic properties of rocks . . . . .        | 211        |
| 1.1.2    | Existence of a shear weakening in carbonates? . . . . .                 | 212        |
| 1.2      | Perspectives . . . . .  | 213        |
| 1.2.1    | Frequency effects in carbonate rock samples . . . . .                   | 213        |
| 1.2.2    | Investigation of the fundamental relations the elastic moduli . . . . . | 213        |



---

## Summary & Perspectives

---

### 1.1 Summary of the results

This work was motivated by two main questions :

1. What is the cause for the "shear weakening" observed in carbonate rocks? And why is it a phenomenon that is specific to carbonates?
2. How does frequency affect a rock's elastic moduli?

#### 1.1.1 Effect of frequency on the elastic properties of rocks

Extensive calibrations allowed for precise measurements of a sample's elastic properties. Two distinct methods have been used, both based on the stress-strain measuring protocol. The first one makes use of confining pressure oscillations to investigate the sample's bulk modulus (**part III**). The second one uses a deviatoric stress oscillation to investigate the sample's Young modulus and Poisson ratio (**part IV**). The methods are applied to investigate the frequency dependence of the elastic moduli of fluid-saturated sandstone samples.

From the measured bulk modulus (**part III**), the existence of three elastic regimes is evidenced for this typical sedimentary rock type. Both in terms of characteristic frequency and of magnitude of the effects, the measurements are consistent with the usual fluid-flow and effective medium theories. For the first time, direct measurement of both the cause (i.e. fluid flow out of the sample) and the consequence (i.e. bulk modulus dispersion and attenuation) of the transition between drained and undrained regimes is reported.

The measurement of frequency-dependent Young modulus and Poisson ratio (**part IV**) allows for measuring both drained/undrained and undrained/unrelaxed transitions in a sedimentary rock sample. Again, the dispersions/attenuations corresponding to the first

transition are interpreted by a global fluid flow out of the sample. Combining Young modulus measurements to the bulk modulus ones, it is directly inferred that these transitions between regimes lead to a bell-shaped dispersion curve for Poisson ratio. This is precisely what is observed from the measured Poisson ratio. It is directly inferred that the  $V_p/V_s$  ratio is expected to show this bell-shaped variation. An explanation for this variation is found from the use of effective medium theories : for some rocks the undrained Poisson ratio is larger than the unrelaxed one. Again, the existing theories fit reasonably well with the measurements both in terms of magnitudes of variations and characteristic frequencies for the variations.

Modelling the experiment and taking into account the experimental boundary conditions is the aim of **part V**. The equations of quasi-static poroelasticity are solved in one dimension (1D). Using the purely drained theoretical boundary condition, results are obtained in terms of pressure build-up and phase shift, leading to consistent dispersion and attenuation predictions. Using the "experimentally undrained" boundary condition, the model allows for considering the dead volume effect. The predictions fit with bulk modulus dispersion and attenuation measured in a Berea sample. However, this 1D model fails to predict the measured frequency dependence of Young modulus and Poisson ratio.

### 1.1.2 Existence of a shear weakening in carbonates ?

Under the consideration that shear weakening from water full saturation may originate from an adsorption effect, **part II** investigates the effect of moisture adsorption on the elastic properties of limestone and sandstone samples. Insights are obtained from this study :

- For the samples studied, no elastic weakening is observed in the limestone samples. Reversely, some of the sandstone samples investigated show large elastic weakening from adsorption. At maximum moisture adsorption, up to about 25 % decrease is obtained.
- When shear weakening is observed from adsorption, it correlates to an even larger weakening in bulk modulus, up to about 40 % decrease for some sandstone samples. Adsorption is thus responsible for a global elastic weakening, and not only a shear weakening, in those samples.
- More than an intrinsic difference between the quartz and calcite minerals, elastic weakening may relate to a microstructural difference. Indeed, it is thought to originate from adsorption at grains' contact, and is thus expected to occur in granular uncemented rocks only. This rules out most of the well-cemented limestone samples. Consistently, the effect was shown to occur only in loosely cemented sandstone samples.

All the measurements can be understood in terms of a simple granular model accounting for both adsorption and degree of cement in a sample.

Under water full saturation, it is shown that no clear weakening is observed on the limestone samples' drained bulk moduli. Reversely, a large change in the Berea sample's bulk drained compressibilities (i.e.  $C_{bc} = K_d^{-1}$  and  $C_{bp}$ ) is observed upon water full saturation. The increase in bulk compressibility (i.e. decrease in  $K_d$ ) amounts to about 40% of the initial value. It may imply that a water-induced elastic weakening is observed. Interestingly, the magnitude of the effect correlates with the results for moisture adsorption, implying that the largely documented "shear weakening" effect may indeed originate from adsorption. It is suggested that "shear weakening" from adsorption occurs solely in poorly cemented granular materials where grains are rounded.

## 1.2 Perspectives

### 1.2.1 Frequency effects in carbonate rock samples

Investigating the frequency dependence of carbonates elastic properties would be a direct extension of the present work. In the present study, two frequency effects were evidenced. One may wonder if the same should happen in carbonates. The first transition being independent of the microstructure, it is expected to occur in any porous and compliant material. Reversely, the second transition is generally expected to occur only if two families of microstructures, with largely differing compressibilities, are present. Indeed, squirt-flow is considered in case of a microcracked rock. This microstructural feature is frequent in sandstones, but not common in limestones. However, it exists a feature in carbonates that is not found in sandstones : the double porosity. Thus, the question of the possible relaxed/unrelaxed transition in carbonates remains open.

### 1.2.2 Investigation of the fundamental relations the elastic moduli

As briefly introduced in the Appendix, the experimental apparatus used in this work allows for independent measurement of various elastic and poroelastic properties for different saturating fluids (e.g.,  $K_s$ ,  $K_d$ ,  $K_u$ ,  $K_\phi$  or  $B$ ). This opens the possibility to verify if the theoretical relations predicted (by thermodynamics or poroelasticity) between the properties are consistent with the data or not. In particular, the usual assumption of homogeneity could be checked. This point may be important for the fluid substitution issue.



---

## Bibliographie

---

- Adam, L., Batzle, M., and Brevik, I. : Gassmann's fluid substitution and shear modulus variability in carbonates at laboratory seismic and ultrasonic frequencies, *Geophysics*, 71, F173–F183, 2006.
- Adam, L., Batzle, M., Lewallen, K., and van Wijk, K. : Seismic wave attenuation in carbonates, *Journal of Geophysical Research*, 114, B06 208, 2009.
- Adamson, A. W. : *Physical chemistry of surfaces* (2nd ed.), Wiley, 1976.
- Adelinet, M., Fortin, J., Guéguen, Y., Schubnel, A., and Geoffroy, L. : Frequency and fluid effects on elastic properties of basalt : Experimental investigations, *Geophysical Research Letters*, 37(2), L02 303, doi :10.1029/2009GL041660, 2010.
- Adelinet, M., Fortin, J., and Guéguen, Y. : Dispersion of elastic moduli in a porous-cracked rock : Theoretical predictions for squirt-flow, *Tectonophysics*, 503, 173–181, 2011.
- Anselmetti, F. and Eberli, G. : Controls on sonic velocity in carbonates, *Pure and Applied Geophysics*, 141, 287–323, 1993.
- Archie, G. : Classification of carbonate reservoir rocks and petrophysical considerations, *AAPG Bulletin*, 36, 278–298, 1952.
- Assefa, S., McCann, C., and Sothcott, J. : Velocities of compressional and shear waves in limestones, *Geophysical prospecting*, 51, 1–13, 2003.
- Baechle, G., Weger, R., Eberli, G., Massaferro, J., and Sun, Y. : Changes of shear moduli in carbonate rocks Implications for Gassmann applicability, *The Leading Edge*, 24, 507–510, 2005.
- Baechle, G., Eberli, G., Weger, R., and Colpaert, A. : Modeling Velocity In Carbonates Using a Dual Porosity DEM Model, in : 2007 SEG Annual Meeting, 2007.

- Baechle, G., Colpaert, A., Eberli, G., and Weger, R. : Effects of microporosity on sonic velocity in carbonate rocks, *The Leading Edge*, 27, 1012–1018, 2008.
- Baechle, G., Eberli, G., Weger, R., and Massaferro, J. : Changes in dynamic shear moduli of carbonate rocks with fluid substitution, *Geophysics*, 74, E135–E147, 2009.
- Barrau, J.-J. and Laroze, S. : *Mécanique des structures*. Tome 1, Masson, 1988.
- Batzle, M., Hofmann, R., Han, D.-H., and Castagna, J. : Fluids and frequency dependent seismic velocity of rocks, *The Leading Edge*, 20, 168–171, 2001.
- Batzle, M. L., Han, D.-H., and Hofmann, R. : Fluid mobility and frequency-dependent seismic velocity Direct measurements, *Geophysics*, 71, N1–N9, 2006.
- Baud, P., Zhu, W., and Wong, T.-f. : Failure mode and weakening effect of water on sandstone, *Journal of Geophysical Research : Solid Earth (1978–2012)*, 105, 16 371–16 389, 2000.
- Birch, F. : The velocity of compressional waves in rocks to 10 kilobars, part 1, *Journal of Geophysical Research*, 65, 1083–1102, 1960.
- Boudet, J. and Ciliberto, S. : Interaction of sound with fast crack propagation, *Physical review letters*, 80, 341, 1998.
- Bourbie, T. and Zinszner, B. : Hydraulic and acoustic properties as a function of porosity in Fontainebleau sandstone, *Journal of Geophysical Research : Solid Earth (1978–2012)*, 90, 11 524–11 532, 1985.
- Brace, W., Walsh, J., and Frangos, W. : Permeability of granite under high pressure, *Journal of Geophysical Research*, 73, 2225–2236, 1968.
- Brantut, N., Schubnel, A., David, E., Héripré, E., Guéguen, Y., and Dimanov, A. : Dehydration-induced damage and deformation in gypsum and implications for subduction zone processes, *Journal of Geophysical Research : Solid Earth (1978–2012)*, 117(B3), 2012.
- Brown, R. J. and Korrington, J. : On the dependence of the elastic properties of a porous rock on the compressibility of the pore fluid, *Geophysics*, 40, 608–616, 1975.
- Casteleyn, L., Robion, P., Collin, P., Menéndez, B., David, C., Desaubliaux, G., Fernandes, N., Dreux, R., Badiner, G., Brosse, E., et al. : Interrelations of the petrophysical, sedimentological and microstructural properties of the Oolithe Blanche Formation (Bathonian, saline aquifer of the Paris Basin), *Sedimentary Geology*, 230, 123–138, 2010.
- Casteleyn, L., Robion, P., David, C., Collin, P.-Y., Menéndez, B., Fernandes, N., Desaubliaux, G., and Rigollet, C. : An integrated study of the petrophysical properties of carbonate

- rocks from the Oolithe Blanche formation in the Paris Basin, *Tectonophysics*, 503, 18–33, 2011.
- Chelidze, T., Spetzler, H., and Sobolev, G. : Absorption of strain waves in porous media at seismic frequencies, *pure and applied geophysics*, 147, 25–55, 1996.
- Choquette, P. and Pray, L. : Geologic nomenclature and classification of porosity in sedimentary carbonates, *AAPG Bulletin*, 54, 207–250, 1970.
- Clark, V., Tittmann, B., and Spencer, T. : Effect of volatiles on attenuation ( $Q^{-1}$ ) and velocity in sedimentary rocks, *Journal of Geophysical Research : Solid Earth (1978–2012)*, 85, 5190–5198, 1980.
- Cleary, M. P. : Elastic and dynamic response regimes of fluid-impregnated solids with diverse microstructures, *International Journal of Solids and Structures*, 14, 795–819, 1978.
- Dana, E. and Skoczylas, F. : Gas relative permeability and pore structure of sandstones, *International Journal of Rock Mechanics and Mining Sciences*, 36, 613–625, 1999.
- David, E. C., Fortin, J., Schubnel, A., Guéguen, Y., and Zimmerman, R. W. : Laboratory measurements of low- and high-frequency elastic moduli in Fontainebleau sandstone, *Geophysics*, 78, D369–D379, 2013.
- Detournay, E. and Cheng, A. H.-D. : *Fundamentals of Poroelasticity*, 1993.
- Digby, P. : The effective elastic moduli of porous granular rocks, *Journal of Applied Mechanics*, 48, 803, 1981.
- Duda, M. and Renner, J. : The weakening effect of water on the brittle failure strength of sandstone, *Geophysical Journal International*, 192, 1091–1108, 2013.
- Dunn, K.-J. : Acoustic attenuation in fluid-saturated porous cylinders at low frequencies, *The Journal of the Acoustical Society of America*, 79, 1709–1721, 1986.
- Dunn, K.-J. : Sample boundary effect in acoustic attenuation of fluid-saturated porous cylinders, *The Journal of the Acoustical Society of America*, 81, 1259, 1987.
- Dürrast, H. and Siegesmund, S. : Correlation between rock fabrics and physical properties of carbonate reservoir rocks, *International Journal of Earth Sciences*, 88, 392–408, 1999.
- Eberli, G., Baechle, G., Anselmetti, F., and Incze, M. : Factors controlling elastic properties in carbonate sediments and rocks, *The Leading Edge*, 22, 654–660, 2003.
- Eslami, J., Grgic, D., and Hoxha, D. : Estimation of the damage of a porous limestone from continuous (P- and S-) wave velocity measurements under uniaxial loading and different hydrous conditions, *Geophysical Journal International*, 183, 1362–1375, 2010.

- Fabricius, I., Bächle, G., and Eberli, G. : Elastic moduli of dry and water-saturated carbonates Effect of depositional texture, porosity, and permeability, *Geophysics*, 75, N65–N78, 2010.
- Fortin, J., Schubnel, A., and Guéguen, Y. : Elastic wave velocities and permeability evolution during compaction of Bleurswiller sandstone, *International Journal of Rock Mechanics and Mining Sciences*, 42, 873–889, 2005.
- Fortin, J., Guéguen, Y., and Schubnel, A. : Effects of pore collapse and grain crushing on ultrasonic velocities and  $V_p/V_s$ , *Journal of Geophysical Research : Solid Earth* (1978–2012), 112(B8), 1978–2012, 2007.
- Fortin, J., Stanchits, S., Dresen, G., and Guéguen, Y. : Micro-mechanisms involved during inelastic deformation of porous carbonate rocks, *Poro-Mechanics IV*, p. 378, 2009.
- Fortin, J., Pimienta, L., Guéguen, Y., Schubnel, A., David, E., and Adelinet, M. : Experimental results on the combined effects of frequency and pressure on the dispersion of elastic waves in porous rocks, *The Leading Edge*, 33, 648–654, 2014.
- Fournier, F. and Borgomano, J. : Critical porosity and elastic properties of microporous mixed carbonate-siliciclastic rocks, *Geophysics*, 74, E93–E109, 2009.
- Gassmann, F. : Elasticity of porous media, *Vierteljahrsschrder Naturforschenden Gesellschaft*, 96, 1–23, 1951.
- Ghabezloo, S. and Sulem, J. : Stress dependent thermal pressurization of a fluid-saturated rock, *Rock Mechanics and Rock Engineering*, 42, 1–24, 2009.
- Ghabezloo, S. and Sulem, J. : Effect of the volume of the drainage system on the measurement of undrained thermo-poro-elastic parameters, *International Journal of Rock Mechanics and Mining Sciences*, 47, 60–68, 2010.
- Goertz, D. and Knight, R. : Elastic wave velocities during evaporative drying, *Geophysics*, 63, 171–183, 1998.
- Gomez, C., Dvorkin, J., and Vanorio, T. : Laboratory measurements of porosity, permeability, resistivity, and velocity on Fontainebleau sandstones, *Geophysics*, 75, E191–E204, 2010.
- Greenspan, L. : Humidity fixed points of binary saturated aqueous solutions, *Journal of research of the national Bureau of Standards, A. Physics and Chemistry A*, 81, 89–96, 1977.
- Guéguen, Y. and Bouteica, M. : *Mechanics of fluid-saturated rocks*, vol. 89, Academic Press, 2004.

- Guéguen, Y. and Kachanov, M. : Effective Elastic Properties of Cracked Rocks - An Overview, in *Mechanics of Crustal Rocks, CSIM Courses and Lectures*, edited by Y. Leroy and F.K. Lehner, vol. 533 pp. 73 - 125, Springer, New York, 2011.
- Hart, D. and Wang, H. : Laboratory measurements of a complete set of poroelastic moduli for Berea sandstone and Indiana limestone, *Journal of Geophysical Research*, 100, 17741–17, 1995.
- Hart, D. and Wang, H. : Variation ofunjacketed pore compressibility using Gassmann's equation and an overdetermined set of volumetric poroelastic measurements, *Geophysics*, 75, N9–N18, 2010.
- Hofmann, R. : Frequency dependent elastic and anelastic properties of clastic rocks, vol. 67, PhD thesis, Colorado School of Mines, 2006.
- Hsieh, P., Tracy, J., Neuzil, C., Bredehoeft, J., and Silliman, S. : A transient laboratory method for determining the hydraulic properties of tightrocksI. Theory, in : *International Journal of Rock Mechanics and Mining Sciences & Geomechanics Abstracts*, vol. 18, pp. 245–252, Elsevier, 1981.
- Jackson, I. and Paterson, M. : Shear modulus and internal friction of calcite rocks at seismic frequencies : pressure, frequency and grain size dependence, *Physics of the earth and planetary interiors*, 45, 349–367, 1987.
- Johnson, K., Kendall, K., and Roberts, A. : Surface energy and the contact of elastic solids, *Proceedings of the Royal Society of London. A. Mathematical and Physical Sciences*, 324, 301–313, 1971.
- Khazanehdari, J. and Sothcott, J. : Variation in dynamic elastic shear modulus of sandstone upon fluid saturation and substitution, *Geophysics*, 68, 472–481, 2003.
- Kirby, S. H. : Introduction and digest to the special issue on chemical effects of water on the deformation and strengths of rocks, *Journal of Geophysical Research*, 89, 3991–3995, 1984.
- Klein, E., Baud, P., Reuschlé, T., and Wong, T. : Mechanical behaviour and failure mode of Bentheim sandstone under triaxial compression, *Physics and Chemistry of the Earth, Part A : Solid Earth and Geodesy*, 26, 21–25, 2001.
- Kümpel, H.-J. : Poroelasticity : parameters reviewed, *Geophysical Journal International*, 105, 783–799, 1991.
- Langmuir, D. : The geochemistry of some carbonate ground waters in central Pennsylvania, *Geochimica et Cosmochimica Acta*, 35, 1023–1045, 1971.

- Le Guen, Y., Renard, F., Hellmann, R., Brosse, E., Collombet, M., Tisserand, D., and Gratier, J.-P. : Enhanced deformation of limestone and sandstone in the presence of high PCO<sub>2</sub> fluids, *Journal of geophysical research*, 112, B05421, 2007.
- Le Ravalec, M. and Guéguen, Y. : High-and low-frequency elastic moduli for a saturated porous/cracked rock-Differential self-consistent and poroelastic theories, *Geophysics*, 61, 1080–1094, 1996.
- Le Ravalec, M., Guéguen, Y., and Chelidze, T. : Elastic wave velocities in partially saturated rocks : saturation hysteresis, *Journal of Geophysical Research*, 101, 837–844, 1996.
- Lin, W. : Compressible fluid flow through rocks of variable permeability, Tech. rep., California Univ., Livermore (USA). Lawrence Livermore Lab, 1977.
- Lucia, F. : Petrophysical parameters estimated from visual descriptions of carbonate rocks : a field classification of carbonate pore space, *Journal of Petroleum Technology*, 35, 629–637, 1983.
- Madonna, C. and Tisato, N. : A new Seismic Wave Attenuation Module to experimentally measure low-frequency attenuation in extensional mode, *Geophysical Prospecting*, 61, 302–314, 2013.
- Madonna, C., Tisato, N., Artman, B., and Saenger, E. : Laboratory Measurements of Seismic Attenuation from 0.01 to 100 Hz, in : 73rd EAGE Conference & Exhibition, 2011.
- Maghsoudy-Louyeh, S. and Tittmann, B. R. : Assessment of hydrous affinity of selected material, *Colloids and Surfaces A : Physicochemical and Engineering Aspects*, 331, 268–274, 2008.
- Mallet, C., Fortin, J., Guéguen, Y., and Bouyer, F. : Effective Elastic Properties of Cracked Solids : An Experimental Investigation, *International journal of fracture*, 182, 275–282, 2013.
- Mavko, G. and Jizba, D. : Estimating grain-scale fluid effects on velocity dispersion in rocks, *Geophysics*, 56, 1940–1949, 1991.
- Mavko, G. and Nur, A. : Melt squirt in the asthenosphere, *Journal of Geophysical Research*, 80, 1444–1448, 1975.
- Mavko, G., Mukerji, T., and Dvorkin, J. : The rock physics handbook : tools for seismic analysis of porous media, Cambridge Univ Pr, 2003.
- Mikhaltsevitch, V., Lebedev, M., Gurevich, B., et al. : A low-frequency laboratory apparatus for measuring elastic and anelastic properties of rocks, in : 2011 SEG Annual Meeting, Society of Exploration Geophysicists, 2011.

- Mikhaltsevitch, V., Lebedev, M., and Gurevich, B. : Laboratory measurements of the elastic and anelastic parameters of limestone at seismic frequencies, chap. 577, pp. 2974–2978, doi :10.1190/segam2013-1395.1, doi :10.1190/segam2013-1395.1, URL <http://library.seg.org/doi/abs/10.1190/segam2013-1395.1>, 2013.
- Mikhaltsevitch, V., Lebedev, M., and Gurevich, B. : A laboratory study of low-frequency wave dispersion and attenuation in water-saturated sandstones, *The Leading Edge*, 33, 616–622, 2014.
- Mindlin, R. : Compliance of elastic bodies in contact : *Transactions of American Society of Mechanical Engineers, Journal of Applied Mechanics*. v16, 1949.
- Moore, C. : Carbonate reservoirs : porosity evolution and diagenesis in a sequence stratigraphic framework, vol. 55, Elsevier Science, 2001.
- Müller, T. M. and Sahay, P. N. : Solid-phase bulk modulus and microinhomogeneity parameter from quasistatic compression experiments, *Geophysics*, 79, A51–A55, 2014.
- Müller, T. M., Gurevich, B., and Lebedev, M. : Seismic wave attenuation and dispersion resulting from wave-induced flow in porous rocks A review, *Geophysics*, 75, 75A147–75A164, 2010.
- Murphy, W., Winkler, K., and Kleinberg, R. : Frame modulus reduction in sedimentary rocks : The effect of adsorption on grain contacts, *Geophysical Research Letters*, 11, 805–808, 1984.
- Murphy, W., Winkler, K., and Kleinberg, R. : Acoustic relaxation in sedimentary rocks : Dependence on grain contacts and fluid saturation, *Geophysics*, 51, 757–766, 1986.
- Murphy, W. F. : Acoustic measures of partial gas saturation in tight sandstones, *Journal of Geophysical Research : Solid Earth* (1978–2012), 89, 11 549–11 559, 1984.
- Murphy III, W. F. : Effects of partial water saturation on attenuation in Massillon sandstone and Vycor porous glass, *The Journal of the Acoustical Society of America*, 71, 1458, 1982.
- Murray, R. and Pray, L. : Dolomitization and limestone diagenesis-an introduction, 1965.
- Nowick, A. and Berry, B. : Anelastic relaxation in crystalline solids, Academic, New York, 1972.
- Nur, A., Mavko, G., Dvorkin, J., and Galmudi, D. : Critical porosity : A key to relating physical properties to porosity in rocks, *The Leading Edge*, 17, 357, 1998.
- O’Connell, R. J. and Budiansky, B. : Seismic velocities in dry and saturated cracked solids, *Journal of Geophysical Research*, 79, 5412–5426, 1974.

- O'Connell, R. J. and Budiansky, B. : Viscoelastic properties of fluid-saturated cracked solids, *Journal of Geophysical Research*, 82, 5719–5735, 1977.
- Ougier-Simonin, A., Fortin, J., Guéguen, Y., Schubnel, A., and Bouyer, F. : Cracks in glass under triaxial conditions, *International Journal of Engineering Science*, 49, 105–121, 2011.
- Pandit, B. and King, M. : The variation of elastic wave velocities and quality factor  $Q$  of a sandstone with moisture content, *Canadian Journal of Earth Sciences*, 16, 2187–2195, 1979.
- Parks, G. A. : Surface and interfacial free energies of quartz, *Journal of Geophysical Research : Solid Earth (1978–2012)*, 89, 3997–4008, 1984.
- Pimienta, L., Fortin, J., and Guéguen, Y. : Investigation of elastic weakening in limestone and sandstone samples from moisture adsorption, *Geophysical Journal International*, 199, 335–347, 2014a.
- Pimienta, L., Sarout, J., Esteban, L., and Delle Piane, C. : Prediction of rocks thermal conductivity from elastic wave velocities, mineralogy and microstructure, *Geophysical Journal International*, p. ggu034, 2014b.
- Ratschbacher, L., Wetzell, A., and Brokmeier, H. : A neutron goniometer study of the preferred orientation of calcite in fine-grained deep-sea carbonate, *Sedimentary geology*, 89, 315–324, 1994.
- Rice, J. R. and Cleary, M. P. : Some basic stress diffusion solutions for fluid-saturated elastic porous media with compressible constituents, *Reviews of Geophysics*, 14, 227–241, 1976.
- Røgen, B., Gommessen, L., and Fabricius, I. : Methods of velocity prediction tested for North Sea chalk : a review of fluid substitution and  $S$  estimates, *Journal of Petroleum Science and Engineering*, 45, 129–139, 2004.
- Røgen, B., Fabricius, I., Japsen, P., Høier, C., Mavko, G., and Pedersen, J. : Ultrasonic velocities of North Sea chalk samples : influence of porosity, fluid content and texture, *Geophysical Prospecting*, 53, 481–496, 2005.
- Sarout, J. : Impact of pore space topology on permeability, cut-off frequencies and validity of wave propagation theories, *Geophysical Journal International*, 189, 481–492, 2012.
- Sigg, L., Xue, H., Kistler, D., and Sshönenberger, R. : Size fractionation (dissolved, colloidal and particulate) of trace metals in the Thur River, Switzerland, *Aquatic Geochemistry*, 6, 413–434, 2000.
- Simmons, G., Wilkens, R., Caruso, L., Wissler, T., and Miller, F. : Physical properties and microstructures of a set of sandstones," *Annual Report to the Schlumberger-Doll Research Center*, 1 January 1982, p, VI-16, 1982.

- Song, I. and Renner, J. : Linear pressurization method for determining hydraulic permeability and specific storage of a rock sample, *Geophysical Journal International*, 164, 685–696, 2006.
- Song, I. and Renner, J. : Analysis of oscillatory fluid flow through rock samples, *Geophysical Journal International*, 170, 195–204, 2007.
- Song, I. and Renner, J. : Hydromechanical properties of Fontainebleau sandstone : Experimental determination and micromechanical modeling, *Journal of Geophysical Research*, 113, B09 211, 2008.
- Spencer Jr., J. : Stress relaxations at low frequencies in fluid-saturated rocks : Attenuation and modulus dispersion, *Journal of Geophysical Research*, 86, 1803–1812, 1981.
- Subramaniyan, S., Quintal, B., Tisato, N., Saenger, E. H., and Madonna, C. : An overview of laboratory apparatuses to measure seismic attenuation in reservoir rocks, *Geophysical Prospecting*, 2014.
- Sulem, J. and Ouffroukh, H. : Hydromechanical behaviour of Fontainebleau sandstone, *Rock Mechanics and Rock Engineering*, 39, 185–213, 2006.
- Sun, S. : Dolomite reservoirs : porosity evolution and reservoir characteristics, *AAPG bulletin*, 79, 186–204, 1995.
- Tisato, N. and Madonna, C. : Attenuation at low seismic frequencies in partially saturated rocks : Measurements and description of a new apparatus, *Journal of Applied Geophysics*, 2012.
- Tittmann, B. : Lunar rock Q in 3000-5000 range achieved in laboratory, *Philosophical Transactions of the Royal Society of London. Series A, Mathematical and Physical Sciences*, 285, 475–479, 1977.
- Tittmann, B. : Internal friction measurements and their implications in seismic Q structure models of the crust, *Geophysical Monograph Series*, 20, 197–213, 1978.
- Tittmann, B. and Housley, R. : High Q (low internal friction) observed in a strongly outgassed terrestrial analog of lunar basalt, *physica status solidi (b)*, 56, K109–K111, 1973.
- Tittmann, B., Clark, V., Richardson, J., and Spencer, T. : Possible mechanism for seismic attenuation in rocks containing small amounts of volatiles, *Journal of Geophysical Research : Solid Earth (1978–2012)*, 85, 5199–5208, 1980.
- Toksöz, M. N. and Johnston, D. H. : Seismic wave attenuation, 2, *Soc of Exploration Geophysicists*, 1981.

- Toksöz, M. N., Cheng, C. H., and Timur, A. : Velocities of seismic waves in porous rocks, *Geophysics*, 41, 621–645, 1976.
- Tutuncu, A. and Sharma, M. : The influence of fluids on grain contact stiffness and frame moduli in sedimentary rocks, *Geophysics*, 57, 1571–1582, 1992.
- Vajdova, V., Baud, P., and Wong, T. : Compaction, dilatancy, and failure in porous carbonate rocks, *Journal of geophysical research*, 109, B05 204, 2004.
- Vajdova, V., Zhu, W., Natalie Chen, T., and Wong, T. : Micromechanics of brittle faulting and cataclastic flow in Tavel limestone, *Journal of Structural Geology*, 32, 1158–1169, 2010.
- Vega, S., Berteussen, K., Sun, Y., and Sultan, A. : Is Gassmann the Best Model For Fluid Substitution In Heterogeneous Carbonates ?, in : 2007 SEG Annual Meeting, 2007.
- Verwer, K., Braaksma, H., and Kenter, J. : Acoustic properties of carbonates : Effects of rock texture and implications for fluid substitution, *Geophysics*, 73, B51–B65, 2008.
- Verwer, K., Eberli, G., Baechle, G., and Weger, R. : Effect of carbonate pore structure on dynamic shear moduli, *Geophysics*, 75, E1–E8, 2010.
- Vialle, S. and Vanorio, T. : Laboratory measurements of elastic properties of carbonate rocks during injection of reactive CO<sub>2</sub>-saturated water, *Geophysical Research Letters*, 38, L01 302, 2011.
- Vincent, B., Fleury, M., Santerre, Y., and Brigaud, B. : NMR relaxation of neritic carbonates : An integrated petrophysical and petrographical approach, *Journal of Applied Geophysics*, 74, 38–58, 2011.
- Volery, C., Davaud, E., Foubert, A., and Caline, B. : Shallow-Marine microporous carbonate reservoir rocks in the Middle East : Relationship with seawater Mg/Ca ratio and eustatic sea level, *Journal of Petroleum Geology*, 32, 313–325, 2009.
- Walsh, J. : The effect of cracks on the uniaxial elastic compression of rocks, *Journal of Geophysical Research*, 70, 399–411, 1965.
- Wang, H. F. : *Theory of linear poroelasticity*, Princeton Series in Geophysics, Princeton University Press, Princeton, NJ, 2000.
- Wang, X.-Q., Schubnel, A., Fortin, J., David, E., Gueguen, Y., and Ge, H.-K. : High V<sub>p</sub>/V<sub>s</sub> ratio : Saturated cracks or anisotropy effects ?, *Geophysical Research Letters*, 39, 2012.
- Wang, Y.-H. and Santamarina, J. : Attenuation in sand : an exploratory study on the small-strain behavior and the influence of moisture condensation, *Granular Matter*, 9, 365–376, 2007.

- Wang, Z. : Seismic properties of carbonate rocks, *Carbonate seismology*, 6, 29–52, 1997.
- Wang, Z. and Nur, A. : Elastic wave velocities in porous media : a theoretical recipe, *Seismic and acoustic velocities in reservoir rocks*, 2, 1–35, 1992.
- Wardlaw, N. : Pore geometry of carbonate rocks as revealed by pore casts and capillary pressure, *AAPG Bulletin*, 60, 245–257, 1976.
- Winkler, K. : Dispersion analysis of velocity and attenuation in Berea sandstone, *J. geophys. Res.*, 90, 793–6, 1985.
- Winkler, K. and Nur, A. : Pore fluids and seismic attenuation in rocks, *Geophysical Research Letters*, 6, 1–4, 1979.
- Winkler, K. W. and Murphy III, W. F. : Acoustic velocity and attenuation in porous rocks, in : *Rock Physics and Phase Relations, A Handbook of Physical Constants*, AGU Reference Shelf 3, American Geophysical Union, 1995.
- Youssef, S., Han, M., Bauer, D., Rosenberg, E., Bekri, S., Fleury, M., and Vizika, O. : High resolution  $\mu$ CT combined to numerical models to assess electrical properties of bimodal carbonates, Abu Dhabi, UAE, 29, 2008.
- Zimmerman, R. : Coupling in poroelasticity and thermoelasticity, *International Journal of Rock Mechanics and Mining Sciences*, 37, 79–87, 2000.
- Zimmerman, R. W., Somerton, W. H., and King, M. S. : Compressibility of porous rocks, *Journal of Geophysical Research : Solid Earth* (1978–2012), 91, 12 765–12 777, 1986.



# Appendices



ANNEXE **A**

---

**Experimental investigation of elastic and poroelastic properties of  
sandstone and limestone samples**

---

## A.1 Principle, Samples & Experimental set-up

### A.1.1 Principle

#### Drained compressibilities

Compressibility coefficients were defined by Zimmerman et al. (1986), using straightforward subscripts to indicate the volume change and its cause (Zimmerman, 2000). The rock's "bulk" volume  $V_b$  is the addition of the solid matrix's ( $V_s$ ) and pore space's ( $V_p$ ) volumes. The ratio of pore volume  $V_p$  over bulk volume  $V_b$  defines an intrinsic property of the rock : its porosity  $\phi$ .

The bulk compressibility coefficients  $C_{bc}$  and  $C_{bp}$  are associated with  $V_b$  variations caused by either a confining pressure ( $P_c$ ) or pore pressure ( $p_f$ ) variation respectively, which leads to :

$$C_{bc} = -\frac{1}{V_b} \left( \frac{\partial V_b}{\partial P_c} \right)_{p_f}, \quad \& \quad C_{bp} = \frac{1}{V_b} \left( \frac{\partial V_b}{\partial p_f} \right)_{P_c}. \quad (\text{A.1})$$

Note that the defined  $C_{bc}$  strictly corresponds to the well-known drained bulk modulus such that  $C_{bc} = K_d^{-1}$ .

The pore compressibility coefficients  $C_{pc}$  and  $C_{pp}$  are associated with  $V_p$  variations caused by either a confining pressure ( $P_c$ ) or pore pressure ( $p_f$ ) variation respectively, which leads to :

$$C_{pc} = -\frac{1}{V_p} \left( \frac{\partial V_p}{\partial P_c} \right)_{p_f}, \quad \& \quad C_{pp} = \frac{1}{V_p} \left( \frac{\partial V_p}{\partial p_f} \right)_{P_c}. \quad (\text{A.2})$$

The compressibility  $C_{pc}$  is sometimes noted  $C_{pc} = K_\phi^{-1}$ .

$C_s = K_s^{-1}$  can also be obtained for the porous rock. For a constant  $P_d$ , both pore and confining pressures apply the same load on the solid matrix so that :

$$C_s^1 = -\frac{1}{V_b} \left( \frac{\partial V_b}{\partial P_c} \right)_{P_d}, \quad \& \quad C_s^2 = -\frac{1}{V_p} \left( \frac{\partial V_p}{\partial P_c} \right)_{P_d}. \quad (\text{A.3})$$

Where  $C_s^1$  and  $C_s^2$  are the skeleton compressibilities. As noted by different authors (e.g., Brown and Korringa, 1975; Müller and Sahay, 2014), only if one neglects the possible micro-inhomogeneity effect will the relations lead to  $C_s = C_s^1 = C_s^2$ . Here, the relation  $C_s = C_s^1$  is assumed. No assumption is however made for  $C_s^2$ .

#### Undrained properties

Poroelasticity accounts for two distinct regimes, both isobaric. The drained regime is that when fluid is allowed to flow in and out of a REV. In the undrained regime, fluid is not allowed to flow out of the REV. In the drained regime, properties can be reached by understanding the fluid flow and matrix deformation responses to a given pressure solicitation.

In the undrained regime, the fluid mass  $m_f$  inside the sample is constant and fluid exerts a mechanical response to the applied pressure. Two parameters characterise this regime : (i) The pore pressure response to the applied stress, known as Skempton coefficient  $B$ , and (ii) The compressibility of the rock when build-up pressure is allowed in it, known as undrained bulk modulus  $K_u$  (or compressibility  $C_u$ ) :

$$K_u^{-1} = C_u = \frac{1}{V_b} \left( \frac{\partial V_b}{\partial P_c} \right)_{m_f}, \quad \& \quad B = \left( \frac{\partial p_f}{\partial P_c} \right)_{m_f}. \quad (\text{A.4})$$

### A.1.2 Samples

Out of the sample dataset presented in table (1.2), only seven limestone samples could be measured. The rocks are (i) a Chauvigny oolitic and micritic limestone samples, (ii) samples of Anstrude and Massangis limestone, (iii) a Tavel limestone sample, and (iv) samples of Lavoux and Euville limestone. The sample dataset have a porosity that is in the range of  $\phi \in [10; 30]$  %. Fontainebleau sandstone samples of porosities in the range of  $\phi \in [3; 18]$  %, and a Berea sandstone sample of 19 % porosity are also measured.

For a precise measurement of the poroelastic properties, the samples' intrinsic transport properties need to be known. For all samples, the permeabilities are measured as a function of effective pressure. From the static ramps, the porosity variation is also measured (from the volumetric strain) as a function of pressure. Figure (A.1) reports the measured permeabilities and porosities for two effective pressures of 1 and 10 MPa.

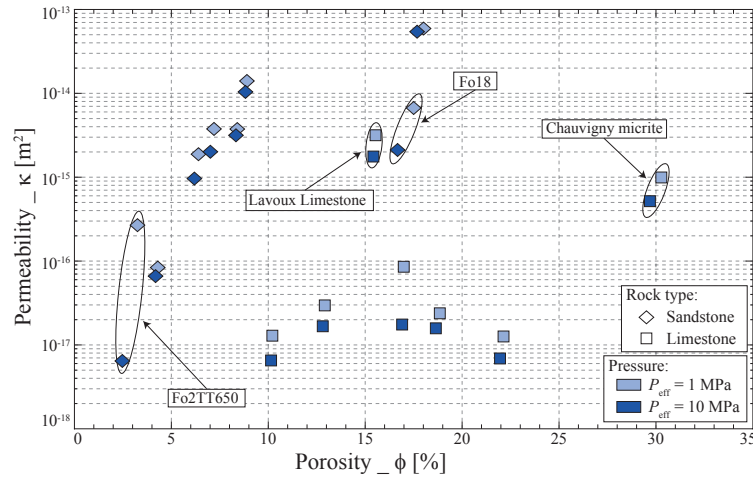


**Figure A.1 :** Measured porosities and permeabilities for two effective pressures of 1 and 10 MPa. Both sandstone (i.e. diamonds) and limestone (i.e. squares) samples are reported for comparison.

Overall, sandstone samples show an increase in permeability with increasing porosity, and limestone samples show a relatively constant range of  $[10^{-17}; 10^{-16}] \text{ m}^2$  whichever the porosity. However, some samples show distinct behaviours. The porosity-permeability

trend does not fit with the measurements on the 18% porosity Fontainebleau sandstone (Fo18). It probably originates from the very loose degree of cement of this sample. Lavoux limestone shows a permeability much higher than the other samples, which probably relates to its low micro- to macro-porosity ratio. Chauvigny micrite shows a permeability higher than the other limestone samples, which is consistent with its larger porosity. Note finally that a Fontainebleau sample of 2% porosity was thermally treated at 650 degC (i.e. Fo2TT650) to create a large microcrack density. As a consequence, permeability at 1 MPa was as large as about  $2 \cdot 10^{-16} \text{m}^2$ . When slightly increasing the confining pressure, permeability becomes as low as about  $5 \cdot 10^{-18} \text{m}^2$ , i.e. in the poro-permeability trend of the Fontainebleau sandstones.

### A.1.3 Experimental set-up

Although the apparatus used is the same as in **part III** and **part IV**, it is reintroduced because additional capacities of the experimental set-up are investigated.

#### Confining set-up

The apparatus aims at measuring simultaneously the complete set of elastic properties from low frequency and low amplitude pressure oscillations. To investigate these properties at different pressures, measurements are conducted in an oil-confining triaxial apparatus (Fortin et al., 2005) that can be used in two different set-ups thanks to an axial piston that can be shifted vertically. In the first set-up, the axial piston is not in contact with the end-platen (and thus the sample), allowing for studying the sample under pure isotropic conditions. In the second set-up, the piston is shifted down to exert a deviatoric stress on the sample. Only the first set-up is used here. This set-up was calibrated to allow for measuring both LF bulk modulus (i.e.  $K_{LF}$ ) and attenuation (i.e.  $Q_K^{-1}$ ) in the frequency range of  $f \in [4 \cdot 10^{-3}; 4 \cdot 10^{-1}] \text{ Hz}$ , using confining pressure oscillations (?). Only low frequency (i.e.  $f \sim 10^{-2} \text{ Hz}$ ) properties are here investigated. The frequency of oscillation remains low enough for the measured compressibilities to remain in the domain of quasi-static poroelasticity.

#### Pore fluid set-up

Pore pressure is controlled externally, and independently of the confining pressure, by a pair of connected Quizix servo-pumps. The pore volume and pressure measurements accuracies are respectively of about  $V_p \sim 0.1 \mu\text{L}$  and  $p_f \sim 0.001 \text{ MPa}$ . Each of the two pumps allows for a fluid pressure in the range of  $[0; 10.5] \text{ MPa}$ , and contains a maximum fluid volume of 40 mL. Additionally, another pressure transducer of  $p_f \sim 0.001 \text{ MPa}$  accuracy is placed near the sample. Valves are placed at both ends of the sample (Fig. A.2a) to decrease as much as possible the pipes' dead volumes, and the pressure sensor is placed near the

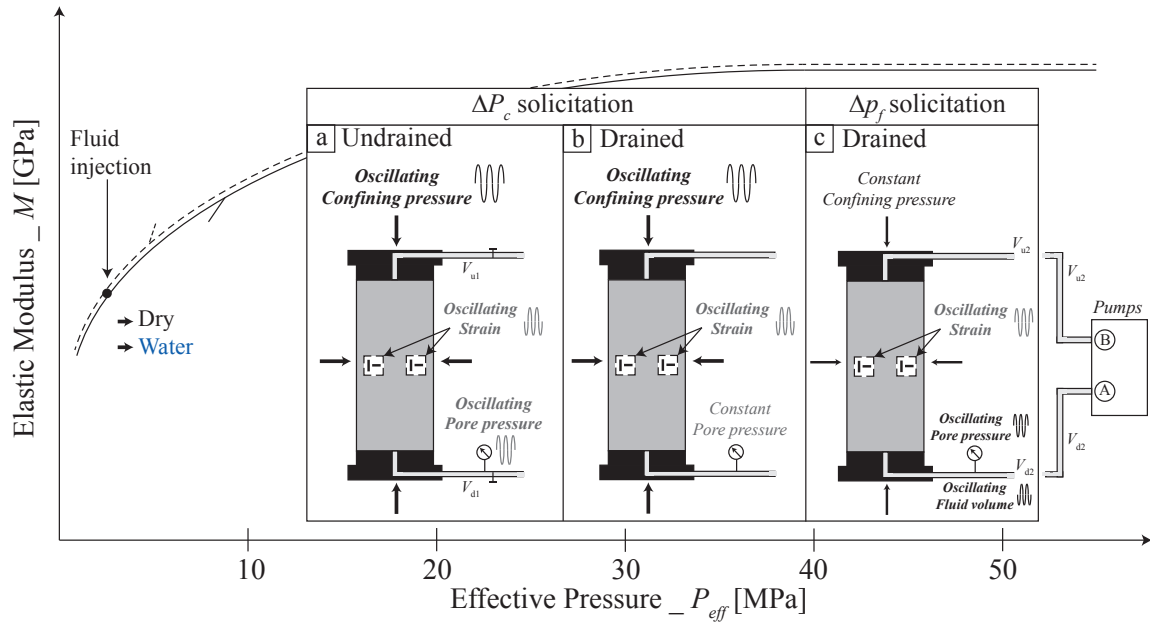


**Figure A.2** : Schematic view of the experimental set-up and the measuring procedures for the poroelastic properties.

bottom end-platen (i.e. inside the dead volume). The valves can either be open or closed. When changing the confining pressure, the first configuration is chosen so that the fluid is kept at a constant pressure of  $p_f \sim 2$  MPa and the sample is drained during the pressure ramps. Either of the two is chosen depending on the measurement of interest.

For the measurements under "experimentally undrained" conditions (Fig. A.2a), valves are closed. The measured dead volumes are  $V_u^1 = 3.433$  mL and  $V_d^1 = 3.205$  mL, leading to a total dead volume of about  $V^1 \sim 6.6$  mL. The total volume of fluid in the undrained system is thus the addition of the sample's volume and this dead volume.

For the measurement under "drained" conditions (Figs. A.2b & A.2c), the first configuration is chosen and valves are open. In case of the confining pressure oscillations (Fig. A.2b), pore pressure is regulated so that the properties remain the ones of the drained sample. Reversely, in case of the pore pressure oscillations (Fig. A.2c), confining pressure is regulated. Note however that another dead volume needs to be considered for these "drained" conditions. It encompasses  $V^1$  and the added volume from the tubing and the pore pressure pumps, i.e.  $V_u^2$  and  $V_d^2$ . Because the volume of fluid filling the pumps was never exactly the same, this second dead volume however varies from sample to sample. Overall, it remains however in the range of [30; 50] mL (i.e. about half-volume for each pump) for all experiments.

The same procedure is followed for both dry and water-saturated conditions. The full saturation of the sample by water is ascertained by a precise injection procedure : (1) vacuum is applied with a vacuum pump at the sample upper end until the measured  $p_f$  (at

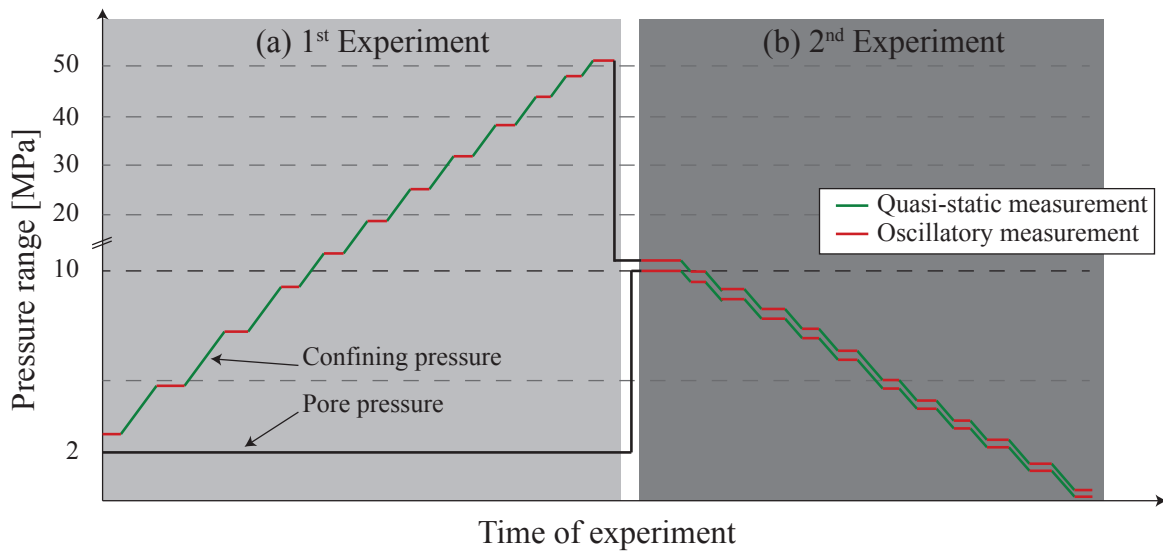


**Figure A.3 :** Schematic view of the measuring protocol for the two different experiments (i.e. grey zones). For both experiments, both static (i.e. green) and oscillatory measurements are made on the sample.

the sample’s bottom) reaches a stable negative value of  $\sim -0.8$  MPa ; (2) then, the fluid is injected at the sample bottom while maintaining the vacuum with the vacuum pump. This injection procedure (using the vacuum pump) complements the density effect (i.e. air pushed up by the denser fluid), and was shown to allow for a 100% fluid saturation. For the sandstone samples in fluid saturated conditions, Terzaghi effective pressure  $P_{eff} = P_c - p_f$  is used that allows for a simple comparison between dry and fluid-saturated conditions.

All limestone samples are measured under either dry or water-saturated conditions. The Berea sample is measured under saturation by four different fluids. First, air is used for the measurements. Then, the sample is fully saturated by glycerine. Finally, it is saturated by a water-glycerine mixture. Permeability measurements showed (Chaps. 2, 3 & 4) that the mixture had a viscosity ten times higher than water (and about 35 times lower than glycerine). As a last step, full saturation by pure water was reached by flushing three to four times the total volume by water.

### Experimental procedures

In addition, two different procedures are tested (Fig. A.3) to better investigate the poroelastic properties of the water-saturated sample.

In the first experiment (Fig. A.3a), the properties are measured for different values of Terzaghi effective pressure, i.e. by increasing step-wise the confining pressure and keeping the pore pressure constant. When increasing the confining and keeping the pore pressure constant, static measurements can be reached under drained conditions. In particular, the porosity variation is monitored. At each step, when  $P_{eff}$  is constant, the properties are measured from low-frequency and low-amplitude pressures oscillations. At 50 MPa, the

confining pressure is decreased slowly down to about  $P_c = 11$  MPa. Then, pore pressure is increased up to about  $p_f = 10$  MPa. After stabilisation, the second experiment is began.

For the second experiment (Fig. A.3b), the aim is to investigate the effect of the pore pressure on the poroelastic properties. Thus, all measurements are made each 1 MPa, for a constant  $P_{eff}$  and for a  $p_f \in [0.1; 10]$  MPa. Again, at each step, low-frequency oscillatory measurements are made. Between each pressure step, static properties are measured from slowly decreasing pore then confining pressure by 1 MPa.

For all limestone samples, the first experiment is applied on dry and water-saturated samples and the second one is applied for water-saturated samples. For the Berea sample, the first experiment is applied to the sample under dry, glycerine and water-glycerine saturations. For the second experiment, the sample is measured while under saturation by pure water.

## A.2 Experimental protocol & properties measured

This study aims at investigating the samples' poroelastic response to low frequency and low amplitude pressure oscillations. The signal processing associated to the oscillations' treatment has been developed in ?. Because the field of elasticity (or poroelasticity) considers small reversible deformations, the present approach aims at measuring strains (i.e. peak-to-peak amplitude) lower than about  $10^{-5}$ . For the samples studied, this implies applying pressure amplitudes below 0.2 MPa. Note that the signals' phase shifts are here discarded to investigate solely the amplitude response. Provided that axial and radial strains should behave the same for a pressure variation in a rock, and assuming the rock to be isotropic, the different measurements are equally considered to build the mean value and the measurement error.

For all measurements except for the unjacketed one (measured under oil saturation), an example of the measuring method is given in case of a Berea sample at  $P_{eff} = 1$  MPa.

### A.2.1 Unjacketed measurement

Because the sample is placed with no rubber jacket to isolate it from the confining medium, the pore pressure (i.e.  $\Delta p_f$ ) inside the sample is expected to equal the applied confining pressure (i.e.  $\Delta P_c$ ) under unjacketed conditions. The sample's matrix is submitted to coupled pressures oscillations, i.e. the Terzaghi effective pressure equals zero. This approximation is experimentally tested by measuring the pore pressure directly in the dead volume. For a given  $\Delta P_c$  (Fig. A.4a), both pore pressure  $\Delta p_f$  (Fig. A.4a) and sample's volumetric strain  $\Delta \epsilon$  (Fig. A.4b) are measured. An example is given for the oil saturated Berea sample at a confining pressure of  $P_c = 1$  MPa.

From the theory of linear poroelasticity, a small reversible strain induced by a pressure variation, when differential pressure is constant, directly relates to the skeleton bulk mo-

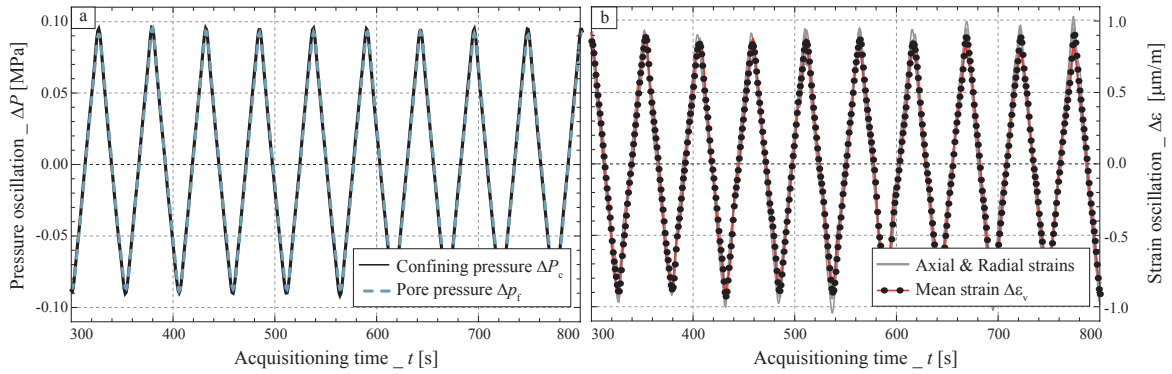


**Figure A.4 :** Principle for the unjacketed measurement for the example of a Berea sample at a confining pressure of 1 MPa. For an applied confining pressure oscillation, (a) pore pressure and (b) strains are recorded.

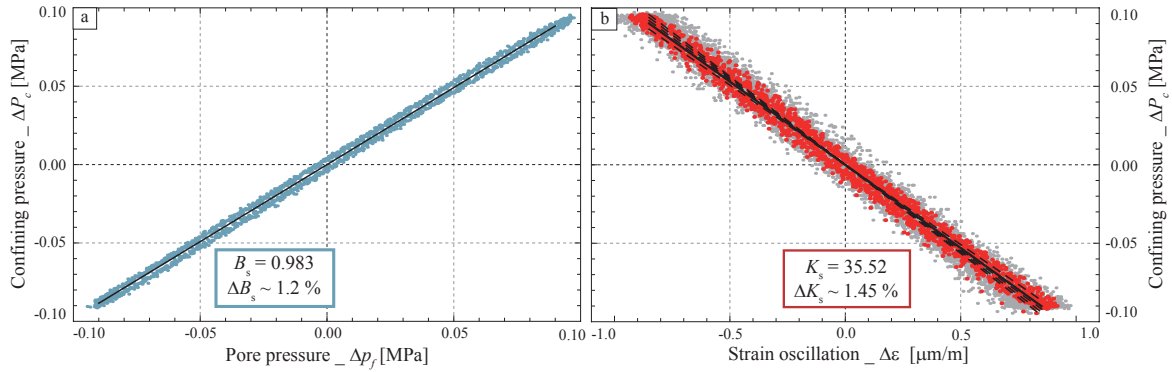


**Figure A.5 :** The properties are obtained from a linear regression between applied pressure and recorded (c) pore pressure and (d) strains. Example of a Berea sample at a confining pressure of 1 MPa.

dulus  $K_s$  (Eq. A.3) Because small pressure oscillations are applied, the derivative of  $\partial P_c$  and  $\partial V_b$  can consistently be approximated by the oscillations amplitudes  $\Delta P_c$  and  $\Delta V_b$ . As the measured volumetric strain (i.e.  $\Delta \epsilon$ ) directly corresponds to the normalised volume variation (i.e.  $\Delta V_b / V_b$ ), the equation simply rewrites as :

$$K_s^{-1} = C_s = \left( \frac{\Delta \epsilon}{\Delta P_c} \right)_{P_{eff}} \quad (A.5)$$

For this example, linear regressions between confining and pore pressure (Fig. A.5a) and between confining pressure and volumetric strain (Fig. A.5b) are calculated.

As shown from the linear regression between  $\Delta P_c$  and  $\Delta p_f$  (Fig. A.5a), differential pressure can consistently be considered as equal to zero during the oscillation. The assumption of a constant  $P_{eff}$  during the measurement thus applies here. The linear regression between confining pressure and strain thus strictly corresponds to the measurement of the skeleton incompressibility  $K_s$  (or compressibility  $C_s$ ). The linear regression leads here to a measured  $K_s$  of about 35.5 GPa (Fig. A.5a). This value is close to the one reported for the quartz of  $K_{qtz} = 37$  GPa. In terms of compressibility, the measurement corresponds to a value of

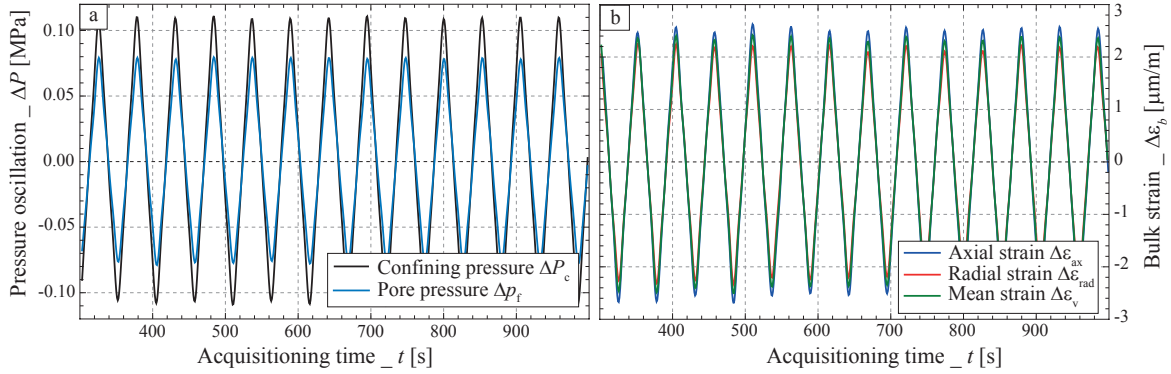


**Figure A.6 :** Principle for the undrained measurement for the example of a Berea sample at an effective pressure of 1 MPa. For an applied confining pressure oscillation, (a) pore pressure and (b) strains are recorded.

$$C_s = 2.82 \cdot 10^{-11} \text{ Pa}^{-1}.$$

### A.2.2 Undrained measurement

Under experimentally undrained conditions, a confining pressure oscillation is applied and pore pressure and the sample's strain are recorded (Fig. A.6).

Consistently, the resulting  $\Delta p_f$  (Fig. A.6a) is lower than the applied  $\Delta P_c$  as compared to theunjacketed measurement. On the reverse, the strain  $\Delta \epsilon$  (Fig. A.6b) is larger for this measurement. Note the slightly different signals shown by the two strain gages, which probably originates from the gluing quality. Note that such deviations in amplitude are not observed at higher confining.

Two parameters can be measured : Skempton coefficient  $B$  and the undrained bulk modulus  $K_u$  (or compressibility  $C_u$ ) from equation (A.4). However, because the dead volume is important at both sample's ends, it cannot be neglected in comparison with the sample's storage capacity (?). The fluid mass  $m_{f1}$  considered constant is not only the one contained in the sample  $m_f$ , but also needs to consider the one contained in the dead volume  $m_d$ . The parameters measured are thus designed as a pseudo-Skempton coefficient  $B^*$  and pseudo-undrained compressibility  $C_u^*$ .

For these small amplitudes of deformation, the properties are measured such that :

$$C_u^* = \left( \frac{\Delta \epsilon}{\Delta P_c} \right)_{m_{f1}}, \text{ \& } B^* = \left( \frac{\Delta p_f}{\Delta P_c} \right)_{m_{f1}}. \quad (\text{A.6})$$

Linear regressions between confining and pore pressure (Fig. A.7b) and between confining pressure and volumetric strain (Fig. A.7b) are obtained.

For  $B^*$ , only one measurement (i.e. one pressure sensor) was available so that one linear regression is reported. The statistical scattering around the regression, noted  $\Delta B^*$ , is thus very low. Reversely, three linear regressions are reported that correspond to measurements from two strain gages and their mean value. The reported  $\Delta C_u^*$  thus accounts for both the

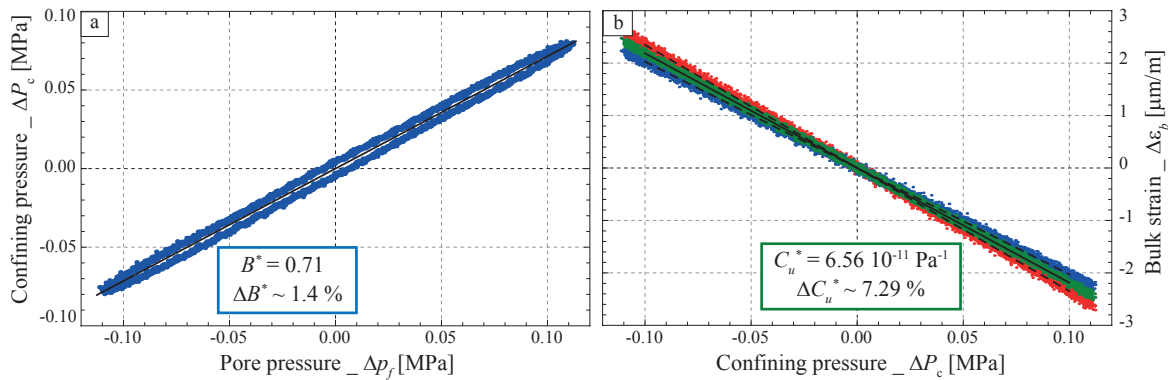


**Figure A.7 :** The properties are obtained from a linear regression between applied pressure and recorded (a) pore pressure and (b) strains. Example of a Berea sample at an effective pressure of 1 MPa.

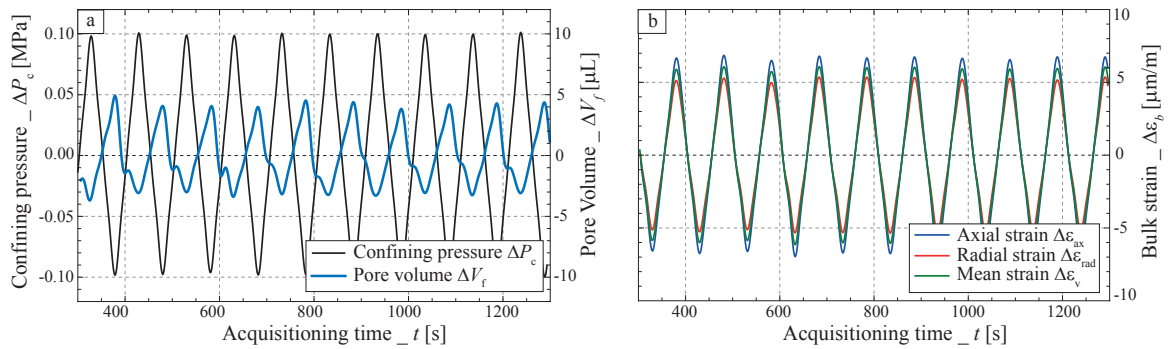


**Figure A.8 :** Principle for the drained measurement in case of confining pressure oscillations. For an applied confining pressure oscillation, (a) fluid volume variations and (b) strains are recorded. Example of a Berea sample at an effective pressure of 1 MPa.

statistical scattering around the regression and the standard deviation between the different strain gages. As a consequence, the error is as high as about 7% for this measurement.

### A.2.3 Drained measurement : Confining pressure oscillations

Under experimentally drained conditions, confining pressure is oscillated and pore pressure is maintained constant. The fluid volume (pumped in and out) and volumetric strains are recorded (Fig. A.8).

As shown from the fluid volume  $\Delta V_f$  (Fig. A.8a), the signal is not triangular-shaped anymore. This effect originates from the slightly delayed pore pressure pumps regulation. As a consequence, the measured strains are also not triangular-shaped (Fig. A.8b). Note again the small difference in strains amplitudes between strain gages. Furthermore, although the pressure amplitude was the same as for the undrained measurement (Fig. A.6a), the strain amplitude is much larger (Fig. A.6b). It originates from a consistent increase in compressibility of the sample's matrix under drained conditions.

Although the strain amplitude is slightly higher than about  $10^{-5}$ , it is again assumed that the poroelasticity field holds. This measuring condition allows to reach two of the

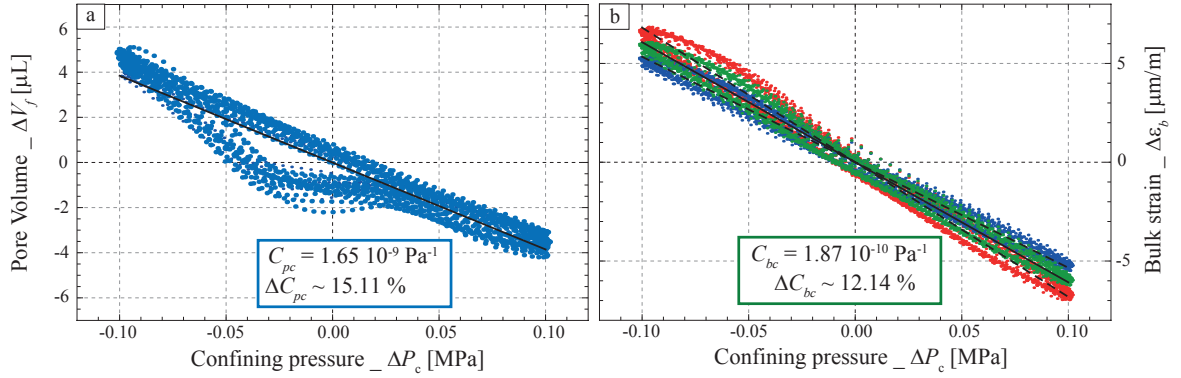


**Figure A.9** : The properties are obtained from a linear regression between applied pressure and recorded (a) fluid volume and (b) strains. Example of a Berea sample at an effective pressure of 1 MPa.

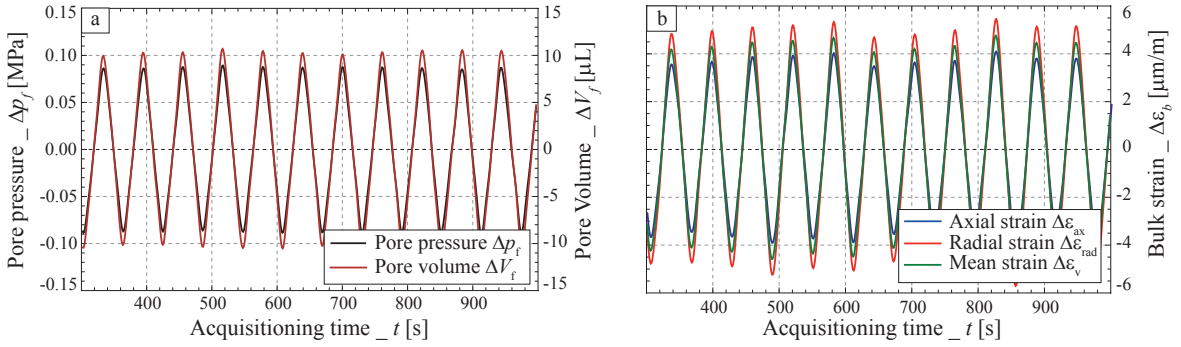


**Figure A.10** : Principle for the drained measurement in case of confining pressure oscillations. For an applied pore pressure oscillation, (a) fluid volume variations and (b) strains are recorded. Example of a Berea sample at an effective pressure of 1 MPa.

drained compressibilities  $C_{bc} = C_d$  and  $C_{pc}$ , such that :

$$C_{bc} = \left( \frac{\Delta \epsilon}{\Delta P_c} \right)_{p_f}, \text{ \& } C_{pc} = \frac{1}{V_p} \left( \frac{\Delta V_p}{\Delta P_c} \right)_{p_f}. \quad (\text{A.7})$$

Linear regressions between confining pressure and fluid volume (Fig. A.9a), between confining pressure and volumetric strain (Fig. A.9b) are obtained.

As compared to the earlier linear regressions, trends are not perfectly linear. The effect is stronger on the fluid volume regression (Fig. A.9a) than for the strain one (Fig. A.9b). It originates from the delayed regulation of the pore pressure pumps.

#### A.2.4 Drained measurement : Pore pressure oscillations

Under drained conditions, pore pressure is oscillated while maintaining the confining pressure constant. For such solicitation, fluid volume change and strains are recorded (Fig. A.8).

During this pore pressure oscillation, both fluid volume and bulk strains are measured.

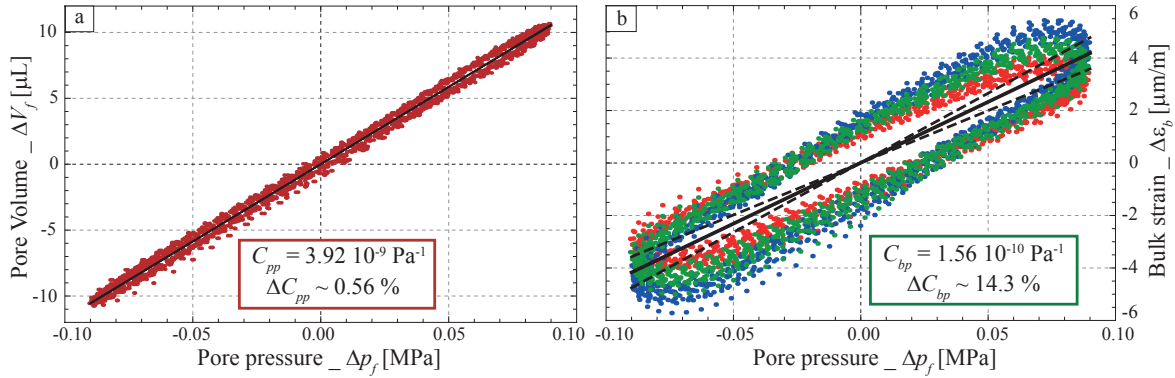


**Figure A.11** : The properties are obtained from a linear regression between applied pore pressure and recorded (a) fluid volume and (b) strains. Example of a Berea sample at an effective pressure of 1 MPa.

Note that the difference in amplitude between the strain gages, still present, shows a change as compared to before (Figs. A.6b & A.8b) : the strain showing the biggest variation is the radial one.

Overall, the amplitudes of strains remain below  $10^{-5}$ , allowing to consistently assume the small reversible strains condition. This measuring condition allows to reach the compressibilities  $C_{bp}$  and  $C_{pp}$  such that :

$$C_{bp} = C_d = \left( \frac{\Delta\epsilon}{\Delta p_f} \right)_{p_c}, \quad \& \quad C_{pp} = \frac{1}{V_p} \left( \frac{\Delta V_p}{\Delta p_f} \right)_{p_c}. \quad (\text{A.8})$$

Linear regressions between pore pressure and fluid volume (Fig. A.9a) and volumetric strain (Fig. A.9b) are obtained.

As shown by the regression of  $C_{bp}$ , an hysteresis appears for the strain measurement (Fig. A.9b) only. It indicates a small phase shift between applied pore pressure and resulting strains oscillations. Even by decreasing the frequency of the oscillation, already lower than for the confining pressure oscillations, this hysteresis could not be deleted. It thus probably relates to the difficulty of fluid to induce a perfectly in-phase strain. Along with the standard deviation between the strains, this hysteresis is thus accounted for in the accuracy of the measurement  $\Delta C_{bp}$ , resulting as high as about 14%.

### A.3 Preliminary results

#### A.3.1 Effect of the fluid volume on the pore compressibilities

Comparing the values of  $C_{pc}$  and  $C_{pp}$ , an order of magnitude difference is obtained for both compressibilities. It may directly imply that those two measurements are erroneous. Indeed, measuring the compressibilities  $C_{pc}$  and  $C_{pp}$  is experimentally challenging because the pore volume variations  $\delta V_p$  cannot be precisely measured. Although it remained pos-

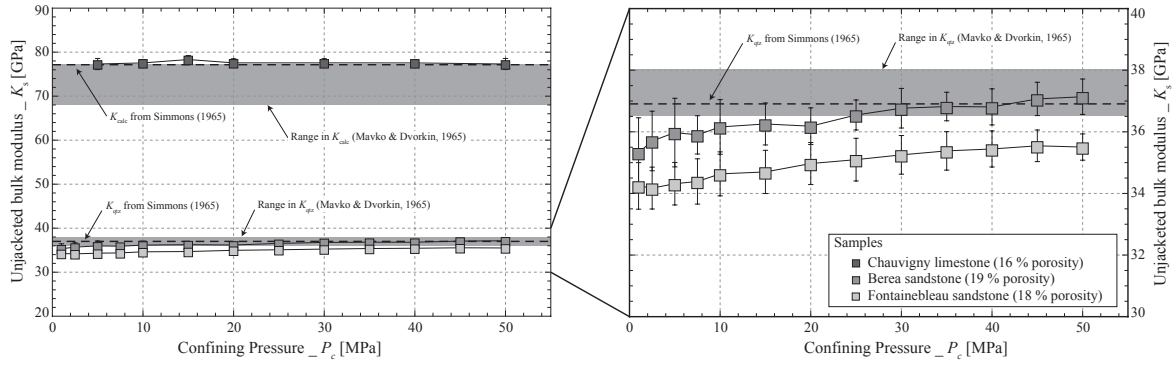


**Figure A.12** : Measured skeleton bulk moduli  $K_s$  as a function of confining pressure for Be19, Fo18 and ChoL. The range of values found (Mavko et al., 2003) for the quartz and calcite mineral bulk moduli  $K_m$  are reported as grey zones.

sible to infer  $\delta V_p$  from the measured fluid volume variation inside the pumps  $\delta V_f$ , the approach of assuming  $\delta V_p = \delta V_f$  resulted erroneous.

Both pore compressibilities are thus discarded at this stage. Reversely, the bulk compressibility lead to consistent results and are thus used in the following.

### A.3.2 Skeleton bulk modulus

Three samples' bulk moduli were measured under purely unjacketed conditions for different confining pressures in the range of  $P_c = [1; 50]$  MPa. The sandstone samples are a Berea sample of 19% porosity (Be19) and a Fontainebleau sample of 18% porosity (Fo18). The limestone sample is a 16% Chauvigny oolitic sample (ChoL). For all three rocks, the fluid used is hydraulic oil. The correspondence between the mineral  $K_s$  and skeleton  $K_\phi$  bulk moduli is investigated (Fig. A.12).

Overall, all three samples's  $K_s$  compare favourably with the reported  $K_m$ .  $K_s$  of ChoL is constant with  $P_c$  and falls in the upper part of the range of reported  $K_{calc}$ . Its value equals the one reported by Simmons et al. (1982) for the calcite mineral of  $K_{calc} = 77$  GPa. It implies that under oil saturation, the value obtained for  $K_s$  is consistent with the theory, i.e.  $K_s = K_m$ . For the case of the sandstone samples, a slight increase in  $K_s$  is observed as  $P_c$  increases. Furthermore, as compared to the range reported for the quartz  $K_m = [36.5; 38]$  GPa (Mavko et al., 2003), the measurements result below these values. Zooming on the measurements (Fig. A.12b), shows that about the same increase in  $K_s$  is observed for both Be19 and Fo18 as  $P_c$  increases. In case of Be19, the increase with  $P_c$  leads to  $K_s = 37$  GPa at higher confining, a value usually chosen as the quartz crystal's bulk modulus. In case of Fo18, the value reached is 35.5 GPa at higher confining, a value about 2 GPa below the quartz  $K_m$ .

Finally, only the sandstone samples show a dependence to pressure, and only Fo18 shows the relation  $K_s < K_m$ . In case of the limestone sample, the value of  $K_s = K_{calc} = 77$  GPa can be consistently used in the following.

### A.3.3 Bulk compressibility of the Berea sandstone

#### Confining pressure oscillations

The pore and bulk compressibility  $C_{bc}$  is investigated as a function of pressure for the Berea sample under dry and fluid-saturated conditions (Fig. A.13). Because the nature of the saturating fluid may affect the poroelastic response, different saturating fluids are tested and compared.

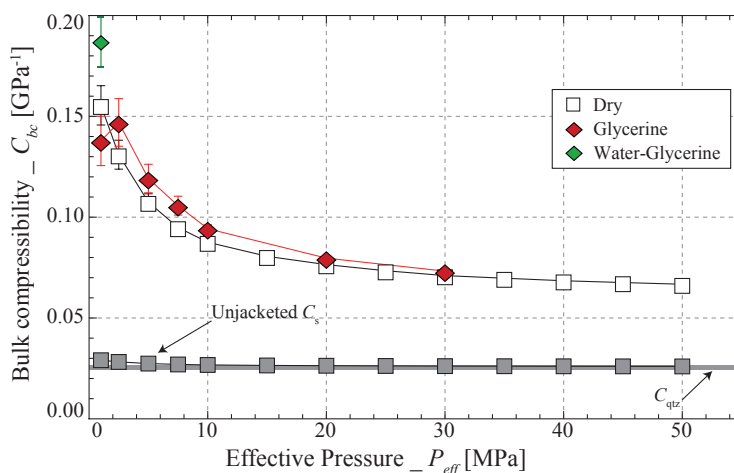


Figure A.13 : Pressure dependence of  $C_{bc}$  and  $C_s$  for the dry and fluid-saturated Berea sample.

A large decrease in  $C_{bc}$  (Fig. A.13a) is measured as pressure increases, which originates from the microcracks' closure. The bulk compressibility  $C_{bc}$  (Fig. A.13a) under dry conditions fits with the ones, under either water-glycerine or glycerine saturation, under purely drained conditions. The fluid nature thus does not affect here the measured  $C_{bc}$ .

The measured  $C_{bc}$  is much larger than the measured  $C_s$ . The difference between the compressibilities decrease as  $P_{eff}$  increases, implying that  $C_s$  is not affected by the microcracks. Because the large porosity of the sample also affects its drained compressibility, a difference remains between  $C_{bc}$  and  $C_s$  at  $P_{eff} = 50$  MPa.

#### Pore pressure pressure oscillations

The bulk compressibility  $C_{bp}$  is investigated as a function of pressure for the Berea sample under dry and fluid-saturated conditions (Fig. A.14).  $C_{bp}$  shows a large decrease when the pressure increases. As for  $C_{bc}$ , the effect may relate to the microcracks' closure.

As for  $C_{bc}$ ,  $C_{bp}$  shows no clear dependence to the saturating fluid. Interestingly, the value measured for  $C_{bp}$  is near the one found for  $C_{bc}$  at lowest confining pressure. This is in fact expected as the ratio between  $C_{bc}$  and  $C_{bp}$  directly relates to the Biot-Willis coefficient  $\alpha$ , which should be near unity for the Berea sample.

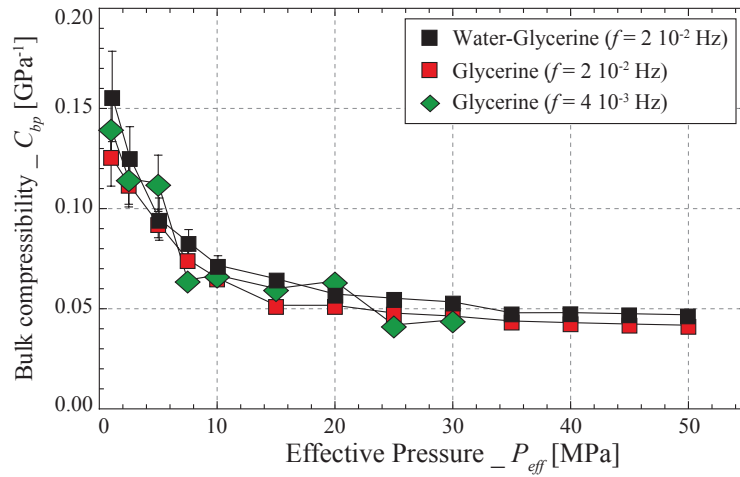


Figure A.14 : Pressure dependence of  $C_{bp}$  of the Berea sandstone sample under saturation by either glycerine or a water-glycerine mixture.

### A.3.4 Bulk compressibility of limestone samples

The assessed bulk compressibilities  $C_{bc}$  and  $C_{bp}$  are obtained. The coefficients are reported as a function of porosity for the seven limestone samples studied (Fig. A.15).

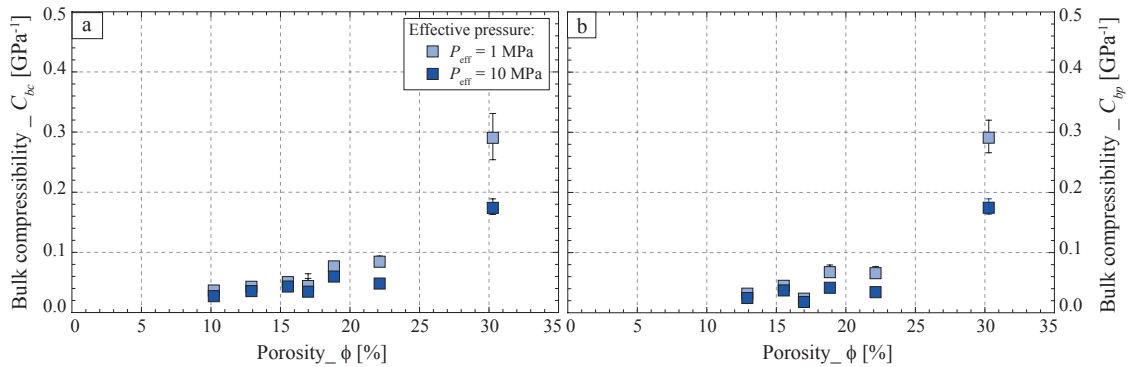


Figure A.15 : (a)  $C_{bc}$  and (b)  $C_{bp}$  as a function of porosity for the seven limestone samples at two effective pressures of 1 and 10 MPa.

A dependence to porosity and pressure is observed for both coefficients. Both  $C_{bc}$  and  $C_{bp}$  increase as porosity increases. Because the pressure effect increases with increasing porosity, the trend changes with pressure. Note that the values obtained for  $C_{bp}$  are in the range of the ones found for  $C_{bc}$ . Interestingly, for the case of the most porous ChmL sample, the values fit. From the relation between these compressibility coefficients, it implies that  $C_{bp} = \alpha C_{bc} = C_{bc}$ , i.e. that the Biot coefficient is equal to  $\alpha = 1$ .

### A.3.5 Effect of the dead volume under undrained conditions

Another interesting information could be obtained from the undrained measurements. As detailed by Ghabezloo and Sulem (2009), owing to an interplay between the dead volume's storage capacity and the sample's one, the dead volume may affect the undrained measurements. As shown by the authors, the effect of this dead volume increases as the sample's storage capacity, and thus the porosity and compressibility, increase. Let us investigate the effect of this dead volume for the most porous ChmL sample of the study.

#### Corrected Skempton coefficient

Theoretical expressions were found by Ghabezloo and Sulem (2009) to account for the dead volume effect. Assuming a constant temperature and that the pressure amplitudes are small enough for the tubing compressibility to be neglected, their equation for the measured Skempton coefficient  $B^*$  rewrites :

$$B^* = \frac{V_s(C_d - C_s)}{V_s S_s + V_f C_f}. \quad (\text{A.9})$$

Where  $V_s$  and  $V_f$  are respectively the sample's and tubing's volumes, and  $S_s$  is the sample's storage capacity. The effect on the undrained compressibility is directly inferred such that :

$$C_u^* = C_d - B^*(C_d - C_s). \quad (\text{A.10})$$

Storage capacity  $S_s$  is a material property that is theoretically obtained from the porosity  $\phi$  and the drained  $C_d$ , fluid  $C_f$  and skeleton  $C_s$  compressibilities (Kümpel, 1991) such that :

$$S_s = (C_d - C_s) + \phi (C_f - C_\phi). \quad (\text{A.11})$$

From the experiments, the sample's drained compressibility and intrinsic porosity are known. The fluid's compressibility is also known. One may assume that :

- $C_\phi = C_s$ .
- $C_s$  is independent of pressure and equal to the mineral's compressibility (i.e.  $K_{calc} = 77 \text{ GPa}$ ).

From these assumptions, it results possible to predict the storage capacity  $S_s$  for all the samples investigated.

Noting the theoretical expression for the Skempton coefficient  $B$ , it is then possible to infer from the measurements, the real Skempton coefficient  $B_{th}$  of the rock investigated such that :

$$B_{th} = B^* \frac{V_s S_s}{V_s S_s - V_f C_f}. \quad (\text{A.12})$$

In case of the most porous ChmL sample, the measured and corrected Skempton coefficients are compared for the different effective pressures of study (Fig. A.16a). An upward shift is observed on the corrected value so that the sample's intrinsic Skempton coefficient shows the same pressure dependence yet starts from  $B = 1$  at  $P_{eff} = 1$  MPa.

### Inferred storage capacity

As a proxy of the skeleton compressibility  $C_\phi$ , one may investigate the inferred storage capacities  $S$  inferred using differing means. The theoretical  $S_s$  is often calculated from Eq. (A.11). However, it implies assuming that  $C_s = C_\phi = C_m$ , which could be questioned in case of a water-rock interaction. Another mean can be used to infer the storage capacities : using the partially undrained measurements, i.e. making use of the dead volume effect.

From Eq. (A.3.5) and (A.3.5), one may calculate the storage capacities (i.e.  $S_B$  and  $S_{Cu}$ ) related to the measurements of  $B^*$  and  $C_u^*$  :

$$S_B = \frac{(C_f - C_s)}{B^*} - \frac{V_f}{V_s} C_f. \quad (\text{A.13})$$

and

$$S_{Cu} = \frac{(C_d - C_s)^2}{(C_d - C_u^*)} - \frac{V_f}{V_s} C_f. \quad (\text{A.14})$$

Provided that the skeleton compressibility  $C_s$  is independent of pressure and equal to  $C_{calc}$  (i.e.  $K_{calc} = 77$  GPa), one may thus infer  $S_B$  and  $S_{Cu}$  as a function of effective pressure. The three storage capacities inferred are compared as a function of effective pressure in case of ChmL (Fig. A.16b).

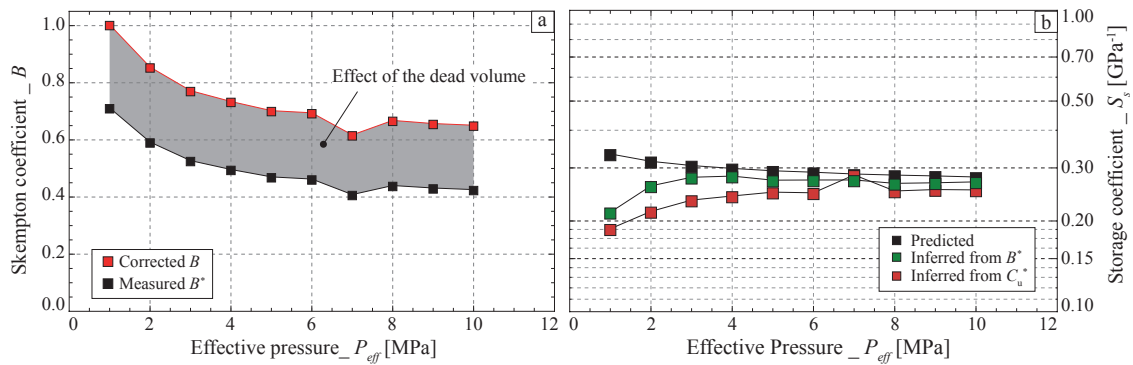


**Figure A.16** : (a) Corrected Skempton coefficient using the theoretical value of storage capacity  $S_s$ , and (b) Comparison between predicted and inferred storage capacity as a function of pressure for the seven limestone samples.

As shown (Fig. A.16b), the theoretical  $S_s$  and the inferred  $S_B$  and  $S_{Cu}$  compare favourably. For all effective pressures, they fall in the range of  $S \in [0.2; 0.3]$  GPa<sup>-1</sup>. For pressures beyond 5 MPa, the values fit. Yet, a deviation is observed for the lowest pressures. While  $S_s$

decreases,  $S_B$  and  $S_{Cu}$  increase as  $P_{eff}$  increases. This difference roots in the value taken for the skeleton compressibility  $C_\phi$ . It implies from the measurements that the sample's  $C_\phi$  is not equal to  $C_{calc}$ , and is not constant with pressure. The value is probably slightly lower at low  $P_{eff}$ , and increases to reach  $C_\phi = C_{calc}$  beyond 5 MPa. This is consistent with the results obtained for  $C_s$  on the loosely cemented sandstone samples (Fig. A.12b).

An important consequence is reached here. Although of about 30% porosity, for this carbonate sample the measurements imply that  $C_\phi = C_s$ . Furthermore,  $C_\phi$  and  $C_s$  are only slightly lower than the calcite compressibility below 5 MPa, and are equal to  $C_{calc}$  beyond. This behaviour may be typical in case of a loosely cemented limestone. No fluid-rock interaction effect are thus observed even in the case of the most porous and unconsolidated carbonate sample studied.

## A.4 Conclusion

A method was developed to measure a large set of elastic properties of a porous sample using low amplitude and low frequency pressure oscillations. This preliminary study aims at investigating the different compressibilities/bulk moduli one can accurately measure. It is shown that, using either the drained or the undrained boundary conditions, up to six independent measurements can be made.

It is shown that additional understanding of the fluid total volume is needed to properly measure the pore compressibilities  $C_{pc}$  and  $C_{pp}$ . The bulk compressibilities  $C_{pc}$  and  $C_{pp}$  can be precisely measured in the pressure range of [1;50] MPa. Under dry, glycerine and water-glycerine saturations, no fluid effect is observed and the coefficients compare well in the Berea sample. The compressibility coefficients are then measured on a set of carbonate samples ranging from 10% to about 30% porosity. Consistently, all properties show a clear dependence to porosity and confining pressure.

An additional procedure is tested through the dead volume effect. Using the most porous limestone sample, it is shown that the storage capacity  $S_s$  can be investigated.